CONTENTS

ABSTRACTS

Yurii Streliaiev, Rostyslav Martynyak, Kostyantyn Chumak
Thermomechanical Slip in Elastic Contact between Identical Materials

The contact problem for interaction between an elastic sphere and an elastic half-space is considered taking into account partial thermomechanical frictional slip induced by thermal expansion of the half-space. The elastic constants of the bodies are assumed to be identical. The Amontons–Coulomb law is used to account for friction. The problem is reduced to non-linear boundary integral equations that correspond to the initial stage of mechanical loading and the subsequent stage of thermal loading. The dependences of the contact stress distribution, relative displacements of the contacting surfaces, dimensions of the stick and slip zones on temperature of the half-space are studied numerically. It was revealed that an increase in temperature causes increases in the shear contact stress and the relative shear displacements of the contacting surfaces. The absolute values of the shear contact stress reach their maximum at the boundaries of the stick zones. The greatest value of the moduli of the relative shear displacements are reached at the boundary of the contact region. The stick zone radius decreases monotonically according to a nonlinear law with increasing temperature.

Vladimir Morkun, Natalia Morkun, Vitaliy Tron, Olga Porkuian, Oleksandra Serdiuk, Tetiana Sulyma
Application of Magnetic and Ultrasonic Methods for Determining Parameters of Ferromagnetic Component in Iron Ore Slurry Flows

The article considers the method for controlling the ferromagnetic component content in slurry flow by ultrasonic and magnetic measurements. One of the basic factors determining the efficiency of magnetic separators at iron ore concentration plants is the quality of distribution of the ground ore into the product containing the ferromagnetic component and the waste rock. Due to the fact that in most cases, magnetic separators extract minerals with strongly magnetic properties, it is essential to find the magnetic component content in the input ore and products of its distribution in order to improve control over the technological process. Currently, low accuracy and reliability make existing means of operative control over the ferromagnetic component content in the slurry flow inefficient. Density of slurry is one of the primary disturbing factors affecting the accuracy of measurements, and this fact determines the necessity of measuring this parameter while controlling the ferromagnetic component content. Combined methods of measurements are a promising trend in designing sensors of useful component content in the slurry flow. The article describes the method for controlling the ferromagnetic component content in slurry flow by ultrasonic and magnetic measurements.

Ould Mohamed Mohamed Vall
Design of Decoupled PI Controllers for Two-Input Two-Output Networked Control Systems with Intrinsic and Network-Induced Time Delays

Proportional integral controller design for two-input two-output (TITO) networked control systems (NCSs) with intrinsic and network-induced time delays is studied in this paper. The TITO NCS consists of two delayed sub-systems coupled in a 1-1/2-2 pairing mode. In order to simplify the controller design, a decoupling method is first applied to obtain a decoupled system. Then, the controllers are designed based on the transfer function matrix of the obtained decoupled system and using the boundary locus method for determining the stability region and the well-known Mikhailov criterion for the stability test. A comparative analysis of the designed controllers and other controllers proposed in previous literature works is thereafter carried out. To demonstrate the validity and efficacy of the proposed method and to show that it achieves better results than other methods proposed in earlier literature works, the implementation in simulation of Wood–Berry distillation column model (methanol–water separation), a well-known benchmark for TITO systems, is carried out.

Vikas Singh Panwar, Anish Pandey, Muhammad Ehtesham Hasan
Generalized Regression Neural Network (GRNN) Architecture-Based Motion Planning and Control of an E-Puck Robot in V-Rep Software Platform

This article focuses on the motion planning and control of an automated differential-driven two-wheeled E-puck robot using Generalized Regression Neural Network (GRNN) architecture in the Virtual Robot Experimentation Platform (V-REP) software platform among scattered obstacles. The main advantage of this GRNN over the feedforward neural network is that it provides accurate results in a short period with minimal error. First, the designed GRNN architecture receives real-time obstacle information from the Infra-Red (IR) sensors of an E-puck robot. According to IR sensor data interpretation, this architecture sends the left and right wheel velocities command to the E-puck robot in the V-REP software platform. In the present study, the GRNN architecture includes the MIMO system, i.e., multiple inputs (IR sensors data) and multiple outputs (left and right wheel velocities). The three-dimensional (3D) motion and orientation results of the GRNN architecture-controlled E-puck robot are carried out in the V-REP software platform among scattered and wall-type obstacles. Further on, compared with the feedforward neural network, the proposed GRNN architecture obtains better navigation path length with minimum error results.

Michal Korbut, Dariusz Szpica
A Review of Compressed Air Engine in The Vehicle Propulsion System

Engines powered by compressed air as a source of propulsion are known for many years. Nevertheless, this type of drive is not commonly used. The main reason for not using commonly is the problem with the low energy density of the compressed air. They offer a number of advantages, primarily focusing on the possibility of significantly lowering the emissions of the engine. Their emissivity mainly depends on the method of obtaining compressed air. This also has an impact on the economic aspects of the drive. Currently there are only a few, ready to implement, compressed air powered engine solutions available on the market. A major advantage is the ability to convert internal combustion engines to run with compressed air. The study provides a literature review of solutions, focusing on a multifaceted analysis of pneumatic drives. Increasing vehicle approval requirements relating to their emissions performance are encouraging for the search of alternative power sources. This creates an opportunity for the development of unpopular propulsion systems, including pneumatic engines. Analysing the works of some researchers, it is possible to notice a significant increase in the efficiency of the drive, which may contribute to its popularisation.

Youssef Benfatah, Amine El Bhih, Mostafa Rachik, Marouane Lafif
An Output Sensitivity Problem for a Class of Fractional Order Discrete-Time Linear Systems

Consider the linear discrete-time fractional order systems with uncertainty on the initial state $\begin{cases} \Delta^{\alpha} x_{i+1} = Ax_i + Bu_i, & i \geq 0 \\ x_0 = \tau_0 + \hat{\tau}_0 \in \mathbb{R}^n, & \hat{\tau}_0 \in \Omega, \\ y_i = Cx_i, & i \geq 0 \end{cases}$ where A, B and C are appropriate matrices, x_0 is the initial state, y_i is the signal output, α the order of the derivative, τ_0 and $\hat{\tau}_0$ are the known and unknown part of x_0, respectively, $u_i = Kx_i$ is feedback control and $\Omega \subset \mathbb{R}^n$ is a polytope convex of vertices $w_1, w_2, \dots, w_p$. According to the Krein–Milman theorem, we suppose that $\hat{\tau}_0 = \sum_{j=1}^{p} \alpha_j w_j$ for some unknown coefficients $\alpha_1 \geq 0, \dots, \alpha_p \geq 0 \quad \text{such that} \quad \sum_{j=1}^{p} \alpha_j = 1$. In this paper, the fractional derivative is defined in the Grünwald–Letnikov sense. We investigate the characterisation of the set $\chi(\hat{\tau}_0, \epsilon)$ of all possible gain matrix K that makes the system insensitive to the unknown part $\hat{\tau}_0$, which means $\chi(\hat{\tau}_0, \epsilon) = \{K \in \mathbb{R}^{m\times n} \; / \; \| \frac{\partial y_i}{\partial \alpha_j} \| \leq \epsilon, \;\; \forall j = 1, \dots, p, \;\; \forall i \geq 0\}$, where the inequality $\| \frac{\partial y_i}{\partial \alpha_j} \| \leq \epsilon$ showing the sensitivity of y_i relatively to uncertainties $\{\alpha_j\}_{j=1}^{p}$ will not achieve the specified threshold $\epsilon > 0$. We establish, under certain hypothesis, the finite determination of $\chi(\hat{\tau}_0, \epsilon)$ and we propose an algorithmic approach to made explicit characterisation of such set.

Per Lindh, Polina Lemenkova
Evaluation of Different Binder Combinations of Cement, Slag and CKD for S/S Treatment of TBT Contaminated Sediments

The seabed in the ports needs to be regularly cleaned from the marine sediments for safe navigation. Sediments contaminated by tributyltin (TBT) are environmentally harmful and require treatment before recycling. Treatment methods include leaching, stabilisation and solidification to remove toxic chemicals from the sediments and improve their strength for reuse in the construction works. This study evaluated the effects of adding three different binder components (cement, cement kiln dust (CKD) and slag) to treat sediment samples collected in the port of Gothenburg. The goal of this study is to assess the leaching of TBT from the dredged marine sediments contaminated by TBT. The various methods employed for the treatment of sediments include the application of varied ratios of binders. The project has been performed by the Swedish Geotechnical Institute (SGI) on behalf of the Cementa (Hei-delbergCement Group) and Cowi Consulting Group, within the framework of the Arendal project. An ex-periment has been designed to evaluate the effects of adding CKD while reducing cement and slag for sediment treatment. Methods that have been adopted include laboratory processing of samples for leaching using different binder combinations, followed by statistical data processing and graphical plot-ting. The results of the experiment on leaching of TBT for all samples are tested with a varied ratio of cement, slag, CKD and water. Specimens with added binders 'cement/CKD' have demonstrated higher leaching compared to the ratio 'cement/slag/CKD' and 'cement/slag'. The 'CKD/slag' ratio has presented the best results followed by the ‘cement/slag/CKD’, and can be used as an effective method of s/s treatment of the sediments. The results have shown that the replacement of cement and slag by CKD is effective at TBT leaching for the treatment of toxic marine sediments contaminated by TBT.

Anna Kasperczuk
Selected Morphotic Parameters Differentiating Ulcerative Colitis from Crohn's Disease

This paper presents a method that binds statistical and data mining techniques, which aims to support the decision-making process in selected diseases of the digestive system. Currently, there is no precise diagnosis for ulcerative colitis (UC) and Crohn's disease (CD). Specialist physicians must exclude many other diseases occurring in the colon. The first goal of this study is a retrospective analysis of medical data of patients hospitalised in the Department of Gastroenterology and Internal Diseases, Bialystok, and finding the symptoms differentiating the two analysed diseases. The second goal is to build a system that clearly points to one of the two diseases UC or CD, which shortens the time of diagnosis and facilitates the future treatment of patients. The work focuses on building a model that can be the basis for the construction of action rules, which are one of the basic elements in the medical recommendation system. Generated action rules indicated differentiating factors, such as mean corpuscular volume, platelets (PLTs), neutrophils, monocytes, eosinophils, basophils, alanine aminotransferase (ALAT), creatinine, sodium and potassium. Other important parameters were smoking and blood in stool.

Paweł Dzienis
Perturbations of the Depth of Liquid Penetration into the Capillary During the Bubble Departures

In the present paper, the influence of bubble size on liquid penetration into the capillary was experimentally and numerically studied. In the experiment, bubbles were generated from a glass capillary (with an inner diameter equal to 1 mm) in a glass tank containing distilled water, tap water or an aqueous solution of calcium carbonate. These liquids differ in the value of their surface tension, which influences the bubble size. During experimental investigations, air pressure fluctuations in the gas supply system were measured. Simultaneously, the videos showing the liquids' penetration into the capillary were recorded. Based on the videos, the time series of liquid movements inside the capillary were recovered. The numerical models were used to study the influence of bubble size on the velocity of liquid flow above the capillary and the depth of liquid penetration into the capillary. It was shown that the air volume flow rate and the surface tension have the greatest impact on the changes of pressure during a single cycle of bubble departure (Δp). The changes in pressure during a single cycle of bubble departure determine the depth of liquid penetration into the capillary. Moreover, the values of Δp and, consequently, the depth of liquid penetration can be modified by perturbations in the liquid velocity above the capillary outlet.

DOI 10.2478/ama-2021-0024 acta mechanica et automatica, vol.15 no.4 (2021)

THERMOMECHANICAL SLIP IN ELASTIC CONTACT BETWEEN IDENTICAL MATERIALS

Yurii STRELIAIEV*,, Rostyslav MARTYNYAK***, Kostyantyn CHUMAK*****

*Faculty of Mathematics, Zaporizhzhia National University, 66, Zhukovsky street, Zaporizhzhia 69600, Ukraine
**Department of Natural Science, Zaporizhzhia Institute of Economics and Information Technologies, 16b, Kyiashka street, Zaporizhzhia 69041, Ukraine
***Department of Mathematical Problems of Contact Mechanics, Pidstryhach Institute for Applied Problems of Mechanics and Mathematics, 3-b, Naukova street, Lviv 79060, Ukraine

strelkiny@gmail.com, m.rostyslav@gmail.com, chumakostya@gmail.com

received 8 November 2020, revised 19 July 2021, accepted 23 July 2021

Abstract: The contact problem for interaction between an elastic sphere and an elastic half-space is considered taking into account partial thermomechanical frictional slip induced by thermal expansion of the half-space. The elastic constants of the bodies are assumed to be identical. The Amontons–Coulomb law is used to account for friction. The problem is reduced to non-linear boundary integral equations that correspond to the initial stage of mechanical loading and the subsequent stage of thermal loading. The dependences of the contact stress distribution, relative displacements of the contacting surfaces, dimensions of the stick and slip zones on temperature of the half-space are studied numerically. It was revealed that an increase in temperature causes increases in the shear contact stress and the relative shear displacements of the contacting surfaces. The absolute values of the shear contact stress reach their maximum at the boundaries of the stick zones. The greatest value of the moduli of the relative shear displacements are reached at the boundary of the contact region. The stick zone radius decreases monotonically according to a nonlinear law with increasing temperature.

Key words: elastic contact, thermomechanical slip, stick and slip zones, contact stresses, integral equation, numerical solution, iterative method

1. INTRODUCTION

Solving contact problems on the interaction of elastic bodies often requires taking account of the friction between the contacting surfaces. The complexity of such problems is usually caused by the fact that the contact surface and the stick and slip zones arising on it are unknown and can have a complex unpredictable shape, which varies with the applied loading. These circumstances lead to nonlinearities in the formulation of such problems that significantly complicates their solving.

The investigations of partial frictional slip for various types of mechanical loading were initiated by Cattaneo (1938) and Mindlin (1949) and are actively continuing thus far. The reviews of such studies are presented in numerous papers (Kalker, 1977; Hills and Urriolagoitia Sosa, 1999; Barber and Ciavarella, 2000; Goryacheva and Martynyak, 2014) and books (Johnson, 1985; Hills et al., 1993; Ostryk and Ulitko, 2006; Popov, 2017; Barber, 2018; Ostryk, 2018).

In real operating conditions, the contacting bodies are often heated, and this can lead to change in the conditions in the contact region. Therefore, taking into account temperature effects plays an important role in the investigation of contact interactions. The major studies in this area are dedicated to investigation of the non-frictional thermoelastic contact (Borodachev, 1962; Grilitskii and Shelestovskii, 1970; Barber, 1973; Dundurs and Panek, 1976; Comninou et al., 1981; Krishtafovich and Martynyak, 1999; Kulchytsky-Zhyhailo et al., 2001; Martynyak and Chumak, 2012; Chumak 2018; Chumak and Martynyak, 2019) and investigation of the effects associated with heat generation due to sliding friction (Barber, 1976; Yevtushenko and Kulchytsky-Zhyhailo, 1996; Grilitskii and Pauk, 1997; Pauk, 2006; Kulchytsky-Zhyhailo et al., 2011).

However, thermal deformations can also cause partial slip of the contacting surfaces when bodies are heated. Determining distributions of the resultant shear contact stress as well as boundaries of slip and stick zones is especially important in the investigation of fretting wear and fatigue of real components of machines and structures (Hills and Urriolagoitia Sosa, 1999). Thermomechanical partial slip has been studied in a few works only. Pauk (2005, 2007) investigated thermally induced partial slip between a flat-ended punch and an elastic half-space with different temperatures. The thermoelastic stick-slip contact problem for two semi-infinite solids in the presence of a single thermoinsulated interface gap was studied by Malanchuk et al. (2011). The effect of thermal conductivity of an interstitial medium on partial slip between a textured half-space and a flat half-space, which is caused by an imposed heat flow, was examined by Chumak et al. (2014).

This paper aims to investigate partial frictional slip between the contacting surfaces of an elastic sphere and an elastic half-space that is caused by sequentially applied mechanical and thermal loads. The effect of the thermal load on the shear contact stress, relative slip of the contacting surfaces, and dimensions of the stick and slip zones will be studied.

DOI 10.2478/ama-2021-0024

2. STATEMENT OF THE PROBLEM

Consider the contact problem for an interaction between an elastic sphere and an elastic half-space. The bodies are assumed to be isotropic and have identical elastic properties characterised by Young's modulus E and Poisson's ratio ν. The initial temperatures of the bodies are zero. The bodies are loaded in two stages. Initially the sphere is pressed into contact with the half-space by a normal force P. The radius a_0 of the resultant contact region is supposed to be small in comparison with the radius R of the sphere ($\mathrm{a}_0 \ll \mathrm{R}$). Then, while the normal force is held constant, the half-space is uniformly heated to the temperature T and the thermal linear expansion of the half-space occurs. The contact surface is assumed to be thermoinsulated. The relative displacements of the points of the contacting surfaces resulting from the thermal expansion of the half-space are partially restrained by friction obeying the Amontons-Coulomb law (Kalker, 1977).

We will consider the problem in a three-dimensional formulation. Let us introduce the coordinate system in such a way that the elastic half-space is determined by the inequality $\mathrm{z} \leq 0$, and the origin of the coordinate system is the point of initial contact between the sphere and the half-space (Fig. 1).

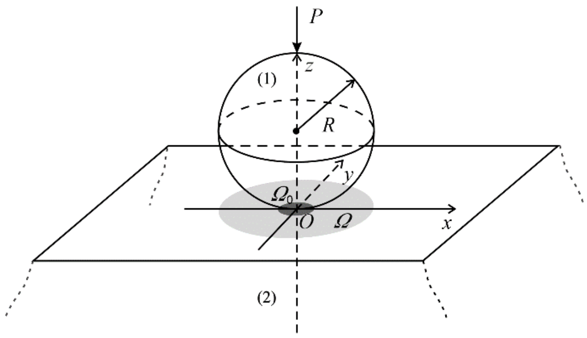

Fig. 1. The schema of contact interaction

Considering that the contact region radius is small in comparison with the sphere radius, the sphere can be replaced by the elastic half-space $\mathrm{z} \geq 0$. Below we will consider the contact boundary conditions separately for each of the two loading stages.

The boundary conditions at the first loading stage are specified in the bounded domain Ω of the plane $\mathrm{z} = 0$, containing an unknown contact region Ω_0. Since the contacting materials are identical, the elastic shear displacements of the points of the contacting surfaces are the same and friction does not arise (Johnson, 1985). Thus the shear stresses on the both contacting surfaces are zero and the boundary conditions in every point $\mathrm{s} = (\mathrm{x}, \mathrm{y}) \in \Omega$ can be written as follows (Barber, 2018):

$$g(s) \geq 0,\ s \in \Omega; \tag{1a}$$

$$p(s) \geq 0,\ s \in \Omega; \tag{1b}$$

$$g(s) \cdot p(s) = 0,\ s \in \Omega. \tag{1c}$$

In the relations expressed in Eq. (1), $\mathrm{g}(\mathrm{s})$ is a function of a gap between the bodies:

$$g(s) = u_z^{(1)}(s,0) - u_z^{(2)}(s,0) + g_0(s) - \Delta, \tag{2}$$

where $\mathrm{u}_\mathrm{z}^{(1)}(\mathrm{s},0)$, $\mathrm{u}_\mathrm{z}^{(2)}(\mathrm{s},0)$ denotes normal elastic displacements of the points of the contacting surfaces; Δ denotes the approach of two bodies; and $\mathrm{g}_0(\mathrm{s})$ denotes the initial gap between the bodies in their undeformed state. As the sphere radius R is large in comparison with the contact region radius, the initial gap $\mathrm{g}_0(\mathrm{s})$ near the origin of the coordinate system can be approximately represented in the following form (Johnson, 1985):

$$g_0(s) = \frac{x^2+y^2}{2R}. \tag{3}$$

The function $p(s)$ in Eq. (1) describes the contribution of a contact pressure in the domain Ω.

The condition (1a) means the non-negativity of the gap $g(s)$ between the bodies (there is no interpenetration), the condition (1b) means the non-negativity of the contact pressure $p(s)$, the condition (1c) means that contact pressure is zero outside the contact region and the gap is zero inside this region.

The relationship between the unknown functions $g(s)$ and $p(s)$, in accordance with the Boussinesq's solution (Johnson, 1985), is expressed in the following integral form

$$g(s) = 2 \cdot \frac{(1-\nu^2)}{\pi E} \int_\Omega \frac{p(s')}{r} ds' + g_0(s) - \Delta, \tag{4}$$

where $r = |s - s'| = \sqrt{(x-x')^2 + (y-y')^2}$.

The relations obtained in Eq. (1) should be supplemented with the following equilibrium condition:

$$P = \int_\Omega p(s) ds. \tag{5}$$

When the approach Δ of the bodies is given, the condition in Eq. (5) is used for determination of the pressing force P ensuring the approach Δ.

Thus, at the first loading stage, the problem is reduced to determination of the function $p(s)$, which satisfies the boundary conditions in Eq. (1) (taking into account the relations in Eq. (4)) at every point of the domain Ω. Once the contact pressure $p(s)$ is found, the contact region Ω_0 is determined from the condition $g(s) = 0$.

Heating the lower half-space to the constant temperature $\mathrm{T} > 0$ gives rise to thermal shear displacements of its boundary. These displacements lead to the appearance of a peripheral annular zone of slippage of the contacting surfaces, where friction forces act, and a central circular zone Ω_1 of stick of the contacting surfaces. The radius of the zone Ω_1 is a_1 ($a_1 < a_0$).

Therefore, the thermal expansion of the surface of the lower half-space in the presence of friction will cause relative shear displacements of the contacting surfaces $u_x(s)$, $u_y(s)$ and the shear stresses $\tau_{zx}^{(1)}(s,0)$, $\tau_{zy}^{(1)}(s,0)$, $\tau_{zx}^{(2)}(s,0)$ $\tau_{zy}^{(2)}(s,0)$ on the contacting surfaces.

When the elastic constants of the bodies are the same, the shear stresses do not affect the geometry of the contact region Ω_0 and the distribution of the contact pressures $p(s)$ (Johnson, 1985). Thus, we will assume that the domain Ω_0 as well as the function $p(s)$ are known and have been determined when solving the problem for the first loading stage.

The following formulas are valid for displacements $u_x(s)$ and $u_y(s)$:

$$u_x(s) = u_x^{(1)}(s,0) - u_x^{(2)}(s,0) - \tilde{u}_x^{(2)}(s), \tag{6a}$$

$$u_y(s) = u_y^{(1)}(s,0) - u_y^{(2)}(s,0) - \tilde{u}_y^{(2)}(s), \tag{6b}$$

where: $u_x^{(1)}(s,0)$, $u_y^{(1)}(s,0)$ and $u_x^{(2)}(s,0)$, $u_y^{(2)}(s,0)$ are the elastic shear displacements of the upper and the lower contacting surfaces that are caused by the contact shear stresses; $\tilde{u}_x^{(2)}(s) = \alpha \cdot x \cdot \mathrm{T}$, $\tilde{u}_y^{(2)}(s) = \alpha \cdot y \cdot \mathrm{T}$ are the shear displacements of the points of the lower contacting surface that are caused by thermal expansion of the lower half-space (α denotes the coefficient of linear thermal expansion) (Nowacki, 1986).

The contact boundary conditions for the second loading stage include the conditions of equality of shear stresses on the surfaces inside the contact region Ω_0

$$\tau_{zx}^{(1)}(s,0) = \tau_{zx}^{(2)}(s,0),\ \tau_{zy}^{(1)}(s,0) = \tau_{zy}^{(2)}(s,0),\ s \in \Omega_0 \quad (7)$$

and the relations of the Amontons–Coulomb law.

In view of Eq. (7), it is sufficient to write the Amontons–Coulomb law for the contact stress acting on the upper contacting surface only.

Denoting

$$q_x(s) \equiv -\tau_{zx}^{(1)}(s,0),\ q_y(s) \equiv -\tau_{zy}^{(1)}(s,0), \quad (8)$$

the relations of the Amontons-Coulomb law can be represented as (Kalker, 1977)

$$|\vec{q}| \le \mu \cdot p(s),\ s \in \Omega_0, \quad (9a)$$

$$|\vec{u}| \ne 0\ \Rightarrow\ \vec{q} = -\mu \cdot p(s) \cdot \frac{\vec{u}}{|\vec{u}|}, s \in \Omega_0, \quad (9b)$$

where: $\vec{q} = \left(q_x(s), q_y(s)\right)$ is the vector of specific shear stress acting on the upper contacting surface at the point s; $\vec{u} = \left(u_x(s), u_y(s)\right)$ is the vector of shear displacement of the upper contacting surface with respect to the lower one at the point s; and μ denotes the coefficient of friction.

Passing from the vectors $\vec{q}$, $\vec{u}$ to their components, the conditions in Eq. (9) can be rewritten in the following equivalent form:

$$\sqrt{q_x^2(s) + q_y^2(s)} \le \mu \cdot p(s),\ s \in \Omega_0; \quad (10a)$$

$$q_x(s)\sqrt{u_x^2(s) + u_y^2(s)} + \mu \cdot p(s) u_x(s) = 0,\ s \in \Omega_0; \quad (10b)$$

$$q_y(s)\sqrt{u_x^2(s) + u_y^2(s)} + \mu \cdot p(s) u_y(s) = 0,\ s \in \Omega_0. \quad (10c)$$

The condition (10a) means that the absolute value of the shear stress at any point of the contact region Ω_0 does not exceed the product of the coefficient of friction μ and the contact pressure value at this point. The conditions (10b) and (10c) mean that for all the points of the contact region where slippage takes place ($|\vec{u}| \ne 0$) the equality $|\vec{q}| = \mu \cdot p(s)$ holds, and the vector of shear stress $\vec{q}$ and vector of the relative displacement of the contacting surfaces $\vec{u}$ have opposite direction. For stick ($|\vec{u}| = 0$), the equalities (10b) and (10c) become identities.

According to the Cerruti solution (Johnson, 1985), the differences in the shear elastic displacements in Eq. (6) can be expressed in the following integral form:

$$u_x^{(1)}(s,0) - u_x^{(2)}(s,0) = \int_\Omega K_{xx}(s,s') q_x(s') ds' + \int_\Omega K_{xy}(s,s') q_y(s') ds', \quad (11a)$$

$$u_y^{(1)}(s,0) - u_y^{(2)}(s,0) = \int_\Omega K_{yx}(s,s') q_x(s') ds' + \int_\Omega K_{yy}(s,s') q_y(s') ds', \quad (11b)$$

where:

$$K_{xx}(s,s') = 2 \cdot \frac{(1-\nu^2)}{\pi E} \cdot \frac{1}{r} + 2 \cdot \frac{\nu(1+\nu)}{\pi E} \cdot \frac{(x-x')^2}{r^3};$$

$$K_{xy}(s,s') = K_{yx}(s,s') = 2 \cdot \frac{\nu(1+\nu)}{\pi E} \cdot \frac{(x-x')(y-y')}{r^3};$$

$$K_{yy}(s,s') = 2 \cdot \frac{(1-\nu^2)}{\pi E} \cdot \frac{1}{r} + 2 \cdot \frac{\nu(1+\nu)}{\pi E} \cdot \frac{(y-y')^2}{r^3};$$

$$r = |s - s'| = \sqrt{(x-x')^2 + (y-y')^2}.$$

Therefore, the problem for the second loading stage is reduced to determining the functions $q_x(s)$, $q_y(s)$, which satisfy the relations obtained in Eq. (10) (taking into account Eqs (6) and (11)) at every point of the contact region Ω_0, and the function $p(s)$ is known from the solution of the problem for the first loading stage. Once the distributions of the shear contact stresses $q_x(s)$, $q_y(s)$ are found, the stick zone Ω_1 is determined from the condition $|\vec{u}| = 0$.

3. INTEGRAL EQUATIONS OF THE CONTACT PROBLEM

To obtain integral equations describing the contact interaction of the bodies at the first and second loading stages, we use the approach proposed in the literature (Aleksandrov, 2015; Alexandrov and Streliaiev, 2014; Streliaiev, 2016).

According to it, consider the helper functions:

$$H(x) = \begin{cases} x, \text{ if } x \ge 0, \\ 0, \text{ if } x < 0, \end{cases} \quad (12)$$

$$Q(x,y,z) = \begin{cases} x, & \text{if } \sqrt{x^2+y^2} \le z, \\ \frac{xz}{\sqrt{x^2+y^2}}, & \text{if } \sqrt{x^2+y^2} > z. \end{cases} \quad (13)$$

The following theorems (provided below without proof) hold for the properties of the helper functions (Aleksandrov, 2015).

Theorem 1. *For any real numbers x, y, the system*

$$\begin{cases} x \ge 0, \\ y \ge 0, \\ x \cdot y = 0 \end{cases} \quad (14)$$

is equivalent to the equality

$$x = H(x - E \cdot y), \quad (15)$$

where E is an arbitrary positive number.

Theorem 2. *For any real numbers x, y, u, v and any non-negative number z, the system of relations*

$$\begin{cases} \sqrt{x^2+y^2} \le z, \\ x \cdot \sqrt{u^2+v^2} + z \cdot u = 0, \\ y \cdot \sqrt{u^2+v^2} + z \cdot v = 0 \end{cases} \quad (16)$$

is equivalent to the system of equalities

$$\begin{cases} x = Q(x - Eu, y - Ev, z), \\ y = Q(y - Ev, x - Eu, z), \end{cases} \quad (17)$$

where E is an arbitrary positive number.

As follows from the Theorem 1, boundary conditions in Eq. (1) with the use of the function H can be expressed as a single nonlinear integral equation for the function $p(s)$ defined in the domain Ω:

DOI 10.2478/ama-2021-0024

$$p(s) = H\big(p(s) - \mathrm{E}_1 \cdot g(s)\big) \tag{18}$$

where E_1 is an arbitrary positive number.

In view of the Theorem 2, the boundary conditions in Eq. (10) are reduced to a system of nonlinear integral equations for the functions $q_x(s),\ q_y(s)$ defined in the domain Ω_0:

$$\begin{cases} q_x(s) = Q\left(q_x(s) - \mathrm{E}_2 u_x(s), q_y(s) - \mathrm{E}_2 u_y(s), \mu \cdot p(s)\right), \\ q_y(s) = Q\left(q_y(s) - \mathrm{E}_2 u_y(s), q_x(s) - \mathrm{E}_2 u_x(s), \mu \cdot p(s)\right), \end{cases} \tag{19}$$

where E_2 is an arbitrary positive number, and the non-negative function $p(s)$ is known from the solution of Eq. (18).

The method proposed by Aleksandrov (2015) is utilised to solve the system of integral Eqs (18) and (19) numerically. This method includes regularisation of integral equations, discretisation of the regularised equations and usage of an iterative process for obtaining an approximate solution to discrete analogs of the regularised equations.

Such discrete analogs can be obtained by defining the domain Ω as an open square which is bounded by straight lines parallel to the axes Ox, Oy. Let us divide the domain Ω for every positive integer n into n^2 square domains $\omega_1, \omega_2, \dots, \omega_{n^2}$ of equal area that are arranged as the square Ω. Assuming that the unknown function $p(s)$ has a constant value p_k on every element ω_k at the first loading stage, we obtain the following system of n^2 non-linear scalar equations for an approximate solution to Eq. (18):

$$p_k = H\left(p_k - \mathrm{E}_1 \cdot \left(\textstyle\sum_{j=1}^{n^2} a_{kj}^1 \cdot p_j - b_k^1\right)\right). \tag{20}$$

We assume that the functions $q_x(s)$ and $q_y(s)$ have constant values q_{2k-1} and q_{2k} on every element ω_k at the second loading stage. Then the discrete analog of the system in Eq. (19) has the following form:

$$\begin{cases} q_{2k-1} = Q\big(q_{2k-1} - \mathrm{E}_2 \cdot \left(\sum_{j=1}^{2n^2} a_{2k-1\,j}^2 \cdot q_j - b_{2k-1}^2\right), \\ \qquad q_{2k} - \mathrm{E}_2 \cdot \left(\sum_{j=1}^{2n^2} a_{2k\,j}^2 \cdot q_j - b_{2k}^2\right), \mu \cdot p_k\big); \\ q_{2k} = Q\big(q_{2k} - \mathrm{E}_2 \cdot \left(\sum_{j=1}^{2n^2} a_{2k\,j}^2 \cdot q_j - b_{2k}^2\right), \\ \qquad q_{2k-1} - \mathrm{E}_2 \cdot \left(\sum_{j=1}^{2n^2} a_{2k-1\,j}^2 \cdot q_j - b_{2k-1}^2\right), \mu \cdot p_k\big). \end{cases} \tag{21}$$

In (20) and (21), $k = \overline{1, n^2}$, numerical parameters a_{ij}^1 and a_{kj}^2 are the elements of the compliance matrix of the contacting bodies, b_i^1 and b_i^2 define the loading conditions at the first and second stages respectively. The approximate solutions of the systems in Eqs (20) and (21) are found using the iterative method (Aleksandrov, 2015).

4. NUMERICAL RESULTS AND THEIR ANALYSIS

Numerical calculations are performed for the coefficient of friction $\mu = 0.5$, Poisson's ratio $\nu = 0.3$ and the dimensionless quantities

$$\bar{x} = \frac{x}{R}, \quad \bar{y} = \frac{y}{R}, \quad \bar{p}(s) = \frac{p(s)}{E}, \quad \bar{q}_x(s) = \frac{q_x(s)}{E},$$

$$\bar{q}_y(s) = \frac{q_y(s)}{E}, \quad \bar{u}_x(s) = \frac{u_x(s)}{R}, \quad \bar{u}_y(s) = \frac{u_y(s)}{R},$$

$$\bar{P} = \frac{P}{E \cdot R^2}, \quad \bar{\Delta} = \frac{\Delta}{R}, \quad \bar{a}_1 = \frac{a_1}{R}, \quad \bar{\mathrm{T}} = \alpha \cdot \mathrm{T}.$$

Fig. 2 shows the contact pressure $\bar{p} = \bar{p}(\bar{x}, 0)$ versus the coordinate $\bar{x}$ when the approach of the bodies equals $\bar{\Delta} = 2.7 \cdot 10^{-4}$ and the corresponding pressing force is $\bar{P} = 3.2 \cdot 10^{-6}$. The solid line corresponds to the Hertz pressure distribution for an axisymmetric normal contact (Johnson, 1985), and the circles correspond to the numerical solution of Eq. (20) (the first loading stage, $\bar{\mathrm{T}} = 0$).

As seen in Fig. 2, the numerical solution of the problem for the first loading stage and the Hertz analytical solution agree very closely.

To analyse the effect of thermomechanical slip on the contact interaction parameters, numerical calculations are performed for various values of temperature $\bar{\mathrm{T}}$ at the fixed value of the pressing force $\bar{P} = 3.2 \cdot 10^{-6}$.

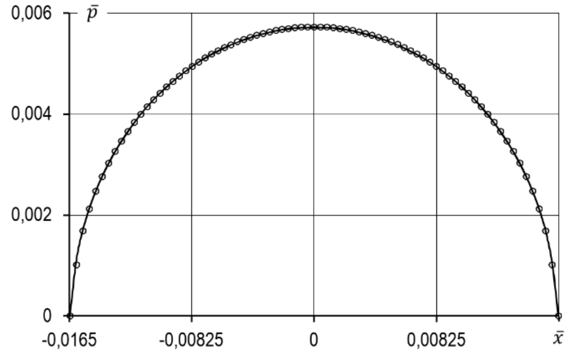

Fig. 2. Contact pressure distribution

Fig. 3 shows the shear contact stress $\bar{q}_x = \bar{q}_x(x, 0)$ versus the coordinate $\bar{x}$ for various values of temperature $\bar{\mathrm{T}}$. The curves have kinks at the points $\bar{x} = \pm\bar{a}_1$ corresponding to the ends of stick zones. As temperature is increased, the absolute value of the shear contact stress $\left|\bar{q}_x(x, 0)\right|$ increases and reaches its maximum at the ends of stick zones. The curve $\left|\bar{q}_x(x, 0)\right|$ within the slip zones coincides with the curve $\mu \cdot \bar{p}(\bar{x}, 0)$, therefore the shear stress is zero at the ends of the contact region. Within the stick zone, the shear stress is less than pressure multiplied by the coefficient of friction and is zero in the center of the contact region (at $\bar{x} = 0$).

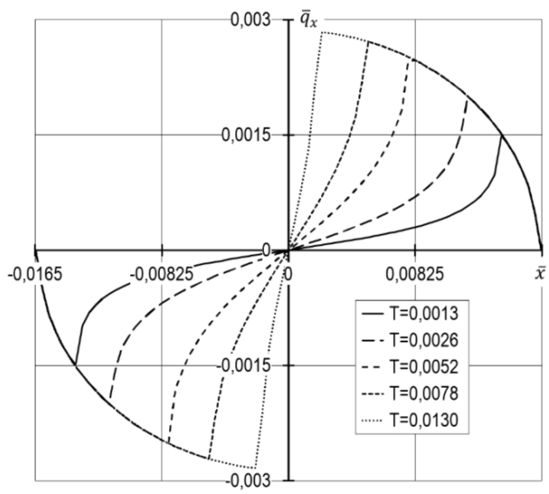

Fig. 3. Shear contact stress distribution

Fig. 4 shows the relative shear displacements $\overline{u}_x = \overline{u}_x(x, 0)$ of the contacting surfaces in the contact region versus the coordinate $\bar{x}$ for various values of temperature $\overline{\mathrm{T}}$. The horizontal sections lying on the axis $O\bar{x}$ correspond to the stick zones, and the curved sections correspond to the slip zones where the relative shear displacements of the surfaces occur. The relative shear displacements increase with increasing temperature, and their maximum value is reached at the boundary of the contact region.

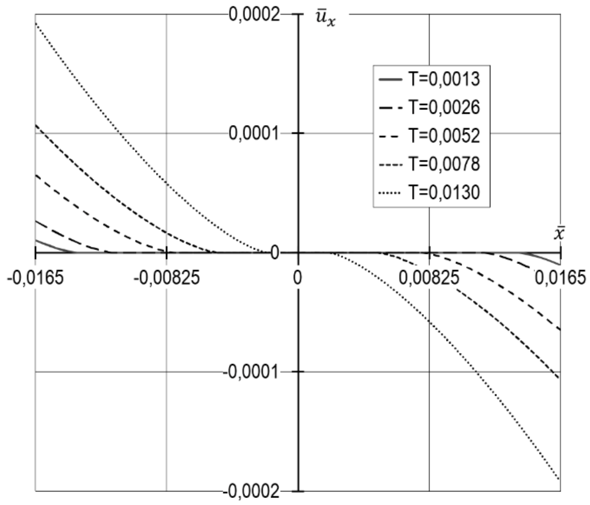

Fig. 4. Relative shear displacements of contacting surfaces versus coordinate

Fig. 5 shows the approximate boundaries of the stick zones calculated numerically for different values of temperature. Here, $\overline{\mathrm{T}} = 0$ corresponds to the contact region at the first loading stage. The contact region does not change at the second stage of thermal loading. The perimeters of the regions with different shades of gray correspond to boundaries of the circular stick zones and annular slip zones which arise at different discrete values of the heating temperature $\overline{\mathrm{T}}$ of the lower half-space (from $\overline{\mathrm{T}} = 0.0013$ to $\overline{\mathrm{T}} = 0.013$).

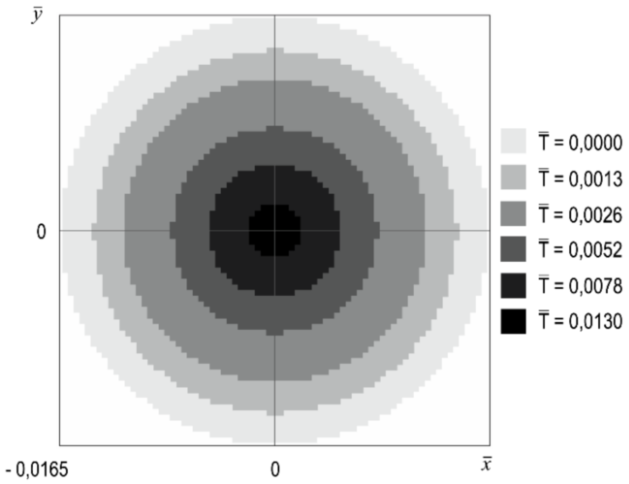

Fig. 5. Shape of stick zones

Fig. 6 shows the stick zone radius $\overline{a}_1$ versus temperature $\overline{\mathrm{T}}$. The circles correspond to the numerical results and the solid line corresponds to the fitting curve. The stick zone radius nonlinearly depends on temperature and decreases monotonically with temperature increasing. The obtained curve suggests that the stick zone radius will asymptotically tend to zero as the temperature tends to infinity, and the stick region itself will contract to a point.

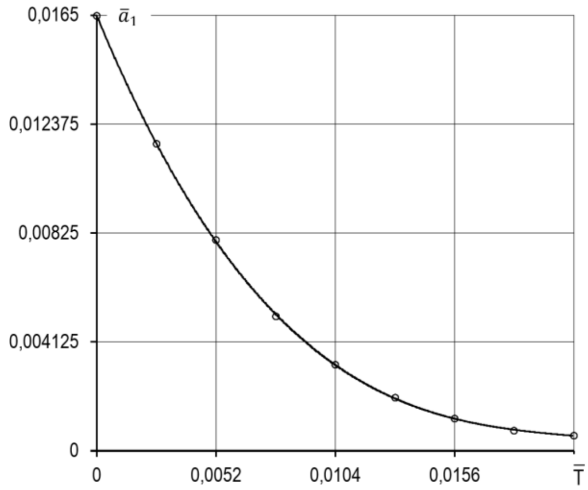

Fig. 6. Stick zone radius versus temperature

5. CONCLUSIONS

The problem for contact interaction between identically elastic sphere and half-space has been formulated taking into account partial thermomechanical frictional slip, which arises in the contact region due to thermal expansion of the half-space.

Nonlinear boundary integral equations that describe the contact interaction of the bodies at successive stages of mechanical and thermal loading were obtained. To solve the equations numerically, the method proposed by Aleksandrov (2015) was utilised. It includes regularisation of the integral equations, discretisation of the regularised equations and the use of an iterative process to obtain an approximate solution of discrete analogs of the regularised equations.

The effect of temperature of the half-space on the distribution of contact stresses, the relative displacements of the contacting surfaces, the dimensions of the stick and slip zones was studied. It was revealed that an increase in temperature causes increases in the shear contact stress and the relative shear displacements of the contacting surfaces. The absolute values of the shear contact stress reach their maximum at the boundaries of the stick zones. The greatest value of the moduli of the relative shear displacements are reached at the boundary of the contact region. The stick zone radius decreases monotonically according to a nonlinear law with increasing temperature.

The obtained results can be useful for analysing different types of failure, such as fretting fatigue, creep failure and crack nucleation.

REFERENCES

1. **Aleksandrov A.I.** (2015), A Method for the Solution of a Three-Dimensional Contact Problem of Interaction of Two Elastic Bodies in the Presence of Friction, *Journal of Mathematical Sciences*, 205(7), 518–534.

DOI 10.2478/ama-2021-0024

2. **Alexandrov A., Streliaiev Y.** (2014), Nonlinear boundary integral equation's method for elastic contact problems, *Eastern-European Journal of Enterprise Technologies*, 3(7), 36–40 (in Russian).
3. **Barber J.R.** (1973), Indentation of a semi-infinite elastic body by a hot sphere, *International Journal of Mechanical Sciences,* 15(10), 813–819.
4. **Barber J.R.** (1976), Some thermoelastic contact problems involving frictional heating, *The Quarterly Journal of Mechanics and Applied Mathematics*, 29(1), 1-13.
5. **Barber J.R.** (2018), *Contact mechanics. Solid Mechanics and Its Applications*, Springer.
6. **Barber J.R., Ciavarella M.** (2000), Contact mechanics, *International Journal of Solids and Structures*, 37(1–2), 29–43.
7. **Borodachev N.M.** (1962), On solution of contact problem of thermoelasticity in a case of axial symmetry, *Izv. Akad. Nauk SSSR, Techn. Mekh. Mashinstr.*, 5, 86–90 (in Russian).
8. **Cattaneo C.** (1938), Sul contatto di due corpi elastici: distribuzione locale degli stozzi, *Rend. Dell'Academia nazionale dei Lincei*, 27(6), 342–348, 434–436, 474–478.
9. **Chumak K.** (2018), The thermoelastic contact problem for wavy surfaces with a heat-conducting medium in interface gaps, *Mathematics and Mechanics of Solids*, 23(10), 1389–1406.
10. **Chumak K., Malanchuk N., Martynyak R.** (2014), Partial slip contact problem for solids with regular surface texture assuming thermal insulation or thermal permeability of interface gaps, *International Journal of Mechanical Sciences*, 84, 138–146.
11. **Chumak K., Martynyak R.** (2019), The combined thermal and mechanical effect of an interstitial gas on thermal rectification between periodically grooved surfaces, *Front Mech Eng,* 5(42), 1–8.
12. **Comninou M., Dundurs J., Barber J.R.** (1981), Planar Hertz contact with heat conduction, *Journal of Applied Mechanics,* 48(3), 549–554.
13. **Dundurs J., Panek C.** (1976), Heat conduction between bodies with wavy surfaces, *International Journal of Heat and Mass Transfer*, 19(7), 731–736.
14. **Goryacheva I.G., Martynyak R.M.** (2014), Contact problems for textured surfaces involving frictional effects, *Proceedings of the Institution of Mechanical Engineers, Part J: Journal of Engineering Tribology,* 228(7), 707–716.
15. **Grilitskii D.V., Pauk V.I.** (1997), The plane contact problem of steady thermoelasticity taking heat generation into account, *Journal of Applied Mathematics and Mechanics*, 61(6), 1007–1012.
16. **Grilitskii D.V., Shelestovskii B.G.** (1970), The axisymmetric contact problem of thermoelasticity for a transversely isotropic half-space, *Soviet Applied Mechanics*, 6(8), 807–811.
17. **Hills D.A., Nowell D., Sackfield A.** (1993), *Mechanics of Elastic Contact*, Butterworth-Heinemann, Oxford.
18. **Hills D.A., Urriolagoitia Sosa G.** (1999), Origins of partial slip in fretting – a review of known and potential solutions, *The Journal of Strain Analysis for Engineering Design*, 34(3), 175–181.
19. **Johnson K.L.** (1985), *Contact mechanics*, Cambridge University Press, Cambridge.
20. **Kalker J.J.** (1977), A survey of the mechanics of contact between solid bodies, *ZAMM*, 57(5), T3–T17.
21. **Krishtafovich A.A., Martynyak R.M.** (1999), Lamination of anisotropic half-spaces in the presence of contact thermal resistance, *International Applied Mechanics*, 35(2),159–164.
22. **Kulchytsky-Zhyhailo R.D., Matysiak S.J., Perkowski D.M.** (2011), Plane contact problems with frictional heating for a vertically layered half-space, *International Journal of Heat and Mass Transfer*, 54(9), 1805–1813.
23. **Kulchytsky-Zhyhailo R.D., Olesiak Z.S., Yevtushenko O.O.** (2001), On thermal contact of two axially symmetric elastic solids, *Journal of Elasticity*, 63(1), 1-17.
24. **Malanchuk N., Martynyak R., Monastyrskyy B.** (2011), Thermally induced local slip of contacting solids in vicinity of surface groove, *International Journal of Solids and Structures*, 48(11–12), 1791–1797.
25. **Martynyak R., Chumak K.** (2012), Effect of heat-conductive filler of interface gap on thermoelastic contact of solids, *International Journal of Heat and Mass Transfer*, 55(4), 1170–1178.
26. **Mindlin R.D.** (1949), Compliance of elastic bodies in contact, *Trans. ASME, J. Appl. Mech.,* 16(3), 259–268.
27. **Nowacki W.** (1986), *Thermoelasticity. 2nd edn.*, PWN-Polish Scientific Publishers.
28. **Ostryk V.I.** (2018), *Factorization method and its generalization in mixed problems of elasticity theory*, VPC «Kyivskyi universytet», Kyiv (in Ukrainian).
29. **Ostryk V.I., Ulitko A.F.** (2006), *The Wiener–Hopf Method in Contact Problems of Elasticity Theory*, Naukova Dumka, Kyiv (in Ukrainian).
30. **Pauk V.** (2006), Plane contact problems involving frictional heating for wavy half-space, *Tribology Letters*, 24(6), 237–242.
31. **Pauk V.** (2007), Plane contact of hot flat-ended punch and thermoelastic half-space involving finite friction, *Journal of Applied Mechanics*, 74(6), 1172–1177.
32. **Pauk W.** (2005), *Wybranie zagadnienia kontaktu cial odksztalcalnych,* Kielce: Wydawnictwo Politechniki Swietokrzyskiej (in Polish).
33. **Popov V.L.** (2017), *Contact Mechanics and Friction. Physical Principles and Applications*, Springer, Berlin.
34. **Streliaiev Yu. M.** (2016). A nonlinear boundary integral equations method for the solving of quasistatic elastic contact problem with Coulomb friction, *Journal of Samara State Technical University, Ser. Physical and Mathematical Sciences*, 20(2), 306–327 (in Russian).
35. **Yevtushenko A.A., Kulchytsky-Zhyhailo R.D.** (1996), Approximation solution of the thermoelastic contact problem with frictional heating in the general case of the profile shape, *Journal of the Mechanics and Physics of Solids*, 44, 243–250.

Yurii Streliaiev: https://orcid.org/0000-0002-4400-7824

Rostyslav Martynyak: https://orcid.org/0000-0001-7613-1427

Kostyantyn Chumak: https://orcid.org/0000-0002-7033-0836

sciendo

DOI 10.2478/ama-2021-0025 acta mechanica et automatica, vol.15 no.4 (2021)

APPLICATION OF MAGNETIC AND ULTRASONIC METHODS FOR DETERMINING PARAMETERS OF FERROMAGNETIC COMPONENTS IN IRON ORE SLURRY FLOWS

Vladimir MORKUN*, Natalia MORKUN*, Vitaliy TRON*, Olga PORKUIAN, Oleksandra SERDIUK*, Tetiana SULYMA*****

*Automation, Computer Science and Technologies Department, Kryvyi Rih National University, Vitalii Matusevich Street, 11, Kryvyi Rih, Ukraine
**Volodymyr Dahl East Ukrainian National University, Central Pr. 59-a, Severodonetsk, Ukraine
***Kryvyi Rih National University, Vitalii Matusevich Street, 11, Kryvyi Rih, Ukraine

morkunv@gmail.com, nmorkun@gmail.com, vtron@ukr.net, porkuian@i.ua, o.serdiuk@i.ua, sts.1811@ukr.net

received 13 August 2019, revised 19 July 2021, accepted 23 July 2021

Abstract: The article considers the method for controlling the ferromagnetic component content in slurry flow by ultrasonic and magnetic measurements. One of the basic factors determining the efficiency of magnetic separators at iron ore concentration plants is the quality of distribution of the ground ore into the product containing the ferromagnetic component and the waste rock. Due to the fact that in most cases, magnetic separators extract minerals with strongly magnetic properties, it is essential to find the magnetic component content in the input ore and products of its distribution in order to improve control over the technological process. Currently, low accuracy and reliability make existing means of operative control over the ferromagnetic component content in the slurry flow inefficient. Density of slurry is one of the primary disturbing factors affecting the accuracy of measurements, and this fact determines the necessity of measuring this parameter while controlling the ferromagnetic component content. Combined methods of measurements are a promising trend in designing sensors of useful component content in the slurry flow. The article describes the method for controlling the ferromagnetic component content in slurry flow by ultrasonic and magnetic measurements.

Key words: ferromagnetic component, ultrasound, slurry, ore, lamb waves

1. INTRODUCTION

The efficiency of controlling processes in iron ore concentration is mostly conditioned by the frequency and accuracy of the data entry of the process parameters (Kupin, 2014; Hauptmann et al., 2002; Stupnik et al., 2015; Semerikov and Slovak, 2011; Modlo et al., 2019).

Ultrasonic waves are applied for controlling the characteristics of technological media (Rzhevsky and Yamshchikov, 1968; Seip et al., 1996; Brazhnikov, 1975; Bond et al., 2003) as they enable signals from any point of the propagation surface and have relatively larger concentration of energy in a wave due to their smaller layer of localisation. The walls of technological vessels and industrial aggregates in iron ore concentration are mostly made of metal sheets to conduct ultrasonic control of parameters of contacting media, thus influencing the efficiency of Lamb waves. These waves are less susceptible to the impacts of disturbing factors than other types of ultrasonic waves. It should be noted that Lamb waves are also less susceptible to the condition of the surface of wave propagation and the action of gas bubbles in the studied medium. In other words, application of Lamb waves ensures the set error in measuring parameters of the ferromagnetic component of the iron ore slurry at the concentration plant (Zhang et al., 2020; Xu and Hu, 2017).

Thus, investigation into Lamb waves propagating on the plate in contact with the iron ore slurry with the purpose of determining the parameters of the ferromagnetic component of the flow is quite promising and topical (Ni and Chen, 2018; Meng and Yan, 2019).

2. LITERATURE ANALYSIS AND PROBLEM

2.1. Statement

Ways of increasing the efficiency of ore material concentration are considered in previous papers (Golik et al., 2015a; 2015b; Liu et al., 2020; Ma et al., 2019; Eremenko et al., 2019). It is worth emphasising that obtaining on-line data on technological process and iron ore characteristics is a problem in technological flows in particular (Lolaev et al., 2018). For exerting control over concentration processes and characteristics of the ore slurry, Morkun et al. (2015a; 2015b) suggest using controlled ultrasonic waves.

Regularities of propagation of ultrasonic waves in liquid under the cavitation mode have been studied previously (Louisnard, 2012a; Yuan et al., 2018; Wan et al., 2020; Zhao et al., 2019). Computing methods allow calculation of the energy dispersed by bubbles. There is a direct dependency of the energy lost by bubbles and attenuation of ultrasonic oscillations, which results in progressive waves. The above-described results (Louisnard, 2012b) enable the calculation of the Bjerknes force and prediction of bubble structures formed under the action of progressive waves.

Multimode Lamb waves have been used as a means of non-destructive control by Ryden et al. (2003). By measuring the various modes in experimental curves of dispersion of Lamb waves and comparing them with theoretical curves, some physical parameters of the medium under study are obtained. It is observed that the dispersion curves of Lamb waves depend only on the parameters of the plate, while their frequency and phase velocity can be standardised according to the velocity of shear waves and the thickness of the medium's layer under study.

As noted previously (Debarnot et al., 2006), the advantage of Lamb waves in the context of nondestructive control of various ultrasonic waves is that one is able to check a larger area by using a minimum number of receivers. As Lamb waves are dispersive, a sinusoidal signal of emission is recommended. Lamb waves were simulated by applying the ATILA software.

Previous investigations (Lee and Staszewski, 2009) also indicate that Lamb waves are the most widely used ultrasonic waves applied for controlling various media. Yet, theoretical analysis of controlled wave propagation is a complicated task to perform. The method for simulating local interaction in wave propagation in metallic structures is considered. It is worth noting that application of the suggested method is complicated by at least two coexisting highly dispersive modes at any set frequency.

The method for controlling the parameters of liquid media by ultrasonic Lamb waves is presented by Subhash and Krishnan (2011). It is shown that changes in wave characteristics can be used as a function depending on the liquid level. As indicated, it is necessary to conduct some additional investigations to determine the optimal conditions of the measured parameters of the liquid medium by applying Lamb waves.

It follows from other studies (Viktorov, 1966; 1975) that availability of the magnetic field causes auxiliary attenuation and velocity dispersion of the volume of ultrasonic waves propagating in the studied medium.

Analysis of scientific sources (Fukumoto et al., 2019; Eskandari and Hasanzadeh, 2021; Parekh et al., 2015; Porkuian et al., 2020; Parekh and Upadhyay, 2017) indicates that in most cases, certain wave types have been used to develop methods of ultrasonic control of the characteristics of heterogeneous media. To solve the set tasks, the choice of a particular wave type requires consideration of a number of strict requirements and limitations imposed on both characteristics of the propagation surface and properties of the controlled medium. Lamb waves can be considered promising for determining the parameters of the ferromagnetic component of the iron ore slurry flow. At the same time, the problem of assessing the scale of impact of the ferromagnetic properties of the slurry's solid phase on the results of the measured parameters of these propagating waves remains unsolved.

3. RESEARCH AIM AND TASKS

The research aims at elaborating the method of controlling the ferromagnetic component content in the slurry flow by studying the impact of the ferromagnetic properties of the slurry's solid phase on the results of ultrasonic and magnetic measurements.

To achieve the set goal, it is necessary to solve the following tasks:

- Study the dependencies of the relative volume magnetic susceptibility of an aggregate on the volume concentration of magnetite inclusions;
- Study the dependency of the magnetic susceptibility of the slurry on the volume concentration of magnetite;
- Develop a scheme of measuring the ferromagnetic component in the iron ore slurry flow by ultrasonic and magnetic methods.

4. MATERIALS AND RESEARCH METHODS

Let us consider the method of measuring the ferromagnetic component in the iron ore slurry by applying Lamb waves to determine the concentration of the slurry solid phase and assess its magnetic susceptibility.

The method of assessing the intensity of Lamb waves is used to define the solid component content in the iron ore slurry.

If the plate along which the Lamb waves are propagating contacts the liquid and the sound velocity in the liquid C_{liq} is smaller than the velocity of the Lamb wave in the plate C, the Lamb wave will attenuate, emitting energy into the liquid. The attenuation factor of the Lamb wave per unit length is determined by the following expression (Viktorov, 1966; 1975; Morkun et al., 2014; Morkun et al., 2015c):

$$k_2 = -i\frac{\rho_{liq}}{\rho}k_1 \cdot A_{s,a}, \tag{1}$$

where ρ_{liq} is the density of the liquid contacting the plate surface; and ρ is the density of the plate material.

$$A_{s,a} = -\frac{ik_t^4 th(S_{s,a}\cdot d)}{8k_{s,a}^2\cdot S_{s,a}\sqrt{k_c^2-k_{s,a}^2}}\left[1+\frac{k_{s,a}^2}{2S_{s,a}^2}+\frac{k_{s,a}^2}{2q_{s,a}^2}- -\frac{4k_{s,a}^2}{k_{s,a}^2+S_{s,a}^2}+\frac{k_{s,a}^2\cdot d}{2S_{s,a}}(thS_{s,a}d-cthS_{s,a}d)- -\frac{k_{s,a}^2\cdot d}{2q_{s,a}}(thq_{sa}d-cthq_{s,a}d)\right]^{-1}, \tag{2}$$

where $k_{s,a}$ is the wave number of symmetric and antisymmetric Lamb waves; d is the plate thickness; k_c is the wave number of ultrasound in the fluid;

$$q_{s,a} = \sqrt{k_{s,a}^2 - k_l^2}; \tag{3}$$

$$S_{s,a} = \sqrt{k_{s,a}^2 - k_t^2}; \tag{4}$$

k_l and k_t are wave numbers of the longitudinal and transversal waves of the plate material.

It should be noted that the attenuation factor of Lamb waves steadily rises while $\rho_{ж}\cdot\rho^{-1}$ increases. It means that k_2 can be presented as

$$k_2 = \frac{\rho_c}{\rho}C_v, \tag{5}$$

where C_v is the value practically independent of liquid density and a function of the wave numbers of Lamb, longitudinal and transversal waves of the plate material.

As the gas phase of the slurry has almost no influence on its density, gas bubbles will not affect the attenuation of Lamb waves. In this case, the slurry density ρ_{liq} will be determined by the volume fraction of the solid phase particles in the slurry W, their average density ρ_{sol} and the liquid density ρ_w:

$$\rho_{liq} = (1-W)\rho_w + W\rho_{sol}. \tag{6}$$

Therefore, the attenuation factor k_2 can be presented as

$$k_2 = \left[(1-W)\frac{\rho_w}{\rho} + W\frac{\rho_{sol}}{\rho}\right]C_\nu. \tag{7}$$

Thus, the intensity of Lamb waves at distance l from the wave source can be determined by the following formula:

$$I_{l,\nu} = I_{0,\nu}\cdot exp\{-k_2 l\} = \\ = I_{0,\nu}\, exp\left\{-[(1-W)\frac{\rho_w}{\rho} + W\frac{\rho_{sol}}{\rho}]C_\nu l\right\}. \tag{8}$$

If in Eq. (8), $W = 0$, we obtain the expression that conditions the intensity of Lamb waves when the plate contacts pure water:

$$I^*_{l,\nu} = I_{0,\nu}\, exp\left\{-\frac{\rho_w}{\rho}C_\nu l\right\}. \tag{9}$$

It is easy to demonstrate that considering Eq. (9), Eq. (8) can be presented as follows:

$$I_{l,\nu} = I^*_{l,\nu}\, exp\left\{-W\frac{[\rho_{sol}-\rho_w]}{\rho}C_\nu l\right\}. \tag{10}$$

As seen from Eq. (10), the signal

$$S = ln\left(\frac{I^*_{l,\nu}}{I_{l,\nu}}\right) = W\frac{[\rho_{sol}-\rho_w]C_\nu l}{\rho}, \tag{11}$$

is proportional to the volume fraction of the solid in the slurry W and does not depend on gas bubbles' availability.

Let us analyse the basic factors determining magnetic susceptibility of the iron ore slurry.

As is known, magnetic susceptibility is determined by the following relation (Bogdanov, 1983):

$$\mu_r = 1 + \chi\rho, \tag{13}$$

where χ is volume magnetic susceptibility.

According to their magnetic properties, ore minerals are divided into strongly and weakly magnetic. Rock-forming minerals are usually non-magnetic.

Magnetite ($FeO{\cdot}Fe_2O_3$) is a basic strongly magnetic iron-bearing mineral. According to Karmazin and Karmazin (1978), it is characterised by the following parameters: Curie point θ = 578° C; saturation magnetisation J_3 = 451–454 kA/m; coercive force H_c = 1.6 kA/m; initial specific magnetic susceptibility χ = (0.18−1.28) × 10^{-2} m³/kg. Magnetic saturation of magnetite starts with magnetisation in the field of 320 kA/m.

Tab. 1 presents the data on the magnetic properties of weakly magnetic iron-bearing minerals. One of the basic peculiarities of strongly magnetic substances is the dependency of their magnetic flux density or magnetisation on the field intensity. Fig. 1 depicts the dependency of specific magnetic susceptibility of magnetite on the magnetic field intensity.

The magnetic properties of magnetite are also dependent on the particle size. When particles become smaller, the coercive force rises, while the specific magnetic susceptibility falls (Karmazin and Karmazin, 1978). Specific magnetic susceptibility is determined using the expression

$$\chi_0 = \frac{\chi}{1+N\rho_{sol}\chi}, \tag{14}$$

where ρ_{sol} is the density of solid particles; N is the demagnetisation factor established to be equal to 0.16 for magnetite (Karmazin and Karmazin, 1978).

Fig. 2 shows the dependency of magnetic susceptibility χ of pure magnetite on particle size r. Specific magnetic susceptibility of the magnetite aggregate with weakly magnetic or non-magnetic minerals depends only on magnetite content. It is explained by the fact that the specific magnetic susceptibility even of martite, with relatively high specific susceptibility of $\chi \approx 9 \times 10^{-6}$, is 100-fold lower than that of magnetite, and that of other weakly magnetic minerals is even several-fold lower.

Tab. 1. Magnetic properties of weakly magnetic iron-bearing minerals

Minerals	**Chemical formula**	**Fe content in pure mineral, %**	**Specific magnetic susceptibility, χ 10^{-8} m³/kg**
Magnetite	Fe_3O_4	72.4	< ~1,20,000
Martite	Fe_2O_3	70.0	< ~880
Hematite	Fe_2O_3	70.0	80–220
Siderite	$FeCO_3$	48.2	~75
Brown hematite	$n\,Fe_2O_3{\cdot}m\,H_2O$	up to 60.0	40–90
Goethite	$FeO{\cdot}OH$	62.9	~32

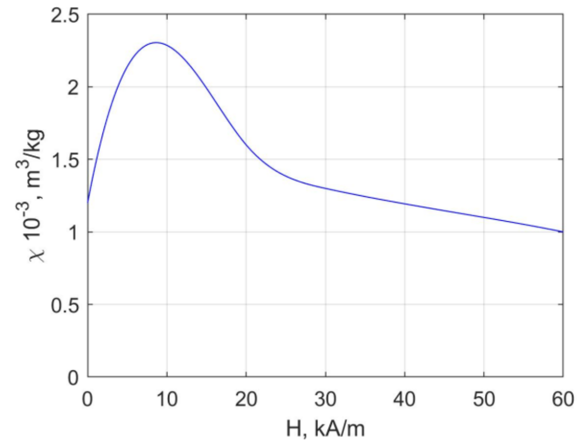

Fig. 1. Dependencies of specific magnetic susceptibility on the magnetic field intensity

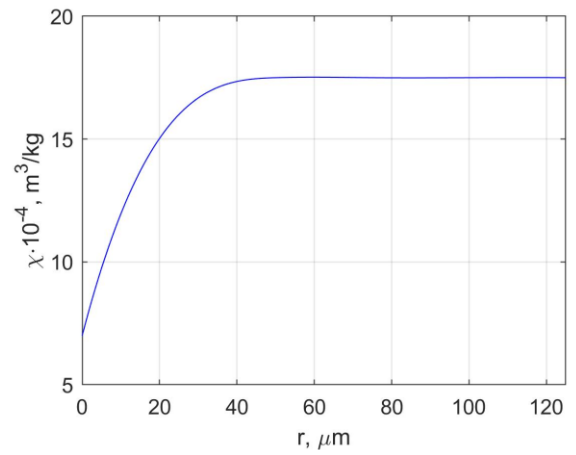

Fig. 2. Dependency of specific magnetic susceptibility χ on magnetite particle size

Fig. 3 provides the dependency of the relative volume magnetic susceptibility λ of the aggregate – as a ratio of the volume susceptibility of the aggregate χ_{aver} to the volume susceptibility of pure magnetite χ – on the volume concentration of magnetite C_m under three variants of non-magnetic inclusions. In the

DOI 10.2478/ama-2021-0025

first variant, inclusions are shaped as ellipsoids the long axis of which is parallel to the field intensity (Fig. 4); in the second variant, they are shaped as balls, and in the third variant, as ellipsoids the long axis of which is perpendicular to the field (Bogdanov, 1983; Karmazin and Karmazin, 1978; Weinberg, 1966; Derkach, 1966).

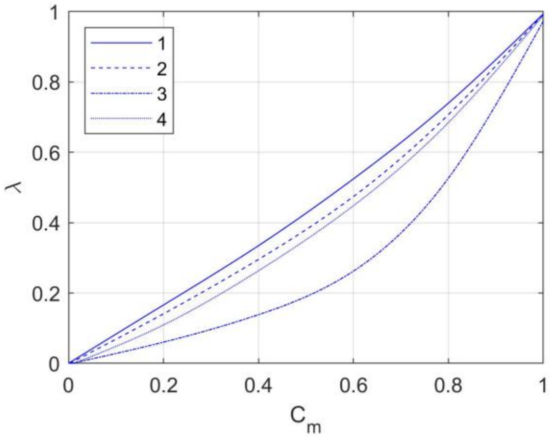

Fig. 3. Dependency of relative volume magnetic susceptibility of the aggregate on the volume concentration of magnetite inclusions: 1 – inclusions shaped as ellipsoids; 2 – inclusions shaped as balls; 3 – inclusions shaped as ellipsoids the long axis of which is perpendicular to the field; 4 – averaged characteristic

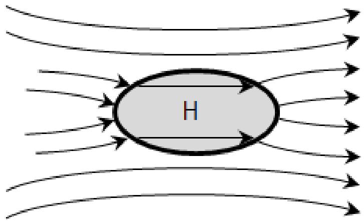

Fig. 4. Scheme of magnetisation in a magnetic field of a ferromagnetic ellipsoid the long axis of which is parallel to the field

It is evident that as the shape of non-magnetic inclusions and location of their long axis in relation to the field in the aggregate can vary, for practical purposes, only averaged values can be used in determining the value of λ.

5. INVESTIGATION RESULTS

For practical purposes, while determining the relative volume magnetic susceptibility of the aggregate under the field intensity of ≈50 kA/m, if ore formations are extracted from magnetite, the following expression is most often used (Karmazin and Karmazin, 1978):

$$\lambda = \frac{\chi_{spl}}{\chi_0} = 10^{-4}\alpha^2, \quad (15)$$

where χ_{spl} is the volume magnetic susceptibility of the aggregate; χ_0 is the volume magnetic susceptibility of particles of pure magnetite, and α is the magnetite content in the aggregate.

When passing from volume magnetic susceptibility to the specific one, it should be taken into account that the density of the aggregate rises when the magnetite content increases. For example, if the slurry solid phase consists of magnetite of ≈5 × 10³ kg/m³ density and rock-forming minerals, such as quartz and silicate, of ≈2.8 × 10³ kg/m³ density, the magnetic susceptibility of the aggregate is

$$\chi_{spl}' = \frac{\chi_{spl}}{\rho_{spl}} \approx \frac{1.13\cdot 10^{-5}\alpha^2}{127+\alpha}, \quad (16)$$

where ρ_{spl} is the density of the aggregate.

Fig. 5 shows the dependency of the relative specific magnetic susceptibility K on the magnetite content in the aggregate α.

As the specific susceptibility of inclusions of weakly magnetic and non-magnetic minerals does not depend on the field intensity and particle shape, their magnetic susceptibility is determined by the following expression:

$$\chi_{spl} = \sum_{i=1}^{\omega} \alpha_{im}\,\chi_{im}, \quad (17)$$

where α_{im} is the content of the weakly magnetic or non-magnetic i-th mineral in the aggregate; χ_{im} is specific magnetic susceptibility of the weakly magnetic or nonmagnetic i-th mineral.

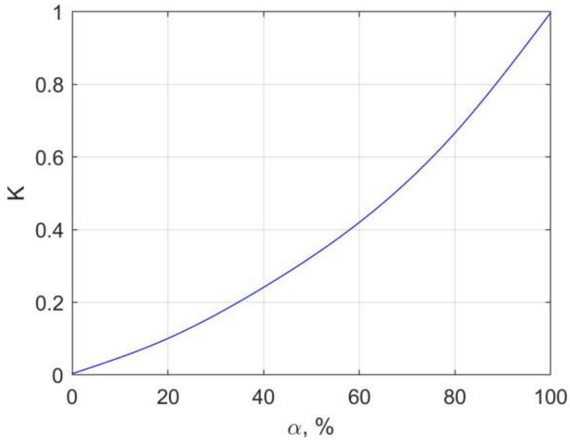

Fig. 5. Dependencies of the relative specific magnetic susceptibility K on the magnetite content in the aggregate α

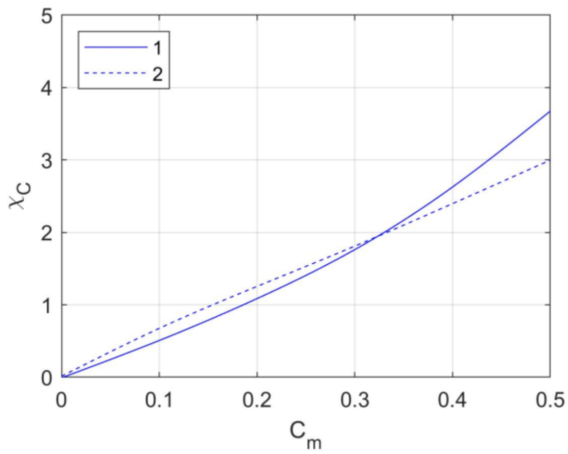

Fig. 6. Dependency of the volume magnetic susceptibility on the volume concentration of magnitite: 1 – theoretical; 2 – experimental

Magnetic susceptibility of the controlled material is dependent not only on the volume concentration of magnetite but also on the medium in which its particles occur. Magnetic susceptibility of the iron ore slurry is almost directly proportional to the magnetite concentration (Bogdanov, 1983; Karmazin and Karmazin, 1978; Weinberg, 1966; Derkach, 1966).

Fig. 6 provides the experimental dependency of slurry susceptibility on volume concentration of magnetite (slurry density is 1,350 g/cm^3, the content of 74 particles makes 75%). Similar dependency is obtained via computation. Differences between the theoretical and experimental results with large magnetite concentrations can be apparently explained by the interaction of particles within the slurry that makes their orientation more complicated.

Let us consider the magnetisation of the ferromagnetic slurry in the magnetic field. As is known, a magnetisation vector or a magnetic moment of the volume unit of a substance is a quantitative criterion of its magnetisation.

$$\vec{I} = \frac{\Delta\vec{p}_m}{\Delta V}, \tag{18}$$

where $\Delta\vec{p}_m$ is the total magnetic moment of the volume ΔV of the magnet.

We denote the volume fraction of the solid component in the slurry by W_τ. Let us select the volume ΔV in the magnetised slurry and determine its magnetisation as a module of the magnetisation vector.

$$|\vec{I}| \equiv I. \tag{19}$$

We denote the value of magnetisation of pure magnetite (100%) by I_M and determine the magnetic moment of the volume ΔV of the slurry if it is within the magnetic field $H > H_n$ (magnetic field intensity under which saturation starts). We shall assume that the value η determines the fraction of the magnetic component in the slurry solid phase. In this case, magnetisation will be determined by the following expression:

$$I_{sl} = \frac{W_\tau \ \eta \Delta V I_M}{\Delta V} = W_\tau \eta I_M. \tag{20}$$

On the other hand, it is known that magnetisation of a substance (including slurry) is determined by the magnetic field intensity H:

$$I_{sl} = \chi H, \tag{21}$$

where χ is the magnetic susceptibility of the substance.

Setting the left and the right parts of Eqs (20) and (21) equal, we obtain

$$\chi H = W_\tau \eta I_M. \tag{22}$$

When using Lamb waves to assess the volume fraction of the slurry solid phase, the following signal is formed (Morkun et al., 2014):

$$S \equiv ln\left(\frac{I_{0,v}}{I_{l,v}}\right) = W_\tau \frac{(\rho_{sol} - \rho_W)}{\rho} C. \tag{23}$$

After dividing the left and the right parts of Eqs (13) and (14), we obtain

$$\frac{\chi H}{ln\left(\frac{I_{0,v}}{I_{l,v}}\right)} = \frac{W_\tau \eta I_M}{W_\tau \frac{(\rho_{sol} - \rho_W)}{\rho} C_v} = \frac{\eta I_M}{\frac{(\rho_{sol} - \rho_W)}{\rho} C_v}. \tag{24}$$

It follows from Eq. (24) that

$$\eta = \left[\frac{(\rho_{sol} - \rho_W)}{\rho I_M} C\right] \frac{\chi H}{ln\left(\frac{I_{0,v}}{I_{l,v}}\right)}. \tag{25}$$

The expression in square brackets is almost a constant value denoted by A. Then, Eq. (25) will become shorter

$$\eta = A \frac{\chi H}{ln\left(\frac{I_{0,v}}{I_{l,v}}\right)} = A \frac{(\mu - 1) H}{ln\left(\frac{I_{0,v}}{I_{l,v}}\right)}, \tag{26}$$

where $\mu_r = 1 + \chi$ is the relative magnetic permeability of the slurry within the magnetic field of intensity H. This formula is the basis for determining the fraction of the magnetic component in the solid phase of the slurry.

6. DISCUSSION OF MATERIALS

The general scheme for measuring the ferromagnetic component in the iron ore slurry flow is given in Fig. 7.

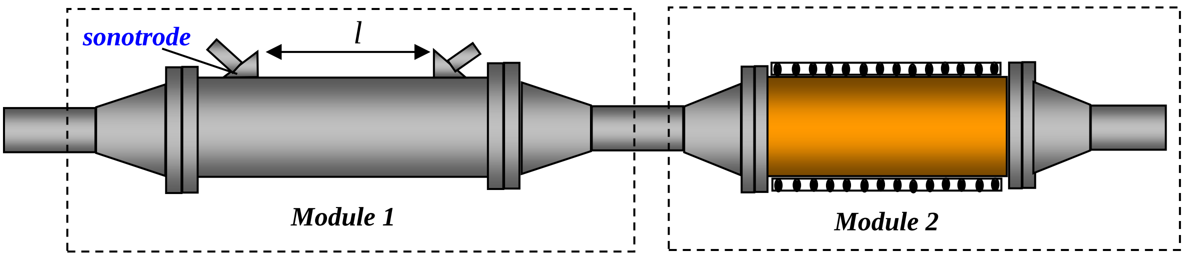

Fig. 7. Scheme for measuring the ferromagnetic component content in the slurry flow

In measuring Module 1, ultrasonic control of the volume fraction of the solid phase of the slurry is performed by means of Lamb waves (5 MHz), which extend from the sonotrode to a receiver, which are arranged at a distance l = 300 mm. In measuring Module 2, the slurry is magnetised and its magnetic susceptibility is measured. Measuring Module 2 is a solenoid containing n winds per unit length (Fig. 8). When direct current is imposed through the solenoid J_o, a homogeneous magnetic field of intensity H appears inside it:

$$H = n \cdot J_0. \tag{27}$$

To determine magnetic susceptibility μ, we apply the known ratio

$$H = \frac{B}{\mu \mu_0}, \tag{28}$$

where B is the magnetic flux density in the slurry, and μ_0 is the magnetic permeability of vacuum.

DOI 10.2478/ama-2021-0025

Thus, it is necessary to measure *B* and *H* to determine μ. If *H* is definitely determined through conduction currents J_o according to Eq. (27), in order to find *B*, we can use classical measuring schemes. Fig. 7 presents one of the ways of determining *B*. If the vessel walls of the measuring module are made of non-magnetic material, we can define the value *B* by means of the auxiliary winding *3* or coil *4*.

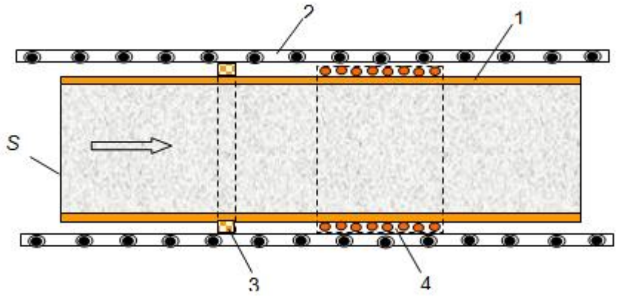

Fig. 8. Measuring Module 2 for determining the magnetic characteristics of the slurry: 1 - walls of the vessel with the slurry; 2 –solenoid winding; 3,4 – auxiliary winding or coil; S – cross-sectional area

While switching on and off the magnetic field, there appears a short-time current in the auxiliary coil and a charge *q* runs along the circuit, the value of which is proportional to the magnetic flux density *B*:

$$q = \frac{N \cdot S \cdot B}{R}, \tag{29}$$

where *N* is the number of winds of the auxiliary coil, *S* is the area of the cross-section determined by the inner diameter of the module, *R* is the full resistance of the measuring circuit (resistance of the winding of the auxiliary coil and input resistance of the measuring device).

Thus, by measuring the full charge of the short-time current in the auxiliary coil, we can determine *B:*

$$B = \frac{q \cdot R}{N \cdot S} \tag{30}$$

$$\mu = \frac{B}{\mu_o H} = \frac{qR}{\mu_o N S n J_o} = qC_1. \tag{31}$$

where $C_1 = \frac{R}{\mu_o N S n J_o}$ is a constant value.

The final expression for finding the fraction of the magnetic component η in the slurry looks as follows:

$$\eta = A\frac{(\mu-1)H}{ln\left(\frac{I_{0,v}}{I_{l,v}}\right)} = (AnJ_o)\frac{(qC_1-1)}{ln\left(\frac{I_{0,v}}{I_{l,v}}\right)} = A_1\frac{(qC_1-1)}{ln\left(\frac{I_{0,v}}{I_{l,v}}\right)}. \tag{32}$$

The constants A_1 and C_1 are determined by calibrating the system. The constant C_1 is determined in laboratory conditions in the way described below.

In the empty measuring Module 2, the charge q_c is measured while switching on/off the magnetic field. If the value of μ_r for the air can be considered equal to '1', the following condition is observed:

$$q_c C_1 - 1 = 0. \tag{33}$$

This results in

$$C_1 = \frac{1}{q_c}. \tag{34}$$

The second calibration stage is conducted in the real slurry. Measurements are conducted in both modules, and the value $\frac{(qC_1-1)}{ln\left(\frac{I_{0,v}}{I_{l,v}}\right)}$ is determined. Then, the slurry is selected for analysing the magnetic component content η. The proportionality factor is found according to Eq. (32):

$$A_1 = \frac{\eta}{\left[\frac{(qC_1-1)}{ln\left(\frac{I_{0,v}}{I_{l,v}}\right)}\right]}. \tag{35}$$

If the measuring Module 2 is made of magnetic material, the auxiliary measuring coil should be placed inside it. A measuring probe placed inside the module can be another option (Fig. 9).

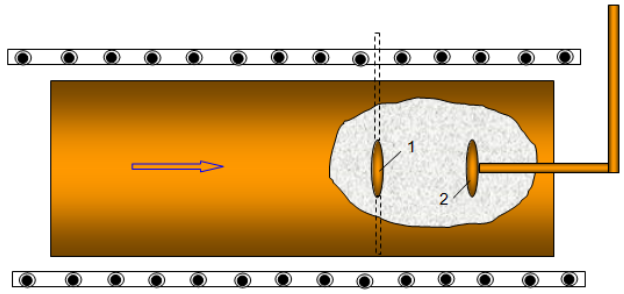

Fig. 9. Variant of measuring Module 2 for determining the magnetic characteristics of the slurry by means of inner probes

The probe should be a prolate ellipsoid to ensure homogeneity of the magnetic field inside the probe (Fig. 10). Besides, it should be made of non-magnetic material. The shape of the ellipsoid should create a narrow clearance corresponding to the washer. With this shape, the magnetic field *B* inside the probe is close to the field in the slurry.

There is either a circular coil or a Hall sensor inside the probe (Fig. 9). For the circular coil, the procedure of determining the magnetic component does not change and is relevant to the above. As for the Hall sensor, instead of measuring the charge, voltage is measured and determined by the following expression:

$$\Delta U = R_x jaB = C_x B. \tag{36}$$

where *j* is the current density; *a* is a design factor of the sensor; and R_x is the Hall constant.

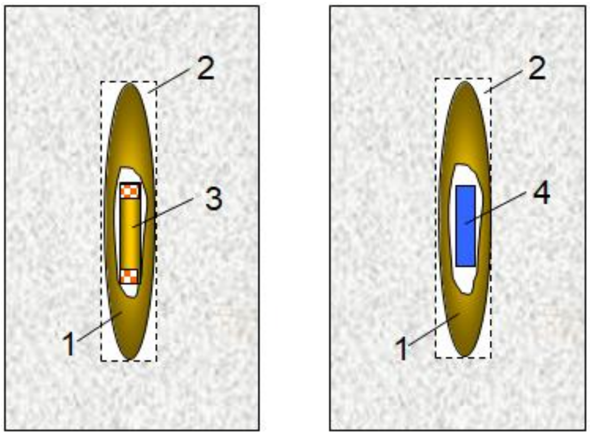

Fig. 10. Structure of the measuring probe: 1 – measuring probe; 2 – internal cavity equivalent to the probe; 3 –measuring coil; 4 – Hall sensor

DOI 10.2478/ama-2021-0025 acta mechanica et automatica, vol.15 no.4 (2021)

It follows from the formula that the magnetic flux density B is proportional to voltage ΔU. So, the magnetic component η in the slurry can be found according to the following expression.

$$\eta = A_2 \frac{(\Delta UC_2 - 1)}{ln\left(\frac{I_{0,\nu}}{I_{l,\nu}}\right)}, \tag{37}$$

which is similar to Eq. (32).

The results of testing the device used for controlling the content of the ferromagnetic component in the slurry flow are given in Fig. 11.

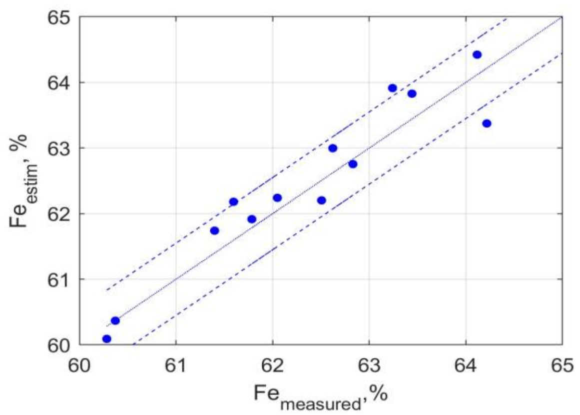

Fig. 11. Testing results of the device for controlling the ferromagnetic component content in the slurry flow

The results of testing of the device used for controlling the content of the ferromagnetic component in the slurry flow by ultrasonic and magnetic measurements indicate that the error in measurement of the iron content in the solid phase of the slurry does not exceed 0.47%.

7. CONCLUSIONS

The results of laboratory and industrial testing of the device developed for controlling the ferromagnetic component content in the slurry flow by ultrasonic and magnetic methods indicate its high accuracy and reliability. Considering the fact that the error of measuring iron content in the solid phase of the slurry does not exceed 0.47%, it can be recommended for wider application at magnetic concentration plants as a CAPCS means.

REFERENCES

1. **Bogdanov, O.S.** (1983), *Ore dressing guide*. Nedra, Moscow. in Russian.
2. **Bond, L.J., Morra, M., Greenwood, M.S., Bamberger, J.A., Pappas, R.A.** (2003), Ultrasonic technologies for advanced process monitoring, measurement, and control, *Proceedings of the 20th IEEE Information and Measurement Technology Conference*, 2, 1288-1293.
3. **Brazhnikov, N.I.** (1975), *Ultrasonic methods*, Energia, Moscow. in Russian.
4. **Debarnot, M. Le Letty, R., Lhermet, N.** (2006), Ultrasonic NDT based on Lamb waves: Development of a dedicated drive and monitoring electronic, *Proceedings of the 3rd EuropeanWorkshop on Structural Health Monitoring*, 1207–1213.
5. **Derkach, V.G.** (1966), *Special Methods for Mineral Processing*. Nedra, Moscow. in Russian.
6. **Eremenko, Y., Poleshchenko, D., Tsygankov, Y.** (2019), Neural network based identification of ore processing units to develop model predictive control system, *Proceedings of XXI International Conference Complex Systems: Control and Modeling Problems (CSCMP)*, 121-124.
7. **Eskandari, M.J., Hasanzadeh, I.** (2021), Size-controlled synthesis of Fe3O4 magnetic nanoparticles via an alternating magnetic field and ultrasonic-assisted chemical co-precipitation, *Materials Science and Engineering B-advanced Functional Solid-State Materials*, 266, 115050.
8. **Fukumoto, T., Tanaka, Y., Sawada, T.** (2019), Change of ultrasonic propagation velocity in an MR fluid under AC magnetic fields, *International Journal of Applied Electromagnetics and Mechanics*, 1(59), 341-347.
9. **Golik, V., Komaschenko, V., Morkun, V., Khasheva, Z.** (2015a), The effectiveness of combining the stages of ore fields development, *Metallurgical and Mining Industry*, 7(5), 401-405.
10. **Golik, V., Komashchenko, V., Morkun, V.** (2015b), Geomechanical terms of use of the mill tailings for preparation, *Metallurgical and Mining Industry*, 7(4), 321-324.
11. **Hauptmann, P., Hoppe, N., Püttmer, A.** (2002), Application of ultrasonic sensors in the process industry, *Measurement Science and Technology*, 13 (8), R73-R83. DOI: 10.1088/0957-0233/13/8/201.
12. **Karmazin, V.I., Karmazin, V.V.** (1978), *Magnetic enrichment methods*, Nedra, Moscow. in Russian.
13. **Kupin, A.** (2014), Application of neurocontrol principles and classification optimization in conditions of sophisticated technological processes of beneficiation complexes, *Metallurgical and Mining Industry*, 6, 16–24.
14. **Lee, C., Staszewski, W. J.** (2009), Modelling of Lamb waves for damage detection in metallic structures: Part I. Wave propagation, Smart *Materials and Structures*, 12(5), 804.
15. **Liu, B.Y., Liu, B.J., Gao, X.W., Zhang, D.S., Hao, D.Z., Li, X.Y.** (2020), A soft sensor based on case-based reasoning for iron ores flotation, *Ironmaking & Steelmaking*, 2(47), 150-158.
16. **Lolaev, A.B., Meshkov, E.I., Kovalyova, M.A.** (2018), Research and development of automated system of solids flow control in the slurry entering the tailings storage facility along a pipeline with a varying degree of filling, *Sustainable Development of Mountain Territories*, 10(2), 253-259. DOI: 10.21177/1998-4502-2018-10-2-253-259.
17. **Louisnard, O.** (2012a), A simple model of ultrasound propagation in a cavitating liquid. Part I: Theory, nonlinear attenuation and traveling wave generation, *Ultrasonics Sonochemistry*, 19(1), 56–65.
18. **Louisnard, O.** (2012b), A simple model of ultrasound propagation in a cavitating liquid. Part II: Primary Bjerknes force and bubble structures, *Ultrasonics Sonochemistry*, 19(1), 66–76.
19. **Ma, L.C., Zhang, Y., Song, G.Q., Ma, Z., Lu, T.Q.** (2019), Ore granularity detection and analysis system based on image processing, *Proceedings of the 2019 31st Chinese Control and Decision Conference (CCDC 2019)*, 359-366.
20. **Meng, Y.Y., Yan, S.** (2019), Thin plate Lamb propagation rule and dispersion curve drawing based on wave theory, *Surface Review and Letters*, 7(26), 1850222.
21. **Modlo, Y.O., Semerikov, S.O., Bondarevskyi, S.L., Tolmachev, S.T., Markova, O.M., Nechypurenko, P.P.** (2019), Methods of using mobile Internet devices in the formation of the general scientific component of bachelor in electromechanics competency in modeling of technical objects, *Proceedings of the 2nd International Workshop on Augmented Reality in Education (AREDU 2019)*, 2547, 217-240.
22. **Morkun, V., Morkun, N., Pikilnyak, A.** (2014), The adaptive control for intensity of ultrasonic influence on iron ore pulp, *Metallurgical and Mining Industry*, 6(6), 8-11.
23. **Morkun, V., Morkun, N., Tron, V.** (2015a), Model synthesis of nonlinear nonstationary dynamical systems in concentrating production using Volterra kernel transformation, *Metallurgical and Mining Industry*, 7(10),6-9.

DOI 10.2478/ama-2021-0025

24. **Morkun, V., Morkun, N., Tron, V.** (2015b), Distributed control of ore beneficiation interrelated processes under parametric uncertainty, *Metallurgical and Mining Industry*, 7(8), 18-21.
25. **Morkun, V., Morkun, N., Tron, V.** (2015c). Distributed closed-loop control formation for technological line of iron ore raw materials beneficiation, *Metallurgical and Mining Industry*, 7(7), 16-19.
26. **Ni, L., Chen, X.** (2018), Mode separation for multimode Lamb waves based on dispersion compensation and fractional differential, *Acta Physica Sinica*, 20(67), 204301.
27. **Parekh, K., Patel, J., Upadhyay, R.V.** (2015), Ultrasonic propagation: A technique to reveal field induced structure in magnetic nanofluids, *Ultrasonics*, 60, 126-132.
28. **Parekh, K., Upadhyay, R.V.** (2017), The effect of magnetic field induced aggregates on ultrasound propagation in aqueous magnetic fluid, *Journal of Magnetism and Magnetic Materials*, 431, 74-78.
29. **Porkuian, O., Morkun, V., Morkun, N., Tron, V., Haponenko, I., Davidkovich, A.** (2020), Influence of the magnetic field on love waves propagation in the solid medium, *Proceedings of IEEE 40th International Conference on Electronics and Nanotechnology (ELNANO)*, 761-766.
30. **Ryden, N., Park, C.B., Ulriksen, P., Miller, R.D.** (2003), Lamb wave analysis for non-destructive testing of concrete plate structures, *Symposium on the Application of Geophysics to Engineering and Environmental Problems (SAGEEP 2003)*.
31. **Rzhevsky, V.V., Yamshchikov, V.S**. (1968), *Ultrasonic monitoring and research in mining*, Nedra, Moscow. in Russian.
32. **Seip, R., VanBaren, P., Cain, C., Ebbini, E.** (1996), Noninvasive real-time multipoint temperature control for ultrasound phased array treatments, *IEEE Transactions on Ultrasonics, Ferroelectrics, and Frequency Control*, 6, 1063–1073.
33. **Semerikov, S., Slovak, K.** (2011), Theory and methodics of mobile mathematical tools using in the process of higher mathematics teaching for students of economic specialties, *Information Technologies and Learning Tools*, 1(21).
34. **Stupnik, M.I., Kalinichenko, V.O., Kalinichenko, O.V., Muzyka, I.O., Fedko, M.B., Pysmennyi, S.V.** (2015), Information technologies as a component of monitoring and control of stress-deformed state of rock mass, *Mining of Mineral Deposits*, 2(9), 175-181.
35. **Subhash, N., Krishnan, B.** (2011), Modelling and experiments for the development of a guided wave liquid level, *Proceedings of the National Seminar & Exhibition on Non-Destructive Evaluation*, 240–244.
36. **Viktorov, I.A.** (1966), *Physical fundamentals of the application of Rayleigh and Lamb ultrasonic waves in technology*, Nauka, Moscow. in Russian.
37. **Viktorov, I.A.** (1975), Elastic waves in a solid half-space with a magnetic field, *Reports of the USSR Academy of Sciences*, 221(5), 1069–1072. in Russian.
38. **Wan, Z.P., He, Z.C., Wang, X.W., Chen, B.Q., Ong, R.H., Zhao, Y.L.** (2020), Heat transfer in a liquid under focused ultrasonic field, *Experimental Thermal and Fluid Science*, 119, 110179.
39. **Weinberg, A.K.** (1966), Magnetic permeability, electrical conductivity, dielectric constant and thermal conductivity of a medium containing spherical and ellipsoidal inclusions, *Reports of the USSR Academy of Sciences*, 169(3), 543-546. in Russian.
40. **Xu, Y.F., Hu, W.X.** (2017), Wideband dispersion removal and mode separation of Lamb waves based on two-component laser interferometer measurement, *Chinese Physics B*, 9(26), 094301.
41. **Yuan, Y., Miao, B.Y., An, Y.** (2018), Cavitation clouds in gas-containing liquids block low-frequency components of ultrasonic waves, *Journal of Applied Physics*, 22(124), 224902.
42. **Zhang, Y.H, Qian, Z.H., Wang, B.** (2020), Modes control of Lamb wave in plates using meander-line electromagnetic acoustic transducers, *Applied Sciences-Basel*, 10(10), 3491.
43. **Zhao, S.N., Yao, C.Q., Zhang, Q., Chen, G.W., Yuan, Q.** (2019), Acoustic cavitation and ultrasound-assisted nitration process in ultrasonic microreactors: The effects of channel dimension, solvent properties and temperature, *Chemical Engineering Journal*, 374, 68-78.

Vladimir Morkun: https://orcid.org/0000-0003-1506-9759

Natalia Morkun: https://orcid.org/0000-0002-1261-1170

Vitaliy Tron: https://orcid.org/0000-0002-6149-5794

Olga Porkuian: https://orcid.org/0000-0003-3595-8211

Oleksandra Serdiuk: https://orcid.org/0000-0003-1244-7689

Tetiana Sulyma: https://orcid.org/0000-0002-8869-040X

DOI 10.2478/ama-2021-0026 acta mechanica et automatica, vol.15 no.4 (2021)

DESIGN OF DECOUPLED PI CONTROLLERS FOR TWO-INPUT TWO-OUTPUT NETWORKED CONTROL SYSTEMS WITH INTRINSIC AND NETWORK-INDUCED TIME DELAYS

Ould Mohamed MOHAMED VALL*

*Department of Computer Engineering and Networks, College of Computer and Information Sciences, Jouf University, Sakaka 72388, Kingdom of Saudi Arabia

medvall@ju.edu.sa

received 21 May 2021, revised 22 July 2021, accepted 27 July 2021

Abstract: Proportional integral controller design for two-input two-output (TITO) networked control systems (NCSs) with intrinsic and network-induced time delays is studied in this paper. The TITO NCS consists of two delayed sub-systems coupled in a 1-1/2-2 pairing mode. In order to simplify the controller design, a decoupling method is first applied to obtain a decoupled system. Then, the controllers are designed based on the transfer function matrix of the obtained decoupled system and using the boundary locus method for determining the stability region and the well-known Mikhailov criterion for the stability test. A comparative analysis of the designed controllers and other controllers proposed in previous literature works is thereafter carried out. To demonstrate the validity and efficacy of the proposed method and to show that it achieves better results than other methods proposed in earlier literature works, the implementation in simulation of Wood–Berry distillation column model (methanol–water separation), a well-known benchmark for TITO systems, is carried out.

Key words: pproportional integral controller, two-input two-output (TITO) systems, networked control systems, stability region boundary locus ,Wood–Berry distillation column model, time delay, Mikhailov criterion

1. INTRODUCTION

Several processes in industry, such as heat exchange, distillation process, and chemical reactions and so on, require the control of two or more output variables. In turn, the control of output variables requires the manipulation of two or more input variables(Ajayi and Oboh, 2012); such systems are known as multi-input multi-output (MIMO) systems. The most common form of MIMO system is a two-input two-output (TITO) system (Zhuang and Atherton, 1993). The problem of control of TITO systems has attracted the attention of many researchers (see: Hamdy et al.,2018;Baruah et al.,2018;Heris et al.,2019; Li et al.,2019; Ustoglu et al., 2016; Qian et al.,2017; Vargas et al.,2013; Maghade and Patre,2013; and references therein). In a TITO system, the interaction between loops makes analysis and design of the controller a very difficult task, and this task becomes more difficult and complex when the system to be controlled involves intrinsic time delays. Therefore, many of the methods dealing with TITO system control proposed in the literature have been interested in reducing the interaction loops by using a decoupling technique in a way that a change in each of the two loops does not affect the other (see: Tanaka et al., 2015; Hazarika and Chidambaram, 2014;Mahapatro and Subudhi, 2020;and references therein). Other research works existing in the literature have been interested on the control of TITO systems with time delays (see: Jeng and Jian, 2017; Jin et al., 2016; Liu et al., 2006; Khandekar and Patre, 2017; Hajare et al., 2017; and references therein).

On the other hand, networked control systems (NCSs), which are systems in which a band-limited network is used by the plant, sensor and controller to share control signals and information among them, have many advantages in terms of reduction of wiring, lower maintenance cost, increased system agility, ease of information sharing and so on (Hong et al., 2017), compared to traditional point to point control systems in which the components and devices are connected via wires. Due to their advantages, NCSs have found application in many fields, such as process control engineering (Sun and El-Farra, 2012; ElFarra and Mhaskar, 2008), teleportation (Liu, 2015), vehicle industry(Jin et al., 2014), power systems (Park, 2015; Yao et al., 2015), transportation systems (Park et al., 2014; Barrero et al., 2014) and so on. One of the major factors that make the control of NCSs a very challenging problem is the presence of inevitable time delay induced by the transmission of control signals and information over a network that may be used by others devices and systems. This justifies why many of research papers related to the control of NCSs with network-induced time delay have been published over the past few decades(see: Li et al., 2016; Zhang et al., 2006; Huang and Nguang, 2009; Liu and Liu, 2020; Mohamed Vall, 2020b; Pang et al., 2016; Mohamed Vall, 2020a; Elahi and Alfi, 2017). However, to the author's best knowledge, in the literature, there are few research works related to the control of TITO NCSs with intrinsic and network-induced time delay (Wang et al., 2000; Sharma and Padhy, 2017; Astrom et al., 2002). Moreover, most of the approaches dealing with this problem are very complex and very time consuming or even not applicable in real-world control problems.

Motivated by the above discussion, we propose, in this paper, a simple and practicable method for the control of TITO NCSs with intrinsic and network-induced time delays. The proposed method comprises two steps: first, a decoupler for the TITO NCS to be controlled is calculated; second, two decoupled proportional integral (PI) controllers for the augmented system, consisting of the obtained decoupler and the TITO NCS to be controlled, are separately designed using the boundary locus method for determining the stability region (Siljak, 1966; Chao and Han,1998; Wang,2011) and the Mikhailov criterion for stability test as presented by Barker (1979) and Mikhailov (1938).

In summary, the main objectives of this work are as follows:

– To design decoupled PI controllers that garantee robustness and good set point tracking, as well as good disturbance rejection, for TITO NCSs with intrinsic and network-induced time delays.
– To carry out a comparative analysis of the designed controllers with other controllers proposed in previous literature works (Hajare and Patre, 2015) and show the superiority of the method proposed in this paper.

The remainder of the paper is organized as follows. In Section 2, the structure of TITO NCSs with network-induced time delays is presented. The proposed method for the control of TITO NCSs with intrinsic and network-induced time delays is presented in Section 3. In Section 4, a simulation example is given to show the validity and effectiveness of the proposed method. Conclusions are given in Section 5.

2. PROBLEM FORMULATION

As mentioned above, this research work deals with the control of TITO-NCSs with intrinsic and network-induced time delays. Fig. 1 shows the structure of a TITO-NCS with network-induced delays. As one can notice in Fig. 1, there are three time delays affecting each sub-system of the whole system, which are as follows:

– delay sensor-to-controller $\tau^{(s_i c_i)}$ $(i = 1,2)$
– delay controller-to-actuator $\tau^{(c_i a_i)}$ $(i = 1,2)$
– controller computation delay $\tau^{(c_i)}$ $(i = 1,2)$

Although controller computation time delay always exists, it is usually small compared to network-induced time delays and can be neglected.

In this paper, for simplicity and without losing generality, we neglect the controller computation time delay and assume that the network-induced delays affecting each sub-system are lumped together as one control time delay τ_i given by the following expression:

$$\tau_i = \tau^{(s_i c_i)} + \tau^{(c_i a_i)} \ (i = 1,2) \tag{1}$$

‘Depending on the medium access control (MAC) protocol of the control network, network-induced delay can be constant, time varying, or even random’ (Zhang et al., 2001). Here, we are considering constant network-induced delay, ‘which can be achieved by using an appropriate network protocol’ (Zhang et al., 2001), and our objective is to design PI controllers to compensate for these time delays. The method proposed contains two steps. In the first step, the system is decoupled in order to simplify the controllers' design and to obtain controllers that can guarantee that changes in the reference signal of a sub-system do not affect the output of the other and vice versa. In the second step, for the decoupled system, PI controllers are designed utilizing the stability boundary locus method.

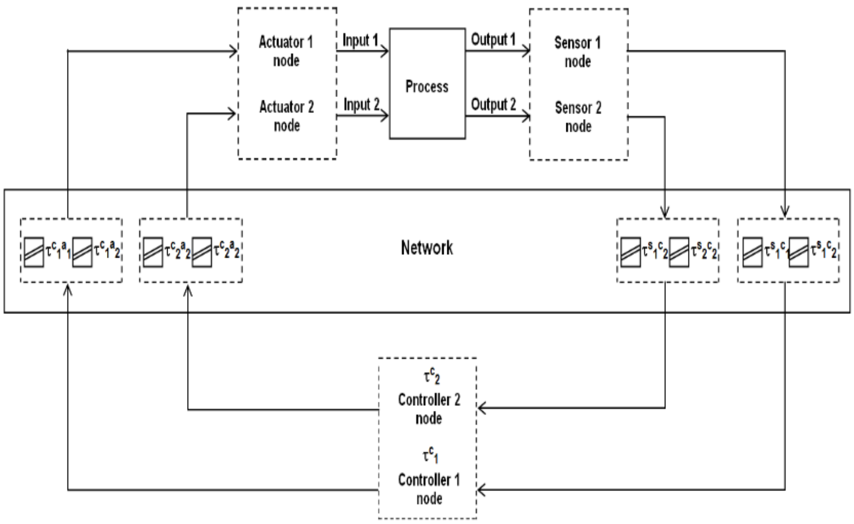

Fig. 1. Structure of TITO-NCS with Network-Induced Time Delays (NCS – networked control system; TITO – two-input two-output)

3. PROPOSED METHOD

3.1. Decoupling of the TITO system

Consider the closed-loop TITO system shown in Fig.2, where $r_1$and r_2 are reference signals;$C_1(s)$ and $C_2(s)$ are two controllers to be designed;$G_{11}(s)$, $G_{12}(s)$, $G_{21}(s)$ and $G_{22}(s)$ are the transfer functions of the system;τ_1, τ_2,τ_3 and τ_4 are the time delays; andy_1 and y_2 are the outputs of the system.

The cross-interaction between the input–output pairs makes the design of the controllers very hard and may – in many control problems – lead to undesirable effects. Therefore, to simplify the controller design and eliminate the effects of loop interactions as much as possible, the following decoupling method is used.

DOI 10.2478/ama-2021-0026 acta mechanica et automatica, vol.15 no.4 (2021)

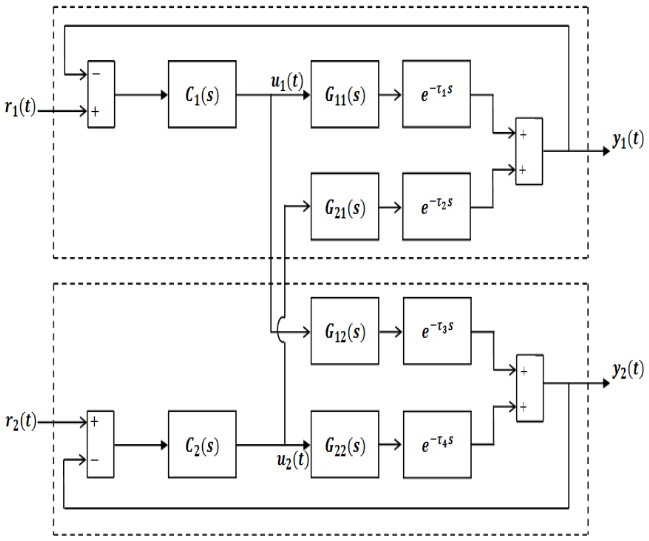

Fig. 2. 1-1/2-2 closed-loop TITO system with time delays (TITO – two-input two-output)

The transfer function matrix of the system shown in Fig.2 is

$$G(s) = \begin{bmatrix} G_{11}(s)e^{-\tau_1 s} & G_{12}(s)e^{-\tau_2 s} \\ G_{21}(s)e^{-\tau_3 s} & G_{22}(s)e^{-\tau_4 s} \end{bmatrix}. \tag{2}$$

Let the transfer function matrix of the decoupler be

$$D(s) = \begin{bmatrix} D_{11}(s) & D_{12}(s) \\ D_{21}(s) & D_{22}(s) \end{bmatrix}. \tag{3}$$

The matrix D(s) should be chosen so that the matrix

$$P(s) = G(s)D(s) \tag{4}$$

is diagonal.

As mentioned above, many decoupling methods for TITO systems have been proposed in the literature. In this paper, we propose to use the decoupler whose transfer function matrix is given in previous studies (Koo et al., 2017; de A. Aguiar and Barros, 2020; Naik et al., 2020).

$$D(s) = \begin{bmatrix} 1 & \frac{-G_{12}(s)e^{-(\tau_2-\tau_1)s}}{G_{11}(s)} \\ \frac{-G_{21}(s)e^{-(\tau_3-\tau_4)s}}{G_{22}(s)} & 1 \end{bmatrix} \tag{5}$$

Fig. 3 shows the structure of a TITO system with the proposed decoupler, where $W_{12}(s) = \frac{-G_{12}(s)e^{-(\tau_2-\tau_1)s}}{G_{11}(s)}$and $W_{21}(s) = \frac{-G_{21}(s)e^{-(\tau_3-\tau_4)s}}{G_{22}(s)}$. Notice that the decoupler is not causal if $\tau_2 - \tau_1 < 0$or/and $\tau_3 - \tau_4 < 0$ (Wanget al., 2000). However, even if the decoupler is not causal, one can introduce simple modifications in its structure so that it becomes causal without affecting the decoupled system's structure (Sharma and Padhy, 2017).

Inserting Eqs. (2) and (5) in Eq. (4) gives the transfer function matrix of the decoupled system as

$$P(s) = \begin{bmatrix} P_{11}(s) & 0 \\ 0 & P_{22}(s) \end{bmatrix}, \tag{6}$$

where $P_{11}(s) = G_{11}(s)e^{-\tau_1 s} - \frac{G_{12}(s)e^{-\tau_2 s}G_{21}(s)e^{-(\tau_3-\tau_4)s}}{G_{22}(s)}$ and

$$P_{22}(s) = G_{22}(s)e^{-\tau_4 s} - \frac{G_{21}(s)e^{-\tau_3 s}G_{12}(s)e^{-(\tau_2-\tau_1)s}}{G_{11}(s)}.$$

Based on the above decoupled system, PI controllers can be designed independently using the stability locus method, as presented in the following sub-sections.

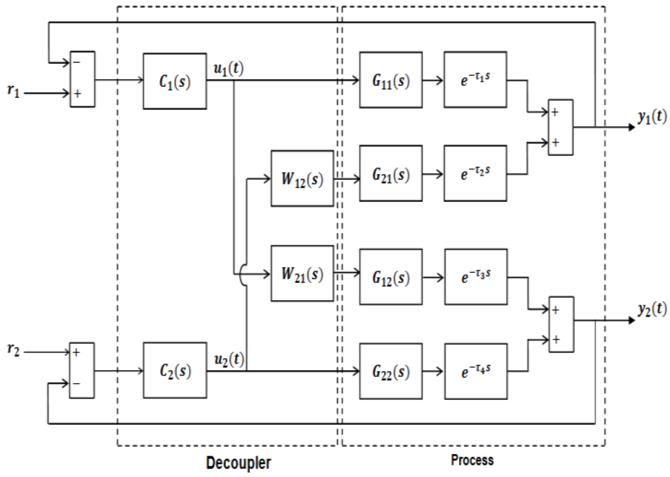

Fig. 3. Decoupling structure

3.2. Calculation of decoupled PI controllers

Suppose that network-induced time delays affect the decoupled system whose transfer function matrix is defined in Eq. (6). The closed-loop transfer functions of the sub-systems constituting the whole system are, thus, given by the following expressions:

$$T_1(s) = \frac{C_1(s)\{G_M(s)e^{(-\tau_1 s)} - G_D(s)e^{-(\tau_2+\tau_3-\tau_4)s}\}e^{-\tau_{N_i 11}s}}{G_{22}(s) + C_1(s)\{G_M(s)e^{(-\tau_1 s)} - G_D(s)e^{-(\tau_2+\tau_3-\tau_4)s}\}e^{-\tau_{N_i 11}s}} \tag{7}$$

$$T_2(s) = \frac{C_2(s)\{G_M(s)e^{(-\tau_4 s)} - G_D(s)e^{-(\tau_3+\tau_2-\tau_1)s}\}e^{-\tau_{N_i 22}s}}{G_{11}(s) + C_2(s)\{G_M(s)e^{(-\tau_4 s)} - G_D(s)e^{-(\tau_3+\tau_2-\tau_1)s}\}e^{-\tau_{N_i 22}s}} \tag{8}$$

where$G_M(s) = G_{11}(s)G_{22}(s)$,$G_D(s) = G_{12}(s)G_{21}(s)$, $C_1(s)$and $C_2(s)$are the two PI controllers to be designed and $\tau_{N_i 11}$and $\tau_{N_i 22}$are the network-induced time delays that affect Loops 1–1 and 2–2, respectively.

To determine the parameters of the controllers, the stability region locus method is used as follows.

3.2.1. Determination of the parameters of $C_1(s)$

Let:

$$C_1(s) = \alpha_1 + \frac{\beta_1}{s}; \tag{9}$$

$$\tau_{11} = \tau_{N_i 11} + \tau_1; \tag{10}$$

$$\tau_{12} = \tau_{N_i 11} + (\tau_2 + \tau_3 - \tau_4). \tag{11}$$

By inserting Eqs. (9), (10) and (11) in Eq. (7), we can express the transfer function $T_1(s)$ as follows:

$$T_1(s) = \frac{\left(\alpha_1 + \frac{\beta_1}{s}\right)\{G_M(s)e^{-\tau_{11}s} - G_D(s)e^{-\tau_{12}s}\}}{G_{22}(s) + \left(\alpha_1 + \frac{\beta_1}{s}\right)\{G_M(s)e^{-\tau_{11}s} - G_D(s)e^{-\tau_{12}s}\}}. \tag{12}$$

By substituting $s = j\omega$, decomposition of the numerators and denominators of $G_M(s)$, $G_D(s)$and $G_{22}(s)$ into their even and odd parts and using Euler's identity, one can express the system characteristic equation as follows:

$$R_{Q_1}(\omega, \alpha_1, \beta_1) + jI_{Q_1}(\omega, \alpha_1, \beta_1) = 0. \tag{13}$$

where$R_{Q_1}$and I_{Q_1} are two functions in ω, α_1, β_1 with constant real coefficients.

Dropping ω for ease and equating $R_{Q_1}(\omega, \alpha_1, \beta_1)$and $I_{Q_1}(\omega, \alpha_1, \beta_1)$to zero result in the following system of equations:

$$\begin{cases} M_{11}\alpha_1 + M_{12}\beta_1 = X_1 \\ M_{21}\alpha_1 + M_{22}\beta_1 = X_2 \end{cases} \tag{14}$$

whereM_{11}, M_{12}, M_{21}, M_{22}, $X_1$and $X_2$are functions in ω with constant real coefficients.

Solving the equation system (14) for α_1 and β_1 gives

$$\begin{cases} \alpha_1 = \frac{N_{\alpha_1}}{D_{\alpha_1}} \\ \beta_1 = \frac{N_{\beta_1}}{D_{\beta_1}} \end{cases}. \tag{15}$$

whereN_{α_1}, D_{α_1}, N_{β_1}andD_{β_1} are functions in ω with constant real coefficients.

Plotting the dependency relation between α_1 and β_1 and the axis $\beta_1 = 0$ on the (α_1, β_1)-plane splits the plane into two regions. One of these regions is a stability region of the system. To determine which region is a stability region, the Mikhailov criterion for stability test is used. Next, once the stability region is determined, the values of the parameters of $C_1(s)$that stabilise the system can be thus determined by choosing a point within the stability region(Chao and Han, 1998).

3.2.2. Determination of the parameters of $C_2(s)$

The parameters of $C_2(s)$ can be determined in a way similar to that for$C_1(s)$.

Let:

$$C_2(s) = \alpha_2 + \frac{\beta_2}{s} \ ; \tag{16}$$

$$\tau_{22} = \tau_{N_i22} + \tau_4 \ ; \tag{17}$$

$$\tau_{21} = \tau_{N_i22} + (\tau_3 + \tau_2 - \tau_1). \tag{18}$$

By inserting Eqs. (16), (17) and (18) in Eq. (8), we can express the transfer function $T_2(s)$ as follows:

$$T_2(s) = \frac{\left(\alpha_2 + \frac{\beta_2}{s}\right)\{G_M(s)e^{-\tau_{22}s} - G_D(s)e^{-\tau_{21}s}\}}{G_{11}(s) + \left(\alpha_2 + \frac{\beta_2}{s}\right)\{G_M(s)e^{-\tau_{22}s} - G_D(s)e^{-\tau_{21}s}\}}. \tag{19}$$

By substituting $s = j\omega$, decomposition of the numerators and denominators of $G_M(s)$, $G_D(s)$and $G_{11}(s)$ into their even and odd parts and using Euler's identity, one can express the system characteristic equation as follows:

$$R_{Q_2}(\omega, \alpha_2, \beta_2) + jI_{Q_2}(\omega, \alpha_2, \beta_2) = 0. \tag{20}$$

where$R_{Q_2}$and I_{Q_2} are two functions in ω, α_2, β_2 with constant real coefficients.

Dropping ω for ease and equating $R_{Q_2}(\omega, \alpha_2, \beta_2)$and $I_{Q_2}(\omega, \alpha_2, \beta_2)$to zero result in the following equation system:

$$\begin{cases} H_{11}\alpha_2 + H_{12}\beta_2 = Z_1 \\ H_{21}\alpha_2 + H_{22}\beta_2 = Z_2 \end{cases}. \tag{21}$$

whereH_{11}, H_{12}, H_{21}, H_{22}, $Z_1$and $Z_2$are functions in ω with constant real coefficients.

Solving the equation system (21) for α_2 and β_2 gives

$$\begin{cases} \alpha_2 = \frac{N_{\alpha_2}}{D_{\alpha_2}} \\ \beta_2 = \frac{N_{\beta_2}}{D_{\beta_2}} \end{cases} \tag{22}$$

whereN_{α_2}, D_{α_2}, N_{β_2}andD_{β_2} are functions in ω with constant real coefficients.

Plotting the dependency relation between α_2 and β_2; and the axis $\beta_2 = 0$ on the (α_2, β_2)-plane splits the plane into two regions. One of them is a stability region of the system. To determine which region is a stability region, the Mikhailov criterion for stability test is used. Then, the values of the parameters of $C_2(s)$that stabilise the system can be thus determined by choosing a point within the stability region (Chao and Han, 1998).

4. SIMULATION EXAMPLE

In this section, a simulation example is given to show the validity and efficacy of the proposed method.

The simulation is carried out in Simulink and TrueTime in the environment of MatLab. The network communication mode is carrier-sense multiple access with collision detection(CSMA/CD; Ethernet), the transmission rate is 80 Kbit/s and the network-induced time delays that affect Loops 1–1 and 2–2 are $\tau_{N_i11} = 0.13$ secand $\tau_{N_i22} = 0.17$ sec, respectively. The sampling period is 0.02 sec. The process to be controlled is a Wood–Berry distillation column model (methanol–water separation), which has the following transfer function matrix (Astrom et al., 2002):

$$G(s) = \begin{bmatrix} \frac{12.8e^{-s}}{16.7s+1} & \frac{-18.9e^{-3s}}{21.0s+1} \\ \frac{6.6e^{-7s}}{10.9s+1} & \frac{-19.4e^{-3s}}{14.4s+1} \end{bmatrix} \tag{23}$$

The transfer function matrix of the decoupler calculated according to Eq. (5) is

$$D(s) = \begin{bmatrix} 1 & \frac{1.48\,(16.7s+1)e^{-2s}}{21.0s+1} \\ \frac{0.34\,(14.4s+1)e^{-4s}}{10.9s+1} & 1 \end{bmatrix}. \tag{24}$$

The transfer function matrix of the decoupled system calculated according to Eq. (6) is

$$P(s) = \begin{bmatrix} P_{11}(s) & 0 \\ 0 & P_{22}(s) \end{bmatrix}, \tag{25}$$

where $P_{11}(s) = \frac{12.8e^{-s}}{16.7s+1} - \frac{6.43\,(14.4s+1)e^{-7s}}{(21.0s+1)(10.9s+1)}$ and $P_{22}(s) = \frac{-19.4e^{-3s}}{14.4s+1} + \frac{9.77\,(16.7s+1)e^{-9s}}{(10.9s+1)(21.0s+1)}$.

Consequently, based on the decoupled system in Eq. (25) and taking into account that Loops 1–1 and 2–2 are affected by the network-induced time delays $\tau_{N_i11} = 0.13$ sec and $\tau_{N_i22} = 0.17$ sec, respectively, and using Eqs (7) and (8), the closed-loop transfer functions of the sub-systems are obtained as follows:

DOI 10.2478/ama-2021-0026

$$T_1(s) = \frac{C_1(s)\left(A(s)e^{-s}+B(s)e^{-7s}\right)e^{-0.13s}}{\frac{-19.4}{14.4s+1}+C_1(s)\left(A(s)e^{-s}+B(s)e^{-7s}\right)e^{-0.13s}}; \quad (26)$$

$$T_2(s) = \frac{C_2(s)\left(A(s)e^{-3s}+B(s)e^{-9s}\right)e^{-0.17s}}{\frac{12.8}{16.7s+1}+C_2(s)\left(A(s)e^{-3s}+B(s)e^{-9s}\right)e^{-0.17s}}; \quad (27)$$

where $A(s) = \frac{-248.32}{(16.7s+1)(14.4s+1)}$, $B(s) = \frac{124.74}{(21.0s+1)(10.9s+1)}$, and $C_1(s) = \alpha_1 + \frac{\beta_1}{s}$ and $C_2(s) = \alpha_2 + \frac{\beta_2}{s}$ are the two PI controllers.

Let us determine the parameters of $C_1(s)$ and $C_2(s)$ based on the theory presented in Sub-section 3.2 of this paper.

By substituting Eq. (26) into Eq. (12), solving Eqs (13)–(14) for α_1 and β_1, and plotting the dependency between the obtained values of α_1 and β_1 and the axis $\beta_1 = 0$ on the (α_1, β_1)-plane, we obtain Fig. 4.

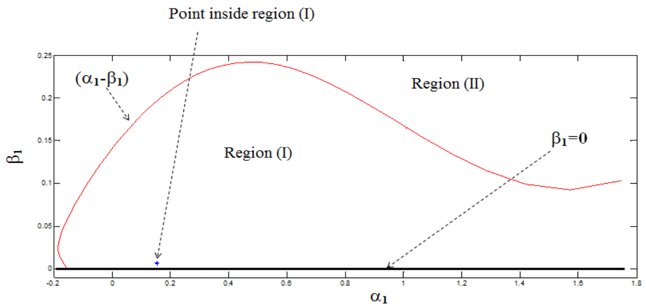

Fig. 4. α_1 versus β_1

As one can see from Fig. 4, the curve (α_1,β_1) and the axis $\beta_1 = 0$ split the (α_1, β_1)-plane into two regions: Region (I) and Region (II).

Now, let us choose the point (0.1532,0.0067) of Region (I) in Fig.4 and check whether the system in Eq. (26) is stable when one chooses the parameters of the controller $C_1(s)$ as $\alpha_1 = 0.1532$ and $\beta_1 = 0.0067$. To check the stability, the Mikhailov criterion for stability test can be used as mentioned earlier in this paper.

By determining the polynomial function $Q_1(j\omega)$ for the transfer function $T_1(s)$ given in Eq. (26) , $\alpha_1 = 0.1532$ and $\beta_1 = 0.0067$, as explained by Barker (1979) and Mikhailov (1938), we obtain the Mikhailov curve shown in Fig. 5. As one can see from Fig. 5, the system is stable since the Mikhailov stability criterion is fulfilled, as also reported by Barker (1979) and Mikhailov (1938).

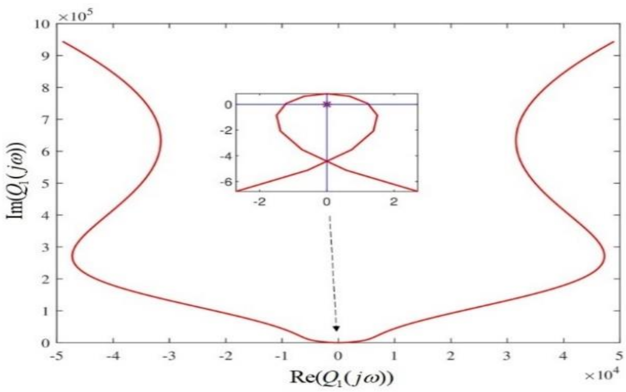

Fig. 5. Loop 1-1 Mikhailov curve for $\alpha_1 = 0.1532$, $\beta_1 = 0.0067$

In a similar way, one can determine the parameters of the controller $C_2(s)$ as those of the controller $C_1(s)$ were determined. By substituting (27) into (19), solving the equations (20)-(21) for α_2 and β_2, and plotting the dependency between the obtained values of α_2 and β_2 and the axis $\beta_2 = 0$ on the (α_2, β_2)- plan, we obtain Fig. 6.

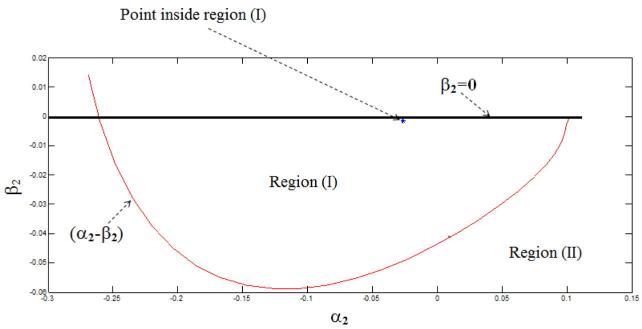

Fig. 6. α_2 versus β_2

As one can see, from Fig. 6., the curve (α_2,β_2) and the axis $\beta_2 = 0$ split the (α_2, β_2)- plan into two regions: Region (I) and Region (II). To determine which of them is a stability region of the system, let's choose the point (-0.0266,-0.0015) of the region (I) and use Mikhailov stability criterion to check whether the system is stable when one chooses the parameters of the controller $C_2(s)$ as $\alpha_2 = -0.0266, \beta_2 = -0.0015$.

By determining the polynomial function $Q_2(j\omega)$ for the transfer function $T_2(s)$ given in (27) , $\alpha_2 = -0.0266, \beta_2 = -0.0015$, as explained in in (Barker, 1979) and (Mikhailov, 1938), we obtain the Mikhailov curve shown in Fig. 7. As one can see, from Fig. 7., the Mikhailov stability criterion holds, as also reported in (Barker, 1979) and (Mikhailov, 1938), the system is, therefore stable.

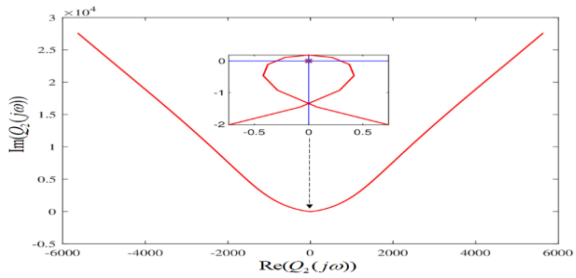

Fig. 7. Loop 2-2 Mikhailov curve for $\alpha_2 = -0.0266, \beta_2 = -0.0015$

To verify the validity and efficacy of the proposed method, the obtained PI controllers: $C_1(s) = 0.1532 + \frac{0.0067}{s}$, $C_2(s) = -0.0266 - \frac{0.0015}{s}$ are applied to the both loops of the decoupled system. In the simulation, a step change in the reference signal r_1 is made at $t = 50$ secand a step change in the reference signal r_2 is made at $t = 150$ sec, respectively. Furthermore, to show the disturbance rejection performance of the obtained controllers, steps disturbance $d_1(t) = 0.1$ at $t = 450$ sec and $d_2(t) = 9$ at $t = 450$ sec are introduced to loop 1 and loop 2, respectively. The simulation results of both set-point tracking and disturbance rejection are shown in Fig. 8 and Fig. 9, respectively. The performance metrics: Settling time (Ts) , Integral Absolute Error (IAE), RMS tracking error (RMSE) and Total Variance (TV) are reported in Tab. 1.

DOI 10.2478/ama-2021-0026

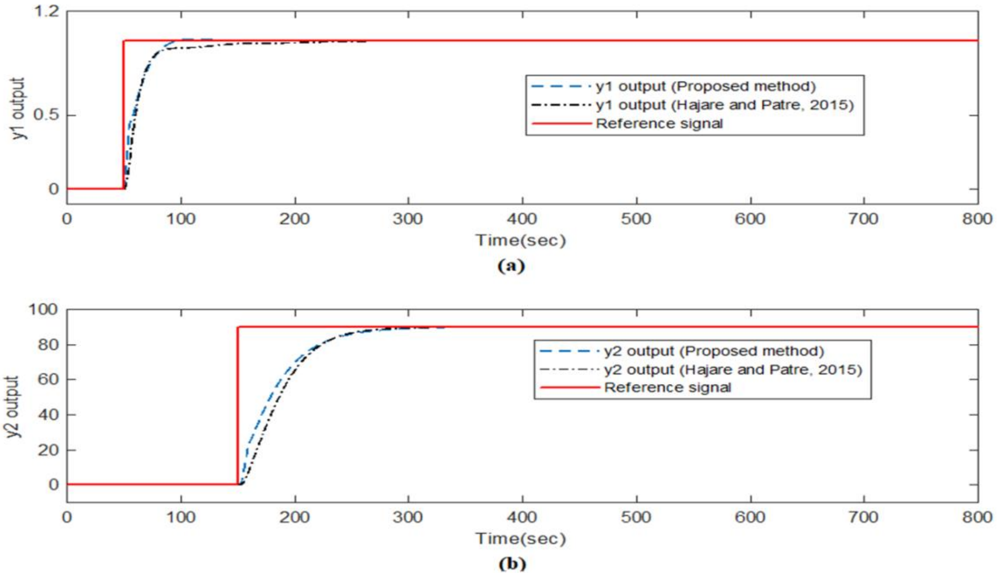

Fig. 8. System outputs: **(a)** Reference signal (red solid line), y_1 (loop1) output (blue dashed line) obtained using the proposed method and y_1 (loop1) output (black dot-dash lines) obtained using the method proposed in (Hajare and Patre, 2015) **(b)** refence signal (red solid line), y_2 (loop2) output (blue dashed line) obtained using the proposed method and y_2 (loop2) output (black dot-dash lines) obtained using the method proposed in (Hajare and Patre, 2015)

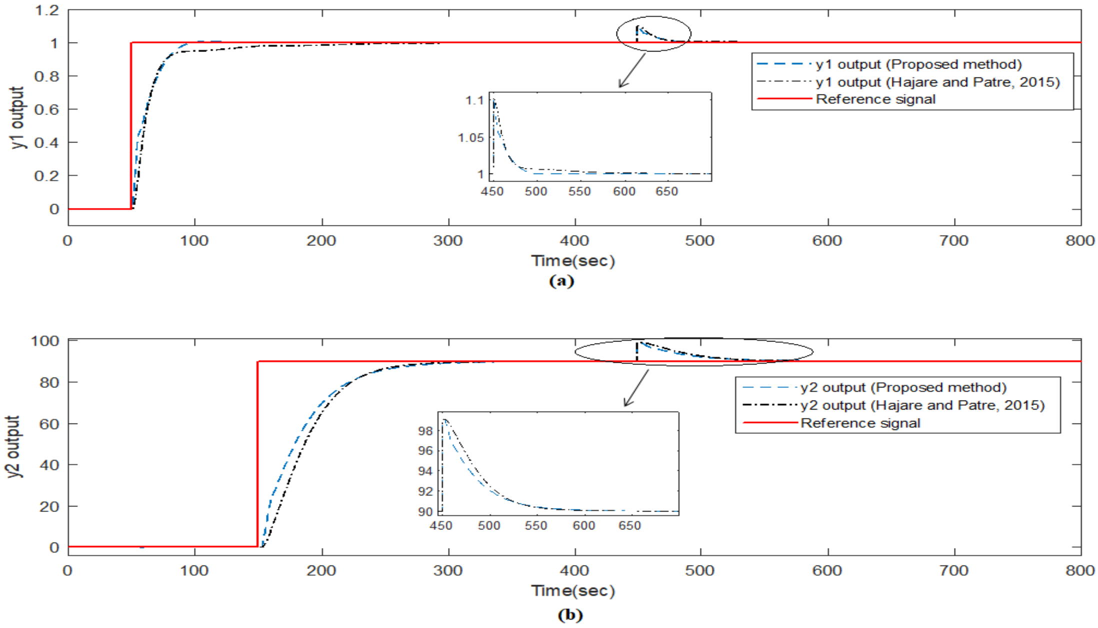

Fig. 9. System outputs with disturbance rejection: **(a)** Reference signal (red solid line), y_1 (loop1) output (blue dashed line) obtained using the proposed method and y_1 (loop1) output (black dot-dash lines) obtained using the method proposed in (Hajare and Patre, 2015) **(b)** refence signal (red solid line), y_2 (loop2) output (blue dashed line) obtained using the proposed method and y_2 (loop2) output (black dot-dash lines) obtained using the method proposed in (Hajare and Patre, 2015)

Tab.1. Performance metrics

Controllers	Input-output	T_s (sec)	RMSE	IAE	TV
Proposed decoupled PI controllers	u_1-y_1 u_2-y_2	41 130	0.09 13.81	12.1131091	0.008174.6
(PID) controllers proposed in Hajare and Patre (2015)	u_1-y_1 u_2-y_2	103.2 119.2	0.12 16.1	17.553586	0.011236.7

IAE – integral absolute error; PI – proportional–integral; PID – proportional–integral–derivative;
RMSE – root mean square tracking error; TV – total variance.

From Fig. 8, it can be seen that the proposed controllers guarantee excellent tracking of the system outputs to the set points and maintain the system stable in both loops. It can be also noticed that the change in the set point of Loop 1 does not affect the response output in the Loop 2 and vice-versa, the change in the set point of the Loop 2 does not affect the response output in the Loop 1. Additionally, the simulation results in Fig. 9 show that the obtained controllers also offer excellent disturbance rejection performance. Moreover, it is evident from the simulation results (shown in Figs. 8 and 9) and the performance metrics (reported in Tab. 1) that the proposed controllers achieve better results than the proportional–integral–derivative (PID) controllers proposed in a previous paper (Hajare and Patre, 2015). For example, it can be seen from Fig. 9 that the proposed controllers take less time and control action to achieve the steady state and zero steady-state error in case of load disturbance.

5. CONCLUSIONS

This paper proposes an approach for the design of decoupled PI controllers for TITO NCSs with intrinsic and network-induced time delays. A decoupler that can reduce interaction between loops and simplify the design of controllers is defined. Moreover, a method based on stability region locus and the Mikhailov criterion for stability test is proposed to determine the parameters of PI controllers to control a TITO NCS with intrinsic and network-induced time delays. A comparative analysis of the designed controllers with other controllers proposed in previous research works has been carried out. The validity and efficacy of the proposed approach are shown through a simulation example, in which the well-known benchmark for TITO systems – the Wood–Berry distillation column model (methanol–water separation) – is built in Simulink and TrueTime in the environment of MatLab; network-induced time delays are included and PI controllers are designed based on the approach proposed. The simulation results show that the designed PI controllers guarantee very good tracking of the system outputs to the set points and maintain the system stable in both loops with excellent disturbance rejection performance. Moreover, the simulation results show that the proposed method achieves better results than other methods proposed in earlier literature works.

REFERENCES

1. **Ajayi T., Oboh I.** (2012), Determination Of Control Pairing for Higher Order Multi-Variable Systems by the Use of Multiple Ratios. *Int, J, Eng&ScientificRes*, 3(3),1–5.
2. **Astrom K.J., Johansson K.H., Wang, Q.G.** (2002), Design of Decoupled PI Controllers for Two-By-Two Systems. In *IEE Proceedings-Control Theory and Applications*, 149, 74–81.
3. **Barker L.K.** (1979), *Mikhailov Stability Criterion for Time-Delayed Systems*. Washington, DC.USA: NASA.
4. **Barrero F., Guevara J., Vargas E., Toral S., Vargas, M.** (2014), Networked Transducers in Intelligent Transportation Systems Based on The IEEE 1451 Standard. *Computer Standards Interfaces*, 36(2), 300–311. doi:10.1016/j.csi.2012.05.004.
5. **Baruah G., Majhi S., Mahanta C.** (2018), Auto-Tuning of PI Controllers for TITO Processes with Experimental Validation. *International Journal of Automation and Computing*, 16. doi:10.1007/s11633-018-1140-0.
6. **Chao G.-L., Han K.W.** (1998), Robust Stability Analysis of Time-Delay Systems Using Parameter-Plane and Parameter-Space Methods. Journal of the Franklin Institute, 335(7), 1249–1262.
7. **de Aguiar A.P.V., Barros P. (**2020), Evaluation and Redesign of The Inverted Decoupler : Open and Closed-Loop Approaches. *Int .J. Control Autom.Syst.*,18, 1435–1444. doi:0.1007/s12555-019-0371-3.
8. **Elahi A., Alfi A.** (2017), Finite-Time H Control of Uncertain Networked Control Systems with Randomly Varying Communication Delays. *ISA transactions*, 69,65–88.
9. **El-Farra N., Mhaskar P.** (2008), Special issue on 'Control of Networked and Complex Process Systems'. *Comput. Chem. Eng.*, 32(9), 1963–1963.
10. **Hajare V., Khandekar A., Patre B.** (2017), Discrete Sliding Mode Controller with Reaching Phase Elimination for TITO Systems. *ISA Transactions*, 66, 32–45. doi:10.1016/j.isatra.2016.10.010.
11. **Hajare V., Patre B. (**2015), Decentralized PID Controller for TITO Systems Using Characteristic Ratio Assignment with An Experimental Application. *ISA transactions*, 59, 385–97.
12. **Hamdy M., Ramadan A., Abozalam B.** (2018), Comparative Study Of Different Decoupling Schemes for TITO Binary Distillation Column via PI Controller. IEEE/CAA Journal of Automatica Sinica, 5(4), 869–877. doi:10.1109/JAS.2016.7510040.
13. **Hazarika S., Chidambaram M. (**2014), Design of Proportional Integral Controllers with Decouplers for Unstable Two Input Two Output Systems. *Industrial & Engineering Chemistry Research*, 53(15), 6467–6476. doi:10.1021/ie403791q.
14. **Heris P.C., Saadatizadeh Z., Babaei E.** (2019), A New Two Input-Single Output High Voltage Gain Converter with Ripple-Free Input Currents and Reduced Voltage on Semiconductors. *IEEE Transactions on Power Electronics*, 34(8), 7693–7702. doi:10.1109/TPEL.2018.2880493.
15. **Hong L., Hongye S., Peng S., Zhan S., Zheng-Guang W.** (2017), *Estimation and Control for Networked Systems with Packet Losses without Acknowledgement*. Springer, Cham. Switzerland. doi:10.1007/978-3-319-44212-9.
16. **Huang D., Nguang S.** (2009), Dynamic Output Feed-Back Control for Uncertain Networked Control Systems with Random Network-Induced Delays. *Int. J. Control Autom. Syst.*, 7(841), doi:10.1007/s12555-009-0517-9.
17. **Jeng J., Jian Y.** (2017), Model-Free Simultaneous Design of Multiloop PID Controllers for TITO Interactive Processes with Time Delays. In *2017 56th Annual Conference of the Society of Instrument and Control Engineers of Japan (SICE)*, 1033–1038. doi:10.23919/SICE.2017.8105580.
18. **Jin Q., Zhu L., Wang Q., Jiang, B.** (2016), PI Controller Design for A TITO System Based on Delay Compensated Structure and Direct Synthesis. *Canadian Journal of Chemical Engineering*, 94(9), 1740–1754. doi:10.1002/cjce.22551.
19. **Jin Y., Kwak D., Kim K.J., Kwak K.S.** (2014), Cyclic Prefixed Single Carrier Transmission in Intra-Vehicle Wireless Sensor Networked Control Systems.In*2014 IEEE 79th Vehicular Technology Conference (VTC Spring)*,1–5.
20. **Khandekar A., Patre B.** (2017), Decentralized Discrete Sliding Mode Controller for TITO Processes with Time Delay with Experimental Application. *International Journal of Dynamics and Control*, 5, 614—-628. doi:10.1007/s40435-015-0202-1.
21. **Koo J., Ha D., Park D., Roh H.J., Ryu S., Kim G.H., Baek K.H., Han C.** (2017), Design of Optical Emission Spectroscopy Based Plasma Parameter Controller for Real-Time Advanced Equipment Control. *Computers Chemical Engineering*, 100, 38–47. doi:10.1016/j.compchemeng.2017.02.009.
22. **Li B., Wu J., Huang L.** (2016), Improved H∞ Control for Networked Control Systems with Network-Induced Delay and Packet Dropout. *J. Cent. South Univ.*, 23(5), 1215–1223.

DOI 10.2478/ama-2021-0026

23. **Li D.Z., He X., Song T.H., Jin, Q.** (2019), Fractional Order IMC Controller Design for Two-Input-Two-Output Fractional Order System. *International Journal of Control, Automation and Systems*, 17. doi:10.1007/s12555-018-0129-3.
24. **Liu B., Liu Y.** (2020), Mixed Event-Triggered Mechanism Modeling and Controlling for Networked Control Systems with Time-Varying Delays and Uncertainties. *ASIAN JOURNAL OF CONTROL*, 22(2), 803–817.
25. **Liu T., Zhang W., Gu, D. (**2006), Analytical Design of Decoupling Internal Model Control (IMC) Scheme for Two-Input Two-Output (TITO) Processes with Time Delays. *Industrial Engineering Chemistry Research*, 45, 3149–3160. doi:10.1021/ie051129q.
26. **Liu Y.C.** (2015), Robust Synchronization of Networked Lagrangian Systems and its Applications to Multi-robot Teleoperation. *IET Control Theory & Applications*, 9(1),129–139.
27. **Maghade D. Patre B.M.** (2013), Pole Placement by PID Controllers to Achieve Time Domain Specifications for TITO Systems. *Transactions of the Institute of Measurement and Control*, 36, 506–522. doi:10.1177/0142331213508803.
28. **Mahapatro S.R. Subudhi B.** (2020), A Robust Decentralized PID Controller Based on Complementary Sensitivity Function for a Multivariable System. *IEEE Transactions on Circuits and Systems II: Express Briefs*, 67(10), 2024–2028. doi:10.1109/TCSII.2019.2943382.
29. **Mikhailov A. (**1938), Method of Harmonic Analysis in Control Theory. (in russian), A Vlomatiku 2., i Telemechllnika, 3, 27-81.
30. **Mohamed Vall O.M** (2020a), Artificial Neural Network-Based Smith Predictor for Compensating Random Time Delays Acting in Networked Control Systems. *International Journal of Control and Automation*, 13(1), 36–44.
31. **Mohamed Vall O.M** (2020b), PI Controller Design for Networked Control Systems with Random Time Delay. *International Journal of Emerging Trends in Engineering Research*,8(1),114–118. doi:10.30534/ijeter/2020/15812020.
32. **Naik R.H., Kumar D., Sujatha P. (**2020), Independent Controller Design for MIMO Processes Based on Extended Simplified Decoupler and Equivalent Transfer Function. *Ain Shams EngineeringJournal*, 11, 343–350.
33. **Pang Z., Liu G., Zhou D., Sun D. (**2016), Data-Based Predictive Control for Networked Nonlinear Systems with Network-Induced Delay and Packet Dropout. *IEEE Transactions on Industrial Electronics*, 63(2), 1249–1257.doi:10.1109/TIE.2015.2497206.
34. **Park P. (2015),** Power Controlled Fair Access Protocol for Wireless Networked Control Systems. *Wireless Networks*, 21, 1499–1516.
35. **Park P., Khadilkar H., Balakrishnan H., Tomlin C.J.** (2014), High Confidence Networked Control for Next Generation Air Transportation Systems. *IEEE Transactions on Automatic Control*, 59(12), 3357–3372. doi:10.1109/TAC.2014.2352011.
36. **Qian G., Wei P., Ruan Z., Lu J.Q.** (2017), A Low-Complexity Modulation Classification Algorithm for MIMO–OSTBC System. *Circuits, Systems, and Signal Processing*, 36. doi:10.1007/s00034-016-0428-y.
37. **Sharma A., Padhy P.** (2017), Design and Implementation of PID Controller for The Decoupled Two In-Put Two Output Control Process. In *2017 4th International Conference on Power, Control Embedded Systems (ICPCES)*, 1–6. doi:10.1109/ICPCES.2017.8117666.
38. **Siljak D.** (1966), Generalization of the Parameter Plane Method. IEEE Transactions on Automatic Control, 11(1), 63–70. doi:10.1109/TAC.1966.1098230.
39. **Sun Y., El-Farra N.** (2012), Resource Aware Quasi-Decentralized Control of Networked Process Systems over Wireless Sensor Networks. *Chemical Engineering Science*, 69(1),93–106. doi: https://doi.org/10.1016/j.ces.2011.10.010.
40. **Tanaka Y., Ogata T., Imagawa, S.** (2015), Decoupled Direct Tracking Control System Based on Use of A Virtual Track for Multilayer Disk with A Separate Guide Layer. *Japan Society of Applied Physics*, 54(9), 09MB03.
41. **Ustoglu I., Eren Y., Soylemez, M.** (2016), Stabilizing Constant Controllers for Two-Input, Two-Output Systems with Reducible and Irreducible Characteristic Equations. *Transactions of the Institute of Measurement and Control*, 39. doi:10.1177/0142331216645649.
42. **Vargas F., Silva E., Chen J.** (2013), Stabilization of Two-Input Two-Output Systems over SNR-Constrained Channels. *Automatica*, 49, 3133–3140. doi:10.1016/j.automatica.2013.07.031.
43. **Wang Q., Huang B., Guo X.** (2000), Auto-Tuning of TITO Decoupling Controllers from Step Tests. *ISA Transactions*, 39(4), 407–418.
44. **Wang Y.J. (**2011), Graphical Computation of Gain and Phase Margin Specifications-Oriented Robust PID Controllers for Uncertain Systems With Time-Varying Delay. Journal of Process Control, 21(4), 475–488.
45. **Yao W., Jiang L., Wu J.W.Q., Cheng S.** (2015), Wide-Area Damping Controller for Power System Inter-Area Oscillations: A Networked Predictive Control Approach. *IEEE Transactions on Control Systems Technology*, 23(1), 27–36. doi:10.1109/TCST.2014.2311852.
46. **Zhang W., Branicky M., Phillips S.** (2001), Stability of Networked Control Systems. *IEEE Control Systems Magazine*, 21(1), 84–99. doi:10.1109/37.898794.
47. **Zhang X., Zheng Y., Lu G.** (2006), Stochastic Stability of Networked Control Systems with Network-Induced Delay and Data Dropout. In *Proceedings of the45th IEEE Conference on Decision and Control*, 5006–5011. doi:10.1109/CDC.2006.376970.
48. **Zhuang M., Atherton D.P. (**1993), PID Controller Design for A TITO System. In *1993 American Control Conference*, 3176–3177. doi:10.23919/ACC.1993.4793493.

Ould Mohamed Mohamed Vall: https://orcid.org/0000-0002-2701-0140

sciendo

DOI 10.2478/ama-2021-0027 acta mechanica et automatica, vol.15 no.4 (2021)

GENERALISED REGRESSION NEURAL NETWORK (GRNN) ARCHITECTURE-BASED MOTION PLANNING AND CONTROL OF AN E-PUCK ROBOT IN V-REP SOFTWARE PLATFORM

Vikas Singh PANWAR*, Anish PANDEY*, Muhammad Ehtesham HASAN*

*School of Mechanical Engineering, KIIT Deemed to be University, An Institute of Eminence, Patia, Bhubaneswar, PIN - 751024, Odisha, India

vikas09panwar@gmail.com, anish06353@gmail.com, hasan.adab@gmail.com

received 1 June 2020, revised 21 August 2021, accepted 31 August 2021

Abstract: This article focuses on the motion planning and control of an automated differential-driven two-wheeled E-puck robot using Generalized Regression Neural Network (GRNN) architecture in the Virtual Robot Experimentation Platform (V-REP) software platform among scattered obstacles. The main advantage of this GRNN over the feedforward neural network is that it provides accurate results in a short period with minimal error. First, the designed GRNN architecture receives real-time obstacle information from the Infra-Red (IR) sensors of an E-puck robot. According to IR sensor data interpretation, this architecture sends the left and right wheel velocities command to the E-puck robot in the V-REP software platform. In the present study, the GRNN architecture includes the MIMO system, i.e., multiple inputs (IR sensors data) and multiple outputs (left and right wheel velocities). The three-dimensional (3D) motion and orientation results of the GRNN architecture-controlled E-puck robot are carried out in the V-REP software platform among scattered and wall-type obstacles. Further on, compared with the feedforward neural network, the proposed GRNN architecture obtains better navigation path length with minimum error results.

Key words: e-puck robot, generalised regression neural network architecture, virtual robot experimentation platform software, scattered obstacle, Infra-Red sensor

1. INTRODUCTION

Research on wheeled robotics can be categorised into two types: navigation control and stability control. For navigation control, we mainly focus on the kinematic part and control the displacement, velocity and acceleration of a wheeled robot. Similarly, we consider the dynamic part of a wheeled robot and apply force to generate torque to achieve stability control over a robot. The researchers use various soft-computing methods like Fuzzy, Neural Network, Neuro-fuzzy, nature-inspired algorithms, and evolutionary algorithms for navigation and stability control. The meaning of navigation control of a wheeled robot is to search a collision-free optimal path from the starting location to the target among obstacles in the workspace. Obstacle avoidance and wall following problems come under navigation control, and the trajectory tracking problem is solved by using stability control torque equations. The authors Elmi and Efe (2020) implemented a grasshopper algorithm to control the motion of a wheeled robot between static and dynamic hurdles. However, the authors present only computer simulations, and real-time experiments on an experimental wheeled robot have not been found. Long et al. (2020) designed the hybridisation of A* algorithm with a bacterial foraging optimisation algorithm, and present the global path planning for an unmanned surface vehicle in a grid map environment.

Ben Jabeur and Seddik (2020) developed an optimised PID neural network with a hybrid fuzzy controller for trajectory tracking and motion control of a two-wheeled mobile robot in unknown and complex environments. Although the 3D experiments of a two-wheeled mobile robot were not carried out in that work, further research in this direction continues. Another work relevant for mention here would be that by Protik et al. (2019), where the authors apply chemical reaction optimisation algorithms with Euclidean-based fitness functions to determine an optimal motion and orientation control for a wheeled robot among uneven obstacles. In Zhao et al. (2020), the authors designed a genetic algorithm optimised type-2 fuzzy controller and implemented this developed controller to minimise the locomotion of a wheeled robot from a start point to the target between scattered obstacles. Pandey et al. (2019) applied an adaptive neuro-fuzzy inference system to perform an autonomous motion between static and dynamic obstacles for a wheeled robot. Multilayer perceptron feedforward neural network (Singh and Thongam, 2018; Pandey and Parhi, 2016) had been implemented for wheeled robot navigation in the computer simulation environment between static and moving objects. Hadi and Younus (2020) designed the path tracking control architecture for a nonholonomic wheeled robot. Moreover, the authors briefly explain the kinematic and dynamic models of a wheeled robot in MATLAB graphical user interface environments. An extensive review article on the navigation of swarm robotics and their various control methods was reported in the reference (Osaba et al., 2019; Nedjah and Junior, 2019).

Grid-map-based navigation and collision avoidance scheme for a wheeled robot were presented by Tripathy et al. (2021). In their work, different grid size environments are considered to show the motion results among obstacles. However, they did not show any real-time 3D navigation results in that work. Narasimhan and Bettyjane (2020) implemented the fuzzy rule-based architecture to design a local path planner for two co-operating wheeled robots in an unstructured environment. Wang (2021) used Genetic Algorithm (GA) to minimise the navigation path length of a wheeled robot in MATLAB software-based grid-map environments. As we know, the convergence rate of the GA is high, and that is why it takes more time to reach the goal from the source point. Almeida et al. (2021) study deep neural network-controlled visual landmarks-based motion planning for a differential-driven automated guided vehicle. The authors of Quan et al. (2021) applied harmony search algorithm and Morphin algorithm for a global path planning of an autonomous mobile robot between moving obstacle conditions. However, only two-dimensional (2D) simulation results were presented in that work. Teli and Wani (2021) designed the hybrid controller by taking the fuzzy method with an artificial potential field method and implemented this controller to steer a wheeled robot autonomously between C and H types of complicated obstacle conditions. Proportional–Integral–Derivative (PID) controller has been used in a study (Khan et al., 2021) for the speed control of both DC motors of a wheeled robot during its navigation and obstacle avoidance behaviours.

The application of different soft-computing methods like grasshopper algorithm (Elmi and Efe, 2020), bacterial foraging optimisation algorithm (Long et al., 2020), chemical reaction optimisation algorithm (Protik et al., 2019), genetic algorithm (Zhao et al., 2020), adaptive neuro-fuzzy inference system (Pandey et al., 2019) and feedforward neural network (Ben Jabeur and Seddik, 2020; Singh and Thongam, 2018; Pandey et al., 2019) in a wheeled robot motion planning problem motivates the authors to undertake the present research. After summarising the above-cited elements in the literature, we have observed that most of the researchers (Ben Jabeur and Seddik, 2020; Singh and Thongam, 2018; Pandey and Parhi, 2016; Almeida et al., 2021) have used feedforward or backpropagation neural network to control the motion and orientation of a wheeled robot among obstacles in various scenarios. Moreover, we have found that the GRNN provides accurate results in a short period with minimal error compared to other neural networks like feedforward or backpropagation neural networks (Specht, 1991). This strength of the GRNN attracts the authors to select this method in the current work. Therefore, in this study, the authors choose GRNN architecture to control the motion of an E-puck robot among scattered and wall-type obstacles. Further on, compared with the feedforward neural network (Singh and Thongam, 2018), the proposed GRNN architecture obtains better navigation path length with minimum path error. The contributions of this work are presented as follows: - Section 2 presents the kinematic study of an automated differential-driven two-wheeled E-puck robot. Section 3 provides the design of a GRNN architecture for motion and orientation planning and control of an E-puck robot among scattered and wall-type obstacles in the V-REP software environment. The outcomes of the experiments and comparative analysis are organised and elaborated in Section 4. Finally, the conclusion and future research work of the present work are summarised in Section 5.

2. KINEMATIC STUDY OF AN AUTOMATED DIFFERENTIAL-DRIVEN TWO-WHEELED E-PUCK ROBOT

This section derives the kinematic equations for an automated differential-driven two-wheeled E-puck robot, which control the motion and orientation of an E-puck robot during navigation among scattered obstacle in the V-REP software platform. Fig. 1 illustrates the schematic representation of kinematic parts of an automated differential-driven two-wheeled E-puck robot in the two-dimensional rigid plane. The E-puck robot is a differential-driven two-wheeled mobile robot developed by École Polytechnique Fédérale de Lausanne. The diameter of the E-puck robot is 7 cm, 5 cm height with the wheel diameter of 4 cm; and the total weight of the DDER is 0.16 kg. The E-puck robot can move in the forward and backward directions; and it can turn with a top speed of 0.15 m/s. It includes eight IR sensors with eight LEDs. IR sensors of the E-puck robot can read the obstacles between 0.01 m to 0.06 m range approximately. Fig. 2 shows the top view of the E-puck robot with the distribution of the eight IR sensors from S_0 to S_8. The following IR sensors readings: S_0, S_1, S_6, and S_7 are used during motion and orientation controls in the present study. The front senor obstacle reading (D_f) takes the minimum data of S_0 and S_7. Similarly, the left senor obstacle reading (D_l) is the least value of S_6 and S_7. Next, we use the minimum data of S_0 and S_1 as a right senor obstacle reading (D_r). The data of D_f, D_l, and D_r, along with left and right wheel velocities, are used in the GRNN architecture to control the motion and orientation of an E-puck robot.

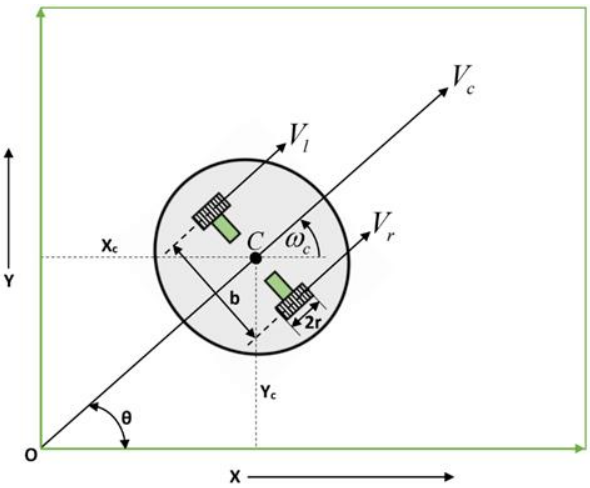

Fig. 1. Schematic representation of kinematic parts of an automated differential-driven two-wheeled E-puck robot in the two-dimensional rigid plane

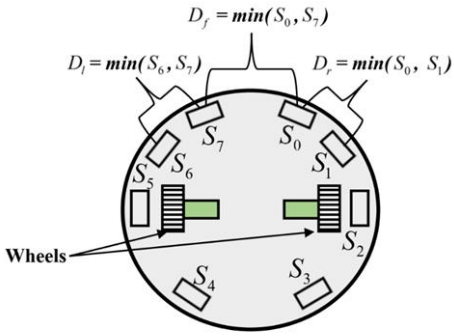

Fig. 2. Top view of an E-puck robot with the distribution of eight IR sensors

Further on, the E-puck robot consists of two independent driving wheels that carry the mechanical chassis of a robot. The two driving wheels attached with the two separate stepper motors drive the E-puck robot. The V_L denotes the left wheel velocity, and

V_R indicates the right wheel velocity in the kinematic equations. The E-puck robot moves in the solid plane, and a rigid chassis makes it. The axes (x_c, y_c) are the current posture of the E-puck robot from the origin O point in the global frame $\{O, X, Y\}$. In Fig. 1, θ denotes the orientation angle of the E-puck robot with respect to an axis (O, X), b is the track width between the left and right wheel drive systems, r is the radius of the driving wheels and C is the center of the mass of E-puck robot system. The following kinematic equations control the velocities and steering angle of the E-puck robot: -

$$V_c = \frac{r}{2} \cdot (\omega_R + \omega_L) = \frac{(V_R + V_L)}{2} \tag{1}$$

$$\omega_c = \dot{\theta} = \frac{r}{2} \cdot (\omega_R - \omega_L) = \frac{(V_R - V_L)}{b} \tag{2}$$

where V_c and ω_c represent the center (mean) linear velocity and center angular velocity of the E-puck robot, respectively, these V_c and ω_c control the motion and orientation of the E-puck robot in the V-REP software platform, respectively. Next, ω_R and ω_L denote the angular velocities of the right and left wheel driving systems, respectively.

Next, the following equations express the velocity (linear and angular) with respect to time (t): -

$$\frac{dx}{dt} = \dot{x}(t) = V_c \cdot \cos\theta = \frac{r}{2} \cdot (\omega_R + \omega_L) \cdot \cos\theta \tag{3}$$

$$\frac{dy}{dt} = \dot{y}(t) = V_c \cdot \sin\theta = \frac{r}{2} \cdot (\omega_R + \omega_L) \cdot \sin\theta \tag{4}$$

$$\frac{d\theta}{dt} = \dot{\theta}(t) = \omega_c = \frac{r}{b} \cdot (\omega_R - \omega_L) \tag{5}$$

3. DESIGN OF A GRNN ARCHITECTURE FOR MOTION AND ORIENTATION PLANNING AND CONTROL OF AN E-PUCK ROBOT AMONG SCATTERED OBSTACLES IN THE V-REP SOFTWARE ENVIRONMENT

This section reveals a brief description of a GRNN architecture that controls the motion and orientation of an E-puck robot among scattered obstacles in the V-REP software platform. GRNN belongs to the family of the Statistical Neural Network (SNN) group, and the rest of this GRNN, the Radial Basis Function Neural Network and Probabilistic Neural Network are also the members of this SNN group. GRNN works based on the regression method, which was developed by Specht in 1991. The main advantage of this GRNN over the feedforward neural network is that it does not need an iterative-based training procedure (Specht, 1991). GRNN makes a linear or non-linear regression function between dependent variables (outputs) and independent variables (inputs) to provide the expected outcome. In the present work, the GRNN architecture takes the IR sensors data information as three inputs (D_f, D_l, and D_r) and wheel velocities (V_L and V_R) as two outputs of an E-puck robot. Tab. 1 reveals the inputs and outputs data set, which are fed into the GRNN architecture to control the motion and orientation of an E-puck robot in the V-REP software platform among scattered obstacles. The ranges of inputs (D_f, D_l, and D_r) have taken from IR sensor range of an E-puck robot, and the ranges of outputs (V_L and V_R) are fixed between 0.063 m/sec to 0.150 m/sec. Fig. 3 shows the basic structure of the MIMO system GRNN architecture, which combines different layers. The GRNN architecture consists of four layers: an input layer, pattern layer, summation layer, and output layer. As shown in Fig. 3, the input layers connect the second pattern layer through the weight of the pattern layer (w_p). Similarly, each pattern layer is connected to the summation layer through the weight of the summation layer (w_s). The summation layer can be divided into the D-summation and S-summation neurons. The different steps of the GRNN architecture can be represented as follows:

$$G\left|\frac{v}{u}\right| = \frac{\int_{-\infty}^{\infty} v \cdot f(u,v)dy}{\int_{-\infty}^{\infty} f(u,v)dy} \tag{6}$$

Eq. (6) expresses the regression equation of the dependent variable (v) on the independent variable (u). In Eq. (6), $u = [u_1, u_1, \dots, u_n]^T$ denotes the number of inputs, and $v = [v_1, v_1, \dots, v_j]^T$ represents the number of outputs. Next, the function $f(u, v)$ calculates the probability density for u and v.

Tab. 1. Inputs and outputs data set for GRNN architecture

D_f in meter	D_l in meter	D_r in meter	V_R in meter/second	V_L in meter/second
0.01	0.024	0.01	0.075125	0.062125
0.024	0.01	0.01	0.075125	0.0775
0.01	0.01	0.024	0.0639	0.0775
0.016	0.032	0.012	0.097875	0.071625
0.032	0.016	0.012	0.097875	0.096375
0.012	0.016	0.032	0.067875	0.099
0.032	0.012	0.016	0.092625	0.101625
0.032	0.032	0.032	0.098125	0.11025
0.048	0.024	0.036	0.100375	0.124875
0.024	0.048	0.036	0.100375	0.110375
0.036	0.024	0.048	0.08225	0.12875
0.014	0.022	0.03	0.0735	0.09625
0.03	0.014	0.022	0.085375	0.102875
0.022	0.03	0.014	0.098625	0.07775

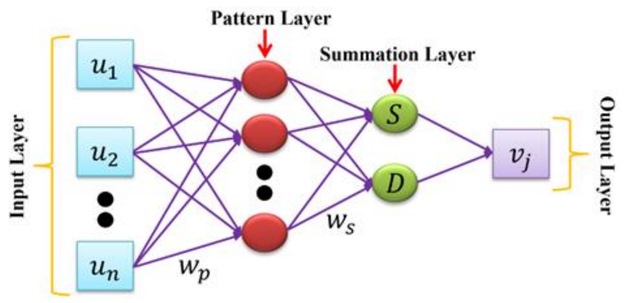

Fig. 3. The basic structure of the MIMO system GRNN architecture

The input layer collects the information from inputs (u) and stores this information. After getting inputs, the number of neurons is allotted to each input. Next, the input neurons of the input layers are sent to the pattern layer. The pattern layer uses a Gaussian function (φ_i) as follows: -

$$\varphi_i = exp\left\{-\frac{(u-U_i)^T(u-U_i)}{2\sigma^2}\right\} \tag{7}$$

where i = 1, 2,…,n; and σ represents the width or spread notation, which adjusts the value of final network outputs, the

DOI 10.2478/ama-2021-0027

present study takes σ = 1. U_i is the training vector of the i^{th} neuron in the pattern layer. In the fourth layer (final layer), the following function calculates the final outputs (v_i) of GRNN architecture:

$$v_i = \frac{\sum_{i=1}^{n} w_i \cdot \varphi_i}{\sum_{i=1}^{n} \varphi_i} \tag{8}$$

where w_i makes the weight connection between the i^{th} neuron of the pattern layer and summation layer node.

4. EXPERIMENTAL RESULTS OF AN E-PUCK ROBOT AMONG THREE-DIMENSIONAL SCATTERED OBSTACLES AND COMPARISON WITH FEEDFORWARD NEURAL NETWORK (SINGH AND THONGAM, 2018) IN THE TWO-DIMENSIONAL PLATFORM

This section reveals the motion and orientation results of GRNN architecture-controlled E-puck robot in the three-dimensional (3D) V-REP software platform among scattered obstacles. Also, the feedforward neural network (Singh and Thongam, 2018) is selected for comparison in the 2D platform. The 3D simulation environments with an E-puck robot and scattered obstacles are built in the V-REP software. The GRNN architecture with inputs and outputs data set and the kinematic equation are scripted in the MATLAB programming language. The remote Application Program Interface (API) function makes an interface between the MATLAB and V-REP software. After interfacing, we run the MATLAB script, and simultaneously we start the simulation in V-REP software. The script sends the motion control command to the E-puck robot in the 3D V-REP software platform, and the GRNN architecture gives the right, and left wheel velocities command to the E-puck robot according to the front, left, and right IR sensor readings. Fig. 4 illustrates the snapshot of an automated differential-driven two-wheeled E-puck robot that performs the experiments in the 3D V-REP software platform among scattered obstacles.

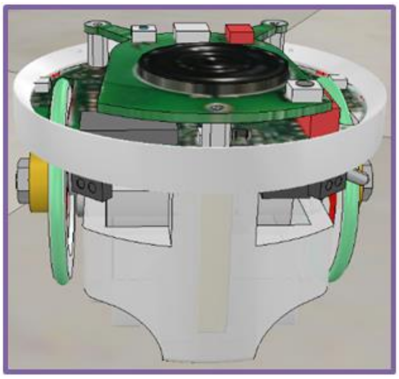

Fig. 4. Automated differential-driven two-wheeled E-puck robot

Further on, Fig. 5 reveals the 3D motion control results of an E-puck robot among scattered obstacles in the V-REP software platform using a GRNN architecture. The axis size is taken 230 × 230 cm^2 in Fig. 5. Next, the E-puck robot begins the motion from (210 cm, 10 cm) and reaches the target location, placed at the left corner (10 cm, 210 cm). Five green color cuboids and four yellow color cylindrical obstacles are randomly placed in the software platform to test the performance of the GRNN architecture in an E-puck robot. At first, the E-puck robot goes to reach the target, and after moving some distance, the E-puck robot finds obstacles within the specified sensory range. Then GRNN architecture is activated and sends the left and right wheel velocity control command to E-puck robot to avoid the obstacles. Fig. 8 shows the real-time recorded angular velocities (degree/seconds) of a right wheel (magenta color) and left wheel (cyan color) of an E-puck robot during motion control in the V-REP software platform of Fig. 5.

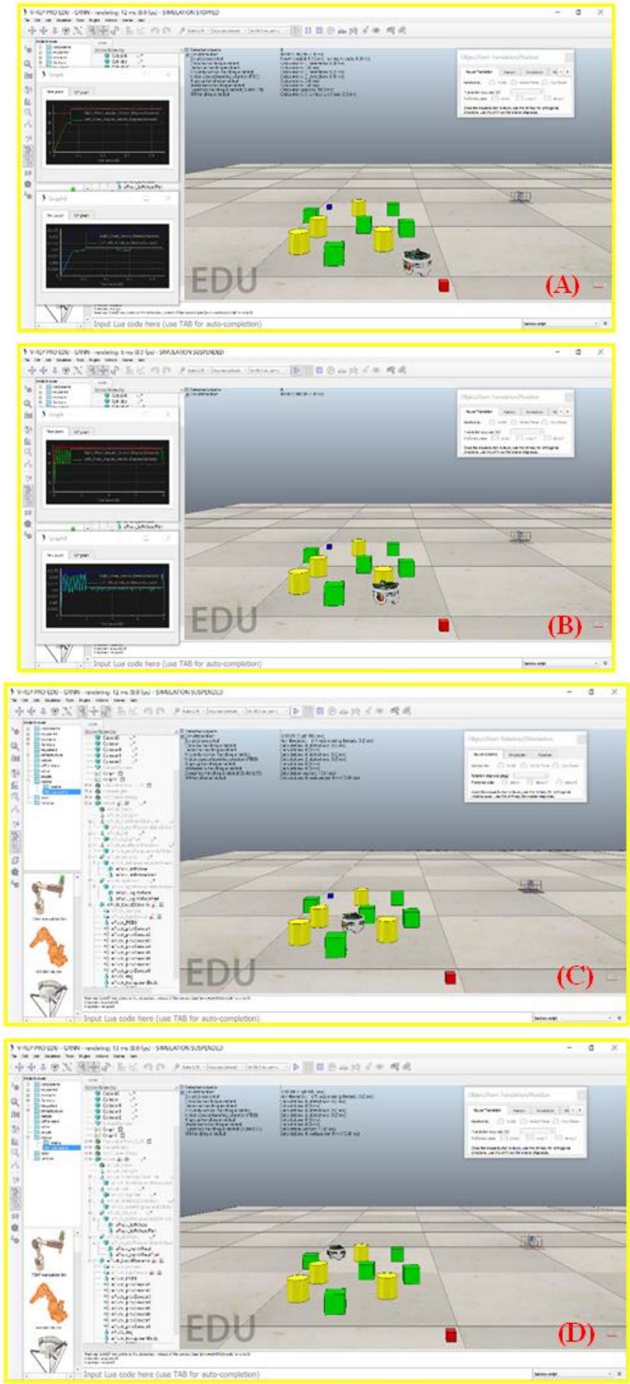

Fig. 5. 3D motion control results of an E-puck robot among scattered obstacles in the V-REP software platform using a GRNN architecture

DOI 10.2478/ama-2021-0027

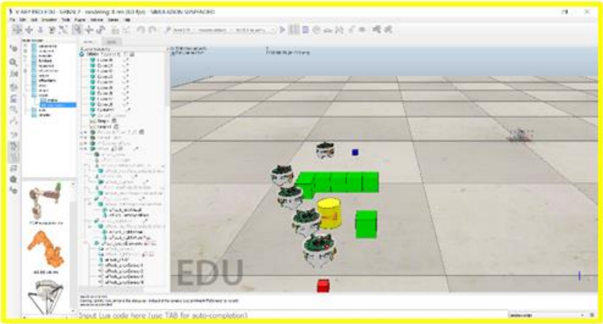

Fig. 6. 3D motion control results of an E-puck robot among wall-typeobstacles in the V-REP software platform using a GRNN architecture

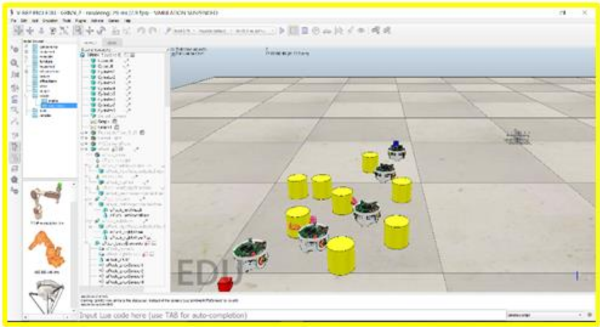

Fig. 7. 3D motion control results of an E-puck robot among many cylindrical shape obstacles in the V-REP software platform using a GRNN architecture

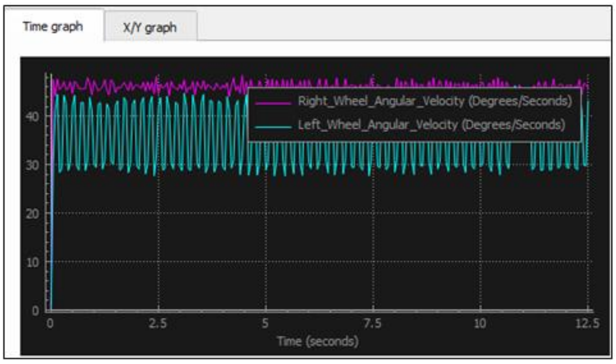

Fig. 8. Real-time recorded angular velocities (degree/seconds) of a right wheel (magenta color) and left wheel (cyan color) of an E-puck robot during motion control in the V-REP software platform of Fig. 5

Similarly, Fig. 9 displays the real-time recorded linear velocities (m/s) of a right wheel (yellow color) and left wheel (blue color) of an E-puck robot during motion control in the V-REP software platform of Fig. 5. As we can see in Fig. 5, the target (blue color small cuboid) is placed at the left corner, and that is why, most of the time, the E-puck robot takes a left turn to reach the goal. It means that the GRNN architecture increases the angular and linear velocity of the right wheel compared to the left wheel, as shown in Figs. 8 and 9, respectively. The E-puck robot covers 130 cm distance to reach the target from the starting location between scattered obstacles and takes 35 s. Figs. 6 and 7 show the motion control results of an E-puck robot among wall-type and many cylindrical shape obstacles in the V-REP software platform using a GRNN architecture, respectively. Further on, these figures present the different positions of an E-puck robot during navigation and obstacle avoidance in a single-single snapshot. The axis size is taken 230 × 230 cm^2 in both Figs. 6 and 7. In Fig. 6, the robot starts moving from (100 cm, 25 cm) and reaches the target location, placed at the coordinate (120 cm, 200 cm). Similarly, in Fig. 7, the robot begins motion from (20 cm, 20 cm) and reaches the target, located at the coordinate (210 cm, 210 cm). In both these figures, it can be seen that after moving some distance, the sensors of the robot detect the obstacles. Then, the GRNN architecture is activated and provides the left and right wheel velocity control command to the E-puck robot to avoid wall-type and many cylindrically shaped obstacles and reach the target successfully without any collision.

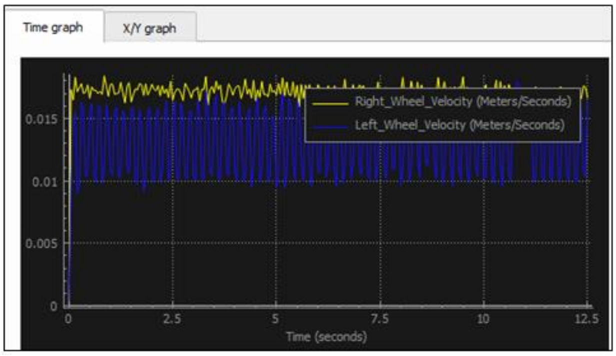

Fig. 9. Real-time recorded linear velocities (meter/seconds) of a right wheel (yellow color) and left wheel (blue color) of an E-puck robot during motion control in the V-REP software platform of Fig. 5

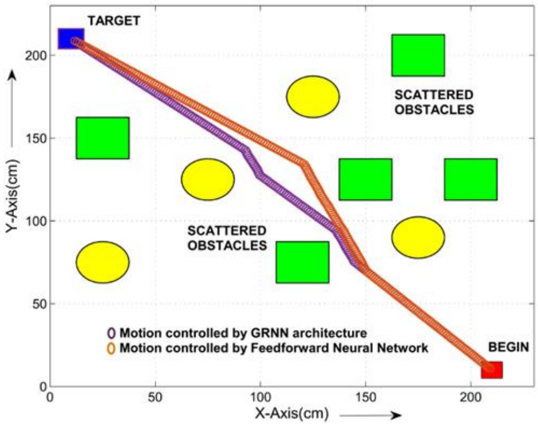

Fig. 10. 2D motion planning and control comparison result between proposed GRNN architecture and feedforward neural network (Singh and Thongam, 2018) among scattered obstacles in the same platform

After obtaining the 3D motion-control results of an E-puck robot, we perform the comparative study between the proposed GRNN architecture and previously developed feedforward neural network (Singh and Thongam, 2018) in the same 2D platform. Fig. 10 reveals the 2D motion planning and control comparison result between the proposed GRNN architecture and feedforward neural network (Singh and Thongam, 2018) among scattered obstacles. The purple color trajectory presents the GRNN architecture controlled motion result of an E-puck robot in Figure Fig. 10. Similarly, the red color trajectory shows the navigation result of a feedforward neural network (Singh and Thongam, 2018) driven E-puck robot. As shown in Figure Fig. 8, the GRNN architecture controlled E-puck robot utilises a shorter distance to reach the target compared to the feedforward neural network (Singh and

Thongam, 2018) driven E-puck robot because GRNN provides accurate network output with minimal error (Specht, 1991). Further on, Tab. 2 compares the GRNN architecture and feedforward neural network (Singh and Thongam, 2018) in terms of trajectory path length and time.

Tab. 2. Result comparison between the GRNN architecture feedforward neural network (Singh and Thongam, 2018) in terms of trajectory path length and time

Name of applied method	Figure number	Begin	Target	Trajectory path length (cm)	Trajectory time (seconds)	Trajectory path length error (cm)
GRNN architecture	Fig. 10	(210 cm, 10 cm)	(10 cm, 210 cm)	130 cm	35 s	1.34 cm
Feedforward neural network (Singh and Thongam, 2018)	Fig. 10	(210 cm, 10 cm)	(10 cm, 210 cm)	138 cm	38 s	2.91 cm

5. CONCLUSION AND FUTURE WORK

This article has presented the motion planning and control technique for an E-puck robot by applying GRNN architecture in the V-REP software platform among scattered obstacles. The GRNN architecture receives real-time obstacle information as inputs from the IR sensors of an E-puck robot. According to IR sensor data interpretation, this architecture sends the left and right wheel velocities command as outputs to the E-puck robot during navigation among obstacles. The programming of GRNN architecture and kinematic equations has been written in the MATLAB script. This script controls the motion and orientation of an E-puck robot in the V-REP software platform through the remote-API function. The different 2D and 3D simulation results demonstrate that the GRNN architecture successfully autonomously controls the motion and orientation of an E-puck robot.

Moreover, as compared to the feedforward neural network (Singh and Thongam, 2018), the proposed GRNN architecture has provided better results in a short period with minimal error. Future work can include dynamic scattered obstacles instead of static obstacles. Also, this presented method can be used for motion and orientation control of multiple E-puck robots.

REFERENCES

1. **Almeida T., Santos V., Mozos O. M., Lourenço B.** (2021), Comparative Analysis of Deep Neural Networks for the Detection and Decoding of Data Matrix Landmarks in Cluttered Indoor Environments. *Journal of Intelligent & Robotic Systems*, 103(1), 1-14.
2. **Ben Jabeur C., Seddik H.** (2020), Design of a PID optimized neural networks and PD fuzzy logic controllers for a two-wheeled mobile robot, *Asian Journal of Control*, 22(1), 1–19.
3. **Elmi Z., Efe M. Ö.** (2020), Online path planning of mobile robot using grasshopper algorithm in a dynamic and unknown environment, *Journal of Experimental & Theoretical Artificial Intelligence*, 32, 1–19.
4. **Hadi N. H., Younus K. K.** (2020), Path tracking and backstepping control for a wheeled mobile robot (WMR) in a slipping environment, *IOP Conference Series: Materials Science and Engineering*, 671, 1–17.
5. **Khan H., Khatoon S., Gaur P.** (2021), Comparison of various controller design for the speed control of DC motors used in two wheeled mobile robots. *International Journal of Information Technology*, 13(2), 713-720.
6. **Long Y., Zuo Z., Su Y., Li J., Zhang H.** (2020), An A*-based Bacterial Foraging Optimisation Algorithm for Global Path Planning of Unmanned Surface Vehicles, *The Journal of Navigation*, 73(3), 1–16.
7. **Narasimhan G. E., Bettyjane J.** (2020), Implementation and study of a novel approach to control adaptive cooperative robot using fuzzy rules. *International Jopurnal of Information Technology*, 1–8. https://doi.org/10.1007/s41870-020-00459-z
8. **Nedjah N., Junior L. S.** (2019), Review of methodologies and tasks in swarm robotics towards standardization, *Swarm and Evolutionary Computation*, 50, 1–26.
9. **Osaba E., Del Ser J., Iglesias A., Yang X. S.** (2019), Soft Computing for Swarm Robotics: New Trends and Applications, *Journal of Computational Science*, 39, 1–4.
10. **Pandey A., Kashyap A. K., Parhi D. R., Patle, B. K.** (2019), Autonomous mobile robot navigation between static and dynamic obstacles using multiple ANFIS architecture, *World Journal of Engineering*, 16(2), 275–286.
11. **Pandey A., Parhi D. R.** (2016), New algorithm for behaviour-based mobile robot navigation in cluttered environment using neural network architecture, *World Journal of Engineering*, 13(2), 129–141.
12. **Pandey K. K., Parhi D. R.** (2019), Trajectory Planning and the Target Search by the Mobile Robot in an Environment Using a Behavior-Based Neural Network Approach, *Robotica*, 37(1), 1–15.
13. **Protik P., Das S., Islam M. R.** (2019, October). Chemical Reaction Optimization for Mobile Robot Path Planning. *International Joint Conference on Computational Intelligence, Springer, Singapore*, 191–203.
14. **Quan Y., Ouyang H., Zhang C., Li S., Gao L.** (2021), Mobile Robot Dynamic Path Planning Based on Self-adaptive Harmony Search Algorithm and Morphin Algorithm. *IEEE Access*, 10.1109/ACCESS.2021.3098706
15. **Singh N.H, Thongam K.** (2018), Neural network-based approaches for mobile robot navigation in static and moving obstacles environments, Intelligent Service *Robotics*, 12(1), 55–67.
16. **Specht D. F.** (1991), A general regression neural network. *IEEE transactions on neural networks*, 2(6), 568–576.
17. **Teli T. A., Wani M. A.** (2021), A fuzzy based local minima avoidance path planning in autonomous robots. *International Journal of Information Technology*, 13(1), 33-40.
18. **Tripathy H. K., Mishra S., Thakkar H. K., Rai D.** (2021), CARE: A Collision-Aware Mobile Robot Navigation in Grid Environment using Improved Breadth First Search. *Computers & Electrical Engineering*, 94, 107327.
19. **Wang M.** (2021), Real-time path optimization of mobile robots based on improved genetic algorithm. *Proceedings of the Institution of Mechanical Engineers, Part I: Journal of Systems and Control Engineering*, 235(5), 646-651.
20. **Zhao T., Xiang Y., Dian S., Guo R., Li S.** (2020), Hierarchical interval type-2 fuzzy path planning based on genetic optimization, *Journal of Intelligent & Fuzzy Systems*, 32, 1-12.

Vikas Singh Panwar: https://orcid.org/0000-0001-5874-2945

Anish Pandey: https://orcid.org/0000-0001-9089-3727

DOI 10.2478/ama-2021-0028 acta mechanica et automatica, vol.15 no.4 (2021)

A REVIEW OF COMPRESSED AIR ENGINE IN THE VEHICLE PROPULSION SYSTEM

Michal Korbut*, Dariusz Szpica**

*Doctoral School, Bialystok University of Technology, 45A Wiejska Str., 15-351 Bialystok, Poland
**Faculty of Mechanical Engineering, Bialystok University of Technology, 45C Wiejska Str., 15-351 Bialystok, Poland

m.korbut@doktoranci.pb.edu.pl, d.szpica@pb.edu.pl

received 20 August 2021, revised 6 September 2021, accepted 13 September 2021

Abstract: Engines powered by compressed air as a source of propulsion are known for many years. Nevertheless, this type of drive is not commonly used. The main reason for not using commonly is the problem with the low energy density of the compressed air. They offer a number of advantages, primarily focusing on the possibility of significantly lowering the emissions of the engine. Their emissivity mainly depends on the method of obtaining compressed air. This also has an impact on the economic aspects of the drive. Currently there are only a few, ready to implement, compressed air powered engine solutions available on the market. A major advantage is the ability to convert internal combustion engines to run with compressed air. The study provides a literature review of solutions, focusing on a multifaceted analysis of pneumatic drives. Increasing vehicle approval requirements relating to their emissions performance are encouraging for the search of alternative power sources. This creates an opportunity for the development of unpopular propulsion systems, including pneumatic engines. Analysing the works of some researchers, it is possible to notice a significant increase in the efficiency of the drive, which may contribute to its popularisation.

Key words: emission reduction, drive sources, pneumatic engine, compressed air engine, pneumatic hybrid

1. INTRODUCTION

As a result of a significant decrease of air quality in large cities and the fight against emissions of harmful substances, more and more restrictive and at the same time more difficult to fulfil legislative limits for exhaust emissions are introduced (Bielaczyc and Woodburn, 2019; Kamguia Simeu and Kim, 2018; Pavlovic et al., 2016; Varella et al., 2017). An additional factor contributing to the tightening of the criteria necessary for the approval of vehicles was the detection of fraud done by the automotive companies during the emissivity tests, which directly contributed to the modification of the driving tests (Puškár et al., 2019). The main changes to the approval tests are the introduction of a new exhaust emission test cycle known as Worldwide Harmonized Light Vehicles Test Procedure (WLTP) replacing the cycle New European Driving Cycle (NEDC) and the implementation of the measurement in real traffic real drive test (RDE) (Hooftman et al., 2018; Sileghem et al., 2014). The main differences between the WLTP cycle and the NEDC cycle are the increased measurement duration time, the more than doubled total distance travelled during the test and the higher average velocity (Ligterink et al., 2016). These changes, together with the complementation of laboratory tests with tests in road traffic, contribute to bringing the test results closer to the real-vehicle emissivity. Another step undertaken by the European Commission is the tightening of the limit on the average CO_2 emissions imposed on vehicle manufacturers, from 2020, CO_2 emissions during vehicle approval can be 95 g/km, a 15% reduction by 2025 and a 37.5% reduction by 2030 (García et al., 2020). This forces automotive companies to look for new solutions for reducing the emissions of internal combustion engines (Fig. 1), including the following:

- ATAC (Active Thermo-Atmosphere Combustion) – heating of the fuel and air mixture causing more rapid combustion (Akira and Hideo, 2004; Onishi et al., 1979; Xingcai et al., 2008);
- ACT (Active Cylinder Technology) – system which deactivates the work in cylinders when driving with a constant load (Gosala et al., 2017; Joshi et al., 2017; Lee et al., 2018; Muhamad Said et al., 2014);
- SPCCI (Spark-Controlled Compression Ignition) – compressed mixture ignition controlled by a spark plug (Hannan et al., 2014; Olesky et al., 2014; Robertson and Prucka, 2019; Shuai et al., 2018);
- HCCI/CAI (Homogeneous Charge Compression Ignition/Controlled Auto-ignition) – combustion of a homogeneous mixture (Jeuland et al., 2004; Khandal et al., 2019; Saiteja and Ashok, 2021; Wang et al., 2010);
- RCCI (Reactivity Controlled Compression Ignition) - combustion using mixtures with different chemical activities (Duraisamy et al., 2020; García et al., 2020; Kakaee et al., 2016; Mikulski et al., 2018; Reitz and Duraisamy, 2015);
- TWC (Three-Way Catalytic Converter) – high performance catalytic reactors (Heck and Farrauto, 2001; Keav et al., 2014; Santos and Costa, 2008);
- DPF (Diesel Particulate Filter) – particulate filters for compression ignition engines (Bensaid et al., 2011; Guan et al., 2015; Khair, 2003; Myung et al., 2009);
- GPF (Gasoline Particulate Filter) – particulate filters for spark ignition engines (Joshi and Johnson, 2018; Ko et al., 2019; Lambert et al., 2017; Xia et al., 2017; Yang et al., 2018);
- SCR (Selective Catalytic Reduction) – selective catalytic reduction systems (Forzatti, 2001; Guan et al., 2014; Latha et al., 2019; Li et al., 2011).

DOI 10.2478/ama-2021-0028

Using this type of system causes considerable complications in the construction of the drive unit and further increasing the costs associated with vehicle manufacturing. In the majority of cases, the reduction level of harmful emissions is, however, not fully satisfactory. Another option is the use of alternative propulsion sources. A number of solutions have been developed over the years, including the use of fuels so that the combustion process is less harmful to the environment, the development of hybrid systems combining an internal combustion engine with another source of propulsion, or using only propulsion systems which do not require combustion. Among the fuels enabling to obtain lower emission results, the liquefied petroleum gas (LPG) (Ashok et al., 2015; Beik et al., 2020; Usman et al., 2020) and compressed natural gas (CNG) (Weaver, 1989; Yeh, 2007) should be mentioned as important ones. Conversion of an internal combustion engine to operate with LPG is popular in the case of passenger cars, although this is not favoured in the more complicated design of the engines. (Borawski, 2015; Mitukiewicz et al., 2015; Szpica et al., 2014). CNG gas as a fuel is more commonly applied in commercial vehicles as well as in work machines (Thiruvengadam et al., 2018). Hybrid systems typically use a combination of an internal combustion engine with an electric drive, nowadays the majority of manufacturers offer vehicles with this type of power system (Hannan et al., 2014; Raslavičius et al., 2017). A less common solution combines a combustion engine with a pneumatic or hydraulic drive (http:/www.groupe-psa.com). In this configuration of the system, energy is accumulated in the form of a pressurised fluid. Drive systems use a hydraulic drive combined with an internal combustion engine enable a high potential for emission reduction through braking energy recovery (Baseley et al., 2007; Zhou et al., 2020). In the case of propulsion systems which do not require a combustion process, fully electric cars predominate and considerable emphasis is also being placed on the development of cars powered by fuel cells (Manoharan et al., 2019; Raslavičius et al., 2015). Vehicles powered only by pneumatic propulsion have not gained significant popularity so far.

Fig. 1. Solutions applied by automotive companies to reduce exhaust emissions

The idea of using compressed air to power vehicles is not new, which dates to the middle of the 19th century (Mishra and Sugandh, 2014). Although the first attempts in a new type of propulsion, carried out on a passenger vehicle by French inventors Andraud and Tessie of Motay (Wasbari et al., 2017), were successful, this solution has not gained popularity. Only the tramway powered by compressed air, developed by Ludwik Mekarski, made this type of propulsion more widespread (Thipse, 2008). It had an innovative heating system for the supplying air using a steam heater, which eliminated the problem of freezing of drive train components caused by the expansion of air (https://www.tramwayinfo.com). Initial tests were carried out on the streets of Paris, while in 1879 in the city of Nantes, vehicles powered by compressed air were introduced into the developing tramway network. The new type of public transport grew in popularity, and over the following years the fleet of Mekarski trams expanded to 94 units only in the city of Nantes (https://www.tramwayinfo.com). Similar solutions of tramways, as well as locomotives of other designers, have found applications in many large cities in the world such as London and New York among others. With the intensive development of the urban electricity network in the early 20th century, compressed air tramways were gradually replaced by electrically powered vehicles. However, it did not lead to a complete suspension of the development of rail vehicles powered by compressed air. They were widely used in mines and other places where other types of power supply were not able to work, e.g. in the construction of tunnels. The H. K. Porter Company started to introduce compressed air powered locomotives for use in mines from the end of the 19th century (https://americanindustrialmining.com). By using an engine in which the air was expanded in two stages, the range between refilling the air tanks was significantly increased. For many years, this type of propulsion system had no alternatives in places requiring special working conditions. The first attempts of building a car powered by compressed air engines date to the turn of the 1920s and 1930s. (Wasbari et al., 2017). Some of the engine solutions have been patented (Archer, 1929; Eliot, 1934; Friar and Holdcroft, 1925; Wittig, 1925), but none of them entered into serial production. The reasons for this are due to the dynamic development of combustion engines and the unlimited access to fossil fuels. The interest in the compressed air engine subject revived with the fuel crisis of the 1970s. Again, attempts were made to implement a new type of propulsion system for cars. The inventors have patented several solutions (Brown, 1972; Cestero, 1985; Johnson, 1983; Miller, 1980; Wagner, 1975). In the early 1990s, French engineer Guy Negre, the founder of MDI company, began work on a prototype of a vehicle powered by compressed air. Over the years, MDI has made several prototypes of small vehicles with a range reaching up to 200 km, although serial production has not been undertaken (https://www.mdi.lu). Inventor Angelo Di Pietro has developed a design for an unconventional pneumatic engine which is ready to be implemented in vehicles (https://www.engineair.com.au; Di Pietro, 1999). During the entire period of motor vehicle development, work on compressed air power solutions has been repeatedly revisited. However, it usually did not lead to the initiation of serial production on a mass scale. Following the current trends in emissions reduction, it is possible to forecast the prospect of long-term development of alternative power sources, including pneumatic engines (Shi et al., 2016).

2. PRIMARY ASPECTS OF PNEUMATIC DRIVES

2.1. Ecological Aspects

The compressed air engine concept is a zero-emission drive, the only product of its operation is the air cooled by the expansion process. In fact, similarly to electric drives, it transfers the problem of emissions from the engine itself, to the stage of energy generation. The emissivity of pneumatic drives is mainly dependent on the method of producing compressed air. With the use of energy from renewable sources, it is possible to achieve zero-emission propulsion. This is facilitated by the multitude of solutions for air compression equipment, as well as the types of power supply. The simplest system is powering an electric compressor with energy created by photovoltaic panels or a wind power plant. Similar solutions are used in compressed air energy storage (CAES) systems (Budt et al., 2016; Luo et al., 2014; Wang et al., 2017; Zhou et al., 2019) to store energy using compressed air. The operation of this system is based on the compression of air at a time of low electricity demand and storing it in underground tanks (Lund and Salgi, 2009). At the time of increased electricity consumption, the compressed air powers the generators which produce electricity. These solutions, similarly to pneumatic drives, are still in the developmental stage, their major problems are the temperature changes during compression and expansion processes, and the losses associated with this. Despite these adversities, so far there are already two facilities in the world using this technology (Chen et al., 2016). At the current stage of development, facilities of this type cannot replace other sources of electricity generation and storage, although they can significantly help to relieve them, which would also contribute to reducing the harmful effects of human activity on the environment. A similar situation occurs with pneumatic drives.

Powering the air compressor with an internal combustion engine contributes to increasing the overall emissivity of the pneumatic drive. However, it should be emphasised that the internal combustion engine used to drive the compressor could be operated in a ‘phlegmatic’ drive mode, within a limited range of specific rotational speeds. In such a case, it is possible to optimise the drive system to a high level in terms of emissivity and fuel consumption.

A further important environmental aspect is the materials from which the compressed air engine can be manufactured. As opposed to the internal combustion engine or electric motor, the pneumatic engine during operation does not become warm, instead cooling as a result of air expansion. During long operation, this may lead to the freezing of certain components, in particular the exhaust manifold. The problem can be simply solved by heating the supply air or using a heat exchanger. In comparison to other drive units, it results in a reducing temperature range in which the engine operates, thus the engine design does not require the use of materials with high resistance parameters and sufficient thermal expandability under varying thermal load (Borawski, 2020; Mieczkowski, 2016a; Myagkov et al., 2014). The possibility of using commonly available engineering materials for the design of the propulsion system has a wide-ranging environmental impact. Specialised materials involve the use of admixtures of elements rarely found in the environment, which extraction and processing often requires the consumption of large amounts of energy. The extraction of these raw materials is also associated with irreversible environmental impacts. If the raw material is only found in a few places on earth, an additional factor generating further emissivity arises – transport to the place of further processing (Sen et al., 2019). The use of unconventional materials in design, which require complex technological processes, also contributes to the complication of repairs of components. It often contributes to the fact that the repair of a component is economically unviable. As a result, the operating period of the product is reduced. Used, end-of-life components cannot always be recycled or utilised, and even if they can, the process is not as easy as with typical engineering materials (Harper et al., 2019). This once again results in the generation of pollution. All of this contributes to generating a carbon footprint even before the vehicle is used, which often is not taken into account in assessing the emissions performance of a specific fuel type (Hawkins et al., 2013). Today, the field of materials science is developing at a dynamic rate, and new materials are created with taking into account environmental issues during their design. Nevertheless, engineers still have to make compromises between the selected parameters. For materials with low strength requirements, it is easier to find a substitute in the form of an alternative raw material, which can be partly made of recycled materials.

The other advantage of running in a lower operating temperature range is the lack of need to use viscosity grade oils in the drive unit (Gołębiowski et al., 2019a, 2019b, 2018). The functional properties of oil in pneumatic engines are only limited to lubrication of the cooperating parts and there is no need for oil to dissipate heat from thermally stressed components. For many years, internal combustion engine manufacturers have been trying to extend oil change intervals by using long-life oils. Studies demonstrate that this does not always have a positive effect on the life span of the drive unit (Kral et al., 2014). In a compressed air powered engine, there is no combustion process which mainly causes oil contamination, directly contributing to the degradation of the lubricant. It enables to extend the maintenance interval of the vehicle. According to MDI Company, for the engine designed by them, one litre of vegetable oil allows to use the engine for 25,000 km (https://air-volution.com.au). From an environmental point of view, this is a considerable reduction in the pollutants generated during the production of synthetic oils. In case of leakage from the engine, vegetable oil causes no harmful effects on nature and its eventual release into the groundwater will not pose a threat of pollution of the environment. It also solves the problem of used oil utilisation, which with the current lubricants used in internal combustion engines contributes to environmental degradation.

A similar situation occurs with the cooling system, the compressed air engine does not require a cooling system using a liquid due to the absence of high temperatures. This eliminates the consumption of one of the basic operating fluids, whose production and possible leaks also contribute to environmental damage. Over the lifetime of the vehicle, assuming an average cooling system volume of approximately 7 litres, and a fluid change of the entire system every 2 years, the savings per vehicle will be significant (Hudgens and Bustamante, 1993). Regarding electric vehicles, as a substitute for engine cooling, the problem of maintaining an adequate temperature of the battery pack has to be taken into account. As the temperature decreases, the efficiency of the battery declines, leading to a reduction in the vehicle’s range, whereas excessively high temperatures may lead to overheating dangerously. For this purpose, thermal management system (TMS) systems are created to maintain the specified temperature in the battery unit (Pesaran, 2001; Zhao et al., 2020). Currently there are various TMS solutions in use, some of the most efficient are active systems using a liquid like glycol or gas like refrigerant R134a (Katoch and Eswaramoorthy, 2020; Kim et al., 2019). Despite testing of the use of an environmentally friendly substance for this purpose, the problem is still not solved, and further efforts to improve a vehicle’s range and reduce recharge times may result in the need for active systems (Wu et al., 2019). In comparison to electric and internal combustion engines, pneumat-

DOI 10.2478/ama-2021-0028

ic engines generate zero or minimal environmental impact in this aspect.

Considering the environmental aspects of an air engine, it is important to pay attention not only to the emissivity of the compressed air preparation stage itself, but also to the overall view of the issue. The simplicity of the design and the low strength requirements of the drive unit components contribute to a significantly lower impact on environmental degradation.

2.2. Economic Aspects

The development of pneumatic drives has repeatedly been displaced by other, more promising types of drives. Partly it is due to the economic circumstances characterising the compressed air supply. Pneumatic drives have for years faced problems due to the physical properties of air. Compressed air as an energy carrier has a low energy density, particularly in relation to liquid fuels. A summary of energy densities for currently used vehicle power sources is given in Fig. 2.

It contributes to the demand for a much higher volume of compressed air needed to achieve the same range compared to other propulsion sources. In a study (Creutzig et al., 2009), a comparison of power systems is presented in a city car as an example. The authors conducted the analysis taking into account a number of factors, including the efficiency of each propulsion source. In order to achieve a range of 115 km, the vehicle used for the analysis needed 4 litres of fuel or, equivalently, 780 litres of compressed air. Such a volume requires a significant amount of space in the vehicle for the compressed air tank. An intermediate solution to the problem is the increasing the pressure of the air storage. This raises the problem of the proper design of the tank as well as the losses occurring during the air compression process. Electric vehicles also have an advantage over compressed air power, although the difference with the internal combustion engine is not as pronounced. On comparing the weight of the fuel, the respective weights found to be 4.8 kg for liquid fuel, 53 kg for compressed air and 140.3 kg for electric power. The range of compressed air and electric vehicles is strongly dependent on their total weight, although it should be noted that the weight of the battery does not change with the level of charge. The large weight of the electric battery pack affects the vehicles driveability and worsens its handling, which becomes apparent also during the 'moose' test (Mazumder et al., 2012; Szpica, 2019). Another problem is the losses caused by the change of air temperature when increasing or decreasing its pressure. Compression of air causes an increase in its energy, which in turn increases the temperature of the gas (Zhang et al., 2014). In ideal conditions, the air would have sufficient time to equilibrate the temperature to ambient temperature – the transformation would then be isothermal. In fact, the operation of most compressors has a character closer to an adiabatic conversion, resulting in a higher energy requirement to compress the same amount of air as in an isothermal conversion. Slowdown compression process is not a good solution due to increased vehicle charging time. Another way is to use multistage compressors, in which heat exchangers are used between the individual compression stages to cool the air (Grazzini and Milazzo, 2012; Yang et al., 2013). The air expansion process in the pneumatic engine has an adiabatic character due to its dynamic nature, where air temperature is reduced as a result of the release of energy accumulated in the air. In this case, also the progressive expansion of the air, additionally with heating to equalise the air temperature is beneficial. In practice; this solution consists of first reducing the air pressure from the value at which it is stored in the tank to an intermediate pressure, and then reducing the pressure to the working pressure prevailing in the engine and heating it before performing work.

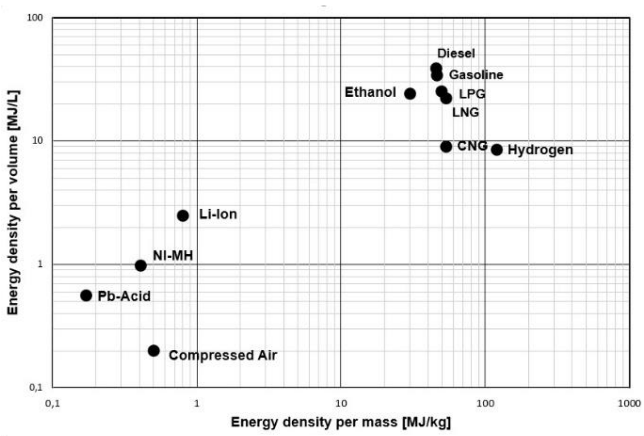

Fig. 2. Summary of energy density parameter for different power sources (Papson et al., 2010)

The economy of pneumatic drives is highly dependent on the achieved efficiency. The designs achieving low efficiency are not only economically unjustifiable, but may also be ultimately environmentally unfriendly as they require significantly more energy in comparison to other propulsion sources. The key to achieving the right efficiency is the appropriate use of available technology to eliminate compression and expansion losses. In addition, compressed air powered engines are not extensively researched, in relation to internal combustion engines or electric drives. There are not many studies dedicated to the evaluation of the impact of power supply conditions on compressed air engine performance. Commercial constructions demonstrate the validity of this type of drive. Developing existing units and new designs can provide measurable benefits in terms of economy.

2.3. Safety Aspects

Until now, official crash test of a vehicle powered by compressed air has not been conducted. In terms of design requirements, the bodywork of such a vehicle does not differ from the currently used solutions. The difference is the presence of a compressed air tank, which has to comply with a number of safety requirements. Compressed air storage in pressure tanks is a well-known, widely used issue. In the case of vehicles, an important element is the proper installation of the tank, ensuring its stable position in the vehicle and protecting it against damage or tearing out. Over the years, the necessary standards and norms have been developed for steel and composite tanks respectively, allowing for safe operation. Inspection of the tanks occurring during the mandatory technical inspection of the vehicle would ensure an appropriate interval for checking the condition of the tank. Legislative standards require an assumed operating lifetime over a minimum of 15 years when calculating the strength of the tank. Regarding LPG gas systems, the approval for the tank is only issued for 10 years, after which the tank must be replaced or renewed, approval for CNG gas the lifetime is 20 years. The warranty period for the battery in currently manufactured electric vehicles is a maximum of 10 years, applicable to only a few manufacturers. However, this does not mean that the battery is no longer usable, although it should be noted that over the years, batteries lose their capacity. This adversely affects the vehicle range, causing more frequent charging, which also contributes to the deterioration of the batteries performance (Hoke et al., 2011). The cost of a new battery pack for an electric car is significantly greater than the replacement of a steel or even composite air tank. Another important element responsible for safety in a vehicle using pneumatic drive is the safety valve. Its operation shall be periodically inspected to ensure that the pressure in the tank cannot rise above the admissible level. If the admissible value is exceeded, which can occur when refilling the compressed air, the valve starts with bleed air until the safe pressure is reached, at which it will automatically close (Crosby Valve Inc., 1997). This solution is much safer than charging the battery of an electric vehicle, which in extreme cases of overcharging can result in a potential fire. Analysing extreme cases of hazards related to the compressed air supply system, attention should be primarily focused on bursting of tanks under high pressure as a result of defects. Compressed air, as opposed to other gases used as propulsion sources, is non-flammable, therefore there is no risk of ignition even if a large volume is released in a short period of time. A real health risk for people in the surroundings is the high sound level during an explosion. To ensure safety, the tank shall be mounted on the vehicle in such a way to minimise the possibility of physical damage to the tank while the vehicle is running. (Thipse, 2008).

2.4. Charging Network for Pneumatic Drives

One of the main problems of developing every vehicle power source is the absence of a charging or refuelling station. In many cases, this is the main reason for the limited popularity of a particular power source and the consequent reduction of its development rate. The expansion of the drive is also strongly influenced by all kinds of taxes relief or other forms of incentives for the development of the necessary infrastructure, a good example of which in recent years is the development of electric drives and the emergence of charging stations (Foley et al., 2010; Morrow et al., 2008). Today, almost every service station has an air compressor, commonly used to pump up a vehicle tyre. The maximum operating pressure of most of the used compressors is only 6 bar, which is below the operating pressure of the pneumatic engine, and definitely lower than the pressure prevailing in the air tanks of the existing prototype vehicles. However, there are devices available to increase the pressure obtained in a compressor, called pressure intensifiers, which could achieve a pressure sufficient to fill the tanks of some of the current prototype designs. This could enable current stations to have a simple and low cost adjustment to power prototype vehicles. Similar solutions could also be applied in other places with compressed air supply infrastructure, such as industrial plants. In the case of pneumatic vehicles, which also allow for the use of the engine as a compressor, an electric vehicle charging station could be used to fill the compressed air tanks. In such a case, an electric engine powered from the charger drives the pneumatic engine. The recharge time then depends on the efficiency of the engine mode of operation as a compressor.

3. COMPRESSED AIR POWERED ENGINES

3.1. MDI Company Engine

The company MDI, founded by engineer Guy Negre, has designed a compressed air piston engine from basic (Thipse, 2008). The engine has pistons with different diameters in an in-line arrangement (Fig. 3). The number of cylinders in the engine has changed over the years as the power unit has developed, but the principle of operation has remained the same.

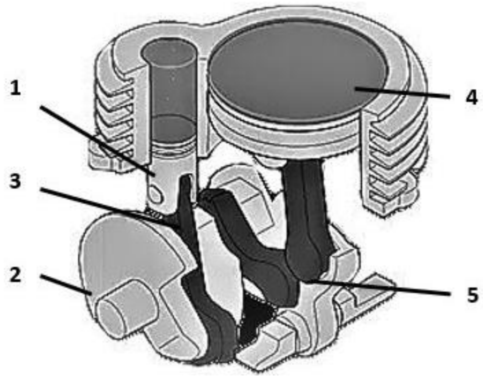

Fig. 3. MDI engine scheme, 1 – piston with smaller diameter, 2 – crankshaft, 3 – connecting rod, 4 – larger piston, 5 - connector, (http://www.thefuture.net.nz)

The piston *(1)*, with a smaller diameter, is connected to the common crankshaft (*2)* by a conventional connecting rod (*3)*. Second, larger piston (*4)* uses an additional connector (*5)*, which changes the kinematics of the piston motion. The purpose of this modification is to lower the piston velocity when approaching the Top Dead Centre (TDC), thus increasing the time of filling the cylinder. Engine operation starts with the opening of a valve, allowing the smaller piston to be supplied with compressed air from the tank. Air at a pressure of 20 bar fills it until it reaches the Bottom Dead Centre (BDC), then the supply valve is closed. The air is pushed into a larger cylinder, however it does not cool excessively due to the small change in pressure. It fills initially the cylinder, then mixes with the supply air from the tank, preheating it, thus improves efficiency. Then both pistons move in order to empty the expanded air. The exhaust system only releases low-temperature air. The engine also features an air heating mode, resulting in a significant increase in the vehicle range. This occurs at the cost of emissions – the system uses a combustion process to heat the air. Fuel consumption is not high and to double the vehicles range it is around 0.3L km/100 km, however the drive is not fully combustion free anymore. The design of the engine, after reversing the operating cycle, allows it to be used also as a compressor for filling the compressed air tank. The currently offered engine variant has a displacement of 430 cm^3, which generates 7 kW and 45 Nm of torque at 1500 rpm (https://www.mdi.lu). The vehicle has a maximum range of 120 km, using only compressed air. A major advantage is the recharging time – when using a station with compressed air, it takes about 2 min to fill the tank. Alternatively, the car can be connected to an electric car charging network, or to an electrical socket in the garage. In this case, the pneumatic engine is used as a compressor to fill the tanks, with a full charge time of 3.5 h.

DOI 10.2478/ama-2021-0028

3.2. EngineAir Company Engine (Di Pietro Engine)

An example of an unconventional engine powered by compressed air is the engine developed by the inventor Angelo Di Pietro. The solutions used in this engine resemble the design of a Wankel engine. The engine (Fig. 4) features a single piston (1), fixed to the shaft by special bearings (2), enabling an eccentric movement during operation (Zwierzchowski, 2017). It operates in an engine cylinder with moving vanes (*3)*. Through the use of springs, the vanes are always pressed against the piston, creating six sealed chambers in which the air is expanded.

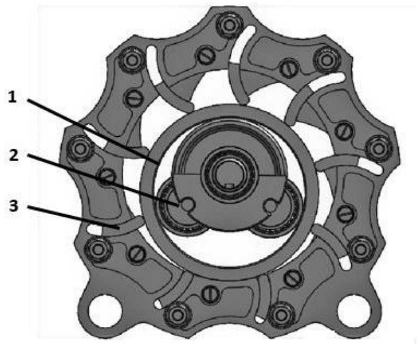

Fig. 4. Di Pietro engine, *1* – piston, *2* – bearing, *3* – vane (Zwierzchowski, 2017)

Supply air is distributed to the individual chambers by means of a rotating cone-shaped element. The operation is based on the expansion of air in successive chambers, thus exerting a force on the outer part of the piston. This sets it in eccentric motion causing, due to its construction, a rotation movement of the output shaft. As the air expands in the chamber, the piston movement causes the opposite chamber, in which work has been done in an earlier cycle, to become empty. Properly selected play between the moving vanes and the cylinder, as well as the operation in pressurised air, allows to maintain a low friction coefficient. This has a very positive effect on engine performance. According to the manufacturer's claims, the engine is able to operate even at a very low pressure of 0.07 bar (https://www.engineair.com.au). Another advantage is the constant torque, which is easily controlled by changing the supply pressure. The engine is characterised by compact dimensions and a low weight of 6 kg. The manufacturer specifies a maximum torque of 40 Nm at a supply pressure of 8 bar. It is possible to increase the engine performance by expanding the dimensions of the working elements (https://www.engineair.com.au).

3.3. Scroll Engine

Another example of an unconventional engine is a design based on the design of a scroll compressor (Ivlev and Misyurin, 2017; Liu and Wu, 2015). The concept of the scroll compressor was developed at the beginning of the 20th century, however the technological possibilities needed for serial production were developed only in the 1970s. The solution though widely used in the refrigeration industry, did not gain popularity as a component for supercharging of an internal combustion engine despite its many advantages. In the design (Fig. 5), two spirals are used – one is fixed (*1)*, and the second performing an eccentric movement (*2)* resulting from the connection to the crankshaft having a minor crank. The motion of the scroll leads to drawing air and the subsequent compression due to the tightening of the space between the scrolls. The compressed air outlet is located in the centre of spiral (*3)*. Spirals do not contact each other during operation, so there is no need for lubrication. It also contributes to quiet operation of the unit.

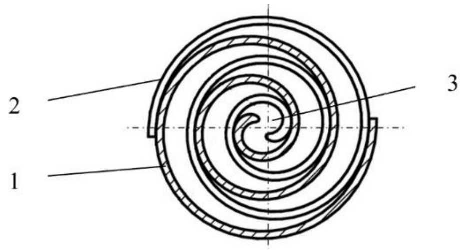

Fig. 5. Scheme of a scroll compressor, 1 – fixed spiral, 2 – moving spiral, 3 – compressor outlet (Liu and Wu, 2015)

The simple design allows the compressor to be easily converted into a pneumatic engine – by supplying compressed air to the compressor outlet (*3)*, the working cycle is reversed. The air then expands in the chambers created between the spirals, starting from the centre. The pressure of compressed air acts on the moving spiral, causing it to move, which creates torque on the shaft to which it is attached. The air is expanded from the inside of the spiral to the outlet at the outer diameter, in successive chambers, thus reducing losses in comparison with a piston engine. In the study (Sergaliyev and Khajiyeva, 2017) the parameters of an engine based on a scroll compressor were examined, the results showing a high specific air consumption, which indicates the expected high performance of the drive. In the literature although many studies on scroll compressors are found, very few items focus on their application in reverse operation. Despite this, scroll engines are one of the more promising solutions. The cost of manufacturing components remains a major problem, despite technological developments.

4. HYBRID SYSTEMS USING AIR ENGINES

In spite of the numerous advantages of the pneumatic engine, a significant problem remains in achieving adequate efficiency as the sole source of drive. This leads to the development of using pneumatic drives as an additional power source in hybrid systems, or using compressed air as a source to improve the efficiency of the internal combustion engine (Dimitrova and Maréchal, 2015). Propulsion systems of this type do not require large compressed air tanks, and the range of the vehicle on both types of power supply is similar to internal combustion vehicles. An additional advantage is the possibility to use the vehicles kinetic energy during engine braking to charge the compressed air tanks, similar to hybrid systems combining an internal combustion engine with an electric drive, which also has a positive effect on the wear of the brake system components (Borawski, 2018).

Researchers at ETH Zurich (Guzzella et al., 2010) presented a concept for a pneumatic hybrid system using a downsized supercharged internal combustion engine as the power source. In downsized engines, there is a common problem with the occurrence of turbo lag, caused among other things by the inertia of the supercharging system. In order to eliminate it, twin charger using mechanical charging and a turbocharger, turbochargers with variable geometry vanes, or twin-turbo systems with turbochargers are used. All these solutions significantly increase the complexity and cost of engine design. The concept from ETH Zurich is an alternative solution that allows the supercharging system to be supported by compressed air stored in a tank. The object of the research was a twin-cylinder turbocharged engine with a displacement of 0.75 dm^3 and power of 61 kW. It was subjected to a modification (Fig. 6) consisting in the replacement of one of the two exhaust valves by a valve called Charge Valve (*1*).

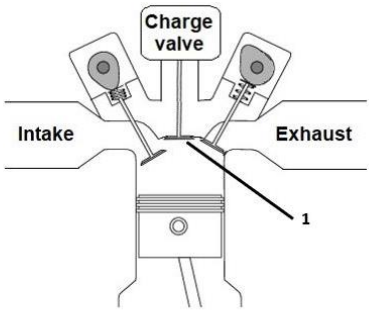

Fig. 6. Concept of pneumatic hybrid system, *1* – charge valve (Guzzella et al., 2010)

This valve, as opposed to the others, is electro-hydraulically operated. It is connected to a compressed air tank with a capacity of 30 litres. The engine can be operated in combustion mode as well as in compressed air mode. The highest performance is achieved in the combined mode – called supercharged mode. This mode involves opening an additional valve during the compression stroke to allow compressed air to be admitted into the cylinder in order to inject more fuel. It has a positive effect on the torque curve, eliminating the air deficiency at lower rotational speeds caused by the turbocharger's operating characteristics. As a result, it is possible to reduce the engine's displacement, which indirectly contributes to reducing combustion. Supercharged mode is only used during low rotational speed engine conditions to assist the turbocharger. The compressed air supply can also be used to start the engine, the response time is then faster than in the case of the combustion mode, which is important when using a start-stop system. The test results showed a reduction in combustion in the NEDC driving cycle of around 30%.

Another example of the use of air propulsion in a hybrid system is the Hybrid Air drive developed by the PSA Group (https://www.groupe-psa.com; Wasbari et al., 2017). It uses a combination of three types of power supply (Fig. 7) – combustion, hydraulic, and pneumatic (compressed nitrogen is used instead of air). The basic drive is a three-cylinder spark-ignition engine (*1*), supported by a hydraulic drive (*3*). Compressed nitrogen is used in this case for energy storage. The drive system consists of a hydraulic pump with a hydraulic motor (*3*) hydraulic fluid tank (*5*), expansion chamber (*4*), and summation gearbox (*2*). The system has three operating modes: combustion mode, air mode and combined mode. In air mode, the vehicle is driven by a hydraulic motor, supplied with hydraulic fluid, which is compressed in an expansion chamber by expanding nitrogen from a tank. This mode is used at velocities <70 km/h. During braking, the wheels drive a hydraulic pump which pushes hydraulic fluid into the expansion chamber and compresses the nitrogen, which acts as an energy accumulator. Combined mode is used when accelerating and driving dynamically, and then the hydraulic motor supports the combustion engine. Internal combustion engine only mode is used when travelling at constant velocities, for example, when driving on a highway.

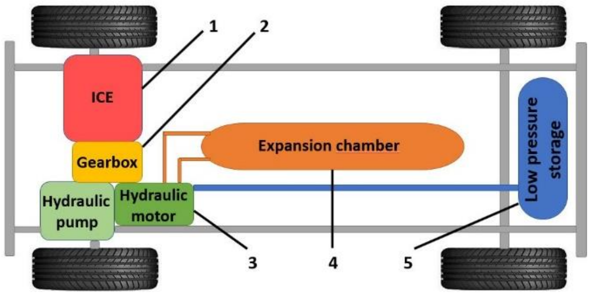

Fig. 7. PSA hybrid system scheme (https://www.groupe-psa.com; Wasbari et al., 2017)

This solution is similar in its properties to electric hybrids. The manufacturer declares a reduction of fuel consumption by 45% in the urban cycle and by 35% in the mixed cycle (https://www.groupe-psa.com). Hydraulic drives have been used for many years in heavy-duty machinery, making them a well-developed type of power supply, which is a big advantage over electric drives. The problem with the design is the requirement of large amount of space for the compressed nitrogen tank and with the current size of the system, makes only sense for small and light vehicles.

Researcher K.D. Huang presented a series of studies on hybrid propulsion systems combining an internal combustion engine with a pneumatic engine (Huang et al., 2005; Huang and Tzeng, 2005). The scheme of the system is presented in Fig. 8. The solution uses a four-stroke internal combustion engine with a displacement of 125 cm^3, operating at a constant rotational speed for supplying the compressor that compresses the air into the tank.

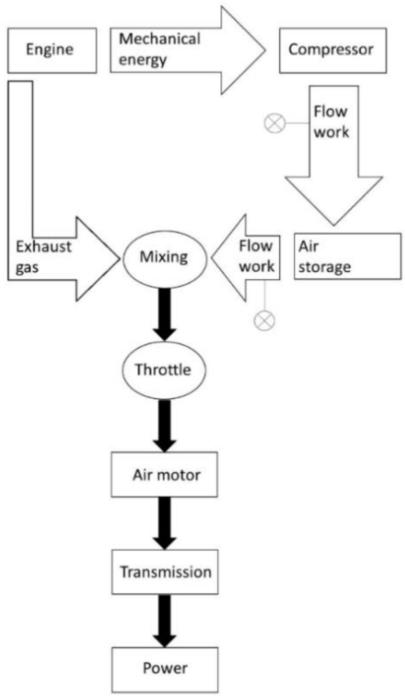

Fig. 8. Block diagram of the hybrid system presented by K. D. Huang (Huang and Tzeng, 2005)

DOI 10.2478/ama-2021-0028

Its function is to equalise pressure and store air. Then the compressed air is dosed by a throttle into the manifold, depending on the current power requirement, where it is expanded at first. The difference with other solutions is the use of a mixing chamber in the manifold of the pneumatic engine. The compressed air is mixed inside with the exhaust gases from the internal combustion engine before entering into the cylinder of the pneumatic engine. This ensures that the heat generated by the internal combustion engine is used to heat the air that directly supplies the pneumatic engine, improving the efficiency of the entire system. In the internal combustion engine, the heat balance is improved; the author declares using about 60% of the waste heat, which contributes to increasing its efficiency. Heating the compressed air before it expands in the cylinder increases the efficiency of the pneumatic engine. The internal combustion engine operating at a constant load can be optimised with regard to fuel consumption and the reduction of exhaust gases by running at the optimal rotational speed in terms of efficiency. Experimental investigations demonstrated an improvement of the drive parameters in relation to the operation of the system without the use of the mixing chamber by about 20%.

5. CONVERSION OF INTERNAL COMBUSTION ENGINE TO COMPRESSED AIR SUPPLY

Many references in the literature can be found on the conversion of the internal combustion engine to compressed air supply. Due to the nature of their work, as well as their simple design, in most cases two-stroke engines are modified (Kumar et al., 2014; Szpica and Korbut, 2020, 2019). However, studies on the conversion of four-stroke engines can also be found (Huang et al., 2013; Nabil, 2019). The idea of the conversion is to generate the force acting on the piston by means of compressed air instead of the combustion process. For this purpose, the engine supply system must be completely changed (Fig. 9). As an element supplying compressed air, solenoid valves *4* are most frequently used, while more rarely the valves opened mechanically as a result of the rotation of the crankshaft. The reason for this is that the solenoid valve enables the compressed air supply to be started independently of the angle of rotation of the crankshaft, which is important for optimising the efficiency parameters of the engine. If the valve opening and closing times need to be shortened, piezoelectric actuators can be used (Caban et al., 2020; Mieczkowski, 2016b). It is usually mounted in place of the spark plug (*5*), which is superfluous in the case of an air engine. Additional advantage of this solution is the compressed air intake located directly above the piston. The supply system also includes a pressure regulator (*3*), which reduces the pressure from the compressed air tank (*1*) to the specified supply pressure.

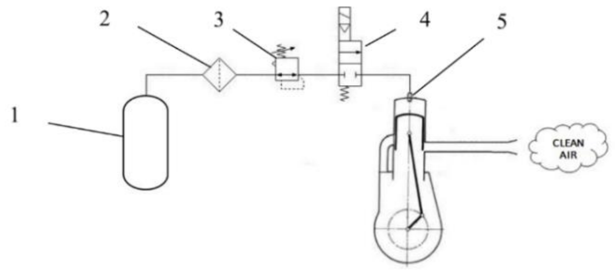

Fig. 9. Scheme of example for modification of an engine supply system to operate with compressed air, 1 – compressed air tank, 2 – filter, 3 – pressure regulator, 4 – solenoid valve, 5 – intake of compressed air

Filter (*2*) is an important part of the supply system, aimed to remove solid particles and condensate from the air. Depending on the type of engine design, additional modifications may be necessary. In the case of two- stroke engines, this includes the provision of lubrication to the engine, as normally the fuel mixture is used for this purpose. Conversion of a four-stroke engine involves a change in operating mode to a two-stroke as, for instance, there is no need to compress the charge. This requires modifications in the timing system (Szoka and Szpica, 2012) and, in the case of direct supply of compressed air to the cylinder, blanking of the intake valves. The timing should ensure the opening of the exhaust valves with every revolution of the crankshaft. Studies also demonstrate the validity of lowering the compression ratio in comparison to an internal combustion engine, using, for example, pads between the engine head and engine block (Kamiński et al., 2020). The conversion of an engine, in particular a two-stroke engine, does not require high financial costs (Nabil, 2019). This allows for the use of parts from existing engines to build propulsion units that do not require combustion. Adequate adjustment of the power supply parameters of the pneumatic engine makes it possible to approach its external indicators to the base combustion units. The results obtained by the researchers (Kumar et al., 2014; Radhakrishna and Gopikrishna, 2017; Wang et al., 2014), presented in Tab. 1, indicate that at higher rotational speeds the efficiency parameters of the pneumatic engine decline. The power achieved is low compared to the base engine, while the torque is comparable. Pneumatic drives are one of the most underdeveloped types of drives and further research may have a positive impact on their performance parameters (Warguła and Kukla, 2020).

Tab. 1. Comparisons of performance results for engines converted to compressed air supply

No.	Researcher	Basic engine power	Compressed air engine power	Basic engine torque	Compressed air engine torque
1	V. Kumar, N. Kumar (Kumar et al., 2014)	4.4 kW	1.39 kW	10.1 Nm	30 Nm
2	L. Radhakrishna, N. Gopikrishna (Radhakrishna and Gopikrishna, 2017)	2.2 kW	0.17 kW	2.94 Nm	1.87 Nm
3	T. Nabil (Nabil, 2019)	8.5 kW	0.245 kW	11.5 Nm	7.8 Nm
4	S. Allam M. Zakaria (Allam and Zakaria, 2018)	3.2 kW	1.74 kW	–	–
5	C. Huang, C. Hu, C. Yu, C. Yu, C. Sung (Huang et al., 2013)	5.5 kW	0.96 kW	7.44 Nm	9.9 Nm
6	M. Kamiński, D. Szpica M. Korbut (Kamiński et al., 2020)	1.84 kW	0.36 kW	3.5 Nm	3.1 Nm

6. PERSPECTIVES FOR FURTHER DEVELOPMENT OF PNEUMATIC ENGINES

The current pneumatic drive designs available on the market working as a single source of propulsion are only capable to power vehicles with limited unladen weight. In addition, their range is lower than currently produced electric vehicles. The situation is different for hybrid systems. Concept studies for the new solutions demonstrate significant improvements in emissions and economy, and the example of PSA's drive train design shows that they have real potential for implementation in production. Similar situation occurred with electric drives in the first decade of the 21st century. The gradual introduction of hybrid drives by manufacturers has convinced customers, among other things, by the low fuel consumption. It has also contributed to the intensification of the development of electric drive technology, which has improved its performance parameters. The direct result of this is the great increase in the popularity of electric drives, and also as the only source of propulsion. The introduction of new exhaust emission limits creates favourable conditions for the development of alternative power sources. The decisive factor is whether the automotive corporations will consider research work towards pneumatic drives.

The numerous developing concepts for complying with the homologation requirements give hope that one of the companies from the automotive industry will undertake the implementation of the topic. Many aspects of air engine operation have not been explored yet, which provides opportunities for further efficiency improvements. The main advantages of pneumatic drives are lower complexity in comparison to electric drives, the possibility of reducing overall emissions, and cheaper construction costs. A positive factor for the chances of pneumatic drives is also the conviction of a clean drive because of operating results only in the form of cooled air. Currently developed concepts of pneumatic drives are shown in Fig. 10. Further development is closely dependent on research work and their results. The road to commercialisation is a long one, making it difficult to expect the rapid appearance of cars powered by compressed air.

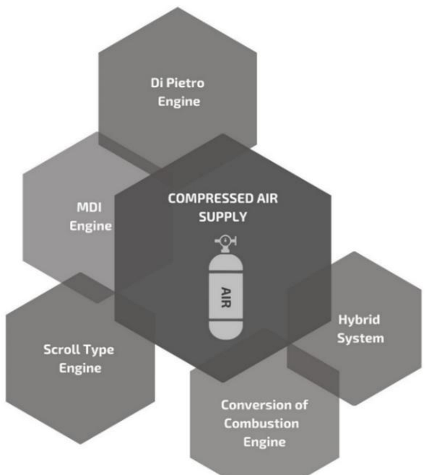

Fig. 10. Currently developed concepts of pneumatic drives

7. CONCLUSIONS

The paper focuses on a multi-faceted analysis of pneumatic drives with regard to their application in powering vehicles. Their use is known for many years, although it never gained any significant popularity. Currently, the development and research of pneumatic drives is also negligible compared to electric drives. Forcing manufacturers to look for alternative propulsion sources, and slowly turning away from conventional internal combustion engines, positively impacts on the potential for refocusing on this type of propulsion. The greatest opportunities can be observed in hybrid systems, as evidenced by the PSA Group solution. The use of energy recovery or the improvement of the thermal balance by using the exhaust gases from the internal combustion engine favourably improves the efficiency of the drives. Current technology and solutions do not allow for the introduction into series production of a vehicle powered solely by a compressed-air engine with a range adequate to other sources of propulsion. The MDI or EngineAir company projects indicate that pneumatic drives have potential and could be used in the future as a cheaper and more environmentally friendly alternative to electric drives. Considering the environmental performance of pneumatic drives, it can be observed that they have a much lower impact on environmental degradation. Nevertheless, further development is mainly determined by efficiency improvements, on which future research should focus.

Nomenclature: ATAC, Active Thermo-Atmosphere Combustion; ACT, Active Cylinder Technology; BDC, Bottom Dead Centre; CAES, compressed air energy storage; CAI, controlled auto-ignition; CNG, compressed natural gas; DPF, diesel particulate filter; GPF, gasoline particulate filter; HCCI, homogeneous charge compression ignition; LPG, liquefied petroleum gas; NEDC, New European Driving Cycle; RCCI, reactivity controlled compression ignition; RDE, real drive test; SCR, selective catalytic reduction; SPCCI, spark-controlled compression ignition; TMS, thermal management system; TWC, three-way catalytic converter; TDC, top dead centre; WLTP, Worldwide Harmonized Light Vehicles Test Procedure;.

REFERENCES

1. **Akira I., Hideo S.** (2004), Analysis of Compression-induced Auto-ignition Combustion Characteristics of HCCI and ATAC Using the Same Engine, *Journal of Mechanical Science and Technology*, Vol. 20, No. 9, 1449–1458.
2. **Allam S., Zakaria M.** (2018), Experimental Investigation of Compressed Air engine Performance, *International Journal of Engineering Inventions*, Vol. 7, 13–20.
3. **Archer H.B.** (1929), US1776963A Compressed-air engine.
4. **Ashok B., Denis Ashok S., Ramesh Kumar C.** (2015), LPG diesel dual fuel engine - A critical review, *Alexandria Engineering Journal*, Vol. 54, No. 2, 105-126.
5. **Baseley S., Ehret C., Greif E., Kliffken M.G.** (2007), Hydraulic hybrid systems for commercial vehicles, *SAE Technical Papers*, Vol. 2007-01-4150, 1-8.
6. **Beik Y., Dziewiątkowski M., Szpica D.** (2020), Exhaust Emissions of an Engine Fuelled by Petrol and Liquefied Petroleum Gas with Control Algorithm Adjustment, *SAE International Journal of Engines*, Vol. 13, No. 5, 1-22.
7. **Bensaid S., Caroca C.J., Russo N., Fino D.** (2011), Detailed investigation of non-catalytic DPF regeneration, *Canadian Journal of Chemical Engineering*, Vol. 89, 401–407.
8. **Bielaczyc P., Woodburn J.** (2019), Trends in Automotive Emission Legislation: Impact on LD Engine Development, Fuels, Lubricants and Test Methods: a Global View, with a Focus on WLTP and RDE Regulations, *Emission Control Science and Technology*, Vol. 5, No. 1, 86–98.
9. **Borawski A.** (2015), Modification of a fourth generation LPG installation improving the power supply to a spark ignition engine, *Eksploatacja i Niezawodnosc*, Vol. 17, 1–6.

DOI 10.2478/ama-2021-0028

10. **Borawski A.** (2018), Simulation Study of the Process of Friction in the Working Elements of a Car Braking System at Different Degrees of Wear, *Acta Mechanica et Automatica*, Vol. 12, No. 3, 221-226.
11. **Borawski A.** (2020), Conventional and unconventional materials used in the production of brake pads – Review, *Science and Engineering of Composite Materials*, Vol. 27, 374-396.
12. **Brown R.** (1972), US3765180A Compressed air engine.
13. **Budt M., Wolf D., Span R., Yan J.** (2016), A review on compressed air energy storage: Basic principles, past milestones and recent developments, *Applied Energy*, Vol. 170, 250–268.
14. **Caban J., Litak G., Ambrożkiewicz B., Gardyński L., Stączek P., Wolszczak P.** (2020), Impact-based piezoelectric energy harvesting system excited from diesel engine suspension, *Applied Computer Science*, Vol. 16, No. 3, 16-29.
15. **Cestero L.G.** (1985), US4651525A Piston reciprocating compressed air engine.
16. **Chen L., Zheng T., Mei S., Xue X., Liu B., Lu Q.** (2016), Review and prospect of compressed air energy storage system, *Journal of Modern Power Systems and Clean Energy*, Vol. 4, 529–541.
17. **Creutzig F., Papson A., Schipper L., Kammen D.M.** (2009), Economic and environmental evaluation of compressed - air cars, *Environmental Research Letters*, Vol. 4, 1-10.
18. **Crosby Valve Inc.** (1997), Pressure Relief Valve, *Engineering Handbook*, 1-93.
19. **Di Pietro A.** (1999), EP1204809B1 Rotary piston engine.
20. **Dimitrova Z., Maréchal F.** (2015), Gasoline hybrid pneumatic engine for efficient vehicle powertrain hybridization, *Applied Energy*, Vol. 151, 168–177.
21. **Duraisamy G., Rangasamy M., Govindan N.** (2020), A comparative study on methanol/diesel and methanol/PODE dual fuel RCCI combustion in an automotive diesel engine, *Renewable Energy*, Vol. 145, 542-556.
22. **Eliot S.** (1934), US1954408A Compressed air engine.
23. **Foley A.M., Winning I.J., Gallachóir B.P.** (2010), State-of-the-art in electric vehicle charging infrastructure, *2010 IEEE Vehicle Power and Propulsion Conference*, 1-6.
24. **Forzatti P.** (2001), Present status and perspectives in de-NOx SCR catalysis, *Applied Catalysis A: General*, Vol. 222, 221-236.
25. **Friar T.D., Holdcroft J.F.** (1925), GB253219A An improved compressed air engine.
26. **García A., Monsalve-Serrano J., Villalta D., Guzmán-Mendoza M.** (2020), Methanol and OMEx as fuel candidates to fulfill the potential EURO VII emissions regulation under dual-mode dual-fuel combustion, *Fuel*, Vol. 287, 1-13.
27. **Gołębiowski W., Wolak A., Zając G.** (2018), Definition of oil change intervals based on the analysis of selected physicochemical properties of used engine oils, *Combustion Engines*, Vol. 172, 44-50.
28. **Gołębiowski W., Wolak A., Zając G.** (2019), The influence of the presence of a diesel particulate filter (DPF) on the physical and chemical properties as well as the degree of concentration of trace elements in used engine oils, *Petroleum Science and Technology*, Vol. 37, 746-755.
29. **Gołębiowski W., Zając G., Wolak A.** (2019), Analysis of Engine Oils from Farm Tractors in the Aspect of their Change, *Agricultural Engineering*, Vol. 23, 25-38.
30. **Gosala D.B., Allen C.M., Ramesh A.K., Shaver G.M., McCarthy J., Stretch D., Koeberlein E., Farrell L.** (2017), Cylinder deactivation during dynamic diesel engine operation, *International Journal of Engine Research*, Vol. 18, No. 10, 991–1004.
31. **Grazzini G., Milazzo A.** (2012), A thermodynamic analysis of multistage adiabatic CAES, *Proceedings of the IEEE*, Vol. 100, 461–472.
32. **Guan B., Zhan R., Lin H., Huang Z.** (2014), Review of state of the art technologies of selective catalytic reduction of NOx from diesel engine exhaust, *Applied Thermal Engineering*, Vol. 66, 395–414.
33. **Guan B., Zhan R., Lin H., Huang Z.** (2015), Review of the state-of-the-art of exhaust particulate filter technology in internal combustion engines, *Journal of Environmental Management*, Vol. 154, 225–258.
34. **Guzzella L., Onder C., Dönitz C., Voser C., Vasile I.** (2010), The pneumatic hybridization concept for downsizing and supercharging gasoline engines, *MTZ worldwide,* Vol. 71, 38–44.
35. **Hannan M.A., Azidin F.A., Mohamed A.** (2014), Hybrid electric vehicles and their challenges: A review, *Renewable and Sustainable Energy Reviews*, Vol. 29, 135–150.
36. **Harper G., Sommerville R., Kendrick E., Driscoll L., Slater P., Stolkin R., Walton A., Christensen P., Heidrich O., Lambert S., Abbott A., Ryder K., Gaines L., Anderson P.** (2019), Recycling lithium-ion batteries from electric vehicles, *Nature*, Vol. 575, 75-86.
37. **Hawkins T.R., Singh B., Majeau-Bettez G., Strømman A.H.** (2013), Comparative Environmental Life Cycle Assessment of Conventional and Electric Vehicles, *Journal of Industrial Ecology*, Vol. 17, 53-64.
38. **Heck R.M., Farrauto R.J.** (2001), Automobile exhaust catalysts, *Applied Catalysis A: General*, Vol. 221, 443–457.
39. **Hoke A., Brissette A., Maksimović D., Pratt A., Smith K.** (2011), Electric vehicle charge optimization including effects of lithium-ion battery degradation, *2011 IEEE Vehicle Power and Propulsion Conference*, 1-8.
40. **Hooftman N., Messagie M., Van Mierlo J., Coosemans T.** (2018), A review of the European passenger car regulations – Real driving emissions vs local air quality, *Renewable and Sustainable Energy Reviews*, Vol. 86, 1–21.
41. http://www.thefuture.net.nz/engine.htm [online cit.: 2021.04.15].
42. https://air-volution.com.au/compressed-air-engine/ [online cit.: 2021.04.16].
43. https://americanindustrialmining.com/porter-locomotives [online cit.: 2021.04.14].
44. https://www.engineair.com.au/ [online cit.: 2021.04.15].
45. https://www.groupe-psa.com/en/newsroom/automotive-innovation/hybrid-air [online cit.: 2021.04.03].
46. https://www.mdi.lu/airpod-2-0 [online cit.: 2021.04.15].
47. https://www.pmreview.com/wpcontent/uploads/2013/01/psa_air_hybrid-1 [online cit.: 2021.04.15].
48. https://www.tramwayinfo.com/Defair.htm [online cit.: 2021.04.15].
49. **Huang C.Y., Hu C.K., Yu C.J., Sung C.K.** (2013), Experimental investigation on the performance of a compressed-air driven piston engine, *Energies,* Vol. 6, 1731-1745.
50. **Huang K.D., Tzeng S.C.** (2005), Development of a hybrid pneumatic-power vehicle, *Applied Energy*, Vol. 80, 47–59.
51. **Huang K.D., Tzeng S.C., Chang W.C**. (2005), Energy-saving hybrid vehicle using a pneumatic-power system, *Applied Energy*, 81, 1–18.
52. **Hudgens R.D., Bustamante R.B.** (1993), Toxicity and disposal of engine coolants, *ASTM Special Technical Publication*, 149-164.
53. **Ivlev V.I., Misyurin S.Y.** (2017), Calculated and experimental characteristics of a scroll machine operating in the air motor mode, *Doklady Physics*, Vol. 62, 42–45.
54. **Jeuland N., Montagne X., Duret P.** (2004), New HCCI/CAI combustion process development: Methodology for determination of relevant fuel parameters, *Oil and Gas Science and Technology*, Vol. 59, No. 6, 571–579.
55. **Johnson J.M.** (1983), US4596119A Compressed air propulsion system for a vehicle.
56. **Joshi A., Johnson T. V.** (2018), Gasoline Particulate Filters — a Review, *Emission Control Science and Technology*, 4, 219–239.
57. **Joshi M.C., Gosala D.B., Allen C.M., Vos K., Van Voorhis M., Taylor A., Shaver G.M., McCarthy J., Stretch D., Koeberlein E., Farrell L.** (2017), Reducing Diesel Engine Drive Cycle Fuel Consumption through Use of Cylinder Deactivation to Maintain Aftertreatment Component Temperature during Idle and Low Load Operating Conditions, *Frontiers in Mechanical Engineering*, 3, 1-15.
58. **Kakaee A.H., Nasiri-Toosi A., Partovi B., Paykani A.** (2016), Effects of piston bowl geometry on combustion and emissions characteristics of a natural gas/diesel RCCI engine, *Applied Thermal Engineering*, Vol. 102, 1462-1472.
59. **Kamguia Simeu S., Kim N.** (2018), Standard Driving Cycles Comparison (IEA) & Impacts on the Ownership Cost, *SAE Technical Papers*, 2018-01-0423, 1-12.

60. **Kamiński M., Korbut M., Szpica D.** (2020), Piston pneumatic engine - Preliminary research, *Transport Means - Proceedings of the International Conference*, Vol. 24, 126–131.
61. **Katoch S.S., Eswaramoorthy M.** (2020), A Detailed Review on Electric Vehicles Battery Thermal Management System, *IOP Conference Series: Materials Science and Engineering*, 912, 1- 11.
62. **Keav S., Matam S.K., Ferri D., Weidenkaff A.** (2014), Structured perovskite-based catalysts and their application as Three-Way Catalytic converters - a review, *Catalysts*, Vol. 4, 226–255.
63. **Khair M.K.** (2003), A review of diesel particulate filter technologies, *SAE Technical Papers*, 2003-01-2303, 1-11.
64. **Khandal S. V., Banapurmath N.R., Gaitonde V.N.** (2019), Performance studies on homogeneous charge compression ignition (HCCI) engine powered with alternative fuels, *Renewable Energy*, Vol. 132, 683–693.
65. **Kim J., Oh J., Lee H.** (2019), Review on battery thermal management system for electric vehicles, *Applied Thermal Engineering*, Vol. 149, 192-212.
66. **Ko J., Kim K., Chung W., Myung C.L., Park S.** (2019), Characteristics of on-road particle number (PN) emissions from a GDI vehicle depending on a catalytic stripper (CS) and a metal-foam gasoline particulate filter (GPF), *Fuel*, Vol. 238, 363–374.
67. **Kral J., Konecny B., Kral J., Madac K., Fedorko G., Molnar V.** (2014), Degradation and chemical change of longlife oils following intensive use in automobile engines, *Measurement: Journal of the International Measurement Confederation*, Vol. 50, 34-42.
68. **Kumar V., Takkar J., Chitransh M., Kumar N., Banka U., Gupta U.** (2014), Development of an advanced compressed air engine kit for small engine, *SAE Technical Papers*, 2014-01-1666, 1-11.
69. **Lambert C., Chanko T., Dobson D., Liu X., Pakko J.** (2017), Gasoline Particle Filter Development, *Emission Control Science and Technology*, Vol. 3, 105–111.
70. **Latha H.S., Prakash K. V, Veerangouda M., Maski D., Ramappa K.T.** (2019), A Review on SCR System for NOx Reduction in Diesel Engine, *International Journal of Current Microbiology and Applied Sciences*, Vol. 8, No. 4, 1553-1559.
71. **Lee N., Park J., Lee J., Park K., Choi M., Kim W.** (2018), Estimation of fuel economy improvement in gasoline vehicle using cylinder deactivation, *Energies*, Vol. 11, 1-12.
72. **Li J., Chang H., Ma L., Hao J., Yang R.T.** (2011), Low-temperature selective catalytic reduction of NOx with NH3 over metal oxide and zeolite catalysts - A review, *Catalysis Today*, Vol. 175, 147-156.
73. **Ligterink N., Mensch P., Cuelenaere R.** (2016), NEDC – WLTP comparative testing, *TNO report: TNO*, Vol. R11285, 1-29.
74. **Liu T., Wu Z.** (2015), Modeling of top scroll profile using equidistant-curve approach for a scroll compressor, *Mathematical Problems in Engineering*, 1-8.
75. **Lund H., Salgi G.** (2009), The role of compressed air energy storage (CAES) in future sustainable energy systems, *Energy Conversion and Management*, Vol. 50, 1172-1179.
76. **Luo X., Wang J., Dooner M., Clarke J., Krupke C.** (2014), Overview of current development in compressed air energy storage technology, *Energy Procedia*, Vol. 62, 603-611.
77. **Manoharan Y., Hosseini S.E., Butler B., Alzhahrani H., Senior B.T.F., Ashuri T., Krohn J.** (2019), Hydrogen fuel cell vehicles; Current status and future prospect, *Applied Sciences (Switzerland)*, Vol. 9, 1-17.
78. **Mazumder H., Al Emran Hassan M.M., Ektesabi M., Kapoor A.** (2012), Performance analysis of EV for different mass distributions to ensure safe handling, *Energy Procedia*, Vol. 14, 949-954,
79. **Mieczkowski G.** (2016), Electromechanical characteristics of piezoelectric converters with freely defined boundary conditions and geometry, *Mechanika*, Vol. 22, No. 4, 265-272.
80. **Mieczkowski G.** (2016), Stress fields at the tip of a sharp inclusion on the interface of a bimaterial, *Mechanics of Composite Materials*, Vol. 52, No. 5, 601-610.
81. **Mikulski M., Balakrishnan P.R., Doosje E., Bekdemir C.** (2018), Variable Valve Actuation Strategies for Better Efficiency Load Range and Thermal Management in an RCCI Engine, *SAE Technical Papers*, 2018-01-0254, 1-14.
82. **Miller T.R.** (1980), US4370857A Pneumatic system for compressed air driven vehicle.
83. **Mishra K.R., Sugandh G.** (2014), Study About Engine Operated By Compressed Air (C.A.E): A Pneumatic Power Source, *Journal of Mechanical and Civil Engineering*. Vol. 11, 99–103.
84. **Mitukiewicz G., Dychto R., Leyko J.** (2015), Relationship between LPG fuel and gasoline injection duration for gasoline direct injection engines, *Fuel*, Vol. 153, 526–534.
85. **Morrow K., Karner D., Francfort J.** (2008), Advanced Vehicle Testing Activity Plug-in Hybrid Electric Vehicle Charging Infrastructure Review Novem Charging Infrastructure Review, U. S. Department of Energy Vehicle Technologies Program, Vol. 34, 1-40.
86. **Muhamad Said M.F., Abdul Aziz A., Abdul Latiff Z., Mahmoudzadeh Andwari A., Mohamed Soid S.N.** (2014), Investigation of Cylinder Deactivation (CDA) Strategies on Part Load Conditions, *SAE Technical Papers*, 2014-01-2549, 1-7.
87. **Myagkov L.L., Mahkamov K., Chainov N.D., Makhkamova I.** (2014), Advanced and conventional internal combustion engine materials, *Alternative Fuels and Advanced Vehicle Technologies for Improved Environmental Performance: Towards Zero Carbon Transportation*, 370-392.
88. **Myung C.L., Lee H., Choi K., Lee Y.J., Park S.** (2009), Effects of gasoline, diesel, LPG, and low-carbon fuels and various certification modes on nanoparticle emission characteristics in light-duty vehicles, *International Journal of Automotive Technology*, Vol. 10, 537–544.
89. **Nabil T.** (2019), Investigation and implementation of compressed air powered motorbike engines, *Engineering Reports*, Vol. 1, 1–13.
90. **Olesky L.M., Lavoie G.A., Assanis D.N., Wooldridge M.S., Martz J.B.** (2014), The effects of diluent composition on the rates of HCCI and spark assisted compression ignition combustion, *Applied Energy*, Vol. 124, 186–198.
91. **Onishi S., Jo S.H., Shoda K., Jo P.D., Kato S.** (1979), Active Thermo-Atmosphere Combustion (ATAC) - A new combustion process for internal combustion engines, *SAE Technical Papers*, 790501, 1-12.
92. **Papson A., Creutzig F., Schipper L.** (2010), Compressed air vehicles: Drive-cycle analysis of vehicle performance, environmental impacts, and economic costs, *Transportation Research Record*, Vol. 2191, 67–74.
93. **Pavlovic J., Marotta A., Ciuffo B.** (2016), CO2 emissions and energy demands of vehicles tested under the NEDC and the new WLTP type approval test procedures, *Applied Energy*, 177, 661-670.
94. **Pesaran A.** (2001), Battery Thermal Management in EVs and HEVs : Issues and Solutions, *Advanced Automotive Battery Conference*, Vol. 10, 1-10.
95. **Puškár M., Jahnátek A., Kádárová J., Šoltésová M., Kovanič Ľ., Krivosudská J.** (2019), Environmental study focused on the suitability of vehicle certifications using the new European driving cycle (NEDC) with regard to the affair “dieselgate” and the risks of NO x emissions in urban destinations, *Air Quality, Atmosphere and Health*, Vol. 12, No. 2, 251–257.
96. **Radhakrishna L., Gopikrishna N.** (2017), Prefabricating and testing of air driven engine, *International Journal of Mechanical Engineering and Technology*, Vol. 8, 238–251.
97. **Raslavičius L., Azzopardi B., Keršys A., Starevičius M., Bazaras Ž., Makaras R.** (2015), Electric vehicles challenges and opportunities: Lithuanian review, *Renewable and Sustainable Energy Reviews*, Vol. 42, 786–800.
98. **Raslavičius L., Keršys A., Makaras R.** (2017), Management of hybrid powertrain dynamics and energy consumption for 2WD, 4WD, and HMMWV vehicles, *Renewable and Sustainable Energy Reviews*, Vol. 68, 380–396.
99. **Reitz R.D., Duraisamy G.** (2015), Review of high efficiency and clean reactivity controlled compression ignition (RCCI) combustion in internal combustion engines, *Progress in Energy and Combustion Science*, Vol. 46, 12–71.

DOI 10.2478/ama-2021-0028

100. **Robertson D., Prucka R.** (2019), A Review of Spark-Assisted Compression Ignition (SACI) Research in the Context of Realizing Production Control Strategies, *SAE Technical Papers*, 2019-24-0027, 1-18.
101. **Saiteja P., Ashok B.** (2021), A critical insight review on homogeneous charge compression ignition engine characteristics powered by biofuels, *Fuel*, Vol. 285, 1-34.
102. **Santos H., Costa M.** (2008), Evaluation of the conversion efficiency of ceramic and metallic three way catalytic converters, *Energy Conversion and Management*, Vol. 49, 291–300.
103. **Sen B., Onat N.C., Kucukvar M., Tatari O.** (2019), Material footprint of electric vehicles: A multiregional life cycle assessment, *Journal of Cleaner Production*, Vol. 209, 1033-1043.
104. **Sergaliyev A.S., Khajiyeva L.A.** (2017), Experimental Research and Mathematical Modeling of Scroll Machine in Air Motor Mode, *Advances in Mechanism Design II*, 145–151.
105. **Shi Y., Li F., Cai M., Yu Q.** (2016), Literature review: Present state and future trends of air-powered vehicles, *Journal of Renewable and Sustainable Energy,* Vol. 8.
106. **Shuai S., Ma X., Li Y., Qi Y., Xu H.** (2018), Recent Progress in Automotive Gasoline Direct Injection Engine Technology, *Automotive Innovation*, Vol. 1, 95-113.
107. **Sileghem L., Bosteels D., May J., Favre C., Verhelst S.** (2014), Analysis of vehicle emission measurements on the new WLTC, the NEDC and the CADC, *Transportation Research Part D: Transport and Environment*, Vol. 32, 70–85.
108. **Szoka W., Szpica D.** (2012), Adaptation of classic combustion engines to compressed air supply, *Acta Mechanica et Automatica*, Vol. 6, 68-73.
109. **Szpica D.** (2019), Coefficient of Engine Flexibility as a Basis for the Assessment of Vehicle Tractive Performance, *Chinese Journal of Mechanical Engineering (English Edition)*, Vol. 32, 1-9.
110. **Szpica D., Korbut M.** (2019), Modelling Methodology of Piston Pneumatic Air Engine Operation, *Acta Mechanica et Automatica*, Vol. 13, 271–278.
111. **Szpica D., Korbut M.** (2020), Model assessment of inlet timing system impact on cylinder indicated pressure course of piston pneumatic engine, *Engineering for Rural Development*, Vol. 19, 711–720.
112. **Szpica D., Piwnik J., Sidorowicz M.** (2014), The motion storage characteristics as the indicator of stability of internal combustion engine - receiver cooperation, *Mechanika*, Vol. 20, No. 1, 108-112.
113. **Thipse S.S.** (2008), Compressed air car, *Tech Monitor*, 6, 33–37.
114. **Thiruvengadam A., Besch M., Padmanaban V., Pradhan S., Demirgok B.** (2018), Natural gas vehicles in heavy-duty transportation - A review, *Energy Policy*, Vol. 122, 253-259.
115. **Usman M., Farooq M., Naqvi M., Saleem M.W., Hussain J., Naqvi S.R., Jahangir S., Jazim Usama H.M., Idrees S., Anukam A.** (2020), Use of gasoline, LPG and LPG-HHO blend in SI engine: A comparative performance for emission control and sustainable environment, *Processes*, Vol. 8, No. 74, 1-15.
116. **Varella R., Duarte G., Baptista P., Sousa L., Villafuerte P.** (2017), Comparison of Data Analysis Methods for European Real Driving Emissions Regulation, *SAE Technical Papers*, 2017-01-0997, 1-14.
117. **Wagner W.C.** (1975), US4124978A Compressed air engine.
118. **Wang J., Lu K., Ma L., Wang J., Dooner M., Miao S., Li J., Wang D.** (2017), Overview of compressed air energy storage and technology development, *Energies*, Vol. 10, 1-22.
119. **Wang Y.W., You J.J., Sung C.K., Huang C.Y.** (2014), The applications of piston type compressed air engines on motor vehicles, *Procedia Engineering*, Vol. 79, 61–65.
120. **Wang Z., He X., Wang J.X., Shuai S., Xu F., Yang D.** (2010), Combustion visualization and experimental study on spark induced compression ignition (SICI) in gasoline HCCI engines, *Energy Conversion and Management*, Vol. 51, No. 5, 908–917.
121. **Warguła Ł., Kukla M.** (2020), Determination of maximum torque during carpentry waste comminution, *Wood Research*, Vol. 65, 771-784.
122. **Wasbari F., Bakar R.A., Gan L.M., Tahir M.M., Yusof A.A.** (2017), A review of compressed-air hybrid technology in vehicle system, *Renewable and Sustainable Energy Reviews*, Vol. 67, 935–953.
123. **Weaver C.S.** (1989), Natural gas vehicles - A review of the state of the art, *SAE Technical Papers,* 892133, 1-24.
124. **Wittig K.** (1925), US1726462A Compressed-air engine.
125. **Wu W., Wang S., Wu W., Chen K., Hong S., Lai Y.** (2019), A critical review of battery thermal performance and liquid based battery thermal management, *Energy Conversion and Management,* Vol. 182, 262-281.
126. **Xia W., Zheng Y., He X., Yang D., Shao H., Remias J., Roos J., Wang Y.** (2017), Catalyzed Gasoline Particulate Filter (GPF) Performance: Effect of Driving Cycle, Fuel, Catalyst Coating, *SAE Technical Papers*, 2017-01-2366, 1-9.
127. **Xingcai L., Libin J., Junjun M., Chen H., Zhen H.** (2008), Effects of an In-Cylinder Active Thermo-Atmosphere Environment on Diesel Engine Combustion Characteristics and Emissions, *Energy Fuels*, Vol. 22, No. 5, 2991–2996.
128. **Yang J., Roth P., Durbin T.D., Johnson K.C., Cocker D.R., Asa-Awuku A., Brezny R., Geller M., Karavalakis G.** (2018), Gasoline Particulate Filters as an Effective Tool to Reduce Particulate and Polycyclic Aromatic Hydrocarbon Emissions from Gasoline Direct Injection (GDI) Vehicles: A Case Study with Two GDI Vehicles, *Environmental Science and Technology*, 52(5), 3275-3284.
129. **Yang Q.C., Zhao Y.Y., Li L.S., Qian Z.G.** (2013), Investigation on working characteristics of micro compressed air energy storage system, *Institution of Mechanical Engineers - 8th International Conference on Compressors and Their Systems,* 151-159.
130. **Yeh S.** (2007), An empirical analysis on the adoption of alternative fuel vehicles: The case of natural gas vehicles, *Energy Policy*, Vol. 35, No. 11, 5865-5875.
131. **Zhang C., Yan B., Wieberdink J., Li P.Y., Van De Ven J.D., Loth E., Simon T.W.** (2014), Thermal analysis of a compressor for application to Compressed Air Energy Storage, *Applied Thermal Engineering*, Vol. 73, No. 2, 1402-1411.
132. **Zhao C., Zhang B., Zheng Y., Huang S., Yan T., Liu X.** (2020), Hybrid Battery Thermal Management System in Electrical Vehicles: A Review, *Energies*, Vol. 13, 1-18.
133. **Zhou Q., Du D., Lu C., He Q., Liu W.** (2019), A review of thermal energy storage in compressed air energy storage system, *Energy*. Vol. 188.
134. **Zhou, S. Walker P., Zhang N.** (2020), Parametric design and regenerative braking control of a parallel hydraulic hybrid vehicle, *Mechanism and Machine Theory*, Vol. 146, 1-15.
135. **Zwierzchowski J.** (2017), Design type air engine Di Pietro, *EPJ Web of Conferences*, Vol. 143, 1-6.

This research was financed through subsidy of the Ministry of Science and Higher Education of Poland for the discipline of mechanical engineering at the Faculty of Mechanical Engineering Bialystok University of Technology WZ/WM-IIM/4/2020.

Michał Korbut: https://orcid.org/0000-0001-7515-3800

Dariusz Szpica: https://orcid.org/0000-0002-7813-8291

DOI 10.2478/ama-2021-0029 acta mechanica et automatica, vol.15 no.4 (2021)

AN OUTPUT SENSITIVITY PROBLEM FOR A CLASS OF FRACTIONAL ORDER DISCRETE-TIME LINEAR SYSTEMS

Youssef BENFATAH*, Amine EL BHIH*, Mostafa RACHIK*, Marouane LAFIF*

*Faculty of Sciences Ben M'Sik, Department of Mathematics and Computer Science, Hassan II University, Casablanca, Sidi Othman BP 7955, Morocco

youssef.benfatah@gmail.com, elbhihamine@gmail.com, m_rachik@yahoo.fr, marouane8@gmail.com,

received 7 February 2021, revised 16 September 2021, accepted 20 September 2021

Abstract: Consider the linear discrete-time fractional order systems with uncertainty on the initial state $\begin{cases}\Delta^{\alpha}x_{i+1} = Ax_i + Bu_i, & i \geq 0\\ x_0 = \tau_0 + \hat{\tau}_0 \in \mathbb{R}^n, & \hat{\tau}_0 \in \Omega,\\ y_i = Cx_i, & i \geq 0\end{cases}$ where A, B and C are appropriate matrices, x_0 is the initial state, y_i is the signal output, α the order of the derivative, τ_0 and $\hat{\tau}_0$ are the known and unknown part of x_0, respectively, $u_i = Kx_i$ is feedback control and $\Omega \subset \mathbb{R}^n$ is a polytope convex of vertices $w_1, w_2, \ldots, w_p$. According to the Krein–Milman theorem, we suppose that $\hat{\tau}_0 = \sum_{j=1}^{p} \alpha_j w_j$ for some unknown coefficients $\alpha_1 \geq 0, \ldots, \alpha_p \geq 0$ such that $\sum_{j=1}^{p} \alpha_j = 1$. In this paper, the fractional derivative is defined in the Grünwald–Letnikov sense. We investigate the characterisation of the set $\chi(\hat{\tau}_0, \epsilon)$ of all possible gain matrix K that makes the system insensitive to the unknown part $\hat{\tau}_0$, which means $\chi(\hat{\tau}_0, \epsilon) = \{K \in \mathbb{R}^{m\times n} \,/\, \| \frac{\partial y_i}{\partial \alpha_j} \| \leq \epsilon, \ \forall j = 1, \ldots, p, \ \forall i \geq 0\}$, where the inequality $\| \frac{\partial y_i}{\partial \alpha_j} \| \leq \epsilon$ showing the sensitivity of y_i relatively to uncertainties $\{\alpha_j\}_{j=1}^{p}$ will not achieve the specified threshold $\epsilon > 0$. We establish, under certain hypothesis, the finite determination of $\chi(\hat{\tau}_0, \epsilon)$ and we propose an algorithmic approach to made explicit characterisation of such set.

Key words: fractional order systems, output sensitivity, discrete-time systems, maximal output set admissible uncertainty

1. INTRODUCTION

Fractional calculus is an extended version of the traditional integer order calculus in which the definition of derivatives is given to a non-integer order. The non-integer derivative concept is used increasingly for modelling of real systems behaviour in different disciplines of engineering and science (Debnath, 2003). These systems have long-memory transients and hereditary properties that can be more accurately described by fractional-order models. In the recent past, there has been an increasing focus on discrete-time fractional systems (Kaczorek, 2007; Kaczorek, 2008; Sierociuk and Dzieliński, 2006; Ferreira and Torres, 2011). Some important developments of the theory of fractional calculus are presented in Kilbas et al., (2006) and Oldham and Spanier (1974).

On the other hand, undesirable parameters appeared during modelling a system; consequently such parameters could have an impact on various elements of the system including initial conditions, control, dynamic, and observations. To deal with this problem, a variety of approaches have been developed by researchers, including the theory of sentinel (Lions), the detectability in Franklin (2001) and Ogata (1995), identifiability in Thomson (2007); Kauffmann and Bretthawer; and Robert and Graham (2007), the H_∞ control theory in Chi-Tsong) 2008) and the frequency domain and robustness (Rosario, 2005; Gu et al., 2005).

1.1. Related work

Concerning the sensitivity of the system output to the disturbance, the readers can refer to Larrache et al. (2020); Rachik and Lhous (2016); Balatif et al. (2016); and Chraïbi et al. (2006). Larrache et al. (2020) considered an infinite dimensional linear system described as

$$\begin{cases}\dot{x}(t) = Ax(t), & t \geq 0,\\ x(0) = x_0 = \alpha 1_{\omega_1} + \beta 1_{\omega_2},\\ y_i = Cx_i + Dv_i, & i \geq 0,\end{cases} \tag{1}$$

where $x(t) \in L^2(\Omega)$, 1_{ω_i} is the indicator function, and Ω is an open bounded of $\mathbb{R}^n$ such that $\Omega = \omega_1 \cup \omega_2$ and $\omega_1 \cap \omega_2 = \emptyset$. The operator A generates a continuous strongly semigroup $\{S(t)\}_{t\geq 0}$ on the space $L^2(\Omega)$, $v_i = Kx_i$, $i \geq 0$ feedback control, $K \in \mathcal{L}(L^2(\Omega), \mathbb{R}^p)$. The initial state x_0 is supposed to be known on ω_1 but not on ω_2. The authors suggest a method to identify within these controls law v_i, $i \geq 0$ making the system insensitive to the impact of these unknown parameters β. The case of the disturbances infecting a linear system's initial state has been investigated in Kolmanovsky and Gilbert (1998) and Namerikawa et al. (2004).

The sentinel theory was initiated and developed by Lions in (Lions, 1992; Lions, 1988). Sawadogo (2020) have used the

DOI 10.2478/ama-2021-0029

sentinel method to control the migration by studying the dynamics of a single species population and whose initial distribution is unknown.

In the literature, the notion of maximal output set is of great significant in the area of control and analysis of linear and nonlinear systems. Numerous studies have been carried out on the construction of the maximal output set (El Bhih et al., 2020; Yamamoto, 2019; Osorio and Ossareh, 2018; Abdelhak and Rachik, 2019; Gilbert and Tan, 1991). Different algorithms have been included in the research literature to specify the maximal state constraint sets (Gilbert and Tan, 1991; Dórea and Hennet, 1996).

1.2. Problem statement

A fundamental requirement for most dynamical systems is to keep a given output function insensitive to the disturbances. In this paper, we suppose that the initial state of the system is composed of two parts: the unknown part noted as $\hat{\tau}_0$ and the known part noted as τ_0. We propose a new technique to characterise the set $\chi(\hat{\tau}_0, \epsilon)$ of all possible gain matrix K, based on the maximal output set $\Upsilon(K, \epsilon)$, so that the sensitivity of the resulting system output would be relatively tolerable, that is, make the system insensitive to the unknown part $\hat{\tau}_0$ of the initial state x_0, of commensurate fractional order discrete-time controlled linear systems which are modelled by equations of fractional state space. To the best of our knowledge, the output sensitivity of such systems has not been treated yet. We propose some new sufficient conditions that ensure the finite determination of the set $\chi(\hat{\tau}_0, \epsilon)$. Moreover, we present an effective algorithm to obtain the maximal output set $\Upsilon(K, \epsilon)$ and then the set $\chi(\hat{\tau}_0, \epsilon)$. The algorithm having theoretical convergence properties are provided in Gilbert and Tan (1991).

Therefore, we study a discrete-time linear control systems of fractional order with uncertainty on the initial state, evolving on $\mathbb{R}^n$. More precisely, we consider the system as

$$\begin{cases} \Delta^\alpha x_{i+1} = Ax_i + Bu_i, & i \geq 0 \\ x_0 = \tau_0 + \hat{\tau}_0 \in \mathbb{R}^n \end{cases} \tag{2}$$

The corresponding output is

$$y_i = Cx_i, \quad i \geq 0 \tag{3}$$

where A is a matrix of order $n \times n$, the system dynamics, B is the input matrix of order $n \times m$ and C is the output matrix of order $p \times n$; α is the order of the derivative, τ_0 is the known part, $\hat{\tau}_0$ is the unknown part and $u_i = Kx_i$ is the feedback control.

The remainder of this paper is organised as follows: In Section 2, we recall a fundamental definition of fractional derivatives (Grünwald-Letnikov), then we consider the discrete-time system proposed in Dzieliński and Sierociuk (2005). With uncertainty on the initial state, we recall the Krein–Millman theorem and some definitions. Section 3 deals with the characterisation of the set of all possible gain matrices which make the system insensitive to the unknown part, based on the maximal output set. New sufficient conditions are provided to show the finite determination of such set. In Section 4, we propose an algorithm approach to identify the index of admissibility. We illustrate some examples and numerical simulations in Section 5. We conclude the paper by in Section 6.

Notation: $\mathbb{R}^n$ the set of real vectors with n components, $\mathcal{L}(\mathbb{R}^n, \mathbb{R}^n)$ the set of real matrices of order $n \times n$, $\mathbb{N}$ the set of nonnegative integers, $\sigma_s^k = \{s, s+1, \ldots, k\} \subset \mathbb{N}$ where $s \leq k$, I_n denotes the identity matrix in $\mathcal{L}(\mathbb{R}^n, \mathbb{R}^n)$. The components of a vector b are noted as $(b)_j$ and the components of a matrix A are noted as $(A)_{ij}$.

2. FRACTIONAL CALCULUS AND DYNAMIC MODELS

To begin our work, we will introduce certain basic notions concerning the fractional calculus that are utilised along the paper. The definition of the discrete fractional derivative in this paper is as follows: Grünwald–Letnikov (Oldham and J. Spanier, 1974; Podlubny, 1999).

Definition 1. The Grünwald–Letnikov (backward) difference of fractional order α of the function $x(.)$ at $k \in [0, +\infty[$ is given as

$$\Delta^\alpha x(k) = \frac{1}{h^\alpha} \sum_{j=0}^{k} (-1)^j \binom{\alpha}{j} x(k-j), \tag{4}$$

where the order of the derivative $\alpha \in]0,1[$, $h \in \mathbb{R}^{*+}$ is a sampling period taken equal to unity in all what follows, and $k \in \mathbb{N}$ is the number of samples for which the approximation of the derivative is calculated.

The term $\binom{\alpha}{j}$ in Definition 2 can be obtained from the following relation:

$$\binom{\alpha}{j} = \begin{cases} 1 & \text{for} \quad j = 0, \\ \frac{\alpha(\alpha-1)\ldots(\alpha-j+1)}{j!} & \text{for} \quad j > 0. \end{cases} \tag{5}$$

Let us consider now the discrete-time linear fractional order system as defined in Dzieliński and Sierociuk (2005), described as

$$\begin{cases} \Delta^\alpha x_{i+1} = Ax_i + Bu_i, \\ x_0 = \tau_0 + \hat{\tau}_0 \in \mathbb{R}^n \end{cases} \tag{6}$$

where $A \in \mathcal{L}(\mathbb{R}^n, \mathbb{R}^n)$ is the system dynamics, $B \in \mathcal{L}(\mathbb{R}^m, \mathbb{R}^n)$ is the input matrix and $C \in \mathcal{L}(\mathbb{R}^n, \mathbb{R}^p)$ is the output matrix; α is the order of the derivative, τ_0 is the known part, $\hat{\tau}_0$ is the unknown part and

$$x_i = \begin{pmatrix} x_i^1 \\ x_i^2 \\ \vdots \\ x_i^n \end{pmatrix} \in \mathbb{R}^n$$

is the state variable.

The associated output function is

$$y_i = Cx_i \in \mathbb{R}^p$$

Its initial value is denoted by x_0. The control low (feedback control) is

$$u_i = Kx_i \in \mathbb{R}^m. \tag{7}$$

In this system, the differentiation order α is taken as the same for all the state variables $x_i^j, j = 1, 2, \ldots, n$, that is

$$\Delta^\alpha x_i = \begin{pmatrix} \Delta^\alpha x_i^1 \\ \Delta^\alpha x_i^2 \\ \vdots \\ \Delta^\alpha x_i^n \end{pmatrix}$$

This is referred to as commensurate order. We will propose a technique to determine among these controls as low which makes the system insensitive to the effect of the unknown part $\hat{\tau}_0$.

We replace $\Delta^\alpha x_{i+1}$ by its value; system (6) could be rewritten as

$$\begin{cases} x_{i+1} = \sum_{j=0}^{i} A_j x_{i-j}, \\ \\ x_0 = \tau_0 + \hat{\tau}_0 \in \mathbb{R}^n \end{cases} \tag{8}$$

where

$$A_0 = A + BK + \alpha I_n \tag{9}$$

and

$$A_j = -(-1)^{j+1} \binom{\alpha}{j+1} I_n, \quad \forall j \geq 1. \tag{10}$$

Remark 1. The model described in (8) can be classified as a discrete-time system with a time-delay in the state. For practical use, the number of simple taken into consideration needs to be reduced to the predefined number L called the memory length and $x_i = 0$ for $i < 0$ (Dzieliński and Sierociuk, 2008).

Thus, system (8) becomes

$$\begin{cases} x_{i+1} = \sum_{j=0}^{L} A_j x_{i-j}, \\ \\ x_0 = \tau_0 + \hat{\tau}_0 \in \mathbb{R}^n \end{cases} \tag{11}$$

Definition 2. The system given by (6) could be rewritten as an infinite dimensional system taking the form

$$\begin{pmatrix} x_{i+1} \\ x_i \\ x_{i-1} \\ \vdots \end{pmatrix} = \tilde{A} \begin{pmatrix} x_i \\ x_{i-1} \\ x_{i-2} \\ \vdots \end{pmatrix} + \tilde{B} u_i \quad , \qquad y_i = \tilde{C} \begin{pmatrix} x_i \\ x_{i-1} \\ x_{i-2} \\ \vdots \end{pmatrix}$$

where $\tilde{A} = \begin{pmatrix} A + \alpha I_n & A_1 & A_2 & \cdots \\ I_n & 0 & 0 & \cdots \\ 0 & I_n & 0 & \cdots \\ \vdots & \vdots & \vdots & \vdots \end{pmatrix}$, $\tilde{B} = \begin{pmatrix} B \\ 0 \\ 0 \\ \vdots \end{pmatrix}$ and $\tilde{C} = (C \quad 0 \quad 0 \quad \cdots)$.

Theorem 1 (*Dzieliński-Sierociuk, 2008) The system given by definition (2) is asymptotically stable if and only if* $\| \tilde{A} \| < 1$, *where* $\|.\|$ *denotes the matrix norm defined as* $max|\lambda_i|$, *where* λ_i *is the* i^{th} *eigenvalue of the matrix* $\tilde{A}$.

The general solution of (11) (Buslowicz, 1983) is given as

$$x_i = G_i x_0 \tag{12}$$

where

$$G_i = \begin{cases} I_n & \text{if} \quad i = 0 \\ \sum_{j=0}^{L} A_j G_{i-1-j} & \text{if} \quad i \geq 1 \end{cases} \tag{13}$$

with $G_i = 0, \quad \forall i < 0$.

Remark 2 From (12) and (13) for $\alpha = 1$ we have

$$x_i = (A + I + BK)^i x_0 \tag{14}$$

for which the corresponding solution of the linear discrete-time systems is

$$\begin{cases} x_{i+1} = (A + I) x_i + B u_i, \quad i \geq 0 \\ x_0 \in \mathbb{R}^n \end{cases} \tag{15}$$

Remark 3 In the case of noncommensurate order we have

$$\begin{cases} x_{k+1} &= \sum_{j=0}^{k} A_j x_{k-j} \\ x_0 &= \tau_0 + \hat{\tau}_0 \in \mathbb{R}^n \\ y_k &= C x_k, \quad k \geq 0 \end{cases} \tag{16}$$

where the matrices A_j are given as

$$A_0 = A + BK + \mathrm{diag}\left(\binom{\alpha_1}{1}, \ldots, \binom{\alpha_n}{1}\right) \tag{17}$$

and for all $j \geq 1$

$$A_j = -(-1)^{j+1} \mathrm{diag} \left\{ \overbrace{\binom{\alpha_1}{j+1}, \ldots, \binom{\alpha_n}{j+1}}^{n-\text{times}} \right\}. \tag{18}$$

If $A \subset \mathbb{R}^n$, then the convex hull of A is the smallest convex set containing A, that is, it consists of all finite convex combinations of elements in A. The closed convex hull of A is the closure of the convex hull of A. Now, we present the theorem of Krein–Milman (see Haim Brezis).

Theorem 2 (*Krein–Milman) Let* $K \subset \mathbb{R}^n$ *be a compact convex set. Then* K *coincides with the closed convex hull of its extreme points. In the following, we will assume that the unknown part* $\hat{\tau}_0 \in \Omega$, *where the set* $\Omega \subset \mathbb{R}^n$ *is a polytope convex of vertices* $w_1, w_2, \ldots, w_p$. *According to Krein–Milman theorem, the unknown part* $\hat{\tau}_0$ *could be written as follows:*

$$\hat{\tau}_0 = \sum_{j=1}^{p} \alpha_j w_j. \tag{19}$$

for some unknown coefficients $\alpha_1 \geq 0, \ldots, \alpha_p \geq 0$, such that $\sum_{j=1}^{p} \alpha_j = 1$.

Definition 3. (Larrache, 2020) An unknown part $\hat{\tau}_0$ is said to be ϵ −tolerable if the corresponding output satisfies the following condition:

$$\| \frac{\partial y_i}{\partial \alpha_j} \| \leq \epsilon, \quad \forall j \in \sigma_1^p, \quad \forall i \geq 0. \tag{20}$$

Otherwise, $\hat{\tau}_0$ is said to be ϵ −intolerable.

Definition 4. For a given $\epsilon > 0$, and a gain matrix $K \in \mathbb{R}^{m \times n}$, the set

$$\Upsilon(K, \epsilon) = \{x \in \mathbb{R}^n / \quad \| y_i \| = \| C G_i x \| \leq \epsilon, \quad \forall i \geq 0\} \tag{21}$$

is called the maximal output set.

Our goal is to characterise the set $\chi(\hat{\tau}_0, \epsilon)$ of all gain matrices K, which makes the systems insensitive to the unknown part $\hat{\tau}_0$, to be explicit as

$\chi(\hat{\tau}_0, \epsilon) = \{K \in \mathbb{R}^{m \times n} / \| \frac{\partial y_i}{\partial \alpha_j} \| \leq \epsilon, \quad \forall j \in \sigma_1^p, \quad \forall i \geq 0\}$.(22)

On the other hand, we have

$$\frac{\partial\, y_i}{\partial\, \alpha_j} = \frac{\partial\, C G_i (\tau_0 + \hat{\tau}_0)}{\partial\, \alpha_j} = C G_i w_j, \quad \forall j \in \sigma_1^p, \quad \forall i \geq 0. \tag{23}$$

This leads to

$\chi(\hat{\tau}_0, \epsilon) = \{K \in \mathbb{R}^{m \times n} / \| C G_i w_j \| \leq \epsilon, \forall j \in \sigma_1^p, \forall i \geq 0\}$.
(24)

In Remark 4, we will show the interest of introducing the set $\Upsilon(K, \epsilon)$ in the characterisation of $\chi(\hat{\tau}_0, \epsilon)$.

DOI 10.2478/ama-2021-0029

Remark 4 The set $\chi(\hat{\tau}_0,\epsilon)$ can be rewritten as

$$\chi(\hat{\tau}_0,\epsilon)=\{K\in\mathbb{R}^{m\times n}\ /\ w_j\in\Upsilon(K,\epsilon),\quad \forall j\in\sigma_1^p\}. \tag{25}$$

Therefore, system (6) is insensitive to the unknown part $\hat{\tau}_0$ if and only if $w_j\in\Upsilon(K,\epsilon),\quad \forall j\in\sigma_1^p$. In order to characterise the set $\Upsilon(K,\epsilon)$ and then our set $\chi(\hat{\tau}_0,\epsilon)$, we introduce the sets $\Upsilon^k(K,\epsilon),\quad k\geq 0$ defined as

$$\Upsilon^k(K,\epsilon)=\{x\in\mathbb{R}^n/\ \ \| y_i\|=\| CG_ix\|\leq\epsilon,\quad \forall i\in\sigma_0^k\}. \tag{26}$$

3. CHARACTERISATION OF THE MAXIMAL OUTPUT SET $\boldsymbol{\Upsilon}\ (\mathbf{K},\boldsymbol{\epsilon})$

The main purpose of this section is to characterise, under certain hypothesis, the maximal output set $\Upsilon(K,\epsilon)$ and then the set $\chi(\hat{\tau}_0,\epsilon)$. We prove the finite determination of the set $\Upsilon(K,\epsilon)$ and then the set $\chi(\hat{\tau}_0,\epsilon)$, and this leads to the algorithmic procedure for the computation of such set.

Definition 5. (Gilbert, 1991; Rachik, 2002) The set $\Upsilon(K,\epsilon)$ is said to be finitely determined, if there exists an integer k such that $\Upsilon(K,\epsilon)=\Upsilon^k(K,\epsilon)$. Let k^* be the smallest integer such that $\Upsilon(K,\epsilon)=\Upsilon^{k^*}(K,\epsilon)$; we call k^* the admissibility index.

Remark 5 $\{\Upsilon^k(K,\epsilon)\}_{k\geq 0}$ is a decreasing sequence, that is, $\forall k\leq s$ we have

$$\Upsilon(K,\epsilon)\subset\Upsilon^s(K,\epsilon)\subset\Upsilon^k(K,\epsilon). \tag{27}$$

Proposition 1. *The set $\Upsilon(K,\epsilon)$ of some gain matrix K is*
(i) Convex,
(ii) Symmetric,
(iii) Contain the origin in its interior,
(iv) Closed.

Proof. (i), (ii) and (iii) from the definition of $\Upsilon(K,\epsilon)$.
(iv) We define for each $k\in\mathbb{N}$ the function T_k as

$$\begin{aligned} T_k:\quad &\mathbb{R}^n \longrightarrow \mathbb{R}^p\\ &x \longmapsto CG_kx. \end{aligned} \tag{28}$$

Then

$$\Upsilon(K,\epsilon)=\cap_{k\geq 0}T_k^{-1}(B(0,\epsilon)) \tag{29}$$

where $B(0,\epsilon)=\{x\in\mathbb{R}^p/\ \|x\|\leq\epsilon\}$.

Since $B(0,\epsilon)$ is closed and $(T_k)_{k\geq 0}, k\in\mathbb{N}$ are continuous functions, then $T_k^{-1}(B(0,\epsilon)), k\in\mathbb{N}$ are closed. Therefore $\Upsilon(K,\epsilon)$ is closed.

We give a necessary condition ensuring the finite determination of the set $\Upsilon(K,\epsilon)$ and then the set $\chi(\hat{\tau}_0,\epsilon)$.

Proposition 2. *If $\Upsilon(K,\epsilon)$ is finitely determined, then there exists an integer k^* such that $\Upsilon^{k^*}(K,\epsilon)=\Upsilon^{k^*+1}(K,\epsilon)$.*

Proof. Suppose $\Upsilon(K,\epsilon)$ is finitely determined. Then

$$\exists k\in\mathbb{N},\qquad \Upsilon(K,\epsilon)=\Upsilon^k(K,\epsilon). \tag{30}$$

On the other hand

$$\Upsilon^k(K,\epsilon)=\Upsilon(K,\epsilon)\subset\Upsilon^{k+1}(K,\epsilon)\subset\Upsilon^k(K,\epsilon) \tag{31}$$

since $\{\Upsilon^k(K,\epsilon)\}_{k\geq 0}$ is a decreasing sequence.

This leads to

$$\Upsilon^k(K,\epsilon)=\Upsilon^{k+1}(K,\epsilon),\qquad \text{for some } k\geq 0 \tag{32}$$

which completes the proof.

An efficient result is then introduced that permits us to determine the set $\Upsilon(K,\epsilon)$ through a finite number of inequations and then the set $\chi(\hat{\tau}_0,\epsilon)$ leads also to the generation of an algorithmic approach to obtain admissibility index k^*. In our study, we consider two cases:
First case: $p=n$ (i.e. the observation space and the state space have the same dimension).
Second case: $p<n$.
First case, $p=n$. In this case C is an $n\times n$ matrix.

Proposition 3. *Suppose the following assumptions hold:*
(i) $\sum_{j=0}^{L}\| A_j\|\leq 1$ and $\Upsilon^k(K,\epsilon)=\Upsilon^{k+1}(K,\epsilon)$ for some k,
(ii) C commutes with A_j for all $0\leq j\leq L$.
Then $\Upsilon(K,\epsilon)$ is finitely determined.

Proof. Clearly $\Upsilon(K,\epsilon)\subset\Upsilon^k(K,\epsilon)$. Let $x_0\in\Upsilon^k(K,\epsilon)$, then

$$\| CG_ix_0\|\leq\epsilon,\quad \forall i\leq k+1.$$

But

$$\| CG_{k+2}x_0\|=\| C\left(\sum_{j=0}^{L}A_jG_{k+1-j}\right)x_0\|$$

$$=\|\sum_{j=0}^{L}\left(CA_jG_{k+1-j}x_0\right)\|$$

$$=\|\sum_{j=0}^{L}\left(A_jCG_{k+1-j}x_0\right)\|$$

$$\leq\sum_{j=0}^{L}\| A_j\|\| CG_{k+1-j}x_0\|$$

$$\leq\epsilon\sum_{j=0}^{L}\| A_j\|$$

since $\| CG_{k+1-j}x_0\|\leq\epsilon,\quad \forall j\in\sigma_0^L$.

Now, using the assumption $\sum_{j=0}^{L}\| A_j\|\leq 1$; it follows that

$$\| CG_{k+2}x_0\|\leq\epsilon.$$

By iteration, we show that

$$\| CG_{k+j}x_0\|\leq\epsilon,\qquad \forall j\geq 2$$

That is,

$$\| CG_ix_0\|\leq\epsilon,\qquad \forall i\geq k+2.$$

Consequently,

$$\| CG_ix_0\|\leq\epsilon,\qquad \forall i\geq 0$$

This leads to

$$x_0\in\Upsilon(K,\epsilon)$$

and complete the proof.

Second case: $\dim B(0,\epsilon)=p<n$.
Since the matrix $C\in\mathcal{L}(\mathbb{R}^n,\mathbb{R}^p)$, we define $\hat{C}$ and $\hat{B}(0,\epsilon)$ as

$$\hat{C}=\begin{pmatrix}C\\0\end{pmatrix}\in\mathcal{L}(\mathbb{R}^n,\mathbb{R}^n)$$

sciendo
DOI 10.2478/ama-2021-0029 acta mechanica et automatica, vol.15 no.4 (2021)

$\widehat{B}(0,\epsilon) = B(0,\epsilon) \times \{0_{\mathbb{R}^{n-p}}\} \subset \mathbb{R}^n$.

Now considering the new observation $\hat{y}_i = \hat{C}x_i$, we easily verify that, for every integer i

$y_i \in B(0,\epsilon) \Leftrightarrow \hat{y}_i \in \widehat{B}(0,\epsilon)$.

Remark 6 The set $\Upsilon(K,\epsilon)$ associated to C and $B(0,\epsilon)$ is equal to the set $\Upsilon(K,\epsilon)$ associated to $\hat{C}$ and $\widehat{B}(0,\epsilon)$.
Since $\dim \widehat{B}(0,\epsilon) = n$, then the result of the first case can be applied to deduce the following proposition.
Proposition 4. *Suppose the following assumptions hold:*
(i) $\sum_{j=0}^{L} \| A_j \| \leq 1$ *and* $\Upsilon^k(K,\epsilon) = \Upsilon^{k+1}(K,\epsilon)$ *for some* k
(ii) $\hat{C}$ *commutes with* A_j *for all* $0 \leq j \leq L$.
Then $\Upsilon(K,\epsilon)$ *is finitely determined.*
Proposition 5. *If* $\| G_k \| \leq \eta_k, \quad \forall k \geq 0$ *with* $\eta_k \longrightarrow 0$ *as* $k \longrightarrow \infty$ *then* $\Upsilon(K,\epsilon)$ *is finitely determined*.
Proof. Let $k \in \mathbb{N}$ and $x \in \mathbb{R}^n$. Then

$\| CG_k x \| \leq \| C \| \| G_k \| \| x \|$

$\leq \eta_k \| C \| \| x \|$

And since η_k converges to zero when $k \longrightarrow \infty$ we deduce that

$$\| CG_k x \| \leq \epsilon, \quad \forall k \geq k_0 \quad \text{for certain} \quad k_0 \geq 0. \tag{33}$$

Let $x_0 \in \Upsilon^{k_0}(K,\epsilon)$. Then

$\| CG_i x_0 \| \leq \epsilon, \quad \forall i \in \sigma_0^{k_0}$

using this time Eq. (33) we obtain

$\| CG_{k_0+1} x_0 \| \leq \epsilon \quad \text{since} \quad k_0 + 1 \geq k_0$.

Hence

$x_0 \in \Upsilon^{k_0+1}(K,\epsilon)$

which completes the proof.

4. ALGORITHMIC DETERMINATION

As a direct consequence of Propositions 3 and 4, we propose in this section a procedure to determine k^*, index of admissibility, and consequently the sets $\Upsilon(K,\epsilon)$ and $\chi(\hat{\tau}_0,\epsilon)$.
Let $\mathbb{R}^p$ be endowed with the following norm:

$$\|x\|_\infty = \max_{1\leq i\leq p} |(x)_i|, \qquad \forall x \in \mathbb{R}^p.$$

We remark that

$\Upsilon^k(K,\epsilon) = \Upsilon^{k+1}(K) \Leftrightarrow \Upsilon^k(K,\epsilon) \subset \Upsilon^{k+1}(K,\epsilon)$

since $\Upsilon^{k+1}(K,\epsilon) \subset \Upsilon^k(K,\epsilon)$.
Thus

$$\begin{aligned}
&\Upsilon^k(K,\epsilon) = \Upsilon^{k+1}(K,\epsilon) \\
&\Leftrightarrow \forall x \in \Upsilon^k(K,\epsilon), \quad \|CG_{k+1}x\|_\infty \leq \epsilon \\
&\Leftrightarrow \forall x \in \Upsilon^k(K,\epsilon), \quad \left|(CG_{k+1}x)_j\right| - \epsilon \leq 0, \forall j \in \sigma_1^p \\
&\Leftrightarrow \sup_{|(CG_i x)_l| - \epsilon \leq 0, \forall l \in \sigma_1^p, \forall i \in \sigma_1^k} \left|(CG_{k+1}x)_j\right| - \epsilon \leq 0, \quad \forall j \in \sigma_1^p.
\end{aligned}$$

This leads to the following algorithm.
Algorithm: Determination of k^*
Require $n, p, L \in \mathbb{N}^*, C, G_i, \epsilon > 0$
$k \leftarrow 0$
for j=1, ...,p **do**
Maximise $J_j(x) = |(CG_{k+1}x)_j| - \epsilon$

Subjet to the constraints $\begin{cases} |(CG_i x)_l| - \epsilon \leq 0 \\ \forall l \in \sigma_1^p, \quad \forall i \in \sigma_0^k. \end{cases}$

end for
$J_j^* \leftarrow \max\{J_j(x)\}$
if $J_j^* \leq 0, \forall j = 1,2,\ldots,p$ **then**
$k^* \leftarrow k$
else
$k \leftarrow k+1$ and return to for
end else
Remark 7 The hypothesis of Proposition 5 in section (3) is sufficient but not necessary. If this condition is not provided, the stopping of the algorithm is not certain. The maximal output set $\Upsilon(K,\epsilon)$ is finitely determined and then the set $\chi(\hat{\tau}_0,\epsilon)$ if the algorithm converges, otherwise it is not.

5. NUMERICAL EXAMPLES

To demonstrate our achieved results, we present in the following section some examples in the two-dimensional case. We will determine the set $\Upsilon_\epsilon(K)$ and then the set $\chi(\hat{\tau}_0,\epsilon)$ as a finite number of inequations using our algorithm. Assuming

$$\textstyle\sum_{j=0}^{L} \| A_j \| < 1 \tag{34}$$

is checked in all the introduced examples, we will select the gain matrix K such that this condition (34) is verified.
Using the property that (Hilfer, 2000)

$$\sum_{j=0}^{L} (-1)^j \binom{\alpha}{j} = \frac{\Gamma(L+1-\alpha)}{\Gamma(1-\alpha)\Gamma(L+1)}$$

and the fact that

$$\textstyle\sum_{j=0}^{L} \| A_j \| = \| A + BK + \alpha I_n \| - \sum_{j=2}^{L} (-1)^j \binom{\alpha}{j} + \left|\binom{\alpha}{L+1}\right|$$

we deduce that the condition $\sum_{j=0}^{L} \| A_j \| < 1$ can be rewritten as follows:

$$\| A + BK + \alpha I_n \| - \sum_{j=2}^{L} (-1)^j \binom{\alpha}{j} + \left|\binom{\alpha}{L+1}\right| < 1$$

For example, for $L = 50$ and $\alpha = 0.4$, we have

$\sum_{j=0}^{L} \| A_j \| = \| A + BK + \alpha I_n \| + 0.4610$.

Then the matrix K must select such that

$\| A + BK + \alpha I_n \| < 0.5390$.

The dotted region will indicate the set $\Upsilon_\epsilon(K,\epsilon)$.
Example 1. *Let us consider the following system:*

$$\begin{cases} x_{i+1} = \sum_{j=0}^{i} A_j x_{i-j} \\ x_0 = \tau_0 + \hat{\tau}_0 \in \mathbb{R}^2 \end{cases}$$

DOI 10.2478/ama-2021-0029

where τ_0 and $\hat{\tau}_0$ are the known and unknown parts of the initial state, respectively.

Let $A, B, C, \alpha, \epsilon$ and L be defined as

$$A = \begin{pmatrix} -1.25 & \frac{11}{24} \\ \frac{5}{12} & -\frac{8}{7} \end{pmatrix}, \qquad B = \begin{pmatrix} 2 & -\frac{1}{3} \\ -\frac{1}{2} & 1 \end{pmatrix}$$

$$C = (1 \quad 2), \qquad \alpha = 0.7, \qquad \epsilon = 0.7, \qquad L = 20.$$

We have

$$A_j = -(-1)^{j+1} \binom{0.7}{j+1} I_2, \quad \forall j \in \{1, 2, \dots, L\}.$$

We select the gain matrix K such that $\| A_0 \| < 0.7395$ (since $\sum_{j=1}^{20} \| A_j \| = 0.2605$). For $K = \begin{pmatrix} 0.5 & 0 \\ 0 & 1 \end{pmatrix}$, we have

$$\widetilde{A} = A + BK = \begin{pmatrix} -\frac{1}{4} & \frac{1}{8} \\ \frac{1}{6} & -\frac{1}{7} \end{pmatrix}$$

$$A_0 = \widetilde{A} + \alpha I_2 = \begin{pmatrix} \frac{9}{20} & \frac{1}{8} \\ \frac{1}{6} & \frac{39}{70} \end{pmatrix}$$

and

$$\sum_{j=0}^{20} \| A_j \| = \| A_0 \| + \sum_{j=1}^{20} \| A_j \| = 0.9426 < 1$$

where $\| A_0 \| = \max_{1 \le j \le 2} \sum_{i=1}^{2} |(A_0)_{ij}|$.

In this example, we take τ_0 that belongs to a hexagon (a polygon with six sides), see Fig. 1.

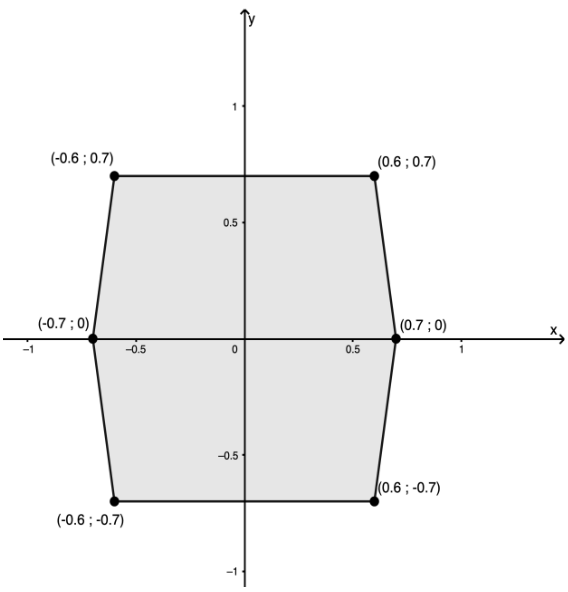

Fig. 1. The set Ω with vertices $w_1, w_2, \dots, w_6$.

$CG_0 \binom{x}{y}, \dots, CG_5 \binom{x}{y}$ are given by:

$$CG_0 \binom{x}{y} = x + 2y$$

$$CG_1 \binom{x}{y} = \frac{47}{60} x + \frac{347}{280} y$$

$$CG_2 \binom{x}{y} = \frac{2789}{4200} x + \frac{117\,409}{117\,600} y$$

$$CG_3 \binom{x}{y} = \frac{2091\,989}{3528\,000} x + \frac{7082\,557}{8232\,000} y$$

$$CG_4 \binom{x}{y} = \frac{267\,585\,763}{493\,920\,000} x + \frac{5303\,791\,039}{6914\,880\,000} y$$

$$CG_5 \binom{x}{y} = \frac{260\,274\,628\,301}{518\,616\,000\,000} x + \frac{3377\,530\,607\,827}{4840\,416\,000\,000} y.$$

Using our algorithm we obtain $k^* = 4$ and then

$$\Upsilon(K, \epsilon) = \left\{ \binom{x}{y} \in \mathbb{R}^2 \setminus \begin{array}{l} |x + 2y| \le 2 \\ \left|\frac{47}{60} x + \frac{347}{280} y\right| \le 2 \\ \left|\frac{2789}{4200} x + \frac{117\,409}{117\,600} y\right| \le 2, \\ \left|\frac{2091\,989}{3528\,000} x + \frac{7082\,557}{8232\,000} y\right| \le 2 \\ \left|\frac{267\,585\,763}{493\,920\,000} x + \frac{5303\,791\,039}{6914\,880\,000} y\right| \le 2 \end{array} \right\}.$$

We can see that $w_1 = \binom{0.7}{0}, w_2 = \binom{0.6}{0.7}, w_3 = \binom{-0.6}{0.7}, w_4 = \binom{-0.7}{0}, w_5 = \binom{-0.6}{-0.7}, w_6 = \binom{0.6}{-0.7} \in \Upsilon(K, \epsilon)$. Hence, the system is insensitive to the unknown part $\hat{\tau}_0$. Consequently, the gain matrix $K \in \chi(\hat{\tau}_0, \epsilon)$.

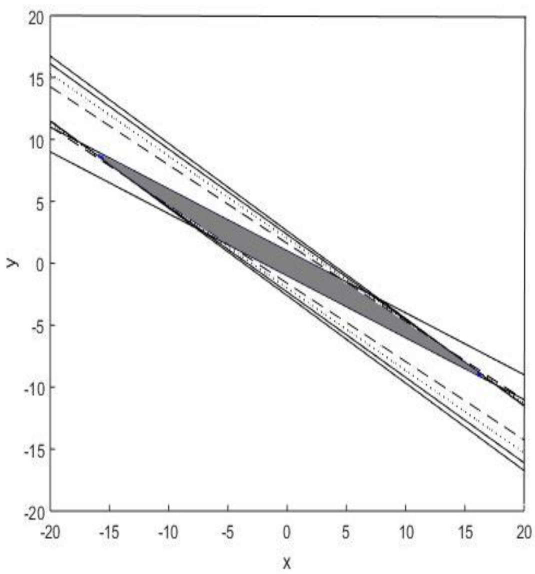

Fig. 2. The set $\Upsilon(K, \epsilon)$ corresponding to $K = \begin{pmatrix} 0.5 & 0 \\ 0 & 1 \end{pmatrix}$ and $\alpha = 0.7$

DOI 10.2478/ama-2021-0029 acta mechanica et automatica, vol.15 no.4 (2021)

Example 2. *Consider the following system:*

$$\begin{cases} x_{i+1} = \sum_{j=0}^{i} A_j x_{i-j} \\ x_0 = \tau_0 + \hat{\tau}_0 \in \mathbb{R}^2 \end{cases}$$

where τ_0 and $\hat{\tau}_0$ are the known and unknown parts of the initial state, respectively, and $A, B, K, C, \alpha, \epsilon$ are described as follows:

$$C = (2 \quad -1), \quad A = \begin{pmatrix} \frac{8}{7} & \frac{2}{3} \\ -\frac{17}{30} & -\frac{2}{9} \end{pmatrix}$$

$$B = \begin{pmatrix} -0.5 \\ \frac{1}{3} \end{pmatrix}, \qquad \alpha = 0.2, \qquad \epsilon = 0.8.$$

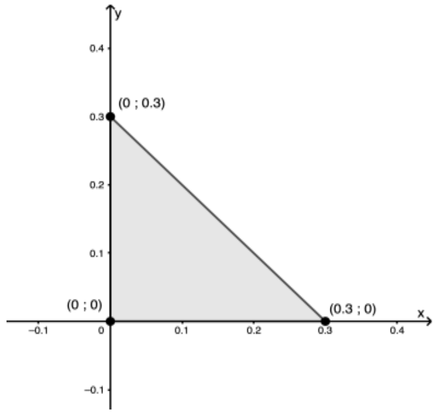

Fig. 3. The set Ω with vertice $w_1 = (0; 0), w_2 = (0.3; 0)$, $w_3 = (0; 0.3)$.

In this example, the memory length L is equal to 30 and we assume τ_0 to belong to a triangle (see Fig. 3). The matrices A_j are given as

$$A_0 = \widetilde{A} + \alpha I_2 = A + BK + \alpha I_2$$

and

$$A_j = -(-1)^{j+1} \binom{\alpha}{j+1} I_3, \qquad j = 1, \dots, L.$$

We select the gain matrix K such that $\| A_0 \| < 0.6311$ (since $\sum_{j=1}^{30} \| A_j \| = 0.3689$). For $K = (2 \quad 1)$ we have

$$A_0 = \begin{pmatrix} \frac{12}{35} & \frac{1}{6} \\ \frac{1}{10} & \frac{14}{45} \end{pmatrix}$$

and

$$\sum_{j=0}^{30} \| A_j \| = \| A_0 \| + \sum_{j=1}^{30} \| A_j \| = 0.8467 < 1$$

where $\| A_0 \| = \max_{1 \le j \le 2} \sum_{i=1}^{2} |(A_0)_{ij}|$.

On the other hand, we have

$$CG_0 \begin{pmatrix} x \\ y \end{pmatrix} = (2 \quad -1) \begin{pmatrix} x \\ y \end{pmatrix} = 2x - y$$

$$CG_1 \begin{pmatrix} x \\ y \end{pmatrix} = (2 \quad -1) \begin{pmatrix} \frac{12}{35} & \frac{1}{6} \\ \frac{1}{10} & \frac{14}{45} \end{pmatrix} \begin{pmatrix} x \\ y \end{pmatrix} = \frac{41}{70} x + \frac{1}{45} y$$

$$CG_2 \begin{pmatrix} x \\ y \end{pmatrix} = (2 \quad -1) \begin{pmatrix} \frac{3149}{14\,700} & \frac{103}{945} \\ \frac{103}{1575} & \frac{1567}{8100} \end{pmatrix} \begin{pmatrix} x \\ y \end{pmatrix} = \frac{1601}{4410} x + \frac{1391}{56\,700} y$$

$$CG_3 \begin{pmatrix} x \\ y \end{pmatrix} = (2 \quad -1) \begin{pmatrix} \frac{369\,917}{2315\,250} & \frac{197\,527}{2381\,400} \\ \frac{197\,527}{3969\,000} & \frac{91\,838}{637\,875} \end{pmatrix} \begin{pmatrix} x \\ y \end{pmatrix} = \frac{7495\,319}{27\,783\,000} x + \frac{391\,441}{17\,860\,500} y.$$

We have used the relation $G_k = \sum_{j=0}^{L} A_j G_{k-1-j}, k \ge 1$ to find the matrices G_k. Using our algorithm we obtain $k^* = 1$ and then the set $\Upsilon(K, \epsilon)$

$$\Upsilon(K, \epsilon) = \left\{ \begin{pmatrix} x \\ y \end{pmatrix} \in \mathbb{R}^2 \setminus \begin{array}{c} |2x - y| \le 0.8 \\ \left|\frac{41}{70} x + \frac{1}{45} y\right| \le 0.8 \end{array} \right\}.$$

Since $w_1 = \begin{pmatrix} 0 \\ 0 \end{pmatrix}, w_2 = \begin{pmatrix} 0.3 \\ 0 \end{pmatrix}, w_1 = \begin{pmatrix} 0 \\ 0.3 \end{pmatrix} \in \Upsilon(K, \epsilon)$, we deduce that the unknown part $\hat{\tau}_0$ does not influence the associated output function. In this case, the chosen matrix K belongs to $\chi(\hat{\tau}_0, \epsilon)$, so it is useful.

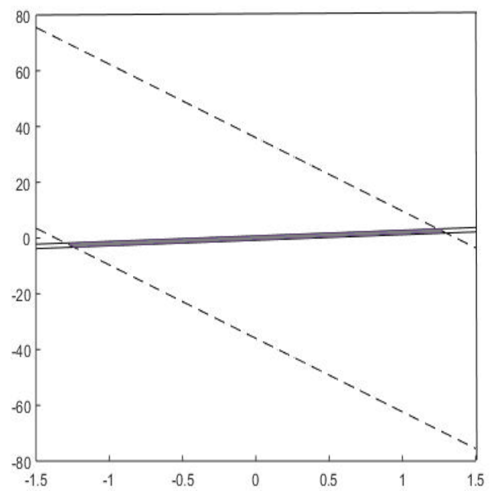

Fig. 4. The set $\Upsilon(K, \epsilon)$ is associated to $K = (2 \quad 1)$ and $\alpha = 0.2$.

Example 3. *For*

$$A = \begin{pmatrix} \frac{37}{12} & -\frac{15}{8} \\ \frac{1}{10} & -\frac{15}{8} \end{pmatrix}, \quad B = \begin{pmatrix} 3 & 1 \\ 0 & 1 \end{pmatrix}$$

$$K = \begin{pmatrix} -1 & 0 \\ 0 & 2 \end{pmatrix}, \quad C = (1 \quad -1)$$

$$\varepsilon = 0.1, \quad \alpha = 0.1, \quad L = 8$$

we obtain

$$CG_0 \begin{pmatrix} x \\ y \end{pmatrix} = x - y$$

$$CG_1\begin{pmatrix}x\\y\end{pmatrix}=(1\quad -1)\begin{pmatrix}\frac{11}{60} & \frac{1}{8}\\ \frac{1}{10} & \frac{9}{40}\end{pmatrix}\begin{pmatrix}x\\y\end{pmatrix}=\frac{1}{12}x-\frac{1}{10}y$$

$$CG_2\begin{pmatrix}x\\y\end{pmatrix}=(1\quad -1)\begin{pmatrix}\frac{41}{450} & \frac{49}{960}\\ \frac{49}{1200} & \frac{173}{1600}\end{pmatrix}\begin{pmatrix}x\\y\end{pmatrix}=\frac{181}{3600}x-\frac{137}{2400}y$$

$$CG_3\begin{pmatrix}x\\y\end{pmatrix}=C\begin{pmatrix}\frac{25\,297}{432\,000} & \frac{3283}{115\,200}\\ \frac{3283}{144\,000} & \frac{13\,067}{192\,000}\end{pmatrix}\begin{pmatrix}x\\y\end{pmatrix}=\frac{1931}{54\,000}x-\frac{11\,393}{288\,000}y$$

$$CG_4\begin{pmatrix}x\\y\end{pmatrix}=C\begin{pmatrix}\frac{56\,471\,173}{1296\,000\,000} & \frac{270\,829}{13\,824\,000}\\ \frac{270\,829}{17\,280\,000} & \frac{28\,859\,813}{576\,000\,000}\end{pmatrix}\begin{pmatrix}x\\y\end{pmatrix}=$$
$$\frac{18\,079\,499}{648\,000\,000}x-\frac{26\,362\,907}{864\,000\,000}y$$

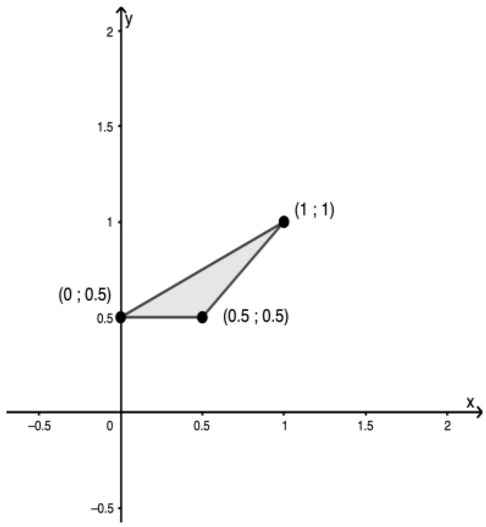

Fig. 5. The set Ω with vertices
$w_1=(0.5;0.5), w_2=(0;0.5), w_3=(1;1)$.

In this example, we assume τ_0 belongs to a triangle (see Fig. 4). Using our algorithm, we obtain $k^*=3$, and then the set

$$\Upsilon(K,\epsilon)=\left\{\begin{pmatrix}x\\y\end{pmatrix}\in\mathbb{R}^2/\begin{array}{l}|x-y|\le 0.1\\ \left|\frac{1}{12}x-\frac{1}{10}y\right|\le 0.1\\ \left|\frac{181}{3600}x-\frac{137}{2400}y\right|\le 0.1\\ \left|\frac{1931}{54\,000}x-\frac{11\,393}{288\,000}y\right|\le 0.1\end{array}\right\}$$

Since $w_1=\begin{pmatrix}0.5\\0.5\end{pmatrix}, w_2=\begin{pmatrix}1\\1\end{pmatrix}\in\Upsilon(K,\epsilon)$ and $w_3=\begin{pmatrix}0\\0.5\end{pmatrix}\notin\Upsilon(K,\epsilon)$, we conclude that the system is influenced by the unknown part $\hat{\tau}_0$. Thus $K=\begin{pmatrix}-1 & 0\\0 & 2\end{pmatrix}\notin\chi(\hat{\tau}_0,\epsilon)$.

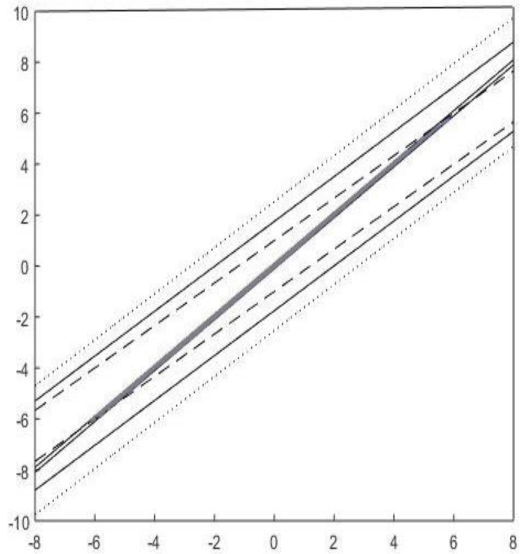

Fig. 6. The set $\Upsilon(K,\epsilon)$ corresponding to $K=\begin{pmatrix}-1 & 0\\0 & 2\end{pmatrix}$ and $\alpha=0.1$.

In examples 1–3, we have identified the set of all possible gain matrices which make the system insensitive to the unknown part $\hat{\tau}_0$ of the initial state x_0 via a finite number of inequations using Algorithm 1 based on the simplex method, which allow solving problems of maximisation that arise in such algorithm. In Figs. 1–3, we have traced the constraints constituting the sets $\Upsilon(K,\epsilon)$.

6. CONCLUSION

In this paper, we have studied the problem of fractional order discrete-time controlled linear systems with unknown part of the initial state using the Grünwald–Letnikov fractional derivative. We have investigated the characterisation of the set $\chi(\hat{\tau}_0,\epsilon)$ of all possible gain matrices so that the sensitivity of the resulting system output would be relatively tolerable based on the study of maximal output set. Some new sufficient conditions to ensure the finite determination of $\chi(\hat{\tau}_0,\epsilon)$ are given. Furthermore, a useful algorithm is produced to identify the index of admissibility k^* and then the set $\chi(\hat{\tau}_0,\epsilon)$. The theoretical results are shown by various examples and numerical simulation. As a natural continuation of this work, we are studying the following problem.

REFERENCES

1. **Abdelhak A. , M. Rachik M.** (2019), Model reduction problem of linear discrete systems: Admissibles initial states, *Archives of Control Sciences*, volume 29(LXV), no. 1, pages 41-55, 2019.
2. **Abdelilah LarracheL., Mustapha LhousL., Soukaina Ben B.RhilaR., Mostafa Rachik R. Abdessamad TridaneT.** (2020), An output sensitivity problem for a class of linear distributed systems with uncertain initial state, *Archives of Control Sciences*, volume 30(LXVI), no. 1, pages 139-155, 2020.
3. **Amine El Bhih.B., Youssef BenfatahB., Mostafa RachikR.** (2020), Exact determination of maximal output admissible set for a class of semilinear discrete systems, *Archives of Control Sciences*, ACS volume 30(LXVI), no. 3, pages 523-552, 10.24425/acs.2020.134676, 2020.

4. **Andrzej Dzielinski A., and Dominik Sierociuk D.** (2008), Stability of Discrete Fractional Order State-space Systems. *Journal of Vibration and Control*, 14: 1543, 2008.
5. **Arild Thomson A.** (2007), *International journal of systems science, Identifiability of dynamic systems*, volume 9, pages 813-825, Issue 2007.
6. **Balatif, O., Rachik, M., Labriji, E. houssine, Rachik, Z**. (2016).), Optimal control problem for a class of bilinear systems via block pulse functions. *IMA Journal of Mathematical Control and Information*, dnw005. doi:10.1093/imamci/dnw005.
7. **Buslowicz M.** (1983), On some properties of the solution of state equation of discrete-time systems with delays, *Zesz.Nauk. Polit. Bial., Elektrotechnika*, vol. 1, pp. 17-29, 1983 in Polish.
8. **Chi-Tsong ehenE.** (2008), *Analog and Digital control system design transfer-function, state space, Algebraic Methods*. State University of New York at Stony Broak, Springer 2008.
9. **Chraïbi, L., Karrakchou, J**., **Rachik, M., Ouansafi, A**. (2006),. Linear quadratic control problem with a terminal convex constraint for discrete-time distributed systems. *IMA Journal of Mathematical Control and Information*, 23(3), 347-370. doi:10.1093/imamci/dni063.
10. **D.W.Gu D.W., P.Hr.Petkov P.Hr. and, M.M.Konstantinov M.M.** (2005), *Robust control design with Matlab*, Springer 2005..
11. **Debnath L.** (2003.), Recent Applications of Fractional Calculus to Science and Engineering. *IJMMS, Hindawi Publishing*, volume 54, pp. 3413-3442, 2003.
12. **Dórea, C. E. T., and Hennet, J. C.** (1996), Computation of Maximal Admissible Sets of Constrained Linear Systems, *Proceedings of the 4th IEEE Mediterranean Symposium on New Directions on Control and Automation*, Maleme, Greece, pp. 286291, 1996.
13. **Dzieliński and A.D., Sierociuk D.** (2005), Adaptive Feedback Control of Fractional Order Discrete-Time State-Space Systems. *Proceedings of the 2005 International Conference on Computational Intelligence for Modelling, Control and Automation, and International Conference on Intelligent Agents*, Web Technologies and Internet Commerce, CIMCA-IAWTIC'05, 2005.
14. **Ferreira, R.A.C., and Torres, D.F.M**. (2011), Fractional h-Difference Equations Arising from the Calculus of Variations, *Applicable Analysis and Discrete Mathematics*, 5, 110-121, 2011.
15. **Franklin** (2001), *Feedback control of dynamic systems*, 5th edition, springer 2001.
16. **Gilbert E. G. and , Tan K. T.** (1991), Linear systems with state and control constraints: the theory and application of maximal output admissible sets, in *IEEE Transactions on Automatic Control*, vol. 36, no. 9, pp. 1008-1020, Sept 1991.
17. **Haim BrezisB.**, *Functional Analysis, Sobolev Spaces and Partial Differential Equations*, ISBN 978-0-387-70913-0, doi:10.1007/978-0-387-70914-7.
18. **Hilfer, R., ed**. (2000), *Application of Fractional Calculus in Physics*, World Scientific, Singapore, 2000.
19. **J.L.Lions J.L.** (1988,), Sur les sentinelles des systèmes distribués.C.R.A.S. Paris, t. 307. Le cas des conditions initiales incomplètes, p. 819-893. *Conditions frontières, termes sources. coefficients incomplètement connus,* p.865-870, 1988..
20. **Joycer OsorioO., Hamid R. OssarehO.** (2018), A Stochastic Approach to Maximal Output Admissible Sets and Reference Governors, *Control Technology and Applications* (CCTA) 2018 IEEE Conference on, pp. 704-709, 2018.
21. **Kaczorek, T.** (2007), Reachability and Controllability to Zero of Cone Fractional Discrete-time Systems, *Archives of Control Sciences*, 17, 357-367, 2007.
22. **Kaczorek, T.** (2008), Reachability of Fractional Positive Continuous-time Linear Systems, *International Journal of Applied Mathematics and Computer Science*, 18, 223-228, 2008.
23. **Kauffmann. M, Bretthawer. G**., Identifiability of the linear closed loop systems, *Control Systems, Robotics and Automation*, volume V, pages 127-138.
24. **Kilbas A. A., Srivastava H. M. and , Trujillo**. **J. J.** (2006), *Theory and Application of Fractional Differential Equations North Holland Mathematics Studies*, Editor Jan van Mill, Elsevier, 2006.
25. **Kolmanovsky I., Gilbert E.G.** (1998), Theory and computation of disturbance invariance sets for discrete-time linear systems, *Mathematical Problems in Engineering: Theory, Methods and Applications*, vol. 4, pp. 317-367, 1998.
26. **Lions J.L.** (1992), *Sentinelles pour les systèmes distribués à données incomplètes,* Recherches en Mathematiques Appliquées 21, Masson, Paris, 1992.
27. **Lions, J.L**. (1988), Sentinels for periodic distributed systems. *Chinese Annals of Math* B. Vol. 10. p 213-225.
28. **Namerikawa T., W. Shinozuka W. , and M., Fujita M.** (2004), : Disturbance and Initial State Uncertainty Attenuation Control for Magnetic Bearings, In *Proceedings 9th International Symposium on Magnetic Bearings*, pp. 3-6, 2004..
29. **Ogata Katsuhiko O.** (1995), *Discrete time control systems*, Prentice Hall internatiounal editions 1995.
30. **Oldham K. B. and ., J. Spanier J.** (1974),. *The Fractional Calculus*. Academic Press, 1974.
31. **Podlubny I.** (1999*), Fractional Differential Equations*. Academic Press, 1999.
32. **Rachik M., M. Lhous M., A. Tridane A.** (2002), On the Maximal Output Admissible Set for a Class of Nonlinear Discrete Systems, *Systems Analysis Modelling Simulation*, 42:11, 1639-1658, DOI: 10.1080/716067174.
33. **Rachik, M., Lhous, M.** (2016), An observer-based control of linear systems with uncertain parameters. *Archives of Control Sciences*, 26(4), 565-576. doi:10.1515/acsc-2016-0031, 2016.
34. **Robert L.Payne R.L., Graham C.GoodwinG.** (2007), *International journal of control*, On the identifiability of linear systems, volume 20, Issues 5, 2007, pages 865-868.
35. **Rosario ToscanoT.** (2005), *Commande et diagnostic des systèmes dynamiques*, Ellipses 2005..
36. **Sawadogo S.** (2020), Control of a migration problem of a population by the sentinel method, *Journal of Nonlinear Evolution Equations and Applications*, Volume 2020, Number 3, pp. 37-53, March 2020..
37. **Sierociuk, D., and Dzieliński, A**. (2006,), Fractional Kalman Filter Algorithm for the States, Parameters and Order of Fractional System Estimation, *International Journal of Applied Mathematics and Computer Science*, 16, 129-140, 2006.
38. **Yamamoto K.** (2019), Time-variant feedback controller based on capture point and maximal output admissible set of a humanoid, *Advanced Robotics*, 33:18, 944-955, 2019.

Acknowledgements: The authors would like to thank the reviewer for his time to help improve this paper. Research reported in this paper was supported by the Moroccan Systems Theory Network.

Data Availability: The disciplinary data used to support the findings of this study have been deposited in the Network Repository (http://www.networkrepository.com).

Youssef Benfatah: https://orcid.org/0000-0001-9497-003X

Amine El Bhih: https://orcid.org/0000-0003-0877-5882

Mostafa Rachik: https://orcid.org/0000-0002-5118-2786

DOI 10.2478/ama-2021-0030

EVALUATION OF DIFFERENT BINDER COMBINATIONS OF CEMENT, SLAG AND CKD FOR S/S TREATMENT OF TBT CONTAMINATED SEDIMENTS

Per LINDH[*,**], **Polina LEMENKOVA**[***]

[*]Swedish Transport Administration, Gibraltargatan 7, Malmö, Sweden
[**]Lund University, Division of Building Materials, Box 118, SE-221-00, Lund, Sweden
[***]Université Libre de Bruxelles. École polytechnique de Bruxelles (Brussels Faculty of Engineering), Laboratory of Image Synthesis and Analysis, Bld. L, Campus de Solbosch, Avenue Franklin Roosevelt 50, Brussels 1000, Belgium

per.a.lindh@gmail.com, polina.lemenkova@ulb.be

received 29 July 2021, revised 20 September 2021, accepted 24 September 2021

Abstract: The seabed in the ports needs to be regularly cleaned from the marine sediments for safe navigation. Sediments contaminated by tributyltin (TBT) are environmentally harmful and require treatment before recycling. Treatment methods include leaching, stabilisation and solidification to remove toxic chemicals from the sediments and improve their strength for reuse in the construction works. This study evaluated the effects of adding three different binder components (cement, cement kiln dust (CKD) and slag) to treat sediment samples collected in the port of Gothenburg. The goal of this study is to assess the leaching of TBT from the dredged marine sediments contaminated by TBT. The various methods employed for the treatment of sediments include the application of varied ratios of binders. The project has been performed by the Swedish Geotechnical Institute (SGI) on behalf of the Cementa (HeidelbergCement Group) and Cowi Consulting Group, within the framework of the Arendal project. An experiment has been designed to evaluate the effects of adding CKD while reducing cement and slag for sediment treatment. Methods that have been adopted include laboratory processing of samples for leaching using different binder combinations, followed by statistical data processing and graphical plotting. The results of the experiment on leaching of TBT for all samples are tested with a varied ratio of cement, slag, CKD and water. Specimens with added binders 'cement/CKD' have demonstrated higher leaching compared to the ratio 'cement/slag/CKD' and 'cement/slag'. The 'CKD/slag' ratio has presented the best results followed by the 'cement/slag/CKD', and can be used as an effective method of s/s treatment of the sediments. The results have shown that the replacement of cement and slag by CKD is effective at TBT leaching for the treatment of toxic marine sediments contaminated by TBT.

Keywords: cement kiln dust, CKD, marine sediments, tributyltin, TBT, leaching, s/s soils

1. INTRODUCTION

The Cement Kiln Dust (CKD) is a fine-grained, solid, highly alkaline material and a by-product of cement (Barnat-Hunek et al., 2018). As an industrial solid waste material, it can be used for replacing cement as a stabiliser and a binary binder (Mansour, 2021). Adding CKD is an effective solution to stabilise the ground for the construction of infrastructure, buildings and roads (Rimal et al., 2019). Besides, adding CKD increases compressive strength (Ribeiro and Morelli, 2009; Shoaei et al., 2017; Shen et al., 2021), resistivity and durability of soils (Abdel-Gawwad et al., 2019; Yaseri et al., 2019). The benefits of CKD as an additive binder in cement consist in increased tensile strength and improved characteristics of cement (Baghriche et al., 2020; Silva et al., 2015). The CKD can be added in various ratios, to improve the properties of soils. Such experiments show a significant increase in compressive strength, for instance, obtained for a CKD–slag mixture with 70% of CKD and 30% of slag at a water/binder ratio of 0.40 (Chaunsali and Peethamparan, 2011). Further examples of the experimental CKD applications are presented in the existing papers (Sariosseiri & Muhunthan, 2008; Yoon et al., 2010; Ahmad et al., 2014; Adeyanju et al., 2020).

Massive amounts of cement produced annually lead to the increase of CKD as a by-product (Najim et al., 2014). Therefore, utilising CKD is quite economical and environmentally friendly contributing to sustainable development. For instance, rational economic reasons for the application of CKD include the reduced costs of the construction works (Al-Homidy et al., 2017), and optimised economic solutions regarding the workflow (Faisal et al., 2021). The environmental benefits of replacing cement by the CKD consist in reduced air pollution due to the decreased CO_2 emissions (Bagheri et al., 2020). Besides, CKD is efficient in wastewater treatment, acting as a coagulant in removing heavy metals (Hasaballah et al., 2021).

Marine sediments need to be regularly removed for safe navigation (Baltic Marine Environment Protection Commission, 2015; Akcil et al., 2015). However, dredged masses of the marine sediments should be treated before the reuse. The treatment includes stabilisation and removal of contaminants. Marine sediments are often contaminated by heavy metals, toxic chemicals and tributyltin (TBT), which presents an environmental problem in coastal regions (Sundqvist et al., 2009; Kim et al., 2011).

Large amounts of dredged sediments polluted by chemicals are harmful to marine ecosystems and human health (Evans, 1999; Antizar-Ladislao, 2008). The TBT belongs to the persistent

DOI 10.2478/ama-2021-0030 acta mechanica et automatica, vol.15 no.4 (2021)

pollutants especially harming the marine environment. Originated as paints on ships protecting hulls against fouling during constructions (Wojtkiewicz et al., 2015; Alzieu, 2000), the TBT has been prohibited since 1989 (Blanck & Dahl, 1998). However, certain amounts of TBT remain in the waters of the Baltic Sea with negative consequences on the environment (Abraham et al., 2017; Eklund & Watermann, 2018). Treatment of the marine sediments contaminated by TBT required the development of special methods (Berto et al., 2007; Furdek Turk et al., 2020; Sheikh et al., 2020; Bandara et al., 2021).

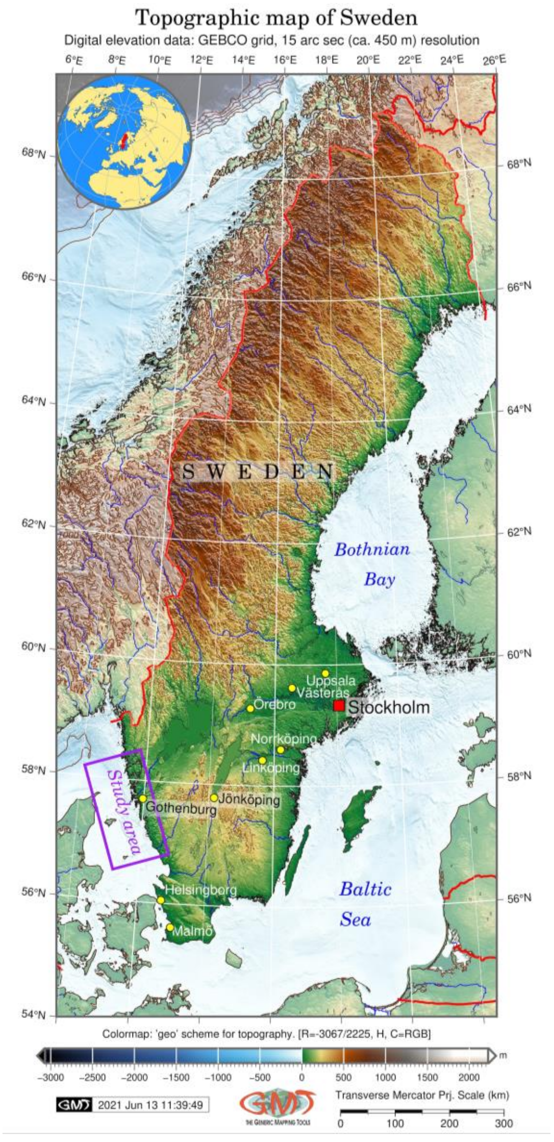

Fig. 1. Location of the study area. Data source: General Bathymetric Chart of the Oceans (GEBCO). RGB colour model. RGB, red, green blue. Mapping: Generic Mapping Tools (GMT). Map source: authors

Leaching as one of such methods has been used and presented in previous works (e.g. Norén et al., 2021; Alshemmari et al., 2020). Leaching is a process of extraction of solute from the carrier substance by a solvent (Richardson et al., 2002). Natural leaching often occurs in cement materials due to natural weathering. In experimental works, leaching can be applied to remove contaminants from sediments. Thus, chemical leaching is a common method for extracting solvents from soils (Shen et al., 2020).

The techniques of leaching were applied in this work for the treatment of marine sediments using guidance standards provided by the Swedish Institute for Standards (SIS), https://www.sis.se/en/ Leaching of metals and chemical pollutants from soils and sediments is widely used as an effective method of environmental treatment of soils under EN 12457-4 and NEN 7275 standards (Lu et al., 2016; Kuterasińska-Warwas & Król, A. 2017) or EN 12457-2 for leaching (Pazikowska-Sapota et al., 2016; Mizerna & Król, 2018).

Besides geochemical treatment, marine sediments should be cleaned and stabilised before their reuse in the construction works, to improve their geotechnical and environmental properties (Herbich, 1990; Li et al., 2019; Houlihan et al., 2021). Stabilisation and binding of the marine sediments, as well as other weak soils, such as clay, loam or silt, can be done by adding CKD using mechanical methods of mixing and geochemical treatment (Wareham and Mackechnie, 2006; Ghavami & Rajabi, 2021).

Various approaches of soil treatment are being continuously reported in the previous works, which reflects the need for improved methods (Moh, 1962; Bandyopadhyay, 1981; Turner 1994; Shoaib et al., 2000; Fabian et al., 2010; Schifano and Fabian, 2010; Fiertak and Stryszewska, 2013; Lindh et al., 2018; Li et al., 2019; Wang et al., 2020). The impact of external effects on soils can be assessed using techniques of data analysis (Dahlin et al., 1999; Nosjean et al., 2020; Lemenkov and Lemenkova, 2021b; Zahran, 2020). Geochemical methods include hydrogeological appraisals, drilling (Shah et al., 2021), image analysis (Källén et al., 2014, 2016). Methods of soil treatment and evaluation of its performance under varying external effects include stabilisation and solidification (s/s) aimed to improve the mechanical performance of soil and increase its strength before recycling (Wang et al., 2011; Tang et al., 2020; Zhang et al., 2018; 2020, 2021; Fan et al., 2021).

Treatment of the marine sediments contaminated by TBT using s/s method presents an environmentally effective method for recycling of soils. The s/s treatment can use various agents, e.g. kaolinite, quicklime, cement (Rađenović et al., 2019). In this way, the s/s technique enables to get environmentally compatible soils with removed heavy metals or organic matter and improved properties (De Gisi et al., 2020). Various methods and techniques of soil treatment are reported in previous studies (Lindh, 2004; Li et al., 2017; Lemenkov and Lemenkova, 2021a).

The purpose of this research is to explore different combinations of binders – CKD, cement and slag – for s/s treatment of the marine sediments contaminated by TBT. The s/s treatment aims to remove the TBT contaminants. The objective of this study is to assess the properties of sediments after treatment by various ratios of binders and to evaluate the applicability of CKD. The specific research question is to assess if the replacement of cement or slag by CKD is optimal for s/s treatment of the marine sediments. The study experiment has been performed in south-western Sweden with sediment samples collected in the Port of Gothenburg (Fig. 1).

2. METHODOLOGY

The project has been performed in the Swedish Geotechnical Institute (SGI) on behalf of the Cementa (HeidelbergCement Group) and Cowi Consulting Group in the framework of the Arendal project. The samples have been dredged and collected from the seabed of the Port of Gothenborg, Sweden (Fig. 1). The

DOI 10.2478/ama-2021-0030

methodology includes the s/s treatment of the sediment samples, statistical data processing and graphical plotting.

The laboratory tests on the stabilisation of the marine sediments were performed in SGI following the standard procedure. Treatment of sediments was based on the guidance of the SIS, ISO 18772:2008 (Swedish Institute for Standards, 2021a). During the s/s treatment of the marine sediments, the TBT constituents were leached from the sediments samples in changed testing conditions: varied ratio of binder and water. The methodology follows the existing procedure of leaching to examine the quality of the marine sediments to stabilise specimens for further recycling.

Leaching tests in sediment samples were performed according to the SIS guidance on leaching for chemical and ecotoxicological tests of soils with high content of contaminants, ISO 18772:2008. Leaching tests were aimed to clean the sediments from the high concentrations of TBT in the collected specimens. The test specimens were demolded before the start of the experiment, which took periods of 2.25 days, 9 days and 36 days. Leaching aimed to improve the physical and chemical properties of soil specimens (low strength, stability and stiffness) and decrease high moisture to ensure the recycling of soils in geotechnical works.

The compressive strength has been measured following the standards of SIS, Geotechnical investigation and testing – Laboratory testing of soil – Part 7: Unconfined compression test, ISO 17892-7:2017 (Swedish Institute for Standards, 2017a). It has been tested as a maximum load that could be applied to evaluate the performance of the s/s sediments under varied tested conditions indicating the durability and resistance of sediment samples. The tests on the compressive strength were performed to evaluate what binder ratio presents the most effective performance for the contaminated marine sediments. The compressive tests aimed to measure the capacity of soils and sediments to withstand loads.

2.1. Hypothesis

The overall hypothesis consists of three assumptions.

1. First, it is possible to replace cement or slag by CKD with the maintained performance of TBT leaching for tested specimens of the marine sediments collected from the Port of Gothenborg.
2. Second, the CKD as a replacement of cement for stabilising marine sediments is an effective means for improving their compressive strength.
3. Third, the diffusion gradient becomes stronger when the amount of water increases concerning surface, which drives the leaching of easily soluble substances.

2.2. Sampling of Dredged Sediments

The marine sediments have been dredged from the seabed of the Port of Gothenborg, Kattegat Strait, southern Sweden.

Sampling took place within the framework of the pilot project Arendal 2 in the SGI. Preparation of specimen sediments has been performed following a standardised workflow. The specimens were collected using sampling techniques (Lindh, 2001, 2003) to obtain representative data which adequately reflects the characteristics of sediments. Specimens of dredged sediments were collected and stored in plastic barrels (Fig. 2). Afterwards the specimens were intensively mixed with binders for 5 min. Blending samples with mortar was done using a mixing device (Fig. 3).

Fig. 2. The barrel used in a project. The size of the barrel was determined to achieve the optimal stirring. The homogeneous sediment masses were obtained for further testing. Photo by Per Lindh

Fig. 3. Mixing tool for the homogenisation of the dredged material. Photo by Per Lindh

2.3. Preparation of Specimens

After mixing and homogenisation, the specimen samples were filled into the cylinder sleeves where they reached a consistency that enabled to pour them. The standard piston sampling cylinder had an inner diameter of 50 mm and a height of 170 mm. The specimens were stored submerged with storage T = 20 °C. Afterwards, the specimens were treated according to the existing standards of SIS:

1. Water ratio has been determined according to the standard of the Geotechnical investigation and testing – Laboratory testing of soil – Part 1: Determination of water content (ISO 17892-1:2014) SS-EN ISO 17892-1 2 (Swedish Institute for Standards, 2014a).
2. Dry matter and density have been determined following the standard of the Geotechnical investigation and testing – Laboratory testing of soil – Part 2: Determination of bulk density (ISO 17892-2:2014) SS-EN ISO 17892-2 3 (Swedish Institute for Standards, 2014b).
3. Grain distribution of sediments was tested using the standard test method for Particle-Size Distribution (Gradation) of Fine-

Grained Soils Using the Sedimentation (Hydrometer) Analysis, STD-80029734 (Swedish Institute for Standards, 2021b).
4. The determination of TBT from the leachate followed the standard organotin compounds: ISO 17353:2004 (Swedish Institute for Standards, 2005 (see Subsection 2.7).

The specimens were mixed with different water content proportions to obtain two variants of mixtures prepared from the marine sediments (Cell 1 and Cell 2). A certain amount of water has been removed and used partially for changing water ratio in sediments and partially for using in leaching tests. Fig. 4 shows the water ratio in the two different mixtures: 168% and 219%, respectively.

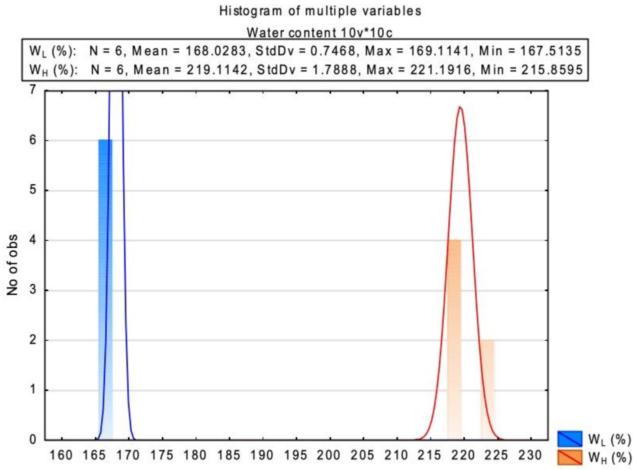

Fig. 4. Histogram showing the two variants of water ratio determined according to the SS-EN ISO 17892-1

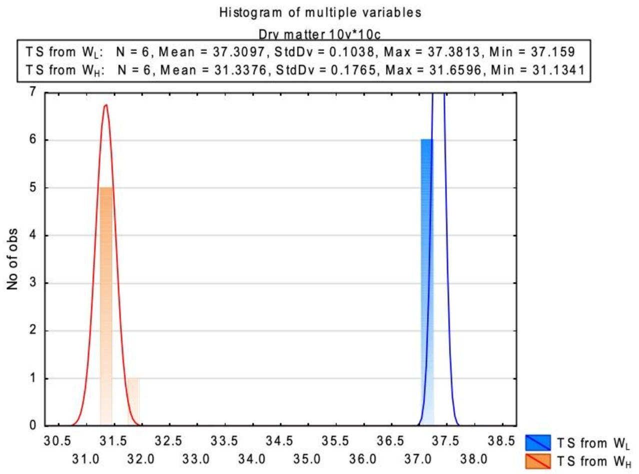

Fig. 5. Histogram showing the proportion of dry matter in the two mixtures of sediment samples

The soil permeability was tested to evaluate the capacity of porous sediments to allow water to pass through, as measured during experiments. The concept of permeability is crucial in hydrogeology as a fracture permeability of soils (Guerriero et al., 2013). The bulk density and dry density of the two mixtures with dredged material are shown as follows. The W_L ("water low" mixture) has a density of 1,316 tons/m^3, and a dry density of 0,491 t/m^3, while the W_H ("water high" mixture) had a density of 1,254 tons/m^3 and a dry density of 0.393 t/m^3. The impact of various ratios of two binders and two water-to-binder ratios (w/b) are investigated. Such proportions were chosen in this study, but the results can also be extrapolated to other ratios in different test conditions. The standard deviation for a higher water ratio is higher (Fig. 4), as it is more difficult to maintain the same homogeneity for the higher water ratio. The actual dry substances were 31.3% and 37.3%, respectively (SS-EN 12880), Fig. 5.

The grain distribution in the dredged marine sediments was determined using the SIS standard for Geotechnical investigation and testing – Identification, description and classification of the rock, ISO 14689:2017 (Swedish Institute for Standards, 2017b). The grain distribution analysis has been done during the initial laboratory test and during the pilot experiment, Fig. 6.

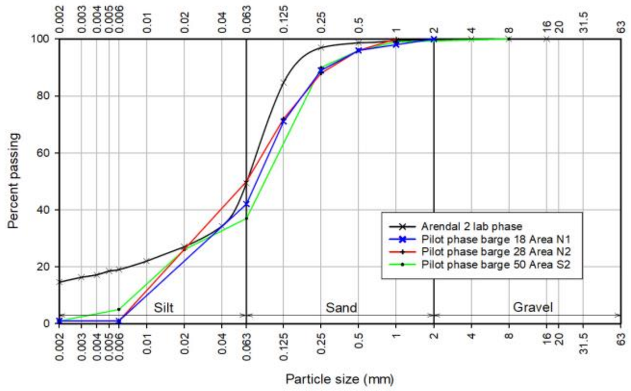

Fig. 6. Graph showing grain distribution in the soil material, classified as silty muddy sand, silty sand and sandy silt

The grain distribution was based on the classification of sediments according to the particle sizes. The sediments have been identified during the pilot laboratory phase of the experiment as the three-grain types: (1) silty muddy sand; (2) silty sand; (3) sandy silt. The material comes from the areas N1, N2 and S1. The clay content in samples used in the pilot phase was almost absent.

2.4. Experimental Setup

The experimental design was based on statistical experimental planning in order to systematically evaluate the performance of specimens under the effects of various binder combinations and water ratios. The mixture optimisation was performed as simplex ternary graphs and process optimisation according to the 2*2-factor experiment. Two independent parameters tested in the study included the following ones: (1) binder combination and (2) water ratio. The amount of binder in a water/binder ratio plays a significant role in final results on the stabilisation of the marine sediments. Thus, the results were checked at the two sets of binder and water ratios (Fig. 7).

2.5. Mixture Optimisation

To determine the optimal mixture between the three different binder components, a simplex experimental test was performed (Fig. 7). A simplex test is summarised as the three different binders represented by the parameters X, Y and Z (as X ▯ Y ▯ Z ▯ 1). The equation spans a triangle where the corners are represented by each binder component, here: (1) cement; (2) slag; (3) CKD.

DOI 10.2478/ama-2021-0030

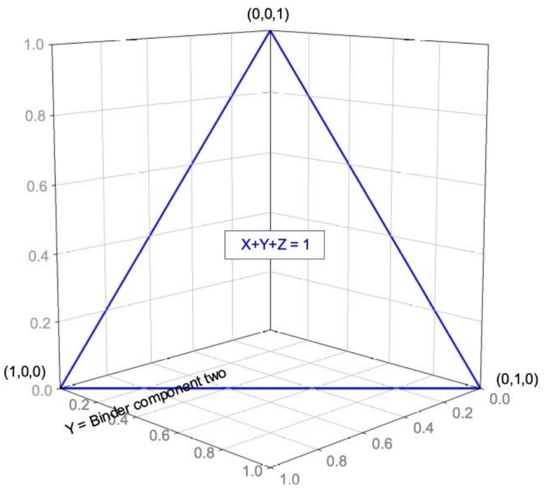

Fig. 7. Graph showing all possible combinations of the three components as different binders presented by a plane with three straight lines bordering the plane. The vertices represent a binder, 1.0 = 100%

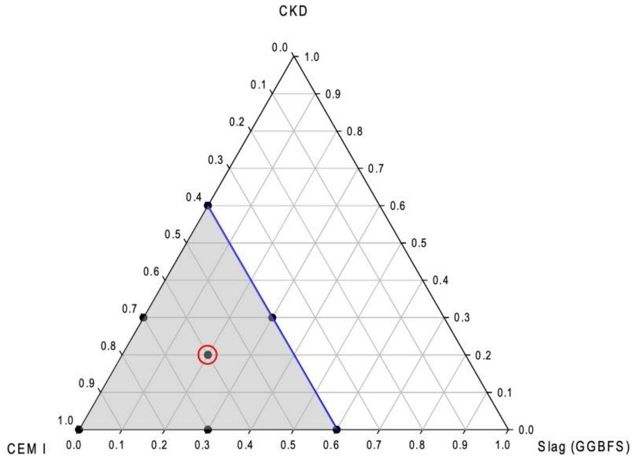

Fig. 8. The grey area shows a constrained simplex centroid experiment (cement, slag and CKD). CKD, cement kiln dust

A mixture of the two binder components can be represented in the inner intersections of the triangle, while a combination of all the three components is shown in the interior of the triangle. The total amount of binder is constant regardless of where the mixture is set up on the triangle, yet the ratio of all three binders vary.

Since only slag or CKD does not act as a binder, a limited simplex centroid experiment has been designed and shown in Fig. 8. Here the limitation is set up to 60% of slag and 60% of CKD. The seven black dots correspond to the selected test samples. A red circle in the middle of the graph (Fig. 8) indicates a double test. Since all samples were double-checked as a double experiment, a sum of 32 (16 ▯ 16) sample experiments has been performed in total.

To increase the resolution, one of the simplex experiments was performed as an augmented simplex experiment (Fig. 9). Some types of binder could be used as a single component as no curing starts, e.g. slag must be activated with a high pH. This problem was solved using a restriction for this binder, e.g., possible combinations were obtained by maximising the slag content or fly ash up to 60%.

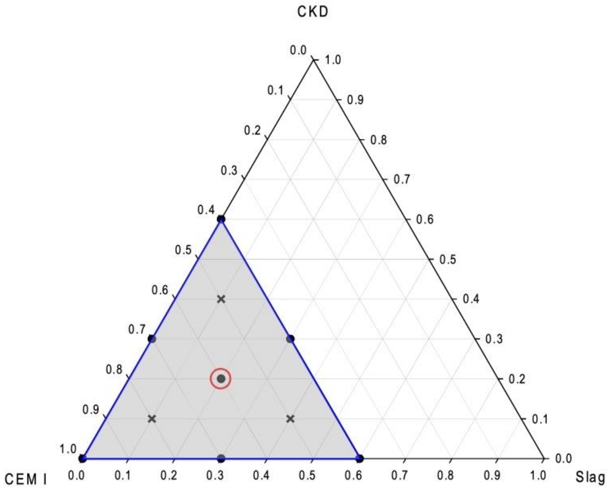

Fig. 9. Augmented simplex experiment for estimation of higher-order interaction effects (cement, slag and CKD). The test points represented by x constitute extra experiments. CKD, cement kiln dust

2.6. Process Control

The process control included technical parameters controlled according to the standards (Swedish Institute for Standards, 2014a, 2014b, 2021a, 2021b) and changed during the experiment aimed to increase the stability. The process parameters included the following variables: (1) amount of binder (2) water ratio in the sediments (3) time of mixing in a workflow process. The binder mixture in this case is not considered as a process parameter, since it has already been defined and determined during the simplex test.

2.6.1. Processes with Two Factors

The process parameters were used as a 2*2-factor experiment in a simple case where only water ratio and binder content were varied. Here, two factors have been tested: (1) the amount of binder; (2) water ratio. The test was performed on the two levels: low and high water ratio, and low and high amount of binder, respectively see Fig. 10.

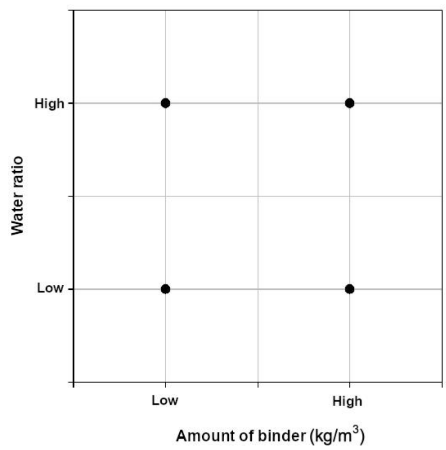

Fig. 10. An example of the 2*2-factor experiment with the amount of binder (cement, slag and CKD) and water ratio as constituent factors. CKD, cement kiln dust

DOI 10.2478/ama-2021-0030 acta mechanica et automatica, vol.15 no.4 (2021)

2.6.2. Combination of Approaches

Combinations of various ratios of water/binder in the tests can significantly affect the results of strength, stabilisation and TBT leaching. Therefore, to combine mixing experiments with factor experiments, these were combined as a multi-stage expanded experiment, Fig. 11. This provided an opportunity to study the interplay between the water ratio and the binder quantity on the performance of tested sediments.

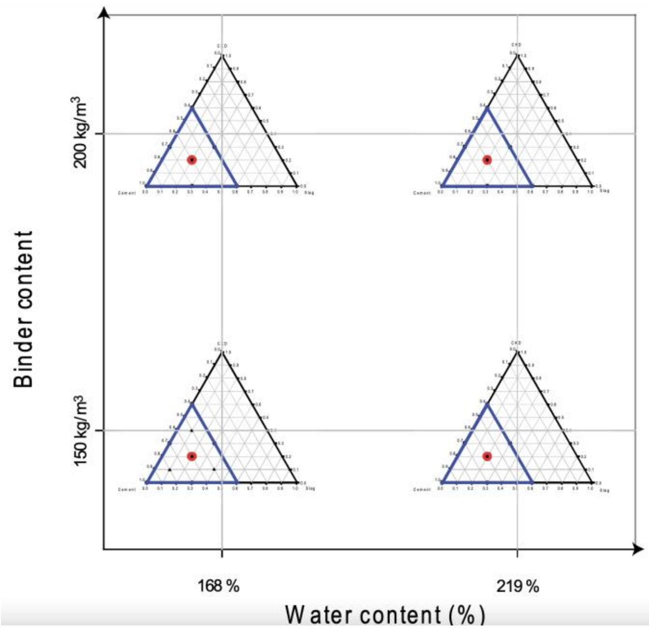

Fig. 11. Simplex experiments arranged following the 2*2-factor experiment. The combined methodology provides both an optimal binder mix (cement, slag and CKD) and an optimal amount of binder concerning the process parameters. CKD, cement kiln dust

Combining simplex experiments with factor experiment aimed to optimise the binder mixture and to determine how the change in mixing parameters affect the result.

2.6.3. Extra Test Setups

The experimental extra test setups (Fig. 11) are based on the methodology of the traditional factor experiment and as a factor experiment in a simplex setup (Fig. 12). The two additional rounds of testing have been performed to determine the limits that could be used to test strength: ED 1 and ED 2 (Fig. 13). These two additional experimental setups were designed as constrained simplex experiments. The experimental setup one (ED1) was designed to optimise the use of CKD and the experimental setup two (ED2) was designed to optimise the use of slag.

The test points marked as black dots were additions to test the limitation of the slag mixture. These experiments were designed to determine the limits of where various binder components can contribute to the increase of the total strength of the dredged sediment masses. Fig. 14 shows different experimental setups with various binder combinations and relative compressive strength. Partial replacement of cement by CKD contributes to the higher strength of the stabilised sediments and increases the environmental quality of mixtures by reducing the amount of cement and replacing it with CKD.

2.7. Determination of the TBT Concentrations from the Leachate

The analysis of the TBT concentrations has been performed by ALS Global. ALS refers to the SIS standard in the accreditation certificate for organotin compounds: ISO 17353:2004 (Swedish Institute for Standards, 2005).

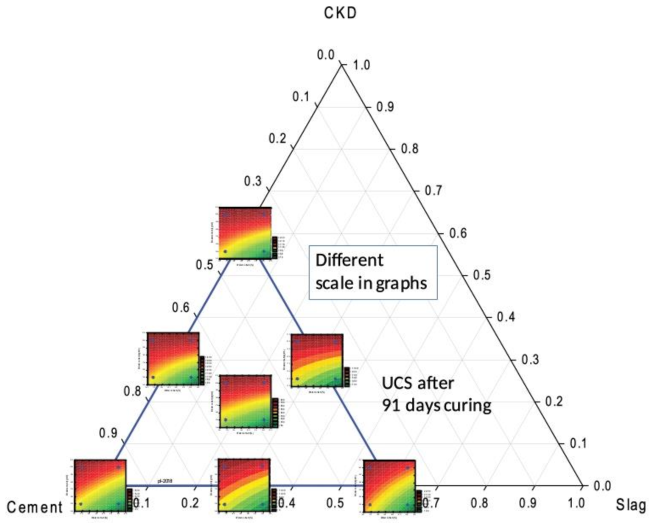

Fig. 12. Ternary diagram showing 2*2-factor experiments reported in a simplex setup of binders (cement, slag and CKD). CKD, cement kiln dust

In this specific test package, the TBT substances have been extracted in a liquid-liquid extraction from water to hexane. The instrument that is then used in the analysis is one Gas Chromatography – Inductively Coupled Plasma – Sector Field Mass Spectrometry (GC-ICP-SFMS), https://www.alsglobal.se/en/isotope-analysis/laboratory. In this approach different TBT's were separated from each other in the GC system.

Separation in GC takes place due to the different sizes of the TBT substances, fat solubility, charge, etcetera. The substances were then passed on to the plasma which excites and ionises the tin atoms which were then passed through the mass spectrometer which can further separate the tin atoms depending on their m/z value (mass-to-charge ratio, in this way one can also distinguish isotopes of the same substance).

Finally, the atoms/molecular fragments reached a detector that generated a signal. This means that the tin atoms reach the detector at different times because the different TBT substances are separated over time in the GC system. In this way, it is possible to correlate a specific TBT to a specific time when the signal (peak) is registered. The area on the peak is in proportion to the amount of substance at that time.

3. RESULTS AND DISCUSSION

The study has evaluated the effect of adding three different binders (cement, CKD and slag) in various proportions and changing water ratio to assess the TBT leaching and strength of the contaminated marine sediments after stabilisation. The results included tests of the following parameters in sediments:

1. compressive strength;
2. permeability;
3. TBT leaching.

The results of the test experiments performed with a factor combination of low water ratio (LW) and low amount of binder (LB), cement, slag and CKD in various proportions showed that the largest increase in the compressive strength occurred with a mixture of 60% slag and 40% cement. Thus, water holding capacity increases with the increased binder content, slag proportion in a binder and curing time suggesting that high-slag binders are the most suitable for removing contaminants.

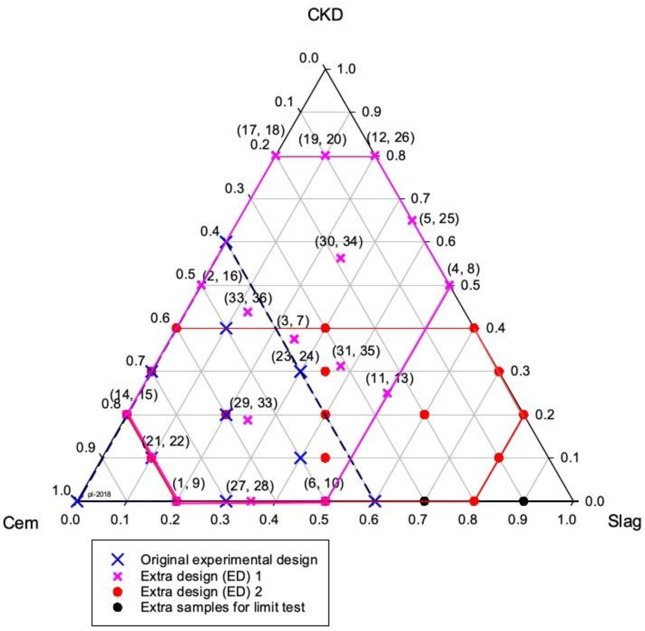

Fig. 13. Ternary diagram of different experiments performed with the factor combination LW and LB, cement, slag and CKD. CKD, cement kiln dust; LB, low amount of binder; LW, low water ratio

3.1. Leaching of TBT with Addition of CKD

The samples of specimens with sediments were evaluated on TBT leaching after 2.25 days, 9 days and 36 days of stabilisation. The results of the leaching test were compared for different content of binder and water ratios. The bracketed pairs of values superimposed on Figs. 14 and 15 indicate the compressive strengths measured for the double experiments for higher and lower water ratio and binder content, which explains the large disparity in some cases, e.g. (5,25), (1,9). Here the combinations that did not show an increase in the compressive strength is caused by a too low pH to activate slag (Fig. 14).

The results on leaching for day 2.25 are shown in Fig. 15. Here the variations in the TBT leaching are shown after 2.25 days of stabilisation for the binder ratio (maximal values): 0.6 slag, 0.4 CKD and high water – low binder ratio at 19, 23, 34 and 37.

The colour values in Fig. 15 show values of the TBT leaching (ng/L) as follows: <480, 580, 680, 780, 880, and >900 for each colour gradation on the ternary diagram from dark green to dark red, accordingly. The highest values (red colours) are notable for higher concentrations of cement and CKD while the lowest (green colours), corresponding to the <480 ng/L correlate with higher proportions of slag.

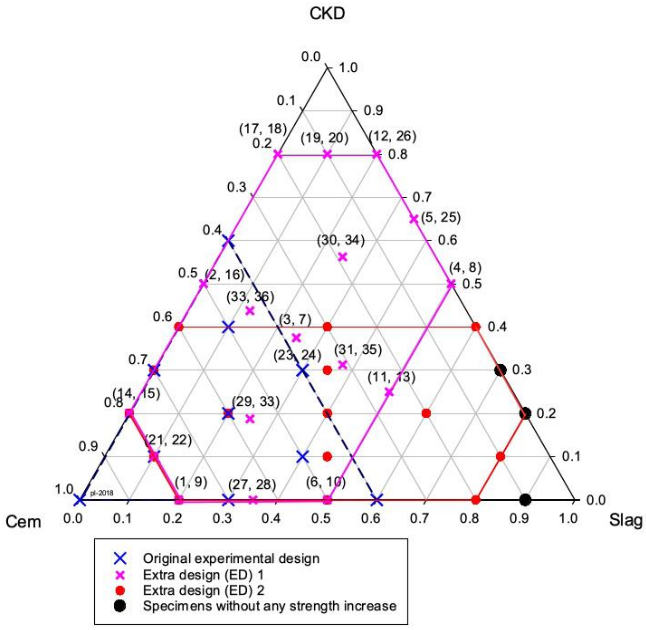

Fig. 14. Ternary diagram showing test and experimental points (approaches) where no growth strength was detected. CKD, cement kiln dust

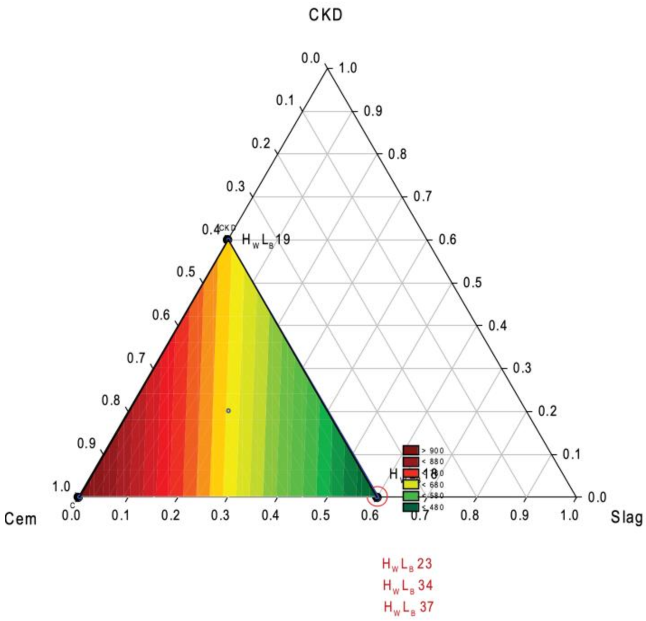

Fig. 15. Ternary diagram showing response area for leaching of TBT after 2.25 days. TBT, tributyltin; CKD, cement kiln dust

Fig. 16 shows a correlation between the increasing pH values of the tested specimens with added CKD and the leaching of TBT. For comparison, mixtures with pure cement and "cement/slag" ratio were used in the pilot project. For statistically independent comparison, the standardised samples were used in this project with pure cement and cement/slag combinations. In general, there is a linear correlation between the increasing pH values and higher leaching despite the different samples.

DOI 10.2478/ama-2021-0030 acta mechanica et automatica, vol.15 no.4 (2021)

The R2 value of 0.62 shows that the pH explains a fairly large part of the variation in leaching of the sediment samples. However, parts of the variation are due to the differences in leaching of TBT over time. Since the points for the recipe cement/slag/CKD are slightly below the trend line, it indicates that samples give a slightly lower leaching effect than expected based on the pH of the leachate. The cement/slag/CKD generated a higher pH value than cement/slag, which should have given higher leaching because the natural pH of soil affects the stability or functionality of agents and different mineralogy. Leaching obtained is judged to be close to equivalent to cement/slag, Fig. 16.

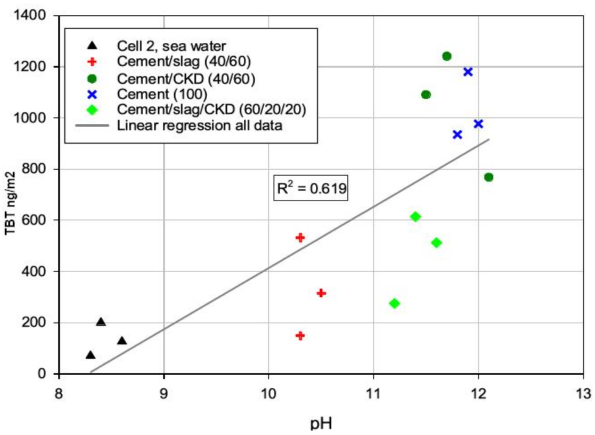

Fig. 16. Correlation between the pH and leached amount of TBT by various binders in defined ratios. TBT, tributyltin; CKD, cement kiln dust

The cement/slag/CKD mixture thus can contribute to the reduced leaching through a mechanism that is not dependent on the pH. Chemical composition and the pH of soils are reflected in their industrial impact (Hiller et al., 2021) with the leaching of heavy metals demonstrating the pH-dependent behavior (Szarek-Gwiazda, 2014; Ai et al., 2019; Suzuki et al., 2020; Sun & Yi, 2021; Nyembwe et al., 2021). In this study, leaching has shown a direct correlation with the higher pH corresponding to the increased leaching (Fig. 16).

3.2. Leaching of TBT Over Time

The sample specimens of sediments were received from the two different batches (Cell 1 and Cell 2). Washing specimens was performed during the first step of the leaching tests. The performance of the laboratory-made specimens in Cell 1 and the *in-situ* specimens stored in Cell 2 demonstrated differences in leaching experiments. Cell 2 provided a more stable leaching pattern with lower mass flows compared to the laboratory-produced specimens that were not subject to leaching.

It can be explained by the technical design of the test: when specimens were removed from Cell 2 at the end of the leaching tests, the soil was already washed out. The hypothesis of washing also explains why shaking experiments on crushed material from Cell 2 showed 10–100 times lower leaching than crushed materials from the laboratory-produced samples during the data evaluation from the pilot test control programme.

In all experiments, the processed samples in the laboratory demonstrated leaching to a greater extent than the field sample from Cell 2 during the first time steps of the experiments (Fig. 17). However, for the most of samples, the differences between the lab and the field sample decreased after 36 days. Such a trend is noted both for the TBT and for potassium. Both substances are assumed to have leaching controlled in whole or in part by leaching in the initial phase.

The results of the experimental tests on leaching TBT over time for all binders (cement, slag and CKD) and changed amounts of water are shown in Fig. 17. The cement/slag/CKD mixture of binder is represented by a double experiment when the sediment specimens were tested on two different occasions.

The results of the experiments on leaching of TBT over time for all samples with varied ratio of binders (cement, slag and CKD) and changed amounts of water demonstrated the following outcomes (Fig. 17): the ratio of cement/slag/CKD 60/20/20: 500 ng/m^2 at day 2.25, 600 ng/m^2 at day 9, 280 ng/m^2 at day 36; cement/CKD 40/60: 780 ng/m^2 at day 2.25, 1220 ng/m^2 at day 9, 1100 ng/m^2 at day 36; cement/slag 40/60 (no CKD): cement/slag 40/60 (no CKD): 580 ng/m^2 at day 2.25, 310 ng/m^2 at day 9, 180 ng/m^2 at day 36. The increase of leaching was observed for the following analysed parameters: a higher amount of water in the experiments, the addition of CKD to cement (ratio of cement/CKD 40/60) contributes to higher leaching compared to ratio cement/slag.

The tests demonstrated notable leaching of TBT from the sediment samples on day 9 and significantly decreased amount of TBT on day 36 compared to the results on day 2.25 of the experiment (Fig. 17). On day 2.25, a relatively high variability is seen between the experiments. On days 9 and 36, the variability is notably lower. The experimental results show that the speed of leaching of TBT from the sediments changes at different ratios of added binders and water for TBT leaching in a seawater environment.

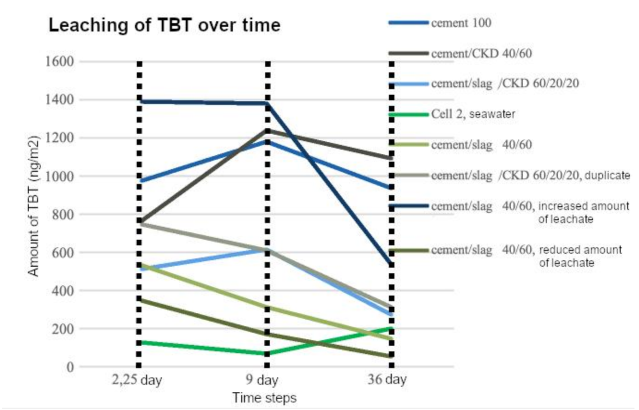

Fig. 17. Leaching of TBT over time for all binders (cement, slag and CKD) and changed amounts of water in leaching experiment. CKD, cement kiln dust; TBT, tributyltin.

The results show that variation of the ratio of the independent binders affects TBT leaching in the sediment specimens. These include binder ratios (cement/slag/CKD), water ratio in sediment samples) and time of the experiment showing time-dependent leaching. The binder and water ratio are the primary factors affecting the TBT leaching of the tested sediment samples.

The pH of mixtures containing cement/slag stabilised around 10–10.5 in the performed lab experiments. Leaching varies considerably between different samples in simplex experimental tests. However, leaching stabilised over time, with a reduced difference between the ratio. Sediment samples that contain ce-

DOI 10.2478/ama-2021-0030

ment/slag/CKD in ratio 60%/20%/20% give similar leaching results as those with ratio cement/slag (60%/40%), which is identical to the results received in a pilot experiment.

Leaching of TBT is affected not only by the pH value but also by leaching conditions (i.e. ratio between leached surface and leachate amount). For example, the leaching of TBT increased at a higher amount of water in the surface leaching tests, because of the buffering effect of the seawater. The results of performed tests on the treatment of the contaminated sediments showed the applicability of CKD as a cement replacement in soil stabilisation and TBT leaching of soil specimens. As the experiment length was limited by 36 days, the results are related to the short-term leaching conditions in the field based on the processing sediments obtain *in situ* from the Port of Gothenborg.

3.3. Unconfined Compressive Strength (UCS)

The results for the UCS are presented for the two experimental setups (one (ED1), designed to optimise the use of CKD and two (ED2), designed to optimise the use of slag), as described in subsection 2.6.3. Figs 18 and 19 show variations in the unconfined compressive strength (UCS) by various combinations of the binder in the specimen. Within tested combinations, the analysis of changes in UCS (gradual changes from dark to light green in Fig. 18 and from green to red colours in Fig. 19) revealed changes in UCS.

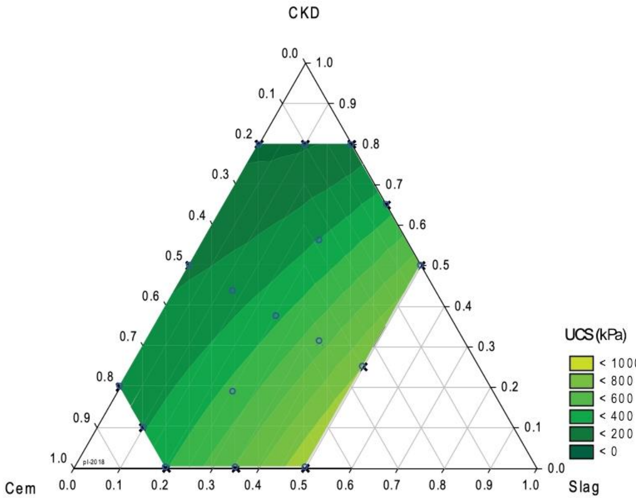

Fig. 18. ED1 compressive strength for binders (cement, slag and CKD). CKD, cement kiln dust; UCS, unconfined compressive strength

Thus, Fig. 18 shows the increase of UCS with the increase of cement in a binder from 0.2 to 0.5 (changes from dark green to light green colours in the horizontal axis) and CKD from 0.2 to 0.8 (left axis areas in Fig. 18) and inversely proportional for slag (an increase of UCS along with the decrease of slag from 0.5 to 0.8, the right axis in Fig. 18). Accordingly, Fig. 19 shows the increase of UCS with the increase of cement in a binder from 0.2 to 0.8 and CKD from 0.6 to 0.8 (bright red areas in Fig. 19).

The significant increase of UCS is noticeable along with the increase of cement proportion from values 0.4 to 0.8 (corresponds to the red areas in Fig. 19). These ratios of binders shown in the ternary diagrams presented an increase of values of UCS with adding of cement (0.30–0.38 increased values from 700 up to 900, orange colours).

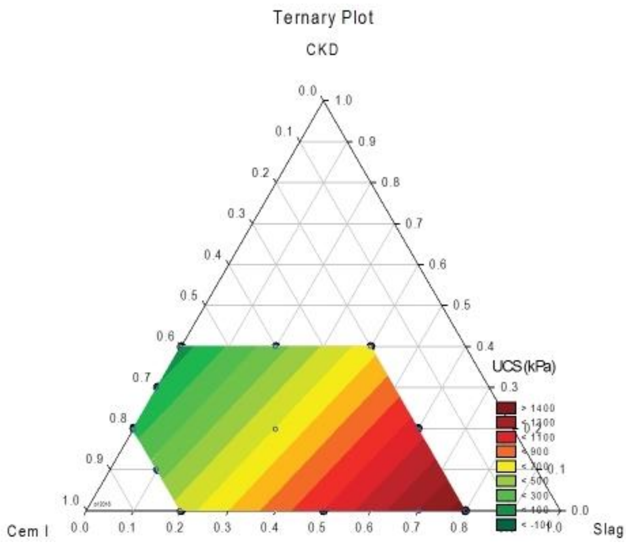

Fig. 19. ED2 compressive strength for binders (cement, slag and CKD). CKD, cement kiln dust; UCS, unconfined compressive strength

Further gradual increase in compressive strength is noticeable and reaches its maximum at values of cement from 0.7 to 0.8 and CKD from 0.8 to 1.0 (crimson red colours, Fig. 19). Adding of slag presents the controversial effects of decreasing the UCS with an increase of slag in the ratio (from 0.0 to 0.4, the right axis in Fig. 19).

4. CONCLUSION

This study presented the results of detailed experiments of the s/s treatment of TBT contaminated sediments using CKD, cement and slag in different proportions. The application of three-component binders for the treatment of marine sediments results in the development of stabilised and solidified compact soils (produced in various combinations of cement, CKD and slag with a varied ratio of water) with removed TBT contaminants.

Treatment of the marine sediments contaminated by TBT is important since cleaned and stabilised sediments can be recycled and reused in the construction works. The performed tests showed variations in leaching of TBT in the specimens at different binder ratios (cement, slag, CKD). The laboratory tests were performed to assess the applicability of CKD as a cement replacement for contaminated sediments and to assess the leaching and strength of samples.

The study demonstrated that CKD has promising applications for s/s treatment of the marine sediments contaminated by TBT. The addition of CKD contributes to a higher pH compared to the binders cement/slag. At the same time, CKD affected leaching, despite the alkaline effect of the material on pH. The samples with only added cement/CKD demonstrated higher leaching compared to the ratio “cement/slag/CKD” and “cement/slag”. The “CKD/slag” ratio presented the best results and can be used for s/s treatment of the sediments.

The results also proved that using CKD as a cement replacement in the treatment of TBT contaminated marine sediments is beneficial not only and environmentally (effective in TBT leaching), but also technically (increased UCS and stability of specimens). Thus, the gradual increase in UCS has been noted and reached its maximum along with the increased values of cement and CKD.

The actuality of this study consists in theoretical and practical aspects. The first includes the increased knowledge on the performance of sediments in tests on leaching and stabilisation. The second includes practical tests of the technical methods on s/s treatment of the contaminated sediments.

Environmental monitoring in Sweden includes coastal regions of the Baltic Sea (Sveriges geologiska undersökning, 2021). Therefore, the development of methods for the s/s treatment of the contaminated marine sediments is an essential task (Cato, 1977; Sánchez-García et al., 2010). Presented laboratory experiments demonstrated changes in leaching in various combinations of binder (cement, CKD, slag) which contributes to the marine environmental monitoring in Sweden.

REFERENCES

1. **Abdel-Gawwad H. A., Heikal M., Mohammed M. S., El-Aleem S. A., Hassan H. S., García S. V., Alomayri T.** (2019), Sustainable disposal of cement kiln dust in the production of cementitious materials. *Journal of Cleaner Production,* 232 1218–1229. https://doi.org/10.1016/j.jclepro.2019.06.016
2. **Abraham M., Westphal L., Hand I., Lerz A., Jeschek J., Bunke D., Leipe T., Schulz-Bull D.** (2017), TBT and its metabolites in sediments: Survey at a German coastal site and the central Baltic Sea. *Marine Pollution Bulletin*, 121, 1–2, 404-410. https://doi.org/10.1016/j.marpolbul.2017.06.020
3. **Adeyanju E., Okeke C. A., Akinwumi I., Busari A.** (2020), Subgrade Stabilization using Rice Husk Ash-based Geopolymer (GRHA) and Cement Kiln Dust (CKD). *Case Studies in Construction Materials*, 13, e00388. https://doi.org/10.1016/j.cscm.2020.e00388
4. **Ahmad S., Hakeem I., Maslehuddin M.** (2014), Development of UHPC mixtures utilizing natural and industrial waste materials as partial replacements of silica fume and sand. The *Scientific World Journal*, 713531. https://doi.org/10.1155/2014/713531
5. **Ai H., Clavier K. A., Watts B. E., Gale S. A., Townsend T. G.** (2019), The efficacy of pH-dependent leaching tests to provide a reasonable estimate of post-carbonation leaching, *Journal of Hazardous Materials*, 373, 204-211. https://doi.org/10.1016/j.jhazmat.2019.03.089
6. **Akcil, A., Erust, C., Ozdemiroglu, S., Fonti, V., Beolchini, F.** (2015), A review of approaches and techniques used in aquatic contaminated sediments: metal removal and stabilization by chemical and biotechnological processes. *Journal of Cleaner Production*, 86, 24-36. https://doi.org/10.1016/j.jclepro.2014.08.009
7. **Al-Homidy A. A., Dahim M. H., Abd El Aal A. K.** (2017), Improvement of geotechnical properties of sabkha soil utilizing cement kiln dust. *Journal of Rock Mechanics and Geotechnical Engineering*, 9, 749–760. https://doi.org/10.1016/j.jrmge.2016.11.012
8. **Alshemmari H., Al-Awadi M., Karam Q., Talebi L.** (2020), Sedimentary butyltin compounds and sediment transport model at the Shuwaikh Port, Kuwait Bay. *Arabian Journal of Geosciences*, 13, 677. https://doi.org/10.1007/s12517-020-05683-2
9. **Alzieu C.** (2000), Impact of Tributyltin on Marine Invertebrates. *Ecotoxicology*, 9, 71–76 https://doi.org/10.1023/A:1008968229409
10. **Antizar-Ladislao B.** (2008), Environmental levels, toxicity and human exposure to tributyltin (TBT)-contaminated marine environment. A review. *Environment International*, 34, 2, 292-308. https://doi.org/10.1016/j.envint.2007.09.005
11. **Bagheri S. M., Koushkbaghi M., Mohseni E., Koushkbaghi S., Tah-mouresi B.** (2020), Evaluation of environment and economy viable recycling cement kiln dust for use in green concrete. *Journal of Building Engineering*, 32, 101809. https://doi.org/10.1016/j.jobe.2020.101809
12. **Baghriche M., Achour S., Baghriche O.** (2020), Combined effect of cement kiln dust and calcined dolomite raw on the properties of performance magnesium phosphate cement. *Case Studies in Construction Materials*, 13, e00386. https://doi.org/10.1016/j.cscm.2020.e00386
13. **Baltic Marine Environment Protection Commission** (2015), HELCOM Guidelines for Management of Dredged Material at Sea and HELCOM Reporting Format for Management of Dredged Material at Sea [Online access: 18.08.2021]. URL: https://helcom.fi/media/publications/HELCOM-Guidelines-for-Management-of-Dredged-Material-at-Sea.pdf
14. **Bandara K. R. V., Chinthaka S. D. M., Yasawardene S. G., Manage P. M.** (2021), Modified, optimized method of determination of Tributyltin (TBT) contamination in coastal water, sediment and biota in Sri Lanka. *Marine Pollution Bulletin*, 166, 112202. https://doi.org/10.1016/j.marpolbul.2021.112202
15. **Bandyopadhyay S. S.** (1981). Soil Stabilization with Preheater Fines. *Journal of the Geotechnical Engineering Division*, 107(5), 654-658. https://doi.org/10.1061/AJGEB6.0010706
16. **Barnat-Hunek D., Góra J., Suchorab Z., Łagód G.** (2018), 5 – cement kiln dust. In: Waste and Supplementary Cementitious Materials in Concrete. (eds.: Siddique, R., Cachim, P.) Woodhead Publishing. *Wood-head Publishing Series in Civil and Structural Engineering*. 149–180. https://doi.org/10.1016/B978-0-08-102156-9.00005-5
17. **Berto D., Giani M., Boscolo R., Covelli S., Giovanardi O., Massironi M., Grassia L.** (2007), Organotins (TBT and DBT) in water, sediments, and gastropods of the southern Venice lagoon (Italy). *Marine Pollution Bulletin*, 55(10-12), 425-35. https://doi.org/10.1016/j.marpolbul.2007.09.005
18. **Blanck H., Dahl B.** (1998), Recovery of marine periphyton communities around a Swedish marina after the ban of TBT use in antifouling paint. *Marine Pollution Bulletin*, 36, 6, 437-442. https://doi.org/10.1016/S0025-326X(97)00209-9
19. **Cato I.** (1977), *Recent sedimentological and geochemical conditions and pollution problems in two marine areas in south-western Sweden*. Striae 6, Societas Upsaliensis Pro Geologia Quaternaria, Uppsala. Ed.: Lars-König Königsson. ISBN: 91-7388-005-1, 158.
20. **Chaunsali P., Peethamparan S.** (2011), Evolution of strength, microstructure and mineralogical composition of a CKD–GGBFS binder. *Cement and Concrete Research*, 41, 197–208. https://doi.org/10.1016/j.cemconres.2010.11.010
21. **Dahlin T., Svensson M., Lindh P.** (1999), DC Resistivity and SASW for Validation of Efficiency in Soil Stabilisation Prior to Road Construction. In: *Proceedings EEGS'99*, Budapest, Hungary, 6-9 September 1999, Ls5, 1–3. https://doi.org/10.3997/2214-4609.201406466
22. **De Gisi S., Todaro F., Mesto E., Schingaro E., Notarnicola M.** (2020), Recycling contaminated marine sediments as filling materials by pilot scale stabilization/solidification with lime, organoclay and activated carbon. *Journal of Cleaner Production*, 269, 122416. https://doi.org/10.1016/j.jclepro.2020.122416
23. **Eklund B., Watermann B.** (2018), Persistence of TBT and copper in excess on leisure boat hulls around the Baltic Sea. *Environmental Science and Pollution Research*, 25, 14595–14605. https://doi.org/10.1007/s11356-018-1614-1
24. **Evans S.M.** (1999), Tributyltin Pollution: the Catastrophe that Never Happened. *Marine Pollution Bulletin*, 38, 8, 629-636. https://doi.org/10.1016/S0025-326X(99)00040-5
25. **Fabian K., Schifano V., De Jong J.** (2010), Design and Pilot Tests of Binder Stabilization of Oily Refinery and Dredged Marine Sediments. In: *GeoFlorida 2010*. February 20-24, 2010, Orlando, Florida, United States, 2472–2481. https://doi.org/10.1061/41095(365)251

DOI 10.2478/ama-2021-0030

26. **Faisal A. A., Ahmed D. N., Rezakazemi M., Sivarajasekar N., Sharma G.** (2021), Cost-effective composite prepared from sewage sludge waste and cement kiln dust as permeable reactive barrier to remediate simulated groundwater polluted with tetracycline. *Journal of Environmental Chemical Engineering*, 9, 105194. https://doi.org/10.1016/j.jece.2021.105194
27. **Fan C., Wang B., Qi Y., Liu Z.** (2021), Characteristics and leaching behavior of MSWI fly ash in novel solidification/stabilization binders. *Waste Management*, 131, 277-285. https://doi.org/10.1016/j.wasman.2021.06.011
28. **Fiertak M., Stryszewska T.** (2013), Resistance of three-component cement binders in highly chemically corrosive environments. *Procedia Engineering*, 57, 278–286. https://doi.org/10.1016/j.proeng.2013.04.038
29. **Furdek Turk M., Ivanić M., Dautović J., Bačić N., Mikac N.** (2020), Simultaneous analysis of butyltins and total tin in sediments as a tool for the assessment of tributyltin behaviour, long-term persistence and historical contamination in the coastal environment, *Chemosphere*, 258, 127307. https://doi.org/10.1016/j.chemosphere.2020.127307
30. **Ghavami S., Naseri H., Jahanbakhsh H., Moghadas Nejad F.** (2021), The impacts of nano-SiO2 and silica fume on cement kiln dust treated soil as a sustainable cement-free stabilizer. *Construction and Building Materials*, 285 122918. https://doi.org/10.1016/j.conbuildmat.2021.122918
31. **Ghavami S., Rajabi M.** (2021), Investigating the Influence of the Combination of Cement Kiln Dust and Fly Ash on Compaction and Strength Characteristics of High-Plasticity Clays. *Journal of Civil Engineering and Materials Application*, 5(1), 9-16. https://doi.org/10.22034/jcema.2020.250727.1040
32. **Guerriero V., Mazzoli S., Iannace A., Vitale S., Carravetta A., Strauss C.** (2013), A permeability model for naturally fractured carbonate reservoirs. *Marine and Petroleum Geology*, 40, 115–134. https://doi.org/10.1016/j.marpetgeo.2012.11.002
33. **Hasaballah A. F., Hegazy T., Ibrahim M., El-Emam D. A.,** (2021), Cement kiln dust as an alternative technique for wastewater treatment. *Ain Shams Engineering Journal,* In Press Corrected Proof. https://doi.org/10.1016/j.asej.2021.04.026
34. **Herbich, J. B.** (1990), Extent of Contaminated Marine Sediments and Cleanup Methodology. *22nd International Conference on Coastal Engineering*. July 2-6, 1990, Delft, The Netherlands, pp. 2894-2907. https://doi.org/10.1061/9780872627765.221
35. **Hiller E., Jurkovič L., Faragó T., Vítková M., Tóth R., Komárek M.** (2021), Contaminated soils of different natural pH and industrial origin: The role of (nano) iron- and manganese-based amendments in As, Sb, Pb, and Zn leachability, *Environmental Pollution*, 285, 117268. https://doi.org/10.1016/j.envpol.2021.117268
36. **Houlihan, M., Bilgen, G., Dayioglu, A. Y., Aydilek, A. H.** (2021), Geoenvironmental Evaluation of RCA-Stabilized Dredged Marine Sediments as Embankment Material. *Journal of Materials in Civil Engineering*, 33(1), 04020435. https://doi.org/10.1061/(ASCE)MT.1943-5533.0003547
37. **Källén H., Heyden A., Åström K., Lindh P.** (2016), Measuring and evaluating bitumen coverage of stones using two different digital image analysis methods. *Measurement*, 84, 56–67. https://doi.org/10.1016/j.measurement.2016.02.007
38. **Källén H., Heyden A., Lindh P.** (2014), Estimation of grain size in asphalt samples using digital image analysis. In: *Proceedings of SPIE – The International Society for Optical Engineering*, article number 921714, 921714–921714. https://doi.org/10.1117/12.2061730
39. **Kim N. S., Shim W. J., Yim U. H., Ha S. Y., An J. G., Shin K. H.** (2011), Three decades of TBT contamination in sediments around a large scale shipyard. *Journal of Hazardous Materials*, 192, 2, 634-642. https://doi.org/10.1016/j.jhazmat.2011.05.065
40. **Kuterasińska-Warwas J., Król A.** (2017), Leaching of heavy metals from cementitious composites made of new ternary cements. In: *E3S Web Conference. International Conference Energy, Environment and Material Systems (EEMS 2017)*, 19, 02019, 1-8.
41. **Lemenkov V., Lemenkova P.** (2021a), Measuring Equivalent Cohesion Ceq of the Frozen Soils by Compression Strength Using Kriolab Equipment. *Civil and Environmental Engineering Reports*, 31, 63–84. https://doi.org/10.2478/ceer-2021-0020
42. **Lemenkov V., Lemenkova P.** (2021b), Using TeX Markup Language for 3D and 2D Geological Plotting. *Foundations of Computing and Decision Sciences*, 46 43–69. https://doi.org/10.2478/fcds-2021-0004
43. **Li Y., Bai W., Shi T.** (2017), A study of the bonding performance of magnesium phosphate cement on mortar and concrete. *Construction and Building Materials*, 142, 459–468. https://doi.org/10.1016/j.conbuildmat.2017.03.090
44. **Li, J.-S., Zhou, Y.-F., Wang, Q.-M., Xue, Q.** (2019). Development of a Novel Binder Using Lime and Incinerated Sewage Sludge Ash to Stabilize and Solidify Contaminated Marine Sediments with High Water Content as a Fill Material. *Journal of Materials in Civil Engineering*, 31(10). https://doi.org/10.1061/(ASCE)MT.1943-5533.0002913
45. **Li, J.-S., Zhou, Y.-F., Wang, Q.-M., Xue, Q., Poon, C. S.** (2019), Development of a Novel Binder Using Lime and Incinerated Sewage Sludge Ash to Stabilize and Solidify Contaminated Marine Sediments with High Water Content as a Fill Material. *Journal of Materials in Civil Engineering*, 31(10), 04019245. https://doi.org/10.1061/(ASCE)MT.1943-5533.0002913
46. **Lindh P.** (2001), Optimizing binder blends for shallow stabilisation of fine-grained soils. *Ground Improvement*, 5, 23–34.
47. **Lindh P.** (2003), Mcv and shear strength of compacted fine-grained tills. in: *Proceedings 12th Asian Regional Conference on Soil Mechanics and Geotechnical Engineering*. 4–8 August 2003, Singapore, 493–496.
48. **Lindh P.** (2004), *Compaction- and strength properties of stabilised and unstabilised fine-grained tills*. PhD Thesis. Lund University, Lund. https://doi.org/10.13140/RG.2.1.1313.6481
49. **Lindh P., Dahlin T., Svensson M.** (2000), Comparisons between different test methods for soil stabilisation, in: *Proceedings of the ISRM International Symposium 2000*, IS 2000; Melbourne; Australia. 19-24 November 2000. 1–5.
50. **Lu H., Wei F., Tang J., Giesy J. P.** (2016), Leaching of metals from cement under simulated environmental conditions, *Journal of Environmental Management*, 169, 319-327. https://doi.org/10.1016/j.jenvman.2015.12.008
51. **Majdi H. S., Shubbar A. A., Nasr M. S., Al-Khafaji Z. S., Jafer H., Abdulredha M., Masoodi Z. A., Sadique M., Hashim K.** (2020), Experimental data on compressive strength and ultrasonic pulse velocity properties of sustainable mortar made with high content of GGBFS and CKD combinations. *Data in Brief*, 31 105961. https://doi.org/10.1016/j.dib.2020.105961
52. **Mansour, B.** (2021), Valorization of Metal Milling Waste in Cement Based Mortars Modified by Replacement of Cement Kiln Dust. *The Journal of Solid Waste Technology and Management*, 47(1), 19-30. https://doi.org/10.5276/JSWTM/2021.19
53. **Mizerna K., Król A.** (2018), Leaching of heavy metals from monolithic waste. *Environment Protection Engineering*, 44(4), 143-158. https://doi.org/10.5277/epe180410
54. **Moh Z. C.** (1962), Soil Stabilization with Cement and Sodium Additives. *Journal of the Soil Mechanics and Foundations Division*, 88(6), 81-105. https://doi.org/10.1061/JSFEAQ.0000478
55. **Najim K. B., Mahmod Z. S., Atea A. K. M.** (2014), Experimental investigation on using cement kiln dust (ckd) as a cement replacement material in producing modified cement mortar. *Construction and Building Materials*, 55, 5–12. https://doi.org/10.1016/j.conbuildmat.2014.01.015
56. **Norén, A., Karlfeldt Fedje, K., Strömvall, A.-M., Rauch, S., Andersson-Sköld, Y.** (2021), Low impact leaching agents as remediation media for organotin and metal contaminated sediments. Journal of Environmental Management, 282, 111906. https://doi.org/10.1016/j.jenvman.2020.111906

57. **Nosjean N., Khamitov Y., Rodriguez S., Yahia-Cherif R.** (2020), Fracture corridor identification through 3D multifocusing to improve well deliverability, an Algerian tight reservoir case study. *Solid Earth Sciences*, 5 31–49. https://doi.org/10.1016/j.sesci.2019.11.009
58. **Nyembwe, K.J., Fosso-Kankeu, El., Waanders, F., Mkandawire, M.** (2021), pH-dependent leaching mechanism of carbonatitic chalcopyrite in ferric sulfate solution, *Transactions of Nonferrous Metals Society of China*, 31(7), 2139-2152. https://doi.org/10.1016/S1003-6326(21)65644-3
59. **Pazikowska-Sapota G., Dembska G., Galer-Tatarowicz K., Zegarowski Ł., Littwin M., Holm G., Kreft-Burman K.** (2016), The tests on stabilization of the contaminated sediments for sustainable management in the Baltic Sea region. *Bulletin of the Maritime Institute in Gdańsk*, 31(1), 11-24.
60. **Peethamparan S., Olek J., Lovell J.** (2008), Influence of chemical and physical characteristics of cement kiln dusts (CKDs) on their hydration behavior and potential suitability for soil stabilization. *Cement and Concrete Research*, 38 803–815. https://doi.org/10.1016/j.cemconres.2008.01.011
61. **Rađenović, D., Kerkez, Đ., Tomašević Pilipović, D., Dubovina, M., Grba, N., Krčmar, D., Dalmacija, B.** (2019), Long-term application of stabilization/solidification technique on highly contaminated sediments with environment risk assessment. *Science of The Total Environment*, 684, 186-195. https://doi.org/10.1016/j.scitotenv.2019.05.351
62. **Ribeiro D. V., Morelli M. R.** (2009), Influence of the addition of grinding dust to a magnesium phosphate cement matrix. *Construction and Building Materials*, 23, 3094–3102. https://doi.org/10.1016/j.conbuildmat.2009.03.013
63. **Richardson J. F., Harker J. H., Backhurst J. R.** (2002), Chapter 10 – leaching, in: Richardson, J.F., Harker, J.H., Backhurst, J.R. (Eds.), Chemical Engineering (Fifth Edition). fifth edition ed. Butterworth-Heinemann, Oxford. *Chemical Engineering Series*, 502–541. https://doi.org/10.1016/B978-0-08-049064-9.50021-7
64. **Rimal S., Poudel R. K., Gautam, D.** (2019), Experimental study on properties of natural soils treated with cement kiln dust. *Case Studies in Construction Materials,* 10, e00223. https://doi.org/10.1016/j.cscm.2019.e00223
65. **Sánchez-García, L., Cato, I., Gustafsson, Ö.** (2010), Evaluation of the influence of black carbon on the distribution of PAHs in sediments from along the entire Swedish continental shelf, *Marine Chemistry*, 119, 1–4, 44-51. https://doi.org/10.1016/j.marchem.2009.12.005
66. **Sariosseiri F., Muhunthan B.** (2008), Geotechnical properties of Palouse loess modified with cement kiln dust and Portland cement. In: Proceedings of geocongress 2008, Geochallenge of sustainability in the Geoenvironment, New Orleans, LA.
67. **Schifano, V. and Fabian, K.** (2010). A Laboratory Study of Binder Stabilization of Oily Refinery and Dredged Marine Sediments. In: *GeoFlorida 2010,* February 20-24, 2010, Orlando, Florida, U.S., 2482–2491. https://doi.org/10.1061/41095(365)252
68. **Shah M., Sircar A., Shah V., Dholakia Y.** (2021), Geochemical and Geothermometry study on hot-water springs for understanding prospectivity of low enthalpy reservoirs of Dholera Geothermal field, Gujarat, India. *Solid Earth Sciences*, In Press Corrected Proof. https://doi.org/10.1016/j.sesci.2021.04.004
69. **Sheikh, M. A., Fasih, M. M., Strand, J., Ali, H. R., Bakar, A. H., Sharif, H. M.** (2020), Potential of silicone passive sampler for Tributyltin (TBT) detection in tropical aquatic systems, *Regional Studies in Marine Science*, 35, 101171. https://doi.org/10.1016/j.rsma.2020.101171
70. **Shen W., Shao J., Burlion N., Liu Z.** (2020), A microstructure-based constitutive model for cement paste with chemical leaching effect. *Mechanics of Materials,* 150, 103571. https://doi.org/10.1016/j.mechmat.2020.103571
71. **Shen W., Wu M., Zhang B., Xu G., Cai J., Xiong X., Zhao D.**: (2021), Coarse aggregate effectiveness in concrete: Quantitative models study on paste thickness, mortar thickness and compressive strength. *Construction and Building Materials,* 289, 123171. https://doi.org/10.1016/j.conbuildmat.2021.123171
72. **Shoaei, P., Zolfaghary, S., Jafari, N., Dehestani, M., & Hejazi, M.** (2017), Investigation of adding cement kiln dust (CKD) in ordinary and lightweight concrete. *Advances in Concrete Construction*, 5(2), 101-115. https://doi.org/10.12989/acc.2017.5.2.101
73. **Shoaib M., Balaha M., Abdel-Rahman A.** (2000), Influence of cement kiln dust substitution on the mechanical properties of concrete. *Cement and Concrete Research*, 30 371–377. https://doi.org/10.1016/S0008-8846(99)00262-8
74. **Shubbar A. A., Jafer H., Abdulredha M., Al-Khafaji Z. S., Nasr M. S., Al Masoodi Z., Sadique M.** (2020), Properties of cement mortar incorpo- rated high volume fraction of GGBFS and CKD from 1 day to 550 days. *Journal of Building Engineering*, 30 101327. https://doi.org/10.1016/j.jobe.2020.101327
75. **Silva R., de Brito J., Dhir R.** (2015), Tensile strength behaviour of recycled aggregate concrete. *Construction and Building Materials*, 83 108–118. https://doi.org/10.1016/j.conbuildmat.2015.03.034
76. **Sun, W., Yi, Y.** (2021), Acid washing of incineration bottom ash of municipal solid waste: Effects of pH on removal and leaching of heavy metals. *Waste Management*, 120, 183-192. https://doi.org/10.1016/j.wasman.2020.11.030
77. **Sundqvist, K.L., Tysklind, M., Cato, I., Bignert, A., Wiberg, K.** (2009), Levels and homologue profiles of PCDD/Fs in sediments along the Swedish coast of the Baltic Sea. *Environmental Science and Pollution Research*, 16, 396–409. https://doi.org/10.1007/s11356-009-0110-z
78. **Suzuki, T., Nakase, K., Tamenishi, T., Niinae, M.** (2020), Influence of pH and Cations Contained in Rainwater on Leaching of Cd(II) from Artificially Contaminated Montmorillonite, *Journal of Environmental Chemical Engineering*, 8(5), 104080. https://doi.org/10.1016/j.jece.2020.104080
79. **Sveriges geologiska undersökning** (2021), Kartvisare Miljöövervakning, havs- och sjösediment (accessed 2021-08-18). https://apps.sgu.se/kartvisare/kartvisare-miljoovervakning-sediment.html
80. **Swedish Institute for Standards** (2005), Water quality – Determination of selected organotin compounds – Gas chromatographic method (ISO 17353:2004). https://www.sis.se/api/document/preview/40636
81. **Swedish Institute for Standards** (2014a), Geotechnical investigation and testing – Laboratory testing of soil – Part 1: Determination of water content (ISO 17892-1:2014). https://www.sis.se/api/document/preview/104733/
82. **Swedish Institute for Standards** (2014b), Geotechnical investigation and testing - Laboratory testing of soil – Part 2: Determination of bulk density (ISO 17892-2:2014) https://www.sis.se/en/produkter/environment-health-protection-safety/soil-quality-pedology/physical-properties-of-soils/sseniso1789222014/
83. **Swedish Institute for Standards** (2017a), Geotechnical investigation and testing – Laboratory testing of soil – Part 7: Unconfined compression test (ISO 17892-7:2017). https://www.sis.se/en/produkter/environment-health-protection-safety/soil-quality-pedology/physical-properties-of-soils/ss-en-iso-17892-72018
84. **Swedish Institute for Standards** (2017b), Standard for Geotechnical investigation and testing – Identification, description and classification of rock, ISO 14689:2017. https://www.sis.se/en/produkter/civil-engineering/earthworks-excavations-foundation-construction-underground-works/ss-en-iso-146892018/

85. **Swedish Institute for Standards** (2019), Markundersökningar - Lakningsprocedurer för efterföljande kemisk och ekotoxikologisk provning av jord och jordmaterial - del 4: Påverkan av pH på lakning med initial syra/bas tillsats (ISO 21268-4:2019). https://www.sis.se/produkter/miljo-och-halsoskydd-sakerhet/jordkvalitet-pedologi/provtagning-och-undersokning-av-jord/ss-en-iso-21268-42019/
86. **Swedish Institute for Standards** (2021a), Soil quality – Guidance on leaching procedures for subsequent chemical and ecotoxicological testing of soils and soil materials (ISO 18772:2008) https://www.sis.se/en/produkter/environment-health-protection-safety/soil-quality-pedology/examination-of-soils/sseniso187722014
87. **Swedish Institute for Standards** (2021b). Standard Test Method for Particle-Size Distribution (Gradation) of Fine-Grained Soils Using the Sedimentation (Hydrometer) Analysis. https://www.sis.se/produkter/externa-kategorier/construction-astm-vol-04/soil-and-rock-ii-d5877--latest-astm-vol-0409/astm-d7928-21e1/
88. **Szarek-Gwiazda, E.** (2014), Potential effect of pH on the leaching of heavy metals from sediments of the Carpathian dam reservoirs. *Geology, Geophysics and Environment*, 40(4), 349-358. http://dx.doi.org/10.7494/geol.2014.40.4.349
89. **Taha B., Nounu G.** (2009), Utilizing waste recycled glass as sand/cement replacement in concrete. *Journal of materials in civil engineering,* 21, 709–721. https://doi.org/10.1061/(ASCE)0899-1561(2009)21:12(709)
90. **Tang, P.-P., Zhang, W.-L., Chen, Y.-H., Chen, G., Xu, J.** (2020), Stabilization/solidification and recycling of sediment from Taihu Lake in China: Engineering behavior and environmental impact. *Waste Management*, 116, 1-8. https://doi.org/10.1016/j.wasman.2020.07.040
91. **Turner J. P.,** (1994). Soil Stabilization Using Oil-Shale Solid Waste. *Journal of Geotechnical Engineering*, 120(4), 646–660. https://doi.org/10.1061/(ASCE)0733-9410(1994)120:4(646)
92. **Viani A., Gualtieri A. F.** (2014), Preparation of magnesium phosphate cement by recycling the product of thermal transformation of asbestos containing wastes. *Cement and Concrete Research*, 58, 56–66. https://doi.org/10.1016/j.cemconres.2013.11.016
93. **Wang L., Chen L., Provis J. L., Tsang D. C., Poon C. S.** (2020), Accelerated carbonation of reactive MgO and Portland cement blends under flowing CO_2 gas. *Cement and Concrete Composites*, 106 103489. https://doi.org/10.1016/j.cemconcomp.2019.103489
94. **Wang, D. X., Abriak, N. E., Zentar, R., Xu, W. Y.,** 2011. Geotechnical Properties of Cement-Based Dredged Marine Sediments As a New Pavement Material. In: *GeoHunan International Conference 2011*. June 9-11, 2011, Hunan, China, 85-92. https://doi.org/10.1061/47629(408)11
95. **Wareham, D. G., Mackechnie, J. R**. (2006), Solidification of New Zealand Harbor Sediments Using Cementitious Materials. *Journal of Materials in Civil Engineering*, 18(2), 311-315. https://doi.org/10.1061/(ASCE)0899-1561(2006)18:2(311)
96. **Wojtkiewicz, M., Stasiek, K., Galer – Tatarowicz, K., Pazikowska – Sapota, G., Dembska, G.** (2015), Validation of analytical method for determination of tributyltin (TBT) in soils and bottom sediments. *Bulletin of the Maritime Institute in Gdańsk*, 30(1), 189-194. https://doi.org/10.5604/12307424.1185609
97. **Yaseri S., Masoomi Verki V., Mahdikhani M.** (2019), Utilization of high volume cement kiln dust and rice husk ash in the production of sustainable geopolymer. *Journal of Cleaner Production*, 230, 592–602. https://doi.org/10.1016/j.jclepro.2019.05.056
98. **Yoon, I.-H., Moon, D. H., Kim, K.-W., Lee, K.-Y., Lee, J.-H., & Kim, M. G.** (2010), Mechanism for the stabilization/solidification of arsenic-contaminated soils with Portland cement and cement kiln dust. *Journal of Environmental Management*, 91(11), 2322-2328. https://doi.org/10.1016/j.jenvman.2010.06.018
99. **Zahran E.** (2020), 3D-modeling and lithostratigraphic correlation of the subsurface upper cretaceous Duwi phosphates at Wadi Ash-Shaghab, East Sibaiya area, southern Egypt. *Solid Earth Sciences*, 5 94–102. https://doi.org/10.1016/j.sesci.2020.04.001
100. **Zhang W., Zhao L., Yuan Z., Li D., Morrison L.** (2021), Assessment of the long-term leaching characteristics of cement-slag stabilized/solidified contaminated sediment. *Chemosphere*, 267, 128926. https://doi.org/10.1016/j.chemosphere.2020.128926
101. **Zhang, W.L., McCabe, B.A., Chen, Y.H., Forkan, T.J.** (2018), Unsaturated behaviour of a stabilized marine sediment: A comparison of cement and GGBS binders, *Engineering Geology*, 246, 57-68. https://doi.org/10.1016/j.enggeo.2018.09.020
102. **Zhang, W.-l., Zhao, L.-y., McCabe, B. A., Chen, Y.-h., Morrison, L.** (2020), Dredged marine sediments stabilized/solidified with cement and GGBS: Factors affecting mechanical behaviour and leachability. *Science of The Total Environment*, 733, 138551. https://doi.org/10.1016/j.scitotenv.2020.138551

Acknowledgements: The project has been supported by the Swedish Geotechnical Institute (SGI), Cementa (HeidelbergCement Group), Cowi Consulting Group and the Port of Gothenburg, Sweden. We thank Annika Åberg and Johannes Kikuchi for technical assistance and support. We are grateful to the two anonymous journal referees for their careful reading, review, critics and detailed comments on the text and graphs which improved the initial version of the manuscript.

Per Lindh: https://orcid.org/0000-0002-0577-9936

Polina Lemenkova: https://orcid.org/0000-0002-5759-1089

DOI 10.2478/ama-2021-0031 acta mechanica et automatica, vol.15 no.4 (2021)

SELECTED MORPHOTIC PARAMETERS DIFFERENTIATING ULCERATIVE COLITIS FROM CROHN'S DISEASE

Anna KASPERCZUK*

* Faculty of Mechanical Engineering, Institute of Biomedical Engineering,
Bialystok Technical University, ul. Wiejska 45C, 15-351 Bialystok, Poland

a.kasperczuk@pb.edu.pl

received 22 May 2020, revised 20 September 2021, accepted 24 September 2021

Abstract: This paper presents a method that binds statistical and data mining techniques, which aims to support the decision-making process in selected diseases of the digestive system. Currently, there is no precise diagnosis for ulcerative colitis (UC) and Crohn's disease (CD). Specialist physicians must exclude many other diseases occurring in the colon. The first goal of this study is a retrospective analysis of medical data of patients hospitalised in the Department of Gastroenterology and Internal Diseases, Bialystok, and finding the symptoms differentiating the two analysed diseases. The second goal is to build a system that clearly points to one of the two diseases UC or CD, which shortens the time of diagnosis and facilitates the future treatment of patients. The work focuses on building a model that can be the basis for the construction of action rules, which are one of the basic elements in the medical recommendation system. Generated action rules indicated differentiating factors, such as mean corpuscular volume, platelets (PLTs), neutrophils, monocytes, eosinophils, basophils, alanine aminotransferase (ALAT), creatinine, sodium and potassium. Other important parameters were smoking and blood in stool.

Keywords: action rule, data mining, colon disease, morphotic parameters, smoking

1. INTRODUCTION

Inflammatory bowel diseases (IBDs) are diseases in the course of which, there is chronic inflammation of the gastrointestinal tract. Their conditions are not fully understood, but it is known that immunological, genetic and environmental factors play a role in the pathogenesis of the disease state (Cappello and Morreale, 2016; Crohn et al., 1932). It is possible that the onset of the disease is induced by reactions between these factors. Some sources say that allergic factors, as well as bacterial and viral infections, are also responsible (Crohn et al., 1932). The group of IBDs includes Crohn's disease (CD) and ulcerative colitis (UC) (Cappello and Morreale, 2016). Despite the fact that they are two separate diseases, their differentiation is difficult for clinicians and requires careful analysis of clinical symptoms, endoscopic and radiological examinations and the histopathological picture. Sometimes, it is not possible to classify a case under any of these diseases. This situation occurs in about 10%–15% of diagnosed patients. Then, they are classified into the group indeterminate colitis (Daniluk et al., 2017).

It is extremely important to understand the greater number of UC and CD differentiating factors, as well as the relationships between the parameters, which will contribute to faster diagnosis of new patients and thus improve the quality of diagnosis and treatment (Daniluk et al., 2017).

1.1. Features of CD

CD is a chronic inflammatory disease that can affect any part of the digestive tract. Clinical symptoms most often depend on the location of the inflammatory changes. Literature indicates abdominal pain (most often in the right hip), gas, weight loss, weakness and fever. Other observed symptoms are perianal abscesses. Inflammatory changes in the digestive tract are discontinuous. Additionally, apart from the mucosa, inflammatory changes also affect all other parts of the intestinal wall (Crohn et al. 1932; Dolapcioglu et al., 2014; Kirsner, 1988).

1.2. Features of UC

UC is a chronic inflammatory disease. Symptoms include frequent diarrhoea with blood or mucus. Fistulas and abscesses are rare. Permanent inflammatory changes are located along the entire length of the large intestine in the form of superficial ulcers. The histological picture shows granulocytes and lymphocytic infiltrates of the mucosa. In the advanced stage, i.e. after about 10 years of the disease, changes in epithelial structure in the form of dysplasia may appear, leading to the formation of tumours (Daniluk et al., 2017; Priyamvada et al., 2015).

The development of medicine has contributed to the possibility of using laboratory tests to assess the burden of IBDs, as symptom-based results are too subjective to predict the treatmentoptions properly and to calculate the risk of relapse. In the present study, we were searchedfor features to distinguish CD from UC easily. Laboratory tests are helpful in assessing the activity of each disease. Morphological tests of blood and determination of various biochemical parameters allow the early detection of changes and side effects of therapy.

DOI 10.2478/ama-2021-0031

2. MATERIALS AND METHODS

2.1. Data Collection

The data used in this study were obtained on patients of the Department of Gastroenterology and Internal Diseases of the Medical University of Bialystok Clinical Hospital. The data acquisition process consisted of interviewing patients with IBD and analyzing their medical records. The patients were diagnosed based on clinical symptoms, morphological, and radiological, endoscopic and histological findings.

. Information on the following laboratory results was collected: white blood cells (WBCs) [$\times 10^3/\mu L$], red blood cells (RBCs) [$\times 10^6/\mu L$], mean corpuscular volume (MCV) [fL], platelets (PLTs) [$\times 10^3/\mu L$], neutrophils [$\times 10^3/\mu L$], lymphocytes [$\times 10^3/\mu L$], monocytes [$\times 10^3/\mu L$], eosinophils [$\times 10^3/\mu L$], basophils [$\times 10^3/\mu L$], glucose [mg/dL], bilirubin [mg/dL], aspartate aminotransferase (AspAT) [lU/L], alanine aminotransferase (ALAT) [lU/L], amylase [lU/L], prothrombin time (PT) [sec], international normalised ratio (INR), fibrinogen [mg/dL], urea [mg/dL], creatinine [mg/dL], sodium [mmol/L], potassium [mmol/L] and C-reactive protein (CRP) [mg/dL]. Sociodemographic data were also taken into account: age, gender, smoking (a smoker is a patient who smoked at least a year without interruption). In addition, symptoms of medical conditions such asblood in the stool and a palpable tumour within the abdominal cavity, were taken into account.

2.2. Feature Selection

The selection of features was performed using statistical methods. The Mann–Whitney test was used for comparison of the CD group with the UC group in the case of quantitative data, if the parameters were not shown to be in normal distribution; Student's *t*-test was used if there was compatibility with normal distribution and homogeneity of variance; and Cochran–Cox test was used if compliance with the normal distribution was shown but there was no homogeneity of variance. In the case of comparison of data on the qualitative scale, a chi-square test was used. The Shapiro–Wilk test was used to check compliance with the normal distribution, and the Leven test was used to test homogeneity of variance. The significance level was assumed as α = 0.05. Selected features were used because of the construction of classifiers using three algorithms of knowledge extraction. For the machine learning algorithms, the cross-validation method was used. It involves the division of the studied statistical sample into subsets: the training and the test sets. The analyses are carried out on the training set, while the test set is used to confirm the reliability of the obtained results.

2.3. Action Rules Mining

Many scientific studies show that the use of post-field methods in the analysis of medical data gives opportunities to improve the quality of diagnoses, that too at an early stage (Bebas et al., 2021). This work focuses on using action rule extraction methods.

Let us assume that $S = (X, A, V)$ is an information system, where X is a non-empty, finite set of objects, A is a non-empty, finite set of attributes, V is a set of all attributes' values (Dardzinska, 2014; Ras and Dardzinska, 2011). Then, $a : X \to V_a$ is a function for any $a \in A$, that returns the value of the attribute of a given object. The set of attributes can be divided into three subsets $A = A_1 \cup A_2 \cup D$. Here, A_1 is a set of stable attributes, A_2 is a set of flexible attributes and the set of decision attributes is described by D (Dardzinska, 2014; Han and Kamber, 2006; Dardzinska and Kasperczuk; 2018; Dardzinska and Rpmaniuk, 2016). By stable attributes, we mean attributes with unchangeable values (e.g. age, gender), while for the flexible attributes, the values can be changed (e.g. blood pressure, weight, haemoglobin level). Information systems can be also seen as decision tables with one stable attribute, flexible attributes and the decision attribute d (Gürdal and Dardzinska, 2017; Kasperczuk and Dardzinska, 2019).

Our goal is to find links between the classification and decision attributes. Classification attributes can be represented as measurements, parameters from the patient's test results, personal data, and so on. The decision is a value related to the acquired knowledge, e.g. given directly by an expert or from observation, such as the diagnosis or treatment made. The decision allocated objects from the decision system, thus creating an easy reference model. Then, the acquired knowledge about the relationships between the classification and decision-making attributes will be used to create action rules that will allow us to find the differences between the two decisions.

The modified action rules algorithm in incomplete system (MARAIS) was developed to support the extraction of knowledge from medical information systems, taking into account the specificity of the data contained in them using the conviction measure. MARAIS is an extension of the well-known action rules discovery based on agglomerative strategy (ARAS) algorithm. Using the created algorithm, classification rules were built and action rules were extracted next. From the set of action rules, the knowledge base was created, which was subjected to qualitative analysis. All the rules were characterised by an extremely high level of support and trust and a sufficiently low value of the belief measure. Based on the acquired knowledge, the symptoms differentiating UC and CD were found. Action rules are logical terms defining knowledge for desirable actions related to the hidden objects in a database. The intent here is to concentrate on objective measures for actionability, which is defined as the extent to which a user can gain benefits from the discovered patterns, such as in the medical domain [10, 17]. Suppose an actionable goal of $r = [\omega * (\alpha \to \beta) \to (\theta \to \psi)]$, where ω, α, β, θ and ψ are descriptions of objects, e.g. in the case of patients, where p is described as the satisfaction of a designed condition and the changeable measure of $(\alpha \to \beta)$ for patients who are registered in a database with the expected result $(\theta \to \psi)$. There are two conceivable perspectives in terms of the strategies of actionability. One is the constituent of post-field analysis at the back end of the knowledge discovery system (Dardzinska, 2013). This approach does not utilise the prior knowledge of the expert systems to lead the rule-generation process, which is purely subjective. The other approach is solely objective. It implements the input knowledge of the domain to control the rule generation process, which leads to determination of instrumental knowledge and compares it with some standard beliefs. In this paper, we concentrate on the object-driven approaches of actionability. Object-driven patterns can be generated straightforward from the dataset and then implemented for the final outcome (Dardzinska, 2013; Ras and Dardzinska, 2011). By object-driven action rule *r* in an information system S, the expression can be represented as follows:

$$r = [[(a1 = \omega 1) * (a2 = \omega 2) * \ldots * (aq = \omega q)] * (b1, \alpha 1 \rightarrow \beta 1) * (b2, \alpha 2 \rightarrow \beta 2) * \ldots * (bp, \alpha p \rightarrow \beta p)] \rightarrow [(d, k1 \rightarrow k2)],$$

where $\{b1, b2, \ldots, bp\}$ are flexible and $\{a1, a2, \ldots, aq\}$ are stable attributes in S. Further, it is assumed that $\omega i \in \mathrm{Dom}(ai), i = 1,2, \ldots, q$ and $\alpha i, \beta i \in \mathrm{Dom}(bi), i = 1,2, \ldots, p$. When $(ai = \omega i)$, the value of the attribute becomes ai and is equal to ωi, and $(bj, \alpha j \rightarrow \beta j)$; it shows that value of the attribute bj has been changed from αj to βj. That is to say, object $x \in$ S supports an action rule *r* in S, if there is an object $y \in S$ such that:

$$(\forall i \leq p)[\,[bi(x) = \alpha i] * [bi(y) = \beta i]], (\forall i \leq q)\ [ai(x) = ai(y) = \omega i], d(x) = k1 \text{ and } d(y) = k2.$$

The aforementioned object-driven perspective induces a set of structures that are implemented mathematically to evaluate a dataset. By implementing the objective approach with action rules, some of the chosen objects may be reclassified from one stage to another by modifying some of the relevant flexible attributes. In a previous paper (Dardzinska and Kasperczuk, 2019), we suggested and formulated a simple rule extraction algorithm to build the action rules of a single classification rule, which we named ARAS. It is a bottom–up approach in a breath-first manner to form all frequent item sets with a qualified part of length k, before forming those qualified parts of length $k+1$. More information on the application domain of an experiment of ARAS is available elsewhere (Dardzinska, 2013; Ras and Dardzinska, 2011).

3. RESULTS

In the experiment, we used the data of patients suffering from UC (86 cases) and CD (66 cases). The analysis was based on the construction of action rules and their application to real medical data. We discretised the data of the selected patients and extracted the highest related attributes in test values. Then, we validated the results along with the patients' history and physical examination results. The results are very promising. More than 95% of the patients were correctly reclassified.

The study group consisted of individuals withUC (N N = 86, women N = 32, men N = 54), and patients with CD (N = 66, women N = 32, men N = 34) were diagnosed.

The age of the patients in the study group was 38.05 ± 16.57 years, with the average age of women being 35.97 ± 15.56 years and that of men being 39.57 ± 17.19 years. The mean age in the CD group was 34.42 ± 14.30 years (mean age of women: 36.19 ± 16.90 years; men: 32.76 ± 11.34 years). The mean age in the group of UC patients was 40.84 ± 17.70 years (mean age of women: 35.75 ± 14.37 years; men: 43.85 ± 18.88 years).

Modelling pointed to variables that are significantly different in the analysed groups. Among the biochemical parameters in the blood tests, MCV ($p = 0.013$), PLTs ($p = 0.018$), neutrophils ($p = 0.043$), monocytes ($p = 0.033$), eosinophils ($p = 0.003$), basophils ($p = 0.001$), ALAT ($p = 0.002$), creatinine ($p = 0.017$), sodium ($p < 0.001$) and potassium ($p = 0.018$) were all-significant. Other important parameters were smoking ($p < 0.001$) and blood in stool ($p < 0.001$).

A number of rules were generated, but only those whose level of support, trust and conviction exceeded those assumed were accepted. From the set of rules extracted using the MARAIS algorithm, the following selected set of action rules was generated:

1. $\text{Creatinine} < 0.69\ AND\ \text{blood in stool} = 0\ AND\ \text{smoking} = 0\ AND\ (PLT < 524.5 \Longrightarrow PLT \geq 524.5) \Longrightarrow (UC \Longrightarrow CD)$

Support: 0.140, Confidence: 1.0, Conviction: 0.03

2. $\text{Creatinine} < 0.69\ AND\ \text{blood in stool} = 1\ AND\ (smoking = 0 \Longrightarrow smoking = 1) \Longrightarrow (UC \Longrightarrow CD)$

Support: 0.159, Confidence: 1.0, Conviction: 0.11

3. $\text{Creatinine} \geq 0.69\ AND\ smoking = 0\ AND\ potassium \geq 4.12\ AND\ MCV < 85.73\ AND\ PLT \geq 273\ AND\ (\text{Neutrophils} < 16.22 \Longrightarrow \text{Neutrophils} \geq 16.22) \Longrightarrow (UC \Longrightarrow CD)$

Support: 0.156, Confidence: 1.0, Conviction: 0.19

4. $\text{Creatinine} \geq 0.69\ AND\ smoking = 0\ AND\ potassium \geq 4.12\ AND\ MCV \geq 89.85\ AND\ \text{Creatinine} < 0.81\ AND\ (MCV \geq 95.5 \Longrightarrow MCV < 95.5) \Longrightarrow (UC \Longrightarrow CD)$

Support: 0.143, Confidence: 1.0, Conviction: 0.02

5. $\text{Creatinine} \geq 0.76\ AND\ smoking = 1\ AND\ sodium \geq 137\ AND\ \text{Eosinophils} \geq 0.33\ AND\ sodium < 138.52\ AND\ (MCV \geq 83.68 \Longrightarrow MCV < 83.68) \Longrightarrow (UC \Longrightarrow CD)$

Support: 0.154, Confidence: 1.0, Conviction: 0.17

6. $\text{Creatinine} < 0.69\ AND\ \text{blood in stool} = 0\ AND\ smoking = 0\ AND\ (PLT \geq 524.5 \Longrightarrow PLT < 524.5) \Longrightarrow (UC \Longrightarrow CD)$

Support: 0.103, Confidence: 1.0, Conviction: 0.12

7. $\text{Creatinine} < 0.69\ AND\ \text{blood in stool} = 1\ AND\ (smoking = 0 \Longrightarrow smoking = 1) \Longrightarrow (UC \Longrightarrow CD)$

Support: 0.112, Confidence: 1.0, Conviction: 0.19

4. DISCUSSUION

The characteristics of UC and CD are often ambiguous. and their diagnosis creates many problems that are difficult to overcome (Daniluk et al. 2017). In diagnosis, it is important to make a quick yet accurate diagnosis. Therefore, it is necessary to look for symptoms that directly differentiate the disorders. This will make it possible to build recommendation systems for specialists, accelerate diagnosis and improve the level of medical services.

The constructed action rules indicate the features that, upon change, cause a transition to another group, thus emphasising the differences between the values of the variables in the analysed groups. Action rules extraction was performed using the MARAIS algorithm. All the rules were characterised by an extremely high level of support and trust, as well as a sufficiently low value of the measure of belief, which – at that time – indicated that the values

DOI 10.2478/ama-2021-0031

of the attributes making up the rule were related. The constructed rules indicate parameters that differ significantly in the indicated groups. These include smoking, PLT levels, neutrophil levels and MCV levels. Additionally, they show quantitative differences concerning the levels of the mentioned parameters in the two analysed groups.

Analysis indicated that people who were diagnosed with UC did not smoke in most cases (N = 76). The number of smokers (N = 48) in relation to non-smokers (N = 18) was significantly higher among patients with CD. This indicates a lower risk of UC in the smoking group. The results obtained are confirmed by the literature (Daniluk et al. 2017).

The exact values of the blood parameters that differentiate UC and CD are not known in the literature. Scientists only mention likely differences, but quantitative data is not known (Dolapcioglu et al., 2014). This article shows what levels of significantly different factors determine the occurrence of UC or CD.

CD and UC are characterised by the dispersed accumulation of lymphocytes in the intestinal mucosa. Lymphocytes are cells of the immune system that belong to the granulocytes that are involved in and underlie the immune response. The literature confirms changes in their number in UC and CD patients, but specific levels are not known. It is important to know whether there are any differences in the level of this parameter between UC and CD (Giuffrida et al., 2018; Sarfati et al., 2015; Priyamvada et al., 2015).

Research indicates that eosinophils play a role in the pathogenesis of IBDs. Laboratory examinations revealed the accumulation and activation of eosinophils in the active inflammatory intestinal mucosa in patients with UC and CD. However, there is a lack of accurate quantitative data and their possible distinction in the two diseases analysed in this paper (Kasperczuk et al., 2019; Merigo et al., 2018). Studies indicate that platelet count (PLT) often increases in association with active inflammation, and therefore may be a differentiating factor between UC and CD.

Another blood morphotic parameters reported in the literature are creatinine and urea. Their levels can change in IBDs. Unfortunately, differences in levels of this important parameter between UC and CD are not exactly known (Daniluk et al., 2017).

Additionally, changes in electrolyte absorption in diarrhea are common in IBD. Therefore, this study investigated the differences in sodium and potassium levels in UC and CD, In IBD, changes in the absorption of electrolytes in diarrhoea are frequent. Therefore, the study examined differences in sodium and potassium levels in UC and CD to see whether they are significantly different (Shiffer et al., 2017; Yazici et al., 2010; Zho and Liu, 2017).

Patients in the two analysed groups show significantly different PLT levels. If creatinine is maintained at the level mentioned in the rule, there is no blood in the faeces and the patient is not a smoker, then a PLT level ≥524.5 x10^3/μL will be characteristic of CD and levels lower than that level will indicate UC.

If the patient's creatinine level is <0.69 mg/dL, there is no blood in the faeces and the person is a smoker, the patient will be diagnosed with CD. This indicates that while maintaining this level of creatinine and with the occurrence of blood in the faeces, smoking will indicate CD; otherwise, the patient will belong to the UC group.

The parameter differentiating these diseases is the level of neutrophils in the blood. If the patient has the creatinine, potassium, MCV and PLT levels specified in the rule but is not a smoker, a neutrophil value <16.22 × 10^3/μL will be characteristic of CD and a value ≥16.22 × 10^3/μL is indicative of UC.

For both diseases, while maintaining levels of other parameters, such as creatinine, potassium and smoking, the MCV level may exceed 89.95 fL; values >95.5 fL indicate UC, while levels between 89.85 fL and 95.5 fL are characteristic of CD,.

If the patient's creatinine level is maintained at a level ≥0.76 mg/dL, the patient is a smoker, the sodium is maintained at 137–138.52 mmol/L, the eosinophil count is ≥0.33 × 10 ^ 3/μL and the MCV is ≥83.68 fL, the patient will be assigned to the CD group.

While maintaining appropriate values of parameters and characteristics (the patient's creatinine level is kept <0.69 × 10 ^ 3 /μL, no blood is found in the faeces, the person is a non-smoker), when the PLT value exceeds 524.5 × 10 ^3/μL, patients have UC; otherwise, they are classified as having CD.

While maintaining an adequate level of creatinine (<0.69 × 10 ^ 3 / μL) and in the presence of blood in the faeces, smoking will cause the person to be classified as suffering from CD; otherwise, the classification will be UC.

5. CONCLUSION

In medical and biological systems, the operating rules show very promising results: the physician can investigate the effect of the choice of treatment on the patient's condition. In addition, the rules of operation indicate those features that cause a transition to another group when they are changed, thus emphasising the differences between the values of the variables in the analysed groups. Research shows new values of important parameters that differentiate the IBDs, such as MCV, PLTs, neutrophils, monocytes, eosinophils, basophils, ALAT, creatinine, sodium and potassium. Other important parameters were smoking and blood in stool. This is extremely important because it can accelerate the diagnostic process of IBD patients.

REFERENCES

1. **Bebas E., Borowska M., Derlatka M., Oczeretko E., Hladunski M., Szumowski P., Mojsak M.** (2021) Machine-learning-based classification of the histological subtype o non-small-cell lung cancer using MRI texture analysis. *Biomedical Signal Processing and Control,* vol. 66, 1-6.
2. **Cappello, M.; Morreale, G.C.** (2016) The Role of Laboratory Tests in Crohn's Disease. *Clin Med Insights Gastroenterol*, 9, 51–62.
3. **Crohn B.B., Ginzburg L., Oppenheimer G.D**. (1932) Regional ileitis. A pathologic and clinical entity, *J Am Med Ass*. 99:1323-1329.
4. **Daniluk J, Daniluk U**, Reszec J, Rusak M, Dabrowska M, Dabrowski A.(2017) Protective effect of cigarette smoke on the course of dextran sulfate sodium-induced colitis is accompanied by lymphocyte subpopulation changes in the blood and colon. *Int J Colorectal Dis*, 32, 1551-1559.
5. **Dardzinska A.** (2013), Action Rules Mining. Springer, pp. 90.
6. **Dardzinska A., Kasperczuk A.** (2018), Decision-making Process in Colon Disease and Crohn's Disease Treatment, *Acta Mechanica et Automatica*, Vol. 12 no. 3, pp. 227-231.
7. **Dardzinska A., Romaniuk A.** (2016), Mining of Frequent Action Rules, Machine Intelligence and Big Data in Industry: 6th *International Conference on Pattern Recognition and Machine Intelligence*, 87-95 .
8. **Dolapcioglu, C.; Soylu, A.; Kendir, T.; Ince, A.T.; Dolapcioglu, H.; Purisa, S.(**2014) Coagulation parameters in inflammatory bowel disease. *Int J Clin Exp Med* , 7, 1442–1448.

9. **Giuffrida, P.; Corazza, G.R.; Di Sabatino, A**. (2018) Old and New Lymphocyte Players in Inflammatory Bowel Disease. *Dig Dis Sci*, 63, 277-288.
10. **Gren, S.T.; Grip, O.** (2016) Role of Monocytes and Intestinal Macrophages in Crohn's Disease and Ulcerative Colitis. *Inflamm Bowel Dis*, 22, 1992-8.
11. **Gürdal O., Dardzinska A.** (2017), A New Approach to Clinical Medicine by Action Rules, *International Journal of Development Research,* 7(1), 11032–11039.
12. **Han J., Kamber M.** (2006), Data Mining: Concepts and Techniques, Morgan Kaufmann Publishers, Second Edition, 21-27.
13. **Kasperczuk A, Daniluk J, Dardzinska A. (**2019) Smart Model to Distinguish Crohn's Disease from Ulcerative Colitis. *Appl. Sci*, 9, 1650.
14. **Kasperczuk A. and Dardzinska A**., (2016), Comparative Evaluation of the Different Data Mining Techniques Used for the Medical Database, *Acta Mechanica et Automatica*, Vol. 10 no. 3, pp. 233-238.
15. **Kirsner J.** B. (1988), Historical aspects of inflammatory bowel disease, *J Clin Gastroenterol* ,10:286-297.
16. **Merigo, F.; Brandolese, A.; Facchin, S.; Missaggia, S.; Bernardi, P.; Boschi, F.**; et al. (2018) Glucose transporter expression in the human colon. *World J Gastroenterol*, 24,775-793.
17. **Priyamvada, S.; Gomes, R.; Gill, R.K.; Seksena, S.; Alrefai, W.A.; Dudeja, P.K.** (2015) Mechanisms Underlying Dysregulation of Electrolyte Absorption in IBD Associated Diarrhea. *Inflamm Bowel Dis*, 21, 2926–2935.
18. **Ras Z., Dardzinska A.** (2011), From Data to Classification Rules and Action,. *International Journal of Intelligent Systems*, Wiley, 26(6), 572-590.
19. **Sarfati, M.; Wakahara, K.; Chapuy, L.; Delespesse, G.** (2015) Mutual Interaction of Basophils and T Cells in Chronic Inflammatory Diseases. *Front Immunol*, 6, 399.
20. **Schieffer, K.M.; Bruffy, S.M.; Rauscher, R.; Koltun, W.A.; Yochum, G.S.; Gallagher, C.G**. (2017) Reduced total serum bilirubin levels are associated with ulcerative colitis. *PLoS One*, 12, e0179267.
21. **Yazici, A.; Senturk, O.; Aygun, C.; Celebi, A.; Caglayan, C.; Hulagu, S.** (2010) Thrombophilic Risk Factors in Patients with Inflammatory Bowel Disease. *Gastroenterology Res*., 3, 112–119.
22. **Zho, G.X.; Liu, Z.J. (**2017) Potential roles of neutrophils in regulating intestinal mucosal inflammation of inflammatory bowel disease. *J Dig Dis*, 495-503.

Research was performed as a part of projects WZ/WM-IIB/2/2021 and financed with use of funds for science of MNiSW.

Anna Kasperczuk: https://orcid.org/0000-0002-5919-5346

DOI 10.2478/ama-2021-0032

PERTURBATIONS OF THE DEPTH OF LIQUID PENETRATION INTO THE CAPILLARY DURING BUBBLE DEPARTURES

Paweł DZIENIS*

* Department of Mechanics and Applied Computer Science, Faculty of Mechanical Engineering, Białystok University of Technology ul. Wiejska 45C, 15-351 Białystok, Poland

p.dzienis@pb.edu.pl

received 19 September 2021, revised 18 October 2021, accepted 22 October 2021

Abstract: In the present paper, the influence of bubble size on liquid penetration into the capillary was experimentally and numerically studied. In the experiment, bubbles were generated from a glass capillary (with an inner diameter equal to 1 mm) in a glass tank containing distilled water, tap water or an aqueous solution of calcium carbonate. These liquids differ in the value of their surface tension, which influences the bubble size. During experimental investigations, air pressure fluctuations in the gas supply system were measured. Simultaneously, the videos showing the liquids' penetration into the capillary were recorded. Based on the videos, the time series of liquid movements inside the capillary were recovered. The numerical models were used to study the influence of bubble size on the velocity of liquid flow above the capillary and the depth of liquid penetration into the capillary. It was shown that the air volume flow rate and the surface tension have the greatest impact on the changes of pressure during a single cycle of bubble departure (Δp). The changes in pressure during a single cycle of bubble departure determine the depth of liquid penetration into the capillary. Moreover, the values of Δp and, consequently, the depth of liquid penetration can be modified by perturbations in the liquid velocity above the capillary outlet.

Keywords: bubbles, bubble departures, liquid movement into the capillary

1. INTRODUCTION

The process of gas flow in a liquid is a very complex problem. This process has been researched in many scientific fields: chemical and process engineering, pharmaceuticals, food production and fertiliser production. Understanding the phenomenon of gas flow in a liquid allows better control of processes associated with aeration or saturation (Cano-Lozano et al., 2017). Moreover, knowledge of the flow of gas bubbles in underwater environments is used in the estimation of the global balance of greenhouse gases (Leifer and Tang, 2007; Vázquez et al., 2015).

Research of gas bubbles in liquids concerns the following: bubble formation (Aoyama et al., 2016, Cano-Lozano et al., 2017), bubble coalescence (Farhat et al., 2021), bubble flow and its trajectories (Liu et al., 2015; Augustyniak and Perkowski, 2021) or chaotic bubble behaviour (Zang and Shoji, 2001; Cieslinski and Mosdorf, 2005; Mosdorf and Shoji, 2003). The time period of bubble formation may be divided into two periods: waiting time and time of bubble growth. During the waiting time (for the low air volume flow rates supplied to the capillary or orifice), the capillary is flooded by liquid, caused by a decrease in pressure in the gas supply system after the bubble departure stage (Ruzicka et al., 2009a; Dzienis and Mosdorf, 2014; Cano-Lozano et al., 2017). Subsequently, the liquid is removed from the capillary because the gas pressure inside the gas supply system increases (Koval'chuk et al., 1999).

In previous papers (Ruzicka et al., 2009a, 2009b; Stanovsky et al., 2011; Dzienis and Mosdorf, 2014; Cano-Lozano et al., 2017), the liquid movement inside the orifice or capillary, after bubble departure, was experimentally and numerically investigated. In other papers (Dukhin et al., 1998a; Dukhin et al., 1998b; Koval'chuk, 1999; Ruzicka et al., 2009a; Stanovsky et al., 2011), the influence of plate thickness, orifice diameter, gas chamber volume (volume of gas supply system), height of the liquid column above the orifice outlet, surface tension and viscosity of the liquid on liquid penetration into the orifice or capillary was investigated. In the paper by Ruzicka et al., (2009a), it was concluded that an increase in the chamber volume causes an increase in the time period between two subsequent bubbles. Moreover, an increase in height of the liquid column over the orifice outlet leads to an increase in time period between subsequent bubbles. Ruzicka et al., (2009a, 2009b) experimentally and numerically studied the oscillations of the gas–liquid interface inside the orifice and showed that the gas–liquid interface inside the orifice modifies the duration of bubble formation. This period decreases when the number of oscillations of the gas–liquid interface decreases. Dzienis and Mosdorf (2014) showed that an increase in the volume of the gas supply system causes an increase in the maximum depth of liquid penetration into the capillary. Moreover, chaotic bubble departures are caused by changes in the velocity of liquid flow above the capillary. It can be assumed that perturbations of liquid flow can be amplified by changes in the size of subsequent departed bubbles and consequently cause chaotic variations in the depth of liquid penetration into the capillary.

In the present paper, the influence of the size of a departed bubble on the liquid's velocity and depth of liquid penetration into the capillary was experimentally and numerically studied. In the experiment, bubbles were generated from a glass capillary in a glass tank containing distilled water, tap water or an aqueous solution of calcium carbonate. These liquids are distinguished by their values of surface tension, which influence the size of the departed bubbles. In the numerical simulation, the influence of bubble size on the liquid's velocity above the capillary outlet and on the depth of penetration of the liquid into the capillary was studied. It is shown that the air volume flow rate and the surface tension have the greatest impact on the pressure changes (Δp) during a single cycle of bubble departure. These changes determine the depth of liquid penetration into the capillary. The values of Δp and, consequently, the depth of liquid penetration can be modified by variations in the liquid's velocity above the capillary outlet.

In Section 2 of this paper, the experimental setup and data characteristics are described. Results of the experimental data analysis are shown in Section 3. In Section 4, numerical simulation and its results are described. Finally, in Section 5, the conclusion is given.

2. EXPERIMENTAL SETUP AND DATA CHARACTERISTICS

In the experimental investigations, bubbles were generated in a glass tank (300 × 150 × 700 mm). The schema of the experimental setup is shown in Fig. 1.

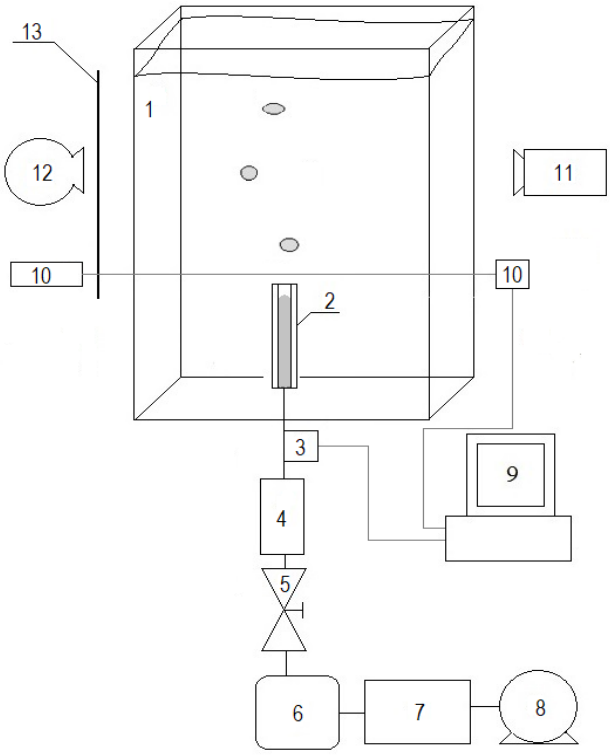

Fig. 1. Experimental setup: 1 – glass tank, 2 - glass capillary, 3 – pressure sensor, 4 - rotameter, 5 – air valve, 6 - air tank, 7 - pressure regulator, 8 - air pump, 9 - computer acquisition system, 10 - laser - phototransistor system, 11 - high speed camera, 12 - light source, 13 - screen.

Bubbles were generated from a glass capillary with inner diameter equal to 1 mm in a glass tank containing distilled water, tap water and aqueous calcium carbonate (c-c in aqueous solution). The surface tension was measured using an STA-1 tensiometer. The accuracy of the tensiometer is equal to 0.1 mN/m. Surface tension of distilled water was 65.3 mN/m, tap water was 72.2 mN/m and calcium carbonate in aqueous solution was 75.4 mN/m.

The capillary was placed at the bottom of the tank. In the first experiment, the tank was filled with distilled water; in the next experiment, the water was removed and the tank was filled with tap water. In the last experiment, the tank was filled with c-c aqueous solution. In all experiments, the liquid temperature was measured with a digital thermometer MAXIM DS18B20 (with an accuracy of 0.1 °C) and was equal to 20 °C. During the experimental investigations, the air volume flow rate was changed. The air volume flow rate was set in the following ranges: for distilled water, 0.005–0.026 l/min; for tap water, 0.005–0.038 l/min; and for c-c aqueous solution, 0.005–0.042 l/min. The step change in air volume flow rate was 0.003 l/min. The air volume flow rates were selected such that liquid penetration into the capillary occurred. In the experiments, the air pressure fluctuations in the gas supply system and videos of the process of liquid penetration into the capillary were recorded. The air pressure fluctuations were measured using the silicon pressure sensor MPX12DP and recorded using the data acquisition system DT9800 series with a sampling frequency of 1 kHz. The pressure in the air tank was set by a proportional pressure reducing valve Metalwork Regtronic. During the experimental investigation, the air pressure was set as 0.3 bar, with an accuracy equal to 0.5%.

The bubble departure process and liquid penetration into the capillary were recorded with a Phantom v1610 high-speed camera. The duration of each video was 30 s. The videos were recorded in grey scale, with a speed of 5,000 fps (frames per second). Videos were divided into frames. The example and selected frames of videos containing one cycle of bubble departure are shown in Fig. 2a. The depth of liquid penetration inside the capillary was measured using a computer programme. The programme counts, on each frame, the number of pixels with high brightness. Bright pixels represent the occurrence of water in the capillary. That programme allows one to receive the time series of liquid penetration into the capillary.

Data from both the high-speed camera and the acquisition station were synchronised using the laser–phototransistor system. The method of synchronisation was described in a previous paper (Dzienis and Mosdorf, 2013). In order to standardise the sampling frequency of the time series of liquid penetration into the capillary and the pressure fluctuations, the time series of pressure fluctuations were re-sampled using a computer programme. Examples of synchronised time series of liquid penetration into the capillary and the pressure fluctuations, for one cycle of bubble departure, are shown in Fig. 2b. The bubble departure occurs at the lowest value of pressure (p_{min}) in the air supply system. During the process of liquid penetration into the capillary, the pressure increases to the maximum value (p_{max}). The onset of bubble growth occurs at the maximum value of pressure (p_{max}), and it causes a decrease of pressure in the gas supply system. It can be concluded that the depth of liquid penetration into the capillary is dependent on pressure fluctuations during one cycle of bubble departure (Δp) (Fig. 2).

When bubbles depart in tap water and c-c aqueous solutions, then increase of air volume flow rate causes the maximum depth of liquid penetration into the capillary to decrease (Fig. 3a). When bubbles depart in distilled water, then for changes in the air volume flow rates within the range of 0.008–0.026 l/min, the maximum depths of liquid penetration were similar to each other. The value of maximum depth of liquid penetration fluctuated in the range of 6.2–6.7 mm (Fig. 3a).

DOI 10.2478/ama-2021-0032

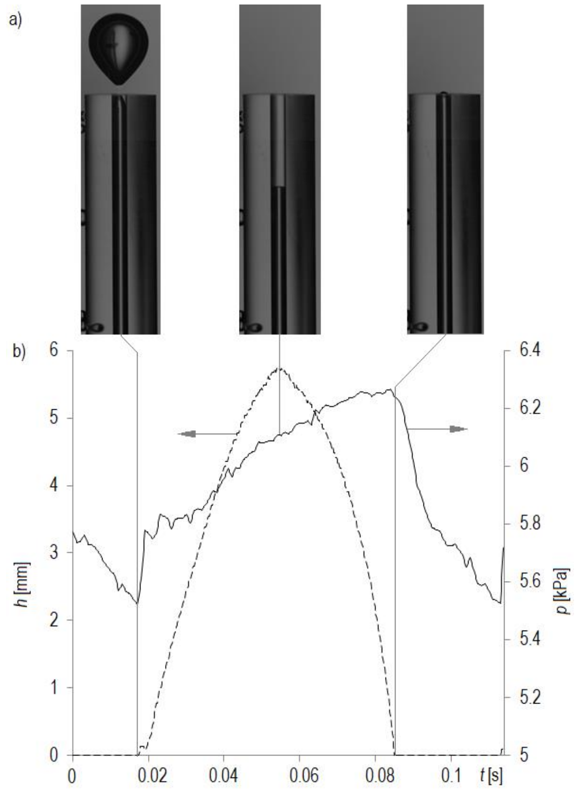

Fig. 2. Examples of video frames and synchronised time series of liquid penetration into the capillary and the pressure fluctuations, for one cycle of bubble departure: (a) frames of videos; (b) time series of liquid penetration into the capillary (dotted line) and the pressure fluctuations (continuous line).

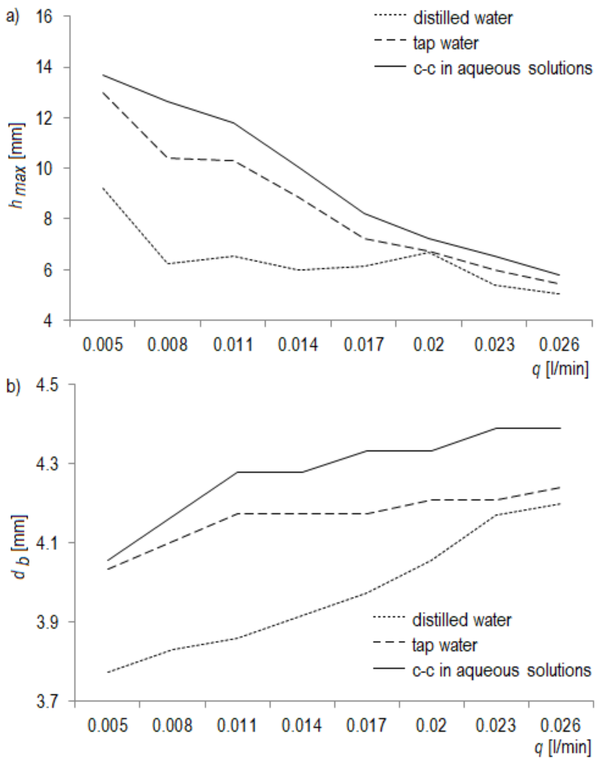

Fig. 3. The changes in maximum depth of liquid penetration into the capillary and departed bubble diameter *vs.* air volume flow rate: (a) maximum depth of liquid penetration into the capillary; (b) bubble diameter just after its departure.

Changes in the bubble diameter (just after its departure) *vs.* air volume flow rate are shown in Fig. 3b. Increase of air volume flow rate causes an increase in the diameters of departed bubbles. The bubble diameter increase *vs.* increase in air volume flow rate is different for the different types of water investigated. The largest increase in diameter of departed bubbles was obtained for bubbles generated in distilled water.

The changes of Δp *vs.* air volume flow rate is presented in Fig. 4. The values of Δp are greater for bubbles generated in tap water and c-c aqueous solution than for bubbles generated in distilled water. Moreover, an increase in air volume flow rate causes a downward trend in the values of Δp for the bubbles departed in tap water and c-c aqueous solution. Another situation is observed in the case of bubble departure in distilled water. The increase of air volume flow rate causes a slight increase in Δp. It can be concluded that the shallower depth of distilled water in the capillary is caused by lower fluctuations of air pressure during a single cycle of bubble departures.

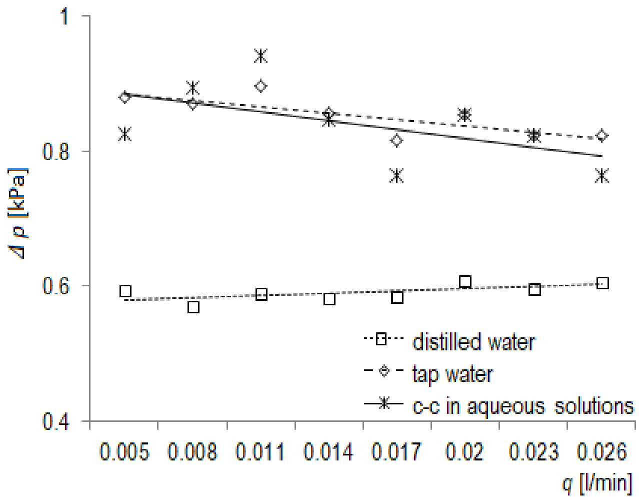

Fig. 4. The changes of Δp *vs.* air volume flow rate for distilled water, tap water and c-c in aqueous solution.

It can be assumed that the changes of Δp and depth of liquid penetration into the capillary, besides the air flow rate, also are dependent on the liquid flow above the capillary generated by departed and moving bubbles. The liquid velocity above the capillary outlet is dependent on the departed bubble's diameter.

3. NUMERICAL SIMULATIONS

The air volume flow rate is one of the most important parameters that influence the maximum depth of liquid movement inside the glass capillary. However, the maximum depth of liquid penetration into the capillary can be indirectly modified by the liquid velocity above the capillary outlet and by modifications of the air pressure fluctuations in the gas supply system (Dzienis and Mosdorf, 2014; Mosdorf et al., 2017). The velocity of liquid flow above the capillary is modified by the diameter of the departed bubble. The schema of liquid flow around a single bubble above the capillary is shown in Fig. 5.

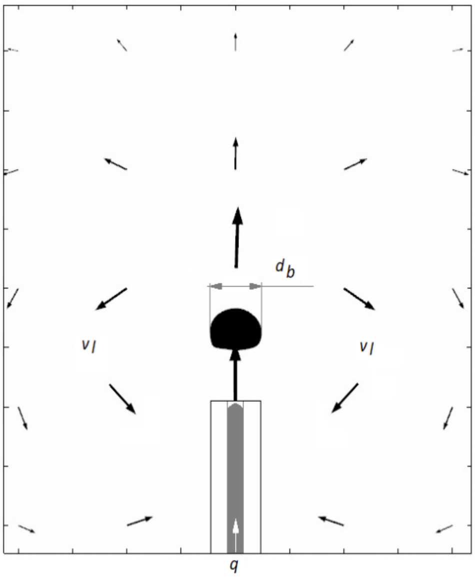

Fig. 5. Schema of liquid flow above the capillary after bubble departure.

The influence of bubble size on liquid velocity above the capillary outlet was numerically studied. The numerical model of bubble departure and bubble flow was prepared in COMSOL Multiphysics with the use of the CFD Module. In this model, the level set method was used (Osher and Sethian, 1988). In this method, the Navier–Stokes equation is solved using the following formulas:

$$\nabla \cdot u = 0 \tag{1}$$

$$\rho \frac{\partial u}{\partial t} + \rho(u \cdot \nabla)u = \nabla \cdot [-pI + \mu(\nabla u + \nabla u^T)] + F + \rho g + \sigma\kappa\delta n \tag{2}$$

where: g – gravity (m/s^2), p – pressure (Pa), t – time (s), u – velocity (m/s) and I - identity matrix. The term $\sigma\kappa\delta n$ denotes the surface tension at the interface, where σ – surface tension coefficient (N/m), κ – curvature, n – is the unit normal to the interface and δ – Dirac delta function concentrated to the interface. The values of κ, n and δ are determined using the following expressions (Osher and Sethian, 1988):

$$n = \frac{\nabla\phi}{|\nabla\phi|} \tag{3}$$

$$\kappa = \nabla\left(\frac{\nabla\phi}{|\nabla\phi|}\right) \tag{4}$$

$$\delta = 6|\nabla\phi||\phi(1+\phi)| \tag{5}$$

The level-set function is a smooth continuous function of ϕ. Near the interface, the function ϕ changes smoothly from '0' to '1'. Regions where ϕ <0.5 show the occurrence of liquid and regions where ϕ >0.5 show the occurrence of gas. The interface is represented by 0.5 contour of the function ϕ (Osher and Sethian, 1988).

The convection of the level set function is described by the following equation:

$$\frac{\partial\phi}{\partial t} + \upsilon \cdot \nabla\phi = 0 \tag{7}$$

The time evolution of the level-set function is described by the following equation (Osher and Sethian, 1988):

$$\frac{\partial\phi}{\partial t} + \upsilon \cdot \nabla\phi = \gamma\nabla \cdot \left(\varepsilon\nabla\phi - \phi(1-\phi)\frac{\nabla\phi}{|\nabla\phi|}\right) \tag{8}$$

The parameter ε determines the thickness of the region in which the function ϕ passes from '0' to '1' and is treated as the size of the elements of the mesh. The parameter γ establishes the re-initialisation or stabilisation numbers of the level-set function (Kass et al., 1987).

The density (ρ) and dynamic viscosity (μ) are described by the following formulas:

$$\rho = \rho_l + (\rho_a - \rho_l)\phi \tag{9}$$

$$\mu = \mu_l + (\mu_a - \mu_l)\phi \tag{10}$$

In Fig. 6, the liquid velocity above the capillary outlet, generated by the moving bubbles (with diameter equal to 3.8 mm, 4.0 mm and 4.2), is presented.

Increase of bubble diameter causes an increase of liquid flow above the capillary outlet. The velocity of liquid flow above the capillary outlet generated by smaller bubbles decreases slower in time than the velocity of liquid flow caused by bigger bubbles (Fig. 6).

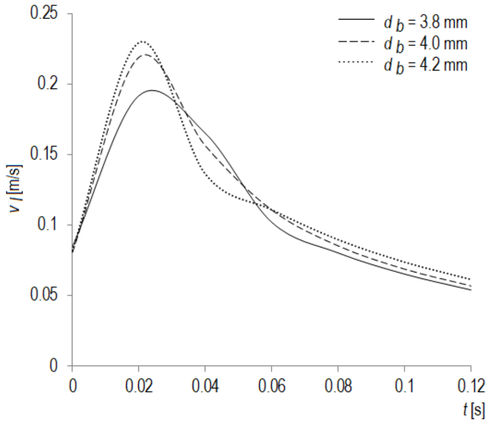

Fig. 6. The liquid velocity above the capillary outlet, generated by moving bubbles with diameter equal to: 3.8 mm, 4.0 mm and 4.2 mm.

In order to determine the influence of liquid velocity above the capillary outlet on liquid penetration into the capillary, the numerical model in SciLab was prepared:

$$\frac{dp_c}{dt} = \frac{p_c}{V_c}\left(q + \pi r_n^2 \frac{dx_l}{dt}\right) \tag{11}$$

$$\frac{d}{dt}\left\{\left[0.5\rho_l\pi r_n^2 x_l + \rho_l \frac{4}{3}\pi(2r_n)^3\right]\frac{dx_l}{dt}\right\} = F_1 - F_2 \tag{12}$$

$$F_1 = -s\Delta p = -\pi r_n^2\left[p_c(t) - \left(p_h + \rho_l g(2x_l) + 2\frac{\sigma}{r_n} - \frac{\rho v_{pp}|v_{pp}|}{2}\right)\right] \tag{13}$$

$$F_2 = 2x8\pi\mu_l x_l \frac{dx_l}{dt} \tag{14}$$

where r_n is the capillary radius (m), x_l is the depth of the liquid penetration into the capillary (m), ρ_l is the liquid density (kg/m^3), μ_l is the liquid viscosity (kg/ms), s is the cross-sectional area of the capillary (m^2), p_c is the gas pressure in the gas supply system (Pa), p_h is the hydrostatic pressure (Pa), v_{pp} is the velocity of the liquid around the growing bubble (m/s), C_o = 2 drag coefficient of moving water inside the capillary.

This model include: the equation of motion of the liquid mass centre, i.e. Eq. (12), and the pressure changes in the air supply system, i.e. Eq. (11) (Ruzicka M.C. et al., 2009b; Dzienis P. and Mosdorf R. 2014). The force F1 in Eq. (13) is related to the pressure difference that occurs in the system. The force F2 in Eq. (14) is related to the resistance to the liquid movement in the capillary. The mass of the liquid that is involved in flooding the capillary is greater than the mass of the liquid inside the capillary. The mass of the liquid that is moving in the capillary is described by : $\frac{4}{3}\rho_l\pi r_n^2 x_l + \rho_l \frac{4}{3}\pi(2r_n)^3$. The reduced mass of the moving liquid is calculated assuming that the kinetic energy of the moving liquid is equal to the kinetic energy of the reduced mass. The profile of the velocity of liquid moving in the capillary is found to have a parabolic velocity profile. Consequently, the mass of the moving liquid is equal to to $\frac{4}{3}\rho_l\pi r_n^2 x_l$, i.e. Eq. (14). The liquid movement stops when the centre of the liquid mass is equal to zero (Ruzicka M.C. et al., 2009b; Dzienis P. and Mosdorf R. 2014).

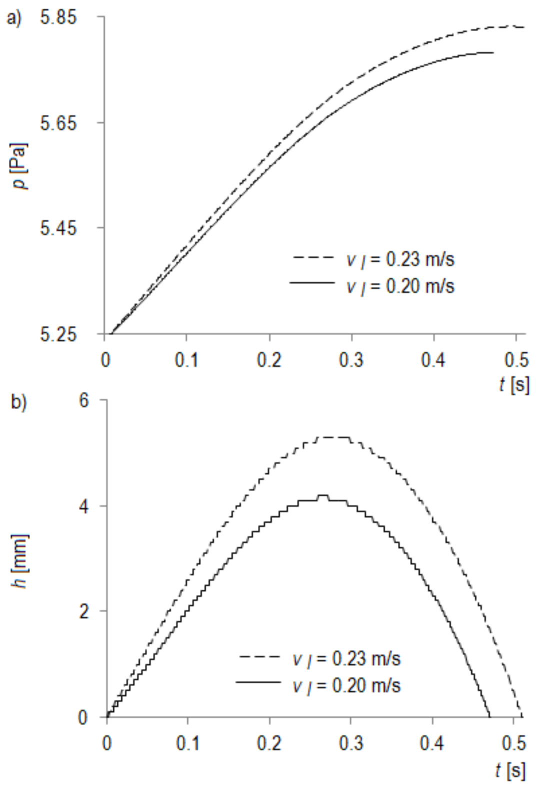

Fig. 7. The pressure changes and the liquid movement into the capillary for a single cycle of bubble departure for liquid velocity above the capillary outlet equal to 0.2 m/s and 0.23 m/s, q = 0.020 l/min, σ = 72 mN/m: (a) the pressure changes; and (b) the liquid movement into the capillary.

During the numerical simulations, the air volume flow rate was equal to 0.020 l/min and the surface tension was equal to 72.2 mN/m. The results of the numerical analysis are shown in Fig. 7. In Fig. 7a, the pressure changes for a single cycle of bubble departure are shown, and in Fig. 7b, the liquid movement into capillary for a single cycle of bubble departure is presented.

The increase in liquid velocity above the capillary causes an increase in the bubble waiting time (Fig. 7a and b). Moreover, the changes in liquid velocity above the capillary outlet cause changes in pressure. When the velocity becomes lower, then the value of p_{max} decreases. Consequently, the value of Δp became lower too (Fig. 7a). When the liquid velocity decreases, the depth of the liquid's penetration inside the capillary increases (Fig. 7b).

The experimental and numerical investigations show that the process of liquid penetration into the capillary during bubble departures is very complex and depends on many factors. The air volume flow rate and the surface tension have the greatest impact on the changes of pressure (Δp) during a single cycle of bubble departure, which determine the depth of liquid penetration into the capillary. Moreover, the values of Δp and the depth of liquid penetration can be modified by variations in liquid velocity above the capillary outlet.

4. CONCLUSIONS

In the present paper, the influence of the size of departed bubbles on the liquid velocity above the capillary and on the depth of liquid penetration into the capillary was experimentally and numerically studied.

The experimental results show that the bubble diameter is dependent on the surface tension and the flow rate of the air volume supplied to the capillary. An increase in surface tension causes an increase in the departing bubble's diameter. Moreover, the changes of surface tension influence the changes of pressure (Δp) during a single cycle of bubble departure. Further, an increase in surface tension causes an increase in Δp. These changes are responsible for the depth of liquid penetration into the capillary. Consequently, an increase in surface tension causes an increase in the depth of liquid penetration.

Based on the results of the numerical investigations, we can see that the liquid velocity above the capillary can modify the changes of pressure (Δp) during a single cycle of bubble departure. When the liquid velocity decreases, Δp decreases. When Δp decreases, the depth of liquid penetration into the capillary decreases, too.

This effect is visible for the case in which bubbles were generated in distilled water. It can be assumed that, on the one hand, the increase in air volume flow rate causes the decrease in Δp. On the other hand, a very large increase in bubble diameter *vs*. increase in air volume flow rate causes the increase in Δp. Consequently, Δp increases slightly (with increase in air volume flow rate) and the liquid penetration into the capillary is almost constant for changes of air volume flow rate.

In order to confirm the numerical investigation of the influence of liquid velocity above the capillary on liquid penetration into the capillary, experimental investigations using the particle image velocimetry method will be performed.

REFERENCES

1. **Aoyama, S., Hayashi, K. Hosokawa, S., Tomiyama A.,** (2016), Shapes of ellipsoidal bubbles in infinite stagnant liquids Int. J. Multiphase. Flow, 79, 23-30.
2. **Augustyniak, J., Perkowski, D. M.,** (2021), Compound analysis of gas bubble trajectories with help of multifractal algorithm, Exp Thermal Fluid Sci., 124, 110351.
3. **Cano-Lozano, J.C., Bolaños-Jiménez, R., Gutiérrez-Montes, C., Martínez-Bazán, C.**, (2017), On the bubble formation under mixed injection conditions from a vertical needle. Int J Multiphase FLows. 97, 23–32.

DOI 10.2478/ama-2021-0032 acta mechanica et automatica, vol.15 no.4 (2021)

4. **Cieslinski, J.T., Mosdorf, R.,** (2005), Gas bubble dynamics experiment and fractal analysis, Int. J. Heat Mass Transfer 48 (9) 1808–1818.
5. **Dukhin S.S., Koval'chuk V.I., Fainerman V.B., Miller R**.,(1998b), Hydrodynamic processes in dynamic bubble pressure experiments Part 3. Oscillatory and aperiodic modes of pressure variation in the capillary, Colloids and Surfaces A: Physicochemical and Engineering Aspects 141, s 253–267.
6. **Dukhin S.S., Mishchuk N.A., Fainerman V.B., Miller R.,** (1998a)., Hydrodynamic processes in dynamic bubble pressure experiments 2. Slow meniscus oscillations, Colloids and Surfaces A: Physicochemical and Engineering Aspects 138 s. 51–63.
7. **Dzienis, P., Mosdorf, R.,** (2013), Synchronization of data recorded using acquisition stations with data from camera during the bubble departure. Adv. Sci. Technol. Res. J. 7 no 20, 29-34.
8. **Dzienis, P., Mosdorf, R.,** (2014) Stability of periodic bubble departures at a low frequency. Chemical Engineering Science. 109, 171–182.
9. **Farhat, M., Chinaud, M., Nerisson, P., Vauquelin, P.,** (2021), Characterization of bubbles dynamics in aperiodic formation, Int J Heat Mass Transfer, 180, 121646.
10. **Kass, M., Witkin, A., Terzopoulos, D.,** (1987), Snakes – Active Contour Models., Int. J. Comp. Vis., 1, 4, 321-331.
11. **Koval'chuk V.I., Dukhin S.S., Fainerman V.B., Miller R.,** (1999), Hydrodynamic processes in dynamic bubble pressure experiments. 4. Calculation of magnitude and time of liquid penetration into capillaries, Colloids and Surfaces A: Physicochemical and Engineering Aspects 151, s 525–536.
12. **Leifer, I., Tang, D.,** (2007), The acoustic signature of marine seep bubbles. J. Acoust. Soc. Am. 121, 35–40.
13. **Liu, L., Yan, H., Zhao, G.,** (2015), Experimental studies on the shape and motion of air bubbles in viscous liquids Exp. Therm. Fluid Sci., 62, 109-121.
14. **Mosdorf, R., Shoji, M.**,(2003), Chaos in bubbling - nonlinear analysis and modelling, Chem. Eng. Sci. 58 (2003) 3837–3846.
15. **Osher, S., Sethian, J. A.,** (1988), Fronts Propagating with Curvature-Dependent Speed: Algorithms Based on Hamilton-Jacobi Formulations. J. Comp. Phys., 79, 1, pp. 12-49.
16. **Ruzicka M.C., R. Bunganic R., Draho˘s J.,** (2009b), Meniscus dynamics in bubble formation. Part II: Model, Chem. Eng. Res. Des., 87, s. 1357–1365.
17. **Ruzicka, M.C., Bunganic, R. Drahos, J.,** (2009a), Meniscus dynamics in bubble formation. Part I: Experiment. Chem. Eng. Res. Des., 87: 1349–1356.
18. **Stanovsky P., Ruzicka M.C., Martins A., Teixeira J.A,** (2011), Meniscus dynamics in bubble formation: A parametric study, Chemical Engineering Science, 66, s. 3258–3267.
19. **Vázquez, A., Manasseh, R., Chicharro, R.** (2015), Can acoustic emissions be used to size bubbles seeping from a sediment bed. 131, 187–196.
20. **Zang L., Shoji M.,** (2001), Aperiodic bubble formation from a submerged orifice, Chemical Engineering Science 56, 5371-5381.

Acknowledgment: I gratefully acknowledge the help of Romuald Paweł Mosdorf (Professor), from Faculty of Mechanical Engineering, Bialystok University of Technology in creating the model of liquid penetration into the capillary.

Paweł Dzienis: https://orcid.org/0000-0001-9200-8760